

HIGH ACCURACY METHODS FOR BOLTZMANN EQUATION AND RELATED KINETIC MODELS

by

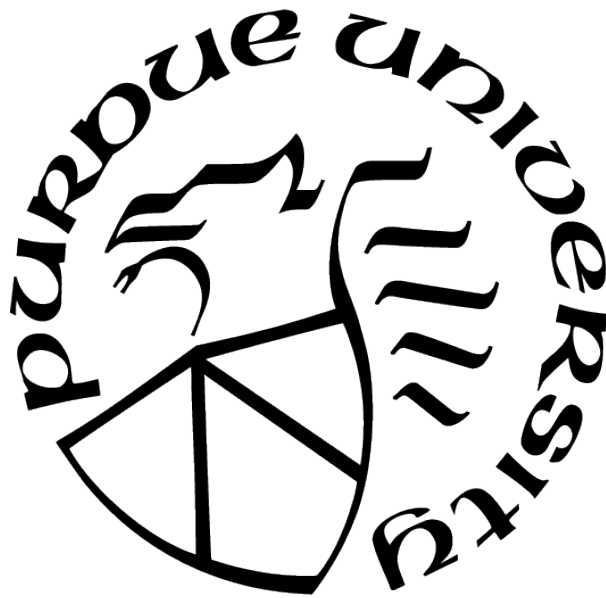
Shashank Jaiswal

A Dissertation

Submitted to the Faculty of Purdue University

In Partial Fulfillment of the Requirements for the degree of

Doctor of Philosophy



School of Aeronautics and Astronautics

West Lafayette, Indiana

May 2021

**THE PURDUE UNIVERSITY GRADUATE SCHOOL
STATEMENT OF COMMITTEE APPROVAL**

Dr. Alina A. Alexeenko, Chair

School of Aeronautics and Astronautics

Dr. Jingwei Hu, Co-Chair

Department of Mathematics

Dr. Gregory A. Blaisdell

School of Aeronautics and Astronautics

Dr. Aaron B. Morris

School of Mechanical Engineering

Approved by:

Dr. William A. Crossley

ACKNOWLEDGMENTS

I would like to extend my gratitude and deepest appreciation to my supervisors Prof. Alina Alexeenko and Prof. Jingwei Hu. Their expertise, understanding, patience and ceaseless support have aided this thesis in innumerable ways.

I am also grateful to Prof. Gregory Blaisdell for his valuable insights, comments, suggestions, and feedback on my Master's thesis which forms the basis of the PhD work. I took one of the best lectures on fluid mechanics from him.

I am also thankful to Dr. Aaron Morris for agreeing to serve on my thesis committee.

I am also thankful to my present and former research peers: Han Luo, Tong Zhu, Gayathri Shivkumar, Israel Sebastiao, Kate Fowee, and Andrew Strongrich for supporting me in a number of ways including technical advice and answers to many queries over the years.

TABLE OF CONTENTS

| | |
|--|----|
| LIST OF TABLES | 7 |
| LIST OF FIGURES | 10 |
| LIST OF SYMBOLS | 16 |
| ABBREVIATIONS | 18 |
| ABSTRACT | 19 |
| 1 INTRODUCTION | 21 |
| 1.1 Numerical methods | 23 |
| 1.2 Collisions and scattering | 25 |
| 1.3 Stiffness issues ($\text{Kn} \rightarrow 0$) | 26 |
| 1.4 Verification and validation | 27 |
| 1.5 Applications | 28 |
| 2 THE EXPLICIT SCHEME FOR BOLTZMANN EQUATION | 30 |
| 2.1 Accurate modelling of diffusion | 30 |
| 2.2 Properties of the collision operator | 31 |
| 2.3 Macroscopic law | 32 |
| 2.4 Non-dimensionalization | 33 |
| 2.5 The fast Fourier spectral method for Boltzmann collision operator | 35 |
| 2.6 The discontinuous Galerkin method for the spatial discretization | 39 |
| 2.7 Discretization in the velocity space | 41 |
| 2.8 The collision operator algorithm | 42 |
| 3 THE IMPLICIT-EXPLICIT SCHEMES FOR BOLTZMANN EQUATION AND RELATED KINETIC MODELS | 46 |
| 3.1 Background and motivation | 46 |
| 3.2 A class of single-species kinetic equations | 49 |

| | | |
|---------|--|-----|
| 3.3 | Non-dimensional form | 51 |
| 3.4 | Implicit-explicit schemes for linear models | 55 |
| 3.4.1 | IMEX-BDF-BGK scheme | 57 |
| 3.4.2 | IMEX-BDF-ESBGK scheme | 58 |
| 3.4.3 | IMEX-BDF-Shakov scheme | 58 |
| 3.5 | Implicit-explicit schemes for Boltzmann equation | 61 |
| 3.5.1 | IMEX-BDF Boltzmann-BGK scheme | 62 |
| 3.5.2 | IMEX-BDF Boltzmann-ESBGK scheme | 63 |
| 3.5.3 | IMEX-BDF Boltzmann-Shakov scheme | 65 |
| 4 | VERIFICATION PROBLEMS | 67 |
| 4.1 | Multi-species: Spatially homogeneous Krook-Wu exact solution | 67 |
| 4.2 | Multi-species: Couette flow | 71 |
| 4.2.1 | Verification | 71 |
| 4.2.1.1 | Bulk properties | 71 |
| 4.2.1.2 | Transport property: Viscosity | 73 |
| 4.2.2 | Scaling Behavior | 75 |
| 4.2.3 | Flat profile | 77 |
| 4.3 | Multi-species: Fourier heat transfer | 77 |
| 4.4 | Multi-species: Oscillatory Couette flow | 81 |
| 4.5 | Multi-species: Normal shock | 81 |
| 4.6 | Multi-species: Self diffusion of Argon-Argon mixture | 85 |
| 4.7 | Multi-species: Mass diffusion of Argon-Krypton mixture | 94 |
| 4.8 | Single species: Spatial and temporal accuracy for a range of Knudsen numbers | 94 |
| 4.9 | Single-species: Couette flow for a range of Knudsen numbers | 102 |
| 4.10 | Single-species: Sod shock tube problem | 107 |
| 4.11 | Single-species: Flow around a micro-electronic chip | 111 |
| 4.11.1 | Numerical details | 112 |
| 4.11.2 | Results and discussion | 113 |
| 4.12 | Single-species: Flow in short microchannels | 115 |

| | | |
|--------|--|-----|
| 4.12.1 | Numerical details | 115 |
| 4.12.2 | Results and discussion | 119 |
| 4.13 | Single-species: Lid-driven cavity flow | 119 |
| 5 | APPLICATION: QUANTIFICATION OF THERMALLY DRIVEN FLOWS IN MICROSYSTEMS | 128 |
| 5.1 | Background and motivation | 128 |
| 5.2 | MIKRA: Micro In-Plane Knudsen Radiometric Actuator | 134 |
| 5.2.1 | Problem Statement | 135 |
| 5.2.2 | Numerical details | 136 |
| 5.2.3 | Results and Discussion | 137 |
| 5.3 | Multi-species MIKRA | 149 |
| 5.3.1 | Problem Statement | 149 |
| 5.3.2 | Numerical details | 150 |
| 5.3.3 | Results and Discussion | 151 |
| 6 | SUMMARY | 154 |
| 7 | RECOMMENDATIONS | 156 |
| | REFERENCES | 157 |
| A | VITA | 171 |

LIST OF TABLES

| | | |
|------|--|-----|
| 3.1 | Coefficients of IMEX-BDF schemes up to third order. | 56 |
| 4.1 | Spatially homogeneous Krook-Wu solution. L^∞ error $\mathcal{E}^{(i)} = \ \partial_t f_{exact}^{(i)} - \partial_t f_{numerical}^{(i)}\ _{L^\infty}$, $i = \{1, 2\}$ at $t = 4$ for different mass ratios. N is the number of discretization points in each velocity dimension and N_ρ is the number of Gauss quadrature points used in the radial direction. Number of quadrature points M used on the sphere is fixed to 6. A fixed velocity domain $[-12, 12]^3$ has been used for all cases. | 70 |
| 4.2 | Numerical parameters for Couette flow [89]. Based upon our observations from Table 4.1, we have used $N_\rho = 8$, in contrast to $N_\rho = 32$ used in [89]. This does not affect the recovered bulk properties as illustrated in Fig. 4.3, however, it speeds up the computation by a factor of 4. | 74 |
| 4.3 | Performance of the solver for Couette flow test cases. The phase-space is defined using a convenient triplet notation $\mathbf{N}_e/\mathbf{K}/\mathbf{N}^3$, which corresponds to \mathbf{N}_e elements in physical space, \mathbf{K} order DG (equivalently $N_p = K - 1$ order polynomial for 1-D domain), and \mathbf{N}^3 points in velocity space. $n\mathbf{G}$ ($n > 1$) denotes GPU/CUDA/MPI/parallel execution on n GPUs shared equally across $(n/3)$ nodes. Work units represent the total simulation time for first 52 timesteps. Efficiency is defined as ratio $(1\mathbf{G}/n\mathbf{G})/n$, where $1\mathbf{G}$ and $n\mathbf{G}$ are execution-times on one GPU and n GPU respectively. $M = 12$ and $N_\rho = 8$ is used for all cases. | 76 |
| 4.4 | Numerical parameters for Fourier heat transfer. The molecular collision parameters for Ar-Kr system are provided in Table 4.7. | 79 |
| 4.5 | Numerical parameters for oscillatory Couette flow. The molecular collision parameters for Ar-Kr system are provided in Table 4.7. | 82 |
| 4.6 | Numerical parameters for normal shock wave [92]. | 84 |
| 4.7 | VHS and VSS model parameters for different mixture systems [24]. | 88 |
| 4.8 | Numerical parameters for Ar-Ar self diffusion. The molecular collision parameters for Ar are provided in Table 4.7. | 89 |
| 4.9 | Numerical parameters for Ar-Kr mass diffusion. The molecular collision parameters for Ar-Kr system are provided in Table 4.7. | 95 |
| 4.10 | Accuracy test for 1D-3V IMEX-BGK equation with $\alpha = 0.49$ | 100 |

| | | |
|------|---|-----|
| 4.11 | Accuracy test for 1D-3V IMEX-ESBGK equation with $\alpha = 0.49 \times 1.5$ | 100 |
| 4.12 | Accuracy test for 1D-3V IMEX-Shakov equation with $\alpha = 0.49$ | 101 |
| 4.13 | Computational cost per time-step per degree of freedom (CPTPD) for 1D-3V IMEX-BGK ($\alpha = 0.49$), IMEX-ESBGK ($\alpha = 0.49 \times 1.5$), and IMEX-Shakov ($\alpha = 0.49$). These cases are run for 100 time-steps, each. For the third order DG scheme that we use, degree of freedom is $3N_e N^3$ with $N = 48$ | 101 |
| 4.14 | Common numerical parameters for Couette flow cases. | 103 |
| 4.15 | Numerical parameters for Couette flow cases. | 103 |
| 4.16 | Performance of the asymptotic and explicit schemes for Couette flow case. Each test-case is conveniently defined by 4 numbers: $(N_e, K, N^3); [-L, L]^3$, which corresponds to N_e elements in physical space, K order DG, N^3 points in velocity space, and L denotes the extent of the isotropic velocity-mesh. The residual is defined as $(\ f^{l+1} - f^n\ _{L^2} / \ f^n\ _{L^2}) / (\ f^2 - f^1\ _{L^2} / \ f^1\ _{L^2})$, where f^n denotes the distribution function at n^{th} timestep. | 106 |
| 4.17 | Numerical parameters for the Sod shock tube problem. The molecular parameters for “Air” are as indicated in Appendix-A of [24]. | 108 |
| 4.18 | N_2 gas VHS parameters used in 2-D single-species DSMC and DGFS simulations. Note that DGFS, being in very early stage of research, treats N_2 as a monoatomic species. | 113 |
| 4.19 | Numerical parameters for flow around micro-electronic chip. | 114 |
| 4.20 | x -component of force on the substrate for MEC-01 case, obtained using DSMC and DGFS simulations. | 114 |
| 4.21 | Numerical parameters for flow in short microchannels. | 118 |
| 5.1 | Numerical parameters for thermo-stress convection in MIKRA Gen1 simulations for DSMC and DGFS using VHS collision model for N_2 molecules. | 136 |
| 5.2 | Numerical parameters for thermo-stress convection in MIKRA Gen1 simulations for DSMC and DGFS using VSS collision model for N_2/H_2O binary mixture. . . | 149 |

| | | |
|-----|---|-----|
| 5.3 | N_2 and H_2O gas VSS parameters used in MIKRA Gen1 DSMC and DGFS simulations. | 150 |
|-----|---|-----|

LIST OF FIGURES

| | | |
|-----|---|----|
| 4.1 | Spatially homogeneous Krook-Wu solution. L^∞ error $\mathcal{E}^{(i)} = \ \partial_t f_{exact}^{(i)} - \partial_t f_{numerical}^{(i)}\ _{L^\infty}$, $i = \{1, 2\}$ at $t = 4$ for different mass ratios. N is the number of discretization points in each velocity dimension and M is the number of spherical design quadrature points used on the sphere. Number of Gauss-Legendre quadrature points N_ρ in the radial direction is fixed to N . A fixed velocity domain $[-12, 12]^3$ has been used for all cases. | 69 |
| 4.2 | Spatially homogeneous Krook-Wu solution. Evolution of $f^{(i)}$, $i = \{1, 2\}$ sliced along the velocity domain centerline, i.e., $f^{(i)}(:, N/2, N/2)$ for different mass ratios. The exact solutions (solid lines) are plotted using $N = 64$. The numerical solutions (symbols) are evaluated using $N = 64$, $M = 6$, $N_\rho = 64$. A fixed velocity domain $[-12, 12]^3$ has been used for all cases. SSP-RK2 with $\Delta t = 0.01$ is used for time stepping. Note that the x-axis has been zoomed to $[-4, 4]$ for better visibility. | 72 |
| 4.3 | Numerical setup for 1D Couette flow. | 73 |
| 4.4 | Variation of normalized y -velocity, and temperature along the domain for Couette flow (Case C-01) obtained with DSMC and DGFS using VSS collision kernel for Argon-Krypton mixture. Symbols denote DSMC solutions, and lines denote DGFS solutions. | 73 |
| 4.5 | Variation of viscosity along the domain for Couette flow (Case C-01) obtained with DSMC and DGFS using VSS collision model for Argon-Krypton mixture. The physical space is discretized using 4 elements: a) $K = 3$, b) $K = 4$. Symbols denote DSMC solutions, and lines denote DGFS solutions. | 75 |
| 4.6 | Percentage of time spent in various parts of Algo. 2 vs. order of DG scheme (K). For both $N^3 = 20^3$ and $N^3 = 32^3$, the collision operator consumes $> 98\%$ of the simulation time. | 78 |
| 4.7 | Variation of normalized temperature $(T^{(i)} - T_l)/(T_r - T_l)$, $i = \{1, 2\}$ along the domain length for Fourier heat transfer obtained with DSMC and DGFS using VHS collision kernel for Argon-Krypton mixture. Symbols denote DSMC solutions, and lines denote DGFS solutions. Numerical parameters are provided in Table 4.4. | 80 |

| | | |
|------|---|----|
| 4.8 | Variation of normalized velocity $u_y^{(i)}/v_a$, $i = \{1, 2\}$ along the domain length for oscillatory Couette flow obtained with DSMC and DGFS using VHS collision model for Argon-Krypton mixture. Symbols denote DSMC solutions, and lines denote DGFS solutions. | 83 |
| 4.9 | Variation of normalized flow properties along the domain for Mach 1.5 normal shock with $n_-^{(2)}/n_- = 0.5$: (a–b) $m_2/m_1 = 0.5$ (Case NS-01) with 8 elements, (c–d) $m_2/m_1 = 0.5$ (Case NS-01) with 16 elements, and (e–f) $m_2/m_1 = 0.25$ (Case NS-02) with 16 elements. Symbols denote results from [92], and lines denote DGFS solutions. Note that the position of the shock wave has been adjusted to the location with the average number density $(n_- + n_+)/2$ as per [92]. | 86 |
| 4.10 | Variation of normalized flow properties along the domain for normal shock with $m_2/m_1 = 0.5$, $n_-^{(2)}/n_- = 0.1$: (a–b) Mach 1.5 (Case NS-03), and (c–d) Mach 3 (Case NS-04). Symbols denote results from [92], and lines denote DGFS solutions. Note that the position of the shock wave has been adjusted to the location with the average number density $(n_- + n_+)/2$ as per [92]. | 87 |
| 4.11 | Variation of number density and diffusion velocity along the domain for self-diffusion cases obtained with DSMC and DGFS using VSS collision kernel for Argon-Argon mixture. Symbols denote DSMC results, and lines denote DGFS results. | 90 |
| 4.12 | Variation of temperature along the domain for self-diffusion cases obtained with DSMC and DGFS using VSS collision kernel for Argon-Argon mixture ($\alpha_{ij} = 1.4$). The physical space is discretized using: a) 4 elements and $K = 3$, b) 8 elements and $K = 4$. Symbols denote DSMC results, and lines denote DGFS results. | 91 |
| 4.13 | Variation of diffusion coefficient along the domain for self-diffusion cases obtained with DSMC and DGFS using VSS collision model for Argon-Argon mixture. Note that only α_{ij} is varied by keeping all other parameters fixed as in Table 4.8. Symbols denote DSMC results, and lines denote DGFS results. | 93 |
| 4.14 | Variation of number density, diffusion velocity, and temperature along the domain for mass-diffusion cases obtained with DSMC and DGFS using VSS collision model for Argon-Krypton mixture. Symbols denote DSMC results, and lines denote DGFS results. | 96 |
| 4.15 | Error decay for linear kinetic schemes. Figure is obtained by taking the maximal \mathcal{E} error, from Tab. (4.10), among all values of ε for a fixed Δt | 99 |

| | | |
|------|--|-----|
| 4.16 | Variation of y -velocity along the domain for Couette flow cases at different Knudsen numbers using IMEX-BDF scheme for linear kinetic models. Lines denote the results from DSMC and symbols denote the results from IMEX-BDF scheme. | 104 |
| 4.17 | Variation of y -velocity along the domain for Couette flow cases at different Knudsen numbers using IMEX-BDF scheme for Boltzmann equation. Lines denote the results from DSMC and symbols denote the results from IMEX-BDF scheme. Boltzmann-BGK refers to Boltzmann equation penalized with BGK operator; Boltzmann-ESBGK refers to Boltzmann equation penalized with ESBGK operator; Boltzmann-Shakov refers to Boltzmann equation penalized with Shakov operator. | 104 |
| 4.18 | Variation of temperature along the domain for Couette flow cases at different Knudsen numbers using IMEX-BDF scheme for linear kinetic models. Lines denote the results from DSMC and symbols denote the results from IMEX-BDF scheme. | 105 |
| 4.19 | Variation of temperature along the domain for Couette flow cases at different Knudsen numbers using IMEX-BDF scheme for Boltzmann equation. Lines denote the results from DSMC and symbols denote the results from IMEX-BDF scheme. Boltzmann-BGK refers to Boltzmann equation penalized with BGK operator; Boltzmann-ESBGK refers to Boltzmann equation penalized with ESBGK operator; Boltzmann-Shakov refers to Boltzmann equation penalized with Shakov operator. | 105 |
| 4.20 | Variation of conserved flow properties, viz. density, mass-flux, and energy for the Sod shock tube problem using asymptotic (A) ESBGK model. The reference compressible Navier-Stokes (C-NS) and Euler (C-Euler) solutions were obtained using a 10000 cell, 2nd order finite volume central scheme based density solver, rhoCentralFoam, available with OpenFOAM-2.3.1. The primary intent, here, is to show conservation properties of the scheme, as well as its capability to capture the Navier-Stokes limit. | 109 |
| 4.21 | Variation of conserved flow properties, viz. density, mass-flux, and energy for the Sod shock tube problem using asymptotic Boltzmann-BGK model. Boltzmann-BGK refers to Boltzmann equation penalized with BGK operator. | 110 |
| 4.22 | Numerical setup for the flow around a micro-electronic chip. | 111 |

| | | |
|------|---|-----|
| 4.23 | Flow properties at steady state for micro-electronic chip obtained from DSMC and DGFS using VHS collision model. For each of these figures, DSMC results (mirrored along y-axis) have been shown in the second quadrant ($-17\mu m \leq x < 0\mu m$), whereas DGFS results have been illustrated in the first quadrant ($0\mu m \leq x < 17\mu m$). Observe the legend for number-density. | 116 |
| 4.24 | Numerical setup for the flow in short microchannels. On the horizontal channel walls, we impose a linearly decreasing temperature profile similar to case I(a) in Ref. [101]. | 117 |
| 4.25 | Flow properties on the horizontal centerline ($y = 0\mu m$) for short microchannel test-case obtained from DSMC and DGFS using VHS collision model. | 119 |
| 4.26 | Flow properties for short microchannel test-case obtained from DSMC and DGFS using VHS collision model. For each of these figures, DSMC results have been shown in the first quadrant ($0\mu m \leq y < 2\mu m$), whereas DGFS results (mirrored along x-axis) have been illustrated in the fourth quadrant ($-2\mu m \leq y < 0\mu m$). Differences in Q_x can be attributed to the fact that DSMC simulations consider rotational degrees-of-freedom of N_2 into account, whereas DGFS doesn't. | 120 |
| 4.27 | Numerical setup for 3-D lid driven cavity flow. | 121 |
| 4.28 | Residual history: $\ f^{n+1} - f^n\ /\ f^n\ _{L_2}$ for different mesh sizes in physical and velocity spaces: (top) $Kn = 0.1$, (bottom) $Kn = 1$. The plot legend is defined using notation N_e^3, N^3 , where N_e refers to number of elements in each direction of physical space, and N refers to number of points in each direction of velocity space. | 122 |
| 4.29 | Variation of shear-stresses on body-diagonals for lid-driven cavity flow at $Kn = 0.1$. Symbols denote DSMC results, dashed lines denote DGFS solutions on diagonal $(10^{-3}, 10^{-3}, 0) - (0, 0, 10^{-3})$ | 124 |
| 4.30 | Variation of flow properties for lid-driven cavity flow at $Kn = 0.1$ from DGFS. | 125 |
| 4.31 | Variation of shear-stresses on body-diagonals for lid-driven cavity flow at $Kn = 1$. Symbols denote DSMC results, dashed lines denote DGFS solutions on diagonal $(10^{-3}, 10^{-3}, 0) - (0, 0, 10^{-3})$ | 126 |
| 4.32 | Variation of flow properties for lid-driven cavity flow at $Kn = 1$ from DGFS. | 127 |
| 5.1 | The CAD model for Gen1 Micro In-Plane Knudsen Radiometric Actuator (MIKRA) [43]. | 134 |

| | | |
|------|---|-----|
| 5.2 | Schematic for numerical simulation of thermo-stress convection in MIKRA Gen1[43]. The interior dashed thin black lines indicate the blocks used for structured mesh generation. Specifically for deterministic DGFS simulations, a linear gradient is applied within blocks such that the cells are finer in the near-vane region. | 135 |
| 5.3 | Spatial mesh used for carrying out DGFS simulations for MIKRA Gen1 device. A linear gradient is applied within blocks such that the cells are finer in the near-vane region. A 3rd order nodal/sem DG scheme has been used. | 138 |
| 5.4 | Variation of flow properties along the domain for MIKRA Gen1 cases (M-01: $\text{Kn} = 1.85$, and M-03: $\text{Kn} = 0.3$) obtained from DSMC (thin black lines), and DGFS (thick red lines). | 139 |
| 5.5 | Continuation of Fig. 5.4. | 140 |
| 5.6 | Sharp curvature in isotherms near the surface of cold vane at $\text{Kn} = 0.3$. This can be interpreted in terms of imbalance of molecules of type <i>A</i> (cold) and type <i>B</i> (hot) at the top-left/top-right ends of the cold vane. | 142 |
| 5.7 | xy component of stress tensor at $\text{Kn} = 0.3$: origin of oval/ellipses at the edges of the vanes. Note the distorted shape of the ellipse between the top-right corner of cold vane and top-left corner of hot vane. Since the temperature gradient is stronger between point <i>A</i> and <i>B</i> , compared to point <i>C</i> and <i>D</i> , we expect the semi-major axis of the ellipse to be larger than the semi-minor axis, and hence the distorted ellipse/oval – an observation consistent with Eqs. (5.1, 5.2) since $\partial T/\partial x \gg \partial T/\partial y$ | 143 |
| 5.8 | Instantaneous streamlines near the vanes of MIKRA Gen1 device at $\text{Kn} = 0.30$ obtained from DGFS using VHS collision model. Observe the vortex formation above the cold vane, and top right corner of hot vane. | 145 |
| 5.9 | Variation of flow speed at steady state for MIKRA Gen1 cases obtained from DSMC and DGFS using VHS collision model. | 147 |
| 5.10 | Variation of flow properties along the domain vertical centerline ($X = 300\mu\text{m}$) for MIKRA Gen1 cases obtained from DSMC (symbols) and DGFS (lines) using VHS collision model. | 148 |

| | | |
|------|--|-----|
| 5.11 | Variation of flow properties along the domain for multi-species MIKRA Gen1 case (MSM-01: $\text{Kn} = 1.85$) obtained with DSMC (thin black lines) and DGFS (thick red lines) using VSS collision model. We want to reemphasize that DSMC simulations consider the rotational degrees of freedom of N_2 and H_2O into account, whereas DGFS, being in very early stages of research, doesn't; and therefore we expect some differences between DSMC and DGFS results. | 153 |
|------|--|-----|

LIST OF SYMBOLS

| | |
|--------------|--|
| v_j | Velocity space coordinates in j direction |
| v_{max} | cut-off limit for velocity space discretization |
| d_{ref} | reference diameter of molecule, m |
| f | distribution function |
| H | H-function |
| k_B | Boltzmann constant |
| Kn | Knudsen number |
| m | mass, kg |
| n | number density, m^{-3} |
| N | number of points in each-direction of velocity space |
| $O()$ | of the order |
| p | pressure, N/m^2 |
| \mathbb{P} | Pressure Stresses, N/m^2 |
| q | Thermal stresses, W/m^2 |
| Pr | Prandtl number |
| R | universal gas constant, J/kgK |
| t | time, s |
| T | temperature, K |
| T_{ref} | Reference temperature, K |
| U_{ref} | Reference velocity, m/s |
| x_i | Physical space coordinates in i direction |
| Δ | increment of change of quantity |
| λ | mean free path of gas |
| κ | thermal conductivity, W/mK |
| μ | dynamic viscosity, $kg/m.s$ |
| μ_{ref} | Reference dynamic viscosity, $kg/m.s$ |
| ρ | mass density, kg/m^3 |
| ν | collision frequency, s^{-1} |

\otimes tensor product

Subscripts:

w Wall condition

in Inlet condition

ABBREVIATIONS

| | |
|--------|--------------------------------------|
| Ar | Argon gas |
| BGK | Bhatnagar-Gross-Krook |
| CFD | Computational Fluid Dynamics |
| CPU | Central Processing Unit |
| DSMC | Direct Simulation Monte Carlo |
| DGFS | Discontinuous Galerkin Fast Spectral |
| ES-BGK | Ellipsoidal Statistical BGK |
| FVM | Finite Volume Method |
| GPU | Graphics Processing Unit |
| HS | Hard sphere |
| NSF | Navier-Stokes Fourier |
| PDF | probability distribution function |
| RMS | Root Mean Square |
| VHS | Variable Hard Sphere |
| VSS | Variable Soft Sphere |
| WENO | Weighted Essentially Non-Oscillatory |

ABSTRACT

The Boltzmann equation, an integro-differential equation for the molecular distribution function in the physical and velocity phase space, governs the fluid flow behavior at a wide range of physical conditions, including compressible, turbulent, as well as flows involving further physics such as non-equilibrium internal energy exchange and chemical reactions. Despite its wide applicability, deterministic solutions of the Boltzmann equation present a huge computational challenge, and often the collision operator is simplified for practical reasons, hereby, referred to as linear kinetic models. These models utilize the moment of the underlying probability distribution to mimic some properties of the original collision operator. But, just because we know the moments of a distribution, doesn't mean we know the actual distribution. The approximation of reality can never supersede the reality itself. Because, all the facts (moments) about the world (distribution) cannot explain the world. The premise lies not in the fact that a certain flow behavior can be correctly predicted; but rather that the Boltzmann equation can reveal and explain previously unsuspected aspects of reality.

Therefore, in this work, we introduce accurate, efficient, and robust numerical schemes for solving the multi-species Boltzmann equation which can model general repulsive interactions. These schemes are high order spatially and temporally accurate, spectrally accurate in molecular velocity space, exhibit nearly linear parallel efficiency on the current generation of processors; and can model a wide-range of rarefied flows including flows involving momentum, heat, and diffusive transport. The single-species variant formed the basis of author's Masters' thesis.

While the first part of the dissertation is targeted towards multi-species flows that exhibit rich non-equilibrium phenomenon; the second part focuses on single-species flows that do not depart significantly from equilibrium. This is the case, for example, in micro-nozzles, where a portion of flow can be highly rarefied, whereas others can be in near-continuum regime. However, when the flow is in near-continuum regime, the traditional deterministic numerical schemes for kinetic equations encounter two difficulties: a) since the near-continuum is essentially an effect of large number of particles in an infinitesimal volume, the average time

between successive collisions decrease, and therefore the discrete simulation timestep has to be made smaller; b) since the number of molecular collisions increase, the flow acquires steady state slowly, and therefore one needs to carry out time integration for large number of time steps. Numerically, the underlying issue stems from stiffness of the discretized ordinary differential equation system. This situation is analogous to low Reynolds number scenario in traditional compressible Navier-Stokes simulations. To circumvent these issues, we introduce a class of high order spatially and temporally accurate implicit-explicit schemes for single-species Boltzmann equation and related kinetic models with the following properties: a) since the Navier-Stokes can be derived from the asymptotics of the Boltzmann equation (using Chapman-Enskog expansion [1]) in the limit of vanishing rarefaction, these schemes preserve the transition from Boltzmann to Navier-Stokes; b) the timestep is independent of the rarefaction and therefore the scheme can handle both rarefied and near-continuum flows or combinations thereof; c) these schemes do not require iterations and therefore are easy to scale to large problem sizes beyond thousands of processors (because parallel efficiency of Krylov space iterative solvers deteriorate rapidly with increase in processor count); d) with use of high order multi-stage time-splitting, the time integration over sufficiently long number of timesteps can be carried out more accurately. The extension of the present methodology to the multi-species case can be considered in the future.

A series of numerical tests are performed to illustrate the efficiency and accuracy of the proposed methods. Various benchmarks highlighting different scattering models, different mass ratios, momentum transport, heat transfer, and diffusive transport have been studied. The results are directly compared with the direct simulation Monte Carlo (DSMC) method. As an engineering use-case, the developed methodology is applied for the study of thermal processes in micro-systems, such as heat transfer in electronic-chips; and primarily, the ingeniously Purdue-developed, Microscale In-Plane Knudsen Radiometric Actuator (MIKRA) sensor, which can be used for flow actuation and measurement.

1. INTRODUCTION

Boltzmann equation describes how a distribution of molecules change when they collide with each other. Boltzmann statistics is a general framework. Applications include, the conventional Boltzmann equation for gaseous transport [2], phonon Boltzmann for phonon transport [3], Vlasov-Maxwell-Boltzmann/Fokker-Planck-Landau for ionic transport in charged plasmas [4], quantum Boltzmann for transport processes in Fermi/Bose gases [5], semiconductor Boltzmann for electronic transport in semi-conductor devices [6], relativistic Boltzmann for astrophysical evolution of the galaxy [7], generalized (active particles) Boltzmann for epidemics and virus mutations [8], etc. Specifically, the Boltzmann equation for gaseous transport is an integro-differential equation for the molecular distribution function in the physical and velocity phase space which governs the fluid flow behavior for a wide range of physical conditions, including compressible, turbulent, as well as flows involving further physics such as non-equilibrium internal energy exchange and chemical reactions.

More precisely, suppose we consider a gas mixture of s species ($s \geq 2$), each represented by a distribution function $f^{(i)}(t, x, v)$, where $t \geq 0$ is the time, $x \in \Omega \subset \mathbb{R}^3$ is the position, and $v \in \mathbb{R}^3$ is the particle velocity; such that $f^{(i)} dx dv$ gives the number of particles of species i to be found in an infinitesimal volume $dx dv$ centered at the point (x, v) of the phase space. The time evolution of $f^{(i)}$ is described by the multi-species Boltzmann equation written as [2], [9]

$$\partial_t f^{(i)} + v \cdot \nabla_x f^{(i)} = \sum_{j=1}^s \mathcal{Q}^{(ij)}(f^{(i)}, f^{(j)}), \quad i = 1, \dots, s. \quad (1.1)$$

Here $\mathcal{Q}^{(ij)}$ is the collision operator that models the binary collisions between species i and j , and acts only in the velocity space:

$$\mathcal{Q}^{(ij)}(f^{(i)}, f^{(j)})(v) = \int_{\mathbb{R}^3} \int_{S^2} \mathcal{B}_{ij}(v - v_*, \sigma) \left[f^{(i)}(v') f^{(j)}(v'_*) - f^{(i)}(v) f^{(j)}(v_*) \right] d\sigma dv_*, \quad (1.2)$$

where (v, v_*) and (v', v'_*) denote the pre- and post- collision velocity pairs. During collisions, the momentum and energy are conserved:

$$\begin{aligned} m_i v + m_j v_* &= m_i v' + m_j v'_*, \\ m_i |v|^2 + m_j |v_*|^2 &= m_i |v'|^2 + m_j |v'_*|^2, \end{aligned} \quad (1.3)$$

where m_i, m_j denote the mass of particles of species i and j respectively. Hence one can parameterize v' and v'_* as follows

$$\begin{aligned} v' &= \frac{v + v_*}{2} + \frac{(m_i - m_j)}{2(m_i + m_j)}(v - v_*) + \frac{m_j}{(m_i + m_j)}|v - v_*|\sigma, \\ v'_* &= \frac{v + v_*}{2} + \frac{(m_i - m_j)}{2(m_i + m_j)}(v - v_*) - \frac{m_i}{(m_i + m_j)}|v - v_*|\sigma, \end{aligned} \quad (1.4)$$

with σ being a vector varying on the unit sphere S^2 . $\mathcal{B}_{ij} = \mathcal{B}_{ji}(\geq 0)$ is the collision kernel characterizing the interaction mechanism between particles. It can be shown that

$$\mathcal{B}_{ij} = B_{ij}(|v - v_*|, \cos \chi), \quad \cos \chi = \frac{\sigma \cdot (v - v_*)}{|v - v_*|}, \quad (1.5)$$

where χ is the deviation angle between $v - v_*$ and $v' - v'_*$.

Given the interaction potential between particles, the specific form of B_{ij} can be determined using the classical scattering theory:

$$B_{ij}(|v - v_*|, \cos \chi) = |v - v_*| \Sigma_{ij}(|v - v_*|, \chi), \quad (1.6)$$

where Σ_{ij} is the differential cross-section given by

$$\Sigma_{ij}(|v - v_*|, \chi) = \frac{b_{ij}}{\sin \chi} \left| \frac{db_{ij}}{d\chi} \right|, \quad (1.7)$$

with b_{ij} being the impact parameter.

Given the distribution function $f^{(i)}$, the physical observables, i.e., the number density, mass density, velocity, and temperature of species i are defined as

$$n^{(i)} = \int_{\mathbb{R}^3} f^{(i)} dv, \quad \rho^{(i)} = m_i n^{(i)}, \quad u^{(i)} = \frac{1}{n^{(i)}} \int_{\mathbb{R}^3} v f^{(i)} dv, \quad T^{(i)} = \frac{m_i}{3n^{(i)}k_B} \int_{\mathbb{R}^3} (v - u^{(i)})^2 f^{(i)} dv. \quad (1.8)$$

The total number density, mass density, and velocity are given by

$$n = \sum_{i=1}^s n^{(i)}, \quad \rho = \sum_{i=1}^s \rho^{(i)}, \quad u = \frac{1}{\rho} \sum_{i=1}^s \rho^{(i)} u^{(i)}. \quad (1.9)$$

Further, the diffusion velocity, stress tensor, and heat flux vector of species i are defined as

$$v_D^{(i)} = \frac{1}{n^{(i)}} \int_{\mathbb{R}^3} c f^{(i)} dv = u^{(i)} - u, \quad \mathbb{P}^{(i)} = \int_{\mathbb{R}^3} m_i c \otimes c f^{(i)} dv, \quad q^{(i)} = \int_{\mathbb{R}^3} \frac{1}{2} m_i c |c|^2 f^{(i)} dv, \quad (1.10)$$

where $c = v - u$ is the peculiar velocity. Finally, the total stress, heat flux, pressure, and temperature are given by

$$\mathbb{P} = \sum_{i=1}^s \mathbb{P}^{(i)}, \quad q = \sum_{i=1}^s q^{(i)}, \quad p = nk_B T = \frac{1}{3} \text{tr}(\mathbb{P}). \quad (1.11)$$

1.1 Numerical methods

The approaches for numerical solution of the Boltzmann equation date back to as early as 1940s [10] using, for example, the now widely used direct simulation Monte Carlo (DSMC) method [11], [12]. Over sufficient small intervals, by decoupling the molecular motion and interaction processes, DSMC first advects the particles deterministically according to their velocities, also termed as *free transport*, and then describes the collisions by statistical models with a specified interaction potential. Under the assumption that molecular interactions are Markov processes, in the limit of infinite number of particles $N \rightarrow \infty$, Wagner established the convergence of Bird's DSMC method to the Boltzmann equation [13]. DSMC is widely used for simulating high-speed phenomena, whereas low-speed and unsteady flows are less

tractable by stochastic simulations due to the inherent statistical noise. It is this stochastic nature of the method that introduces high statistical noise in low-speed flows, and imposes strict constraints on cell-size and time-step. Moreover, the formal accuracy of particle time-stepping is linear. The stiffness properties of the Boltzmann equation further aggravates the time-step constraints. To overcome these limitations, improved particle-based approaches have been proposed [14], including hybrid continuum/particle solvers [15], [16], variance reduction methods [17], and simplified Bernoulli trials [18]; but these ideas have been rarely used beyond the academic research setting even in the new generation of DSMC solvers [19].

The other approaches are the deterministic methods based on discretization of governing differential equations on representative grids. These deterministic methods are free of statistical noise, and are suitable for studying low speed flows. However, the multi-dimensional nature of the Boltzmann equation and the collision integral becomes a bottleneck resulting in excessive use of time and computing resources. The main difficulty lies in its quadratic collision term since quadratic algorithmic complexity is difficult to apply to large problem sizes. Not surprisingly, over the past years, the deterministic methods that approximate the Boltzmann collision operator/equation have undergone considerable development. A comprehensive review can be found in [20], [21]. Of all these, the fastest known, based on Fourier transforms, are referred to as *fast Fourier spectral method* [22]. The complexity for a single evaluation of the collision operator is reduced from $O(N^2)$ (quadratic complexity / direct calculation) to $O(N \log N)$, where N is a measure of the *discrete* velocity space, $N = \dim v$, $v \in \mathbb{R}^3$. But the approach in [22] is valid for single-species *hard-sphere (HS)* interactions (HS model deviates from experimental observations [23]); and is, therefore, rather, a technology demonstrator; and difficult to apply for problems of engineering significance.

This leads to the following objective:

Objective 1. *Construct a deterministic, accurate, robust, and efficient method for solving the multi-species Boltzmann equation of some engineering value.*

1.2 Collisions and scattering

The choice of interaction potential substantially affects the simulation fidelity and computational complexity. There has been a significant development in this regard in the DSMC community. DSMC has a rich development history, and we want to leverage and build a future upon the shoulders of the past. Early implementations of the DSMC method relied on purely repulsive HS interaction model [11]. The HS model, however, deviates from experimental observations for common gases [23] due to a square-root viscosity variation with temperature. The variable hard sphere (VHS) model proposed by Bird [24] results in a more general power-law viscosity variation with temperature; and has been widely used for DSMC simulations of *single-species* gas flows due to its computational efficiency and ease of implementation. The VHS model, however, deviates from experimental observations for common *multi-species* flows [25], [26] involving diffusive transport. Later, several variations of the VHS model were proposed, including, the variable soft sphere (VSS) [26], M-1 [27], generalized soft sphere (GSS) [28], all of which belong to a class of repulsive interactions. The VSS model modifies the scattering law of the VHS model by using a scattering parameter (α) that allows reproduction of measured diffusion coefficients in addition to the viscosity coefficient. M-1 model is a modification of VHS model to have a linear distribution of scattering angles in terms of the impact parameter. This modification allows M-1 to reproduce correct viscosity and diffusivity without the need of an additional parameter (α) [29]. The GSS model, although general, needs additional parameters for reproducing the viscosity and diffusion coefficients (see Ref. [24], [30] for additional details/equations for these models).

A deterministic method for general repulsive interactions with $O(N^{4/3} \log N)$ complexity was devised for spatially homogeneous single-species Boltzmann equation in [31]; and extended to spatially non-homogeneous case with high-order spatial/temporal accuracy in author's Masters' thesis [32].

This leads to the following objective:

Objective 2. *Construct a deterministic method for multi-species Boltzmann equation that can handle general repulsive interactions: the special cases of these are the aforementioned, which are widely used in DSMC simulations. The formulation should be consistent with kinetic theory and DSMC. This ensures that the results from deterministic method can be verified easily; which in turn helps with easy adaptation of the method.*

1.3 Stiffness issues ($\text{Kn} \rightarrow 0$)

The efficiency of a conventional kinetic simulation, deterministic or stochastic, is directly correlated to the degree of rarefaction. A widely-used indicator of rarefaction is Knudsen number, Kn , defined as the ratio of the gas mean free path λ , i.e., on average the distance travelled by a molecule before it collides with another; and the characteristic length H_0 of the system. When the Knudsen number, Kn , of flow is decreased, the *explicit* deterministic numerical schemes for Boltzmann equation encounters two difficulties: a) since the mean collision time (average time elapsed between successive collisions) decreases, the timestep has to be made smaller, b) since the number of collisions per unit volume increase, the entropy generation process is slowed down (implications of Cercignani’s conjecture, Villani et al. [33]), the flow acquires steady state slowly, and therefore one needs to carry out time integration for large number of time steps.

The stiffness issues are not limited to the kinetic equations. For example, an explicit scheme for Large eddy simulations at low Mach numbers is too slow; whereas an implicit scheme is too computationally expensive for problems of practical interest. Moreover, the implicit schemes require iterations, and hence are difficult to scale on large problem sizes beyond ten thousand processors. This realization has been a driving force behind the use of implicit-explicit (IMEX) schemes in CFD, for example, large eddy simulations [34], [35]. An IMEX scheme integrates stiff parts of an ordinary differential equation (ODE) implicitly and the non-stiff parts explicitly in time. These schemes help avoid iterations as much as possible, and can be computationally efficient than both fully-implicit and fully-explicit schemes.

Objective 3. *Construct an implicit-explicit scheme for the stiff Boltzmann equation for single-species case ($s = 1$) to begin with. Such a scheme should have the following properties:*

- 1) the timestep should be independent of the Knudsen number*
- 2) the collision kernel should be evaluated explicitly without use of any iteration*
- 3) it should utilize high order time-stepping so that the time integration over sufficiently long number of timesteps, needed for modelling near-continuum flows, can be carried out more accurately*
- 4) it should be high order accurate in physical space for minimum dispersion*
- 5) it should be applicable for modelling both rarefied and near-continuum compressible flows.*
- 6) When Kn is small, $O(10^{-3})$, Navier-Stokes can be recovered from the asymptotics of the Boltzmann equation. Hence, the results from the implicit-explicit Boltzmann equation should be consistent with that recovered from Navier-Stokes.*

1.4 Verification and validation

The developed schemes should be verified and validated on a number of benchmark problems. Proper validation and verification (V&V) insures reproducibility. Reproducibility develops an implicit trust with the end-user, and hence helps with the wider adoption of the developed methods.

Objective 4. *Construct a large set of validation and verification problems that can assess the capability of the developed numerical scheme and the associated implementation:*

- validation and verification problems should cover problems involving mass, momentum, energy, and diffusive transport.*
- the scheme should run in 2-D, 3-D.*

- *the scheme should be able to handle general boundary conditions: periodic, Dirichlet, time-evolving.*
- *the scheme should be stable for different initial/boundary conditions.*
- *the scheme should be high order accurate.*
- *the scheme should be able to deal with stiff problems.*

1.5 Applications

The deterministic methods can accurately describe a wide range of non-continuum flow phenomena such as shocks, expansions into vacuum [36] as well as velocity and thermal slip at gas-solid interfaces [37], [38], and thermally-induced slow flows at microscale. As an application of the developed methodology, we will apply the developed scheme for the latter case, i.e., study of low-speed flows in micro-electro mechanical systems.

Under sufficiently rarefied flow conditions, an application of temperature gradient, say, between two parallel plates separated by few mean free paths, induces a low velocity gas flow commonly identified as thermo-stress convection effects [39] which, for example, gives rise to well-known Crooke's [40] radiometric phenomenon. This thermo-stress convection — which is essentially a form of force, hereby, referred as Knudsen force — can be applied for micro-structure actuation. In slightly more complex scenarios, one can stack an array of parallel-plates to significantly enhance the Knudsen force output [41]–[43]. Strongrich [42] demonstrated the possibility of amplifying the Knudsen forces as well as reversing its direction by combining thermal gradients between several solid bodies. The idea was further explored, resulting in development of a Microscale In-Plane Knudsen Radiometric Actuator (MIKRA) sensor for flow actuation and measurement [43]–[45]. As a practical test case of the developed idea, we will study the flow in MIKRA sensor.

Objective 5. *Apply the developed deterministic method for the study of the low-speed thermally-driven flows in micro-electro mechanical systems.*

Results for the 1D simulations in this thesis were obtained using 1D code located at https://github.com/-jaishw7/dgfs1D_gpu, whereas the results for the 2D/3D simulations were obtained using 2D/3D code located at <https://github.com/jaishw7/frfs>.

2. THE EXPLICIT SCHEME FOR BOLTZMANN EQUATION

In this section, we detail the details of the deterministic method for multi-species Boltzmann. The single-species is simply recovered by setting the number of species, s , to one.

2.1 Accurate modelling of diffusion

An appropriate modelling of binary interaction of molecular species is crucial for reproducing the flow transport properties, and consequently the flow physics.

With a few exceptions, e.g. Hard Sphere (HS) model, the explicit form of Σ_{ij} can be hard to obtain since b_{ij} is related to χ implicitly. To avoid this complexity, phenomenological collision kernels are often used in practice with the aim to reproduce the correct transport coefficients. Koura et al. [26] introduced the so-called Variable Soft Sphere (VSS) model by assuming

$$\chi = 2 \cos^{-1} \{ (b_{ij}/d_{ij})^{1/\alpha_{ij}} \}, \quad (2.1)$$

where α_{ij} is the scattering parameter, and d_{ij} is the diameter borrowed from Bird's Variable Hard Sphere (VHS) model (cf. eqn. (4.79) in [24]):

$$d_{ij} = d_{\text{ref},ij} \left[\left(\frac{2k_B T_{\text{ref},ij}}{\mu_{ij} |v - v_*|^2} \right)^{\omega_{ij}-0.5} \frac{1}{\Gamma(2.5 - \omega_{ij})} \right]^{1/2}, \quad (2.2)$$

with Γ being the Gamma function, $\mu_{ij} = \frac{m_i m_j}{m_i + m_j}$ the reduced mass, $d_{\text{ref},ij}$, $T_{\text{ref},ij}$, and ω_{ij} , respectively, the reference diameter, reference temperature, and viscosity index. Substituting the eqns. (1.7)-(2.2) into (1.6), one can obtain B_{ij} as

$$B_{ij} = b_{\omega_{ij}, \alpha_{ij}} |v - v_*|^{2(1-\omega_{ij})} (1 + \cos \chi)^{\alpha_{ij}-1}, \quad (2.3)$$

where $b_{\omega_{ij}, \alpha_{ij}}$ is a constant given by

$$b_{\omega_{ij}, \alpha_{ij}} = \frac{d_{\text{ref}, ij}^2}{4} \left(\frac{2k_B T_{\text{ref}, ij}}{\mu_{ij}} \right)^{\omega_{ij}-0.5} \frac{1}{\Gamma(2.5 - \omega_{ij})} \frac{\alpha_{ij}}{2^{\alpha_{ij}-1}}. \quad (2.4)$$

In particular, the VHS kernel is obtained when $\alpha_{ij} = 1$ and $0.5 \leq \omega_{ij} \leq 1$ ($\omega_{ij} = 1$: Maxwell molecules; $\omega_{ij} = 0.5$: HS); and the VSS kernel is obtained when $1 < \alpha_{ij} \leq 2$ and $0.5 \leq \omega_{ij} \leq 1$.

2.2 Properties of the collision operator

It can be shown that the collision operator $\mathcal{Q}^{(ij)}$ satisfies the following weak forms:

$$\begin{aligned} \int_{\mathbb{R}^3} \mathcal{Q}^{(ij)}(f^{(i)}, f^{(j)})(v) \varphi(v) dv &= \int_{\mathbb{R}^3} \int_{\mathbb{R}^3} \int_{S^2} \mathcal{B}_{ij}(v - v_*, \sigma) \left[f^{(i)}(v') f^{(j)}(v'_*) - f^{(i)}(v) f^{(j)}(v_*) \right] \\ &\quad \cdot \frac{\varphi(v) + \varphi(v_*) - \varphi(v') - \varphi(v'_*)}{4} d\sigma dv dv_*, \\ \int_{\mathbb{R}^3} \mathcal{Q}^{(ij)}(f^{(i)}, f^{(j)})(v) \varphi(v) dv + \int_{\mathbb{R}^3} \mathcal{Q}^{(ji)}(f^{(j)}, f^{(i)})(v) \phi(v) dv \\ &= \int_{\mathbb{R}^3} \int_{\mathbb{R}^3} \int_{S^2} \mathcal{B}_{ij}(v - v_*, \sigma) \left[f^{(i)}(v') f^{(j)}(v'_*) - f^{(i)}(v) f^{(j)}(v_*) \right] \frac{\varphi(v) + \phi(v_*) - \varphi(v') - \phi(v'_*)}{2} d\sigma dv dv_*. \end{aligned} \quad (2.5)$$

Using these weak forms, it is easy to derive

$$\begin{aligned} \int_{\mathbb{R}^3} \mathcal{Q}^{(ij)}(f^{(i)}, f^{(j)}) dv &= 0, \\ \int_{\mathbb{R}^3} \mathcal{Q}^{(ij)}(f^{(i)}, f^{(j)}) m_i v dv + \int_{\mathbb{R}^3} \mathcal{Q}^{(ji)}(f^{(j)}, f^{(i)}) m_j v dv &= 0, \\ \int_{\mathbb{R}^3} \mathcal{Q}^{(ij)}(f^{(i)}, f^{(j)}) m_i |v|^2 dv + \int_{\mathbb{R}^3} \mathcal{Q}^{(ji)}(f^{(j)}, f^{(i)}) m_j |v|^2 dv &= 0, \end{aligned} \quad (2.6)$$

and the well-known Boltzmann's H-theorem

$$\sum_{i,j=1}^s \int_{\mathbb{R}^3} \mathcal{Q}^{(ij)}(f^{(i)}, f^{(j)}) \ln f^{(i)} dv \leq 0. \quad (2.7)$$

(2.7) implies that the total entropy of the system decays with time:

$$\sum_{i=1}^s \left\{ \partial_t \int_{\mathbb{R}^3} f^{(i)} \ln f^{(i)} dv + \nabla_x \cdot \int_{\mathbb{R}^3} v f^{(i)} \ln f^{(i)} dv \right\} \leq 0, \quad (2.8)$$

and the equality holds if and only if $f^{(i)}$ attains the local equilibrium

$$f^{(i)} = \frac{n^{(i)}}{(2\pi R_i T)^{3/2}} \exp\left(-\frac{(v-u)^2}{2R_i T}\right) := \mathcal{M}^{(i)}, \quad (2.9)$$

where $R_i = k_B/m_i$ is the specific gas constant.

2.3 Macroscopic law

One can take the moments of eqn. (1.1) to obtain the following local conservation laws:

$$\begin{aligned} \partial_t \int_{\mathbb{R}^3} f^{(i)} dv + \nabla_x \cdot \int_{\mathbb{R}^3} v f^{(i)} dv &= 0, \\ \sum_{i=1}^s \left\{ \partial_t \int_{\mathbb{R}^3} m_i v f^{(i)} dv + \nabla_x \cdot \int_{\mathbb{R}^3} m_i v \otimes v f^{(i)} dv \right\} &= 0, \\ \sum_{i=1}^s \left\{ \partial_t \int_{\mathbb{R}^3} \frac{1}{2} m_i |v|^2 f^{(i)} dv + \nabla_x \cdot \int_{\mathbb{R}^3} \frac{1}{2} m_i v |v|^2 f^{(i)} dv \right\} &= 0, \end{aligned} \quad (2.10)$$

which, using the previously defined macroscopic quantities, can be recast as

$$\begin{aligned} \partial_t n^{(i)} + \nabla_x \cdot (n^{(i)} u^{(i)}) &= 0 \implies \partial_t \rho + \nabla_x \cdot (\rho u) = 0, \\ \partial_t (\rho u) + \nabla_x \cdot (\rho u \otimes u + \mathbb{P}) &= 0, \\ \partial_t E + \nabla_x \cdot (Eu + \mathbb{P}u + q) &= 0, \end{aligned} \quad (2.11)$$

where $E = 3nk_B T/2 + \rho u^2/2$ is the total energy. Note that this system is not closed. However, replacing $f^{(i)}$ by $\mathcal{M}^{(i)}$ in (2.11) yields a closed system, i.e., the compressible Euler equations. With more involved calculations (so-called Chapman-Enskog expansion), one can derive the Navier-Stokes equations. We omit the detail but mention that the heat flux term will contain the diffusion velocity $v_D^{(i)}$, a property unique to the mixtures (see for instance [9]).

2.4 Non-dimensionalization

For easier manipulation, we perform a nondimensionalization of the eqn. (1.1). We first choose the characteristic length H_0 , temperature T_0 , number density n_0 , and mass m_0 , and then define the characteristic velocity $u_0 = \sqrt{2k_B T_0/m_0}$ and time $t_0 = H_0/u_0$. We rescale t , x , v , m_i , and $f^{(i)}$ as follows:

$$\hat{t} = \frac{t}{t_0}, \quad \hat{x} = \frac{x}{H_0}, \quad \hat{v} = \frac{v}{u_0}, \quad \hat{m}_i = \frac{m_i}{m_0}, \quad \hat{f}^{(i)} = \frac{f^{(i)}}{n_0/u_0^3}, \quad (2.12)$$

and rescale the collision kernel as

$$\hat{\mathcal{B}}_{ij} = \frac{\mathcal{B}_{ij}}{B_{0,ij}}, \quad (2.13)$$

where

$$B_{0,ij} = u_0 \sqrt{1 + m_i/m_j} \pi d_{\text{ref},ij}^2 (T_{\text{ref},ij}/T_0)^{\omega_{ij}-0.5}. \quad (2.14)$$

Then the eqn. (1.1) becomes (dropping $\hat{\cdot}$ for simplicity)

$$\partial_t f^{(i)} + v \cdot \nabla_x f^{(i)} = \sum_{j=1}^s \frac{n_0 H_0}{u_0} B_{0,ij} \int_{\mathbb{R}^3} \int_{S^2} \mathcal{B}_{ij} \left[f^{(i)}(v') f^{(j)}(v'_*) - f^{(i)}(v) f^{(j)}(v_*) \right] d\sigma dv_*. \quad (2.15)$$

The factor

$$\frac{u_0}{n_0 H_0 B_{0,ij}} = \frac{\frac{u_0}{n_0 B_{0,ij}}}{H_0} = \text{Kn}_{ij} \quad (2.16)$$

is the Knudsen number defined as the ratio of the mean free path and characteristic length scale, hence

$$\text{Kn}_{ij} = \frac{1}{\sqrt{1 + m_i/m_j} \pi n_0 d_{\text{ref},ij}^2 (T_{\text{ref},ij}/T_0)^{\omega_{ij}-0.5} H_0}. \quad (2.17)$$

One can also define the “average” Knudsen number for each species i as

$$\text{Kn}_i = \left(\sum_{j=1}^s \frac{1}{\text{Kn}_{ij}} \right)^{-1}. \quad (2.18)$$

This is consistent with eqn. (4.76) in [24].

Therefore, the dimensionless Boltzmann equation for the VSS kernel (2.3) reads as

$$\partial_t f^{(i)} + v \cdot \nabla_x f^{(i)} = \sum_{j=1}^s \frac{1}{\text{Kn}_{ij}} \mathcal{Q}^{(ij)}(f^{(i)}, f^{(j)})(v), \quad (2.19)$$

with

$$\mathcal{Q}^{(ij)}(f^{(i)}, f^{(j)})(v) = \int_{\mathbb{R}^3} \int_{S^2} B_{ij}(|v - v_*|, \cos \chi) [f^{(i)}(v') f^{(j)}(v'_*) - f^{(i)}(v) f^{(j)}(v_*)] \, d\sigma \, dv_*, \quad (2.20)$$

$$B_{ij} = \frac{\alpha_{ij}}{\sqrt{1 + m_i/m_j} \mu_{ij}^{\omega_{ij}-0.5} 2^{1+\alpha_{ij}} \Gamma(2.5 - \omega_{ij}) \pi} |v - v_*|^{2(1-\omega_{ij})} (1 + \cos \chi)^{\alpha_{ij}-1}. \quad (2.21)$$

Remark 2.4.1. *We adopt the VSS kernel in this work for easy comparison with DSMC solutions. The fast algorithm for the collision operator does not rely on the specific form (2.21) (see Section 2.5).*

In addition, we rescale the macroscopic quantities as

$$\hat{n}^{(i)} = \frac{n^{(i)}}{n_0}, \quad \hat{\rho}^{(i)} = \frac{\rho^{(i)}}{m_0 n_0}, \quad \hat{u}^{(i)} = \frac{u^{(i)}}{u_0}, \quad \hat{T}^{(i)} = \frac{T^{(i)}}{T_0}, \quad \hat{\mathbb{P}}^{(i)} = \frac{\mathbb{P}^{(i)}}{\frac{1}{2} m_0 n_0 u_0^2}, \quad \hat{q}^{(i)} = \frac{q^{(i)}}{\frac{1}{2} m_0 n_0 u_0^3}, \quad (2.22)$$

then in rescaled variables (again dropping $\hat{}$ for simplicity)

$$\begin{aligned} n^{(i)} &= \int_{\mathbb{R}^3} f^{(i)} \, dv, \quad \rho^{(i)} = m_i n^{(i)}, \quad u^{(i)} = \frac{1}{n^{(i)}} \int_{\mathbb{R}^3} v f^{(i)} \, dv, \quad T^{(i)} = \frac{2m_i}{3n^{(i)}} \int_{\mathbb{R}^3} (v - u^{(i)})^2 f^{(i)} \, dv, \\ \mathbb{P}^{(i)} &= 2m_i \int_{\mathbb{R}^3} (v - u) \otimes (v - u) f^{(i)} \, dv, \quad q^{(i)} = m_i \int_{\mathbb{R}^3} (v - u) |v - u|^2 f^{(i)} \, dv, \end{aligned} \quad (2.23)$$

and the Maxwellian (2.9) becomes

$$\mathcal{M}^{(i)} = n^{(i)} \left(\frac{m_i}{\pi T} \right)^{3/2} \exp \left(-\frac{m_i |v - u|^2}{T} \right). \quad (2.24)$$

Remark 2.4.2. *It is often convenient to define the so-called parallel ($T_{\parallel}^{(i)}$) and perpendicular ($T_{\perp}^{(i)}$) components of temperature as*

$$T_{\parallel}^{(i)} = \frac{2m_i}{n^{(i)}} \int_{\mathbb{R}^3} (v_x - u_x^{(i)})^2 f^{(i)} dv, \quad T_{\perp}^{(i)} = \frac{2m_i}{n^{(i)}} \int_{\mathbb{R}^3} (v_y - u_y^{(i)})^2 f^{(i)} dv, \quad (2.25)$$

where subscripts x and y denote the first and second components of respective vector fields.

2.5 The fast Fourier spectral method for Boltzmann collision operator

The main difficulty of numerically solving the multi-species Boltzmann equation (2.19) lies in the collision operator (2.20). In this section, we introduce a fast Fourier spectral method (in the velocity space) to approximate this operator. Discussion for the spatially inhomogeneous equation will be given in the next section.

We first perform a change of variables v_* to $g = v - v_*$ in (2.20) to obtain

$$\mathcal{Q}^{(ij)}(f^{(i)}, f^{(j)})(v) = \int_{\mathbb{R}^3} \int_{S^2} B_{ij}(|g|, \sigma \cdot \hat{g}) \left[f^{(i)}(v') f^{(j)}(v'_*) - f^{(i)}(v) f^{(j)}(v_*) \right] d\sigma dg, \quad (2.26)$$

where \hat{g} is the unit vector along g and

$$v' = v - \frac{m_j}{m_i + m_j} g + \frac{m_j}{m_i + m_j} |g| \sigma, \quad v'_* = v - \frac{m_j}{m_i + m_j} g - \frac{m_i}{m_i + m_j} |g| \sigma. \quad (2.27)$$

Next we need to choose a finite computational domain $\mathcal{D}_L = [-L, L]^3$. This is based on the following criterion (similar discussion for the single-species case can be found in [46]).

Assume the support of functions $f^{(i)}, f^{(j)}$ can be approximated by a ball with radius S : $\text{Supp}(f^{(i)}(v), f^{(j)}(v)) \subset \mathcal{B}_S$, then one has

- $\text{Supp}(\mathcal{Q}^{(ij)}(f^{(i)}, f^{(j)})(v)) \subset \mathcal{B}_{\sqrt{1+m_j/m_i}S}.$

This is because if $|v| > \sqrt{1 + m_j/m_i}S$, then $f^{(i)}(v) = 0$; also $m_i|v'|^2 + m_j|v'_*|^2 \geq m_i|v|^2 > (m_i + m_j)S^2$, then either $|v'| > S$ or $|v'_*| > S$, so $f^{(i)}(v') = 0$ or $f^{(j)}(v'_*) = 0$; either way $\mathcal{Q}^{(ij)}(f^{(i)}, f^{(j)})(v) = 0$.

- It is enough to truncate g to a ball \mathcal{B}_R with $R = 2S$:

$$\mathcal{Q}^{(ij)}(f^{(i)}, f^{(j)})(v) = \int_{\mathcal{B}_R} \int_{S^2} B_{ij}(|g|, \sigma \cdot \hat{g}) \left[f^{(i)}(v') f^{(j)}(v'_*) - f^{(i)}(v) f^{(j)}(v_*) \right] d\sigma dg. \quad (2.28)$$

This is because if $2S < |g| = |v - v_*| \leq |v| + |v_*|$, then $|v| > S$ or $|v_*| > S$, so $f^{(i)}(v) = 0$ or $f^{(j)}(v_*) = 0$; also $2S < |g| = |v - v_*| = |v' - v'_*| \leq |v'| + |v'_*|$, then $|v'| > S$ or $|v'_*| > S$, so $f^{(i)}(v') = 0$ or $f^{(j)}(v'_*) = 0$; either way $\mathcal{Q}^{(ij)}(f^{(i)}, f^{(j)})(v) = 0$.

- Since $|v| \leq \sqrt{1 + m_j/m_i}S$ and $|g| \leq 2S$ in $\mathcal{Q}^{(ij)}(f^{(i)}, f^{(j)})(v)$, we have

$$\begin{aligned} |v_*| &= |v - g| \leq |v| + |g| \leq (2 + \sqrt{1 + m_j/m_i})S; \\ |v'| &= \left| v - \frac{m_j}{m_i + m_j}g + \frac{m_j}{m_i + m_j}|g|\sigma \right| \leq |v| + \frac{2m_j}{m_i + m_j}|g| \leq (4m_j/(m_i + m_j) + \sqrt{1 + m_j/m_i})S; \\ |v'_*| &= \left| v - \frac{m_j}{m_i + m_j}g - \frac{m_i}{m_i + m_j}|g|\sigma \right| \leq |v| + |g| \leq (2 + \sqrt{1 + m_j/m_i})S. \end{aligned}$$

- To avoid aliasing, need

$$2L \geq \left(\max(4m_j/(m_i + m_j), 2) + \sqrt{1 + m_j/m_i} \right) S + S. \quad (2.29)$$

Remark 2.5.1. From (2.29), it can be seen that the computational domain needs to be very large for large mass ratios $m_j/m_i \gg 1$. This is a common issue appearing in multi-species problems. Possible remedies include adaptive mesh in velocity space (cf. [47]), using an asymptotic model valid for large mass ratios (cf. [48]), or introducing independent velocity grid for each species wherein different collision types for every (i, j) pair are treated independently (cf. [49], [50]). In this work, we only consider moderate mass ratios and postpone these studies to a future work.

Now we approximate $f^{(i)}$ (similarly for $f^{(j)}$) by a truncated Fourier series on \mathcal{D}_L :

$$f^{(i)}(v) \approx \sum_{k=-\frac{N}{2}}^{\frac{N}{2}-1} \hat{f}_k^{(i)} e^{i\frac{\pi}{L}k \cdot v}, \quad \hat{f}_k^{(i)} = \frac{1}{(2L)^3} \int_{\mathcal{D}_L} f^{(i)}(v) e^{-i\frac{\pi}{L}k \cdot v} dv, \quad (2.30)$$

note here an abuse of notation: the summation over the 3D index k means $-N/2 \leq k_i \leq N/2 - 1$, where k_i is each component of k . Upon substitution of $f^{(i)}$, $f^{(j)}$ into $\mathcal{Q}^{(ij)}(f^{(i)}, f^{(j)})$ and a Galerkin projection to the same Fourier space, we obtain the k -th Fourier mode of the collision operator as

$$\hat{\mathcal{Q}}_k^{(ij)} = \sum_{\substack{l, m = -\frac{N}{2} \\ l+m=k}}^{\frac{N}{2}-1} G^{(ij)}(l, m) \hat{f}_l^{(i)} \hat{f}_m^{(j)}, \quad (2.31)$$

with the weight

$$G^{(ij)}(l, m) = \int_{\mathcal{B}_R} \int_{S^2} B_{ij}(|g|, \sigma \cdot \hat{g}) \left[e^{-i\frac{\pi}{L} \frac{m_j}{m_i+m_j} (l+m) \cdot g + i\frac{\pi}{L} |g| \left(\frac{m_j}{m_i+m_j} l - \frac{m_i}{m_i+m_j} m \right) \cdot \sigma} - e^{-i\frac{\pi}{L} m \cdot g} \right] d\sigma dg.$$

Without special treatment, the summation (2.31) has to be evaluated directly, resulting in a computational cost of $O(N^6)$. Furthermore, the weight $G^{(ij)}(l, m)$ needs to be precomputed and the storage requirement is $O(N^6)$. This can quickly become a bottleneck even for moderate N . Motivated by our previous work for the single-species Boltzmann equation [31], [32], we propose the following strategy to accelerate the direct summation as well as alleviate its memory bottleneck.

For the gain term (positive part) of $G^{(ij)}(l, m)$, we decompose it as

$$G^{(ij)+}(l, m) = \int_0^R \int_{S^2} F^{(ij)}(l+m, \rho, \sigma) e^{i\frac{\pi}{L} \rho \left(\frac{m_j}{m_i+m_j} l - \frac{m_i}{m_i+m_j} m \right) \cdot \sigma} d\sigma d\rho, \quad (2.32)$$

where $\rho = |g|$ is the radial of g and

$$F^{(ij)}(l+m, \rho, \sigma) = \rho^2 \int_{S^2} B_{ij}(\rho, \sigma \cdot \hat{g}) e^{-i\frac{\pi}{L} \rho \frac{m_j}{m_i+m_j} (l+m) \cdot \hat{g}} d\hat{g}, \quad (2.33)$$

while for the loss term (negative part) of $G^{(ij)}(l, m)$,

$$G^{(ij)-}(m) = \int_0^R \int_{S^2} \int_{S^2} \rho^2 B_{ij}(\rho, \sigma \cdot \hat{g}) e^{-i\frac{\pi}{L}\rho m \cdot \hat{g}} d\sigma d\hat{g} d\rho. \quad (2.34)$$

The idea is to precompute $F^{(ij)}(l + m, \rho, \sigma)$ and $G^{(ij)-}(m)$ up to a high accuracy, and approximate the integral in (2.32) on the fly using a quadrature rule:

$$G^{(ij)+}(l, m) \approx \sum_{\rho, \sigma} w_\rho w_\sigma F^{(ij)}(l + m, \rho, \sigma) e^{i\frac{\pi}{L}\rho \left(\frac{m_j}{m_i + m_j} l - \frac{m_i}{m_i + m_j} m \right) \cdot \sigma}, \quad (2.35)$$

where for the radial direction, we use the Gauss-Legendre quadrature with $N_\rho = O(N)$ points (since the integral oscillates roughly on $O(N)$); for the integral over the sphere, we use the M -point spherical design quadrature [51], [52] (usually $M \ll N^2$).

Therefore, the gain term of the collision operator can be approximated as

$$\hat{\mathcal{Q}}_k^{(ij)+} \approx \sum_{\rho, \sigma} w_\rho w_\sigma F^{(ij)}(k, \rho, \sigma) \sum_{\substack{l, m = -\frac{N}{2} \\ l+m=k}}^{\frac{N}{2}-1} \left(e^{i\frac{\pi}{L}\rho \frac{m_j}{m_i + m_j} l \cdot \sigma} \hat{f}_l^{(i)} \right) \left(e^{-i\frac{\pi}{L}\rho \frac{m_i}{m_i + m_j} m \cdot \sigma} \hat{f}_m^{(j)} \right). \quad (2.36)$$

Written in the above form, we see that the inner sum is a convolution of two functions so that it can be evaluated efficiently in $O(N^3 \log N)$ operations via the fast Fourier transform (FFT). Together with the outer sum, the total complexity of evaluating $\hat{\mathcal{Q}}_k^{(ij)+}$ (for all k) is $O(MN^4 \log N)$ (recall the total number of quadrature points needed for ρ and σ is $O(MN)$).

On the other hand, the loss term of the collision operator can be written as

$$\hat{\mathcal{Q}}_k^{(ij)-} = \sum_{\substack{l, m = -\frac{N}{2} \\ l+m=k}}^{\frac{N}{2}-1} \hat{f}_l^{(i)} \left(G^{(ij)-}(m) \hat{f}_m^{(j)} \right), \quad (2.37)$$

which is readily a convolution, hence can be evaluated in $O(N^3 \log N)$.

Putting both pieces together, we have obtained a fast algorithm of complexity $O(MN^4 \log N)$ for evaluating the collision operator $\mathcal{Q}^{(ij)}(f^{(i)}, f^{(j)})$, where $M \ll N^2$. In addition, the memory requirement to store the weight $F^{(ij)}(l+m, \rho, \sigma)$ and $G^{(ij)-}(m)$ is $O(MN^4)$.

2.6 The discontinuous Galerkin method for the spatial discretization

The previously introduced fast spectral method allows us to compute the collision operator efficiently. To solve the full spatially inhomogeneous equation (2.19), we also need an accurate and efficient spatial and time discretization. Here we adopt the RKDG (Runge-Kutta discontinuous Galerkin) method [53] widely used for hyperbolic type equations. Since the transport term is linear in the Boltzmann equation, the application of DG method is straightforward. We give a brief description below for completeness.

We first decompose the physical domain Ω into N_e variable-sized disjoint elements $D_{\mathbf{x}}^e$:

$$\Omega \approx \bigcup_{e=1}^{N_e} D_{\mathbf{x}}^e, \quad D_{\mathbf{x}}^e \cap D_{\mathbf{x}}^{e'} = \emptyset, \quad \forall e \neq e', \quad 1 \leq e, e' \leq N_e. \quad (2.38)$$

In each element $D_{\mathbf{x}}^e$, we approximate the distribution function $f^{(i)}(t, \mathbf{x}, v)$ for each species by a polynomial of order N_p :

$$\mathbf{x} \in D_{\mathbf{x}}^e : \quad f_e^{(i)}(t, \mathbf{x}, v) = \sum_{l=1}^K \mathcal{F}_{e,l}^{(i)}(t, v) \phi_l^e(x), \quad 1 \leq i \leq s, \quad (2.39)$$

where $\phi_l^e(x)$ is the basis function supported in $D_{\mathbf{x}}^e$, K is the total number of terms in the local expansion, and $\mathcal{F}_{e,l}^{(i)}(t, v)$ is the elemental degree of freedom.

We form the residual by substituting the expansion (2.39) into the eqn. (2.19):

$$\mathcal{R}_e^{(i)} = \sum_{l=1}^K \phi_l^e \partial_t \mathcal{F}_{e,l}^{(i)} + \sum_{l=1}^K \mathcal{F}_{e,l}^{(i)} v \cdot \nabla_{\mathbf{x}} \phi_l^e - \sum_{j=1}^s \frac{1}{\text{Kn}_{ij}} \sum_{l_1, l_2=1}^K \mathcal{Q}^{(ij)}(\mathcal{F}_{e,l_1}^{(i)}, \mathcal{F}_{e,l_2}^{(j)}) \phi_{l_1}^e \phi_{l_2}^e, \quad 1 \leq i \leq s, \quad (2.40)$$

where we used the quadratic property of the collision operator. We then require that the residual is orthogonal to all test functions. In the Galerkin formulation, the test function is the same as the basis function, thus

$$\int_{D_{\mathbf{x}}^e} \mathcal{R}_e^{(i)} \phi_m^e d\mathbf{x} = 0, \quad 1 \leq m \leq K, \quad 1 \leq i \leq s. \quad (2.41)$$

Substituting (2.40) into (2.41) and applying the divergence theorem, we obtain

$$\begin{aligned} & \sum_{l=1}^K \left(\int_{D_{\mathbf{x}}^e} \phi_m^e \phi_l^e d\mathbf{x} \right) \partial_t \mathcal{F}_{e,l}^{(i)} - \sum_{l=1}^K \mathcal{F}_{e,l}^{(i)} v \cdot \int_{D_{\mathbf{x}}^e} \phi_l^e \nabla_{\mathbf{x}} \phi_m^e d\mathbf{x} \\ &= - \int_{\partial D_{\mathbf{x}}^e} \phi_m^e \left(F_*^{(i)} \cdot \hat{n}^e \right) d\mathbf{x} + \sum_{j=1}^s \frac{1}{\text{Kn}_{ij}} \sum_{l_1, l_2=1}^K \mathcal{Q}^{(ij)}(\mathcal{F}_{e,l_1}^{(i)}, \mathcal{F}_{e,l_2}^{(j)}) \left(\int_{D_{\mathbf{x}}^e} \phi_m^e \phi_{l_1}^e \phi_{l_2}^e d\mathbf{x} \right), \end{aligned} \quad (2.42)$$

where \hat{n}^e is the local outward pointing normal and $F_*^{(i)}$ denotes the numerical flux. Specifically, the surface integral in the above equation is defined as follows

$$\int_{\partial D_{\mathbf{x}}^e} \phi_m^e \left(F_*^{(i)} \cdot \hat{n}^e \right) d\mathbf{x} = \sum_{E \in \partial D_{\mathbf{x}}^e} \int_E \phi_m^e \left(F_{*,E}^{(i)} \cdot \hat{n}_E^e \right) d\mathbf{x}, \quad (2.43)$$

with \hat{n}_E^e and $F_{*,E}^{(i)}$ being the outward normal and numerical flux along the face E . In our implementation, we choose the upwind flux:

$$F_{*,E}^{(i)} = \begin{cases} v f_e^{(i)}(t, \mathbf{x}_{E, \text{int}(D_{\mathbf{x}}^e)}, v), & v \cdot \hat{n}_E^e \geq 0 \\ v f_e^{(i)}(t, \mathbf{x}_{E, \text{ext}(D_{\mathbf{x}}^e)}, v), & v \cdot \hat{n}_E^e < 0 \end{cases} \quad (2.44)$$

where *int* and *ext* denote interior and exterior of the face e respectively.

Finally, define the mass matrix \mathcal{M}_{ml} , stiffness matrix \mathcal{S}_{ml} , and the tensor $\mathcal{H}_{ml_1 l_2}$ as

$$\begin{aligned} \mathcal{M}_{ml}^e &= \int_{D_{\mathbf{x}}^e} \phi_m^e(x) \phi_l^e(x) d\mathbf{x}, \quad \mathcal{S}_{ml}^e = \int_{D_{\mathbf{x}}^e} \phi_l^e(x) \nabla_{\mathbf{x}} \phi_m^e(x) d\mathbf{x}, \\ \mathcal{H}_{ml_1 l_2}^e &= \int_{D_{\mathbf{x}}^e} \phi_m^e(x) \phi_{l_1}^e(x) \phi_{l_2}^e(x) d\mathbf{x}, \end{aligned} \quad (2.45)$$

then (2.42) can be written as

$$\sum_{l=1}^K \mathcal{M}_{ml}^e \partial_t \mathcal{F}_{e,l}^{(i)} - \sum_{l=1}^K v \cdot \mathcal{S}_{ml}^e \mathcal{F}_{e,l}^{(i)} = - \int_{\partial D_{\mathbf{x}}^e} \phi_m^e (F_*^{(i)} \cdot \hat{n}^e) d\mathbf{x} + \sum_{j=1}^s \frac{1}{\text{Kn}_{ij}} \sum_{l_1, l_2=1}^K \mathcal{H}_{m l_1 l_2}^e \mathcal{Q}^{(ij)} (\mathcal{F}_{e, l_1}^{(i)}, \mathcal{F}_{e, l_2}^{(j)}), \quad (2.46)$$

for $1 \leq m \leq K$, $1 \leq i \leq s$.

(2.46) is the DG system we are going to solve in each element $D_{\mathbf{x}}^e$ of the physical domain. The fast spectral method introduced in the previous section is used to evaluate the term $\mathcal{Q}^{(ij)} (\mathcal{F}_{e, l_1}^{(i)}, \mathcal{F}_{e, l_2}^{(j)})$.

2.7 Discretization in the velocity space

To further discretize the system (2.46) in the velocity space, we employ a finite difference (or discrete velocity) discretization. Each velocity component c_i ($i \in \{1, 2, 3\}$) is discretized uniformly with N points in the interval $[-L, L]$. The grid points are chosen as $-L + (j - 1/2)\Delta v$, with $j = 1, \dots, N$ and $\Delta v = 2L/N$ (the choice of L is given below). For brevity we will use v^j to denote the 3D velocity grid point.

The reason of using the uniform velocity grid is because the fast algorithm for the collision operator is based on Fourier transform, which is naturally done on a uniform mesh. Simply speaking, it takes the function values at the grid points as input, does the calculation (including forward and backward FFTs) in a black box solver, and outputs the values of the collision operator at the same grid points. As such, the method can achieve spectral accuracy (subject to domain truncation error which is usually very small); furthermore, the simple mid-point rule would also allow one to construct the moments with spectral accuracy.

With the above setup, we just need to solve the system (2.46) at each velocity grid v^j and in each spatial element $D_{\mathbf{x}}^e$. The macroscopic quantities defined in (2.23): for example, number

density in the spatial element D_x^i can be recovered using numerical integration (mid-point rule) of the distribution function over the entire velocity grid,

$$n_e^{(i)}(t, \mathbf{x}) = \sum_j f_e^{(i)}(t, \mathbf{x}, v^j) \Delta v^3. \quad (2.47)$$

Note that n^i , the number density of species i , is polynomials defined in each element since $f^i(t, \mathbf{x}, v^j)$ is polynomial.

2.8 The collision operator algorithm

In multi-species implementation, with the high amount of involved computation, our motive is to avoid spurious computation for every timestep. We first outline the procedure for pre-computing variables that can be stored and reused during the course of the simulation.

- First, we precompute $(\pi/L \rho l \cdot \sigma)$. We use Gauss-Legendre-Quadrature (GLQ) for integration. So ρ , the GLQ zeros, is an array of size N_ρ (since the integrand oscillates on the scale of $O(N)$, the total number of quadrature points needed should be $\sim O(N)$). Additionally, we use *spherical design* [51] quadrature on sphere. So, σ , the spherical-quadrature zeros, is an array of size M . l as previously defined is the 3-D velocity-space index, and is therefore an array of size N^3 . Based upon these $(\pi/L \rho l \cdot \sigma)$ is precomputed and stored as a $N_\rho \times M \times N^3$ flattened row-major array a_{xyz} . This is described in steps 1–9 of Algo. (1).
- Second, we compute $F(l + m, \rho, \sigma)$ as per Eq. (2.33). Note that $k = l + m$ is velocity-space index of size N^3 . Since $l + m$, ρ , and σ do not change with time, the term $F(l + m, \rho, \sigma)$ is precomputed and stored as a $N_\rho \times M \times N^3$ flattened row-major array $b_{xyz}^{(ij)}$ for every collision pair (i, j) . This is described in step 13 of Algo. (1).
- Third, we perform precomputation needed for loss-term $G^{(ij)-}(m)$ as per Eq. (2.34). The output is stored as a N^3 flattened row-major array $c_z^{(ij)}$ for every collision pair (i, j) . This is described in step 14 of Algo. (1).

Algorithm 1: Pre-computation for Collision-Algorithm

Input: Number of points in each-direction of velocity mesh N , number of quadrature points for low-rank decomposition N_ρ , number of points on half-sphere M , number of points on pre-computation sphere $M^{(\text{pre})}$, spherical quadrature weight w_σ , spherical quadrature-points σ (vector-field size: M), pre-computation spherical quadrature weight $w_\sigma^{(\text{pre})}$, pre-computation spherical quadrature-points $\sigma^{(\text{pre})}$ (vector-field size: $M^{(\text{pre})}$), Gauss quadrature-weights w_ρ (size: N_ρ), Gauss quadrature-points ρ (size: N_ρ), first collision parameter $\gamma_{ij} = 2(\omega_{ij} - 1)$, second collision parameter $\eta_{ij} = (\alpha_{ij} - 1)$, size of velocity mesh L , normalized mass m_i, m_j of species-pair (i, j)

Output: a, b, c

Declare:
 a (size: $MN_\rho N^3$), b^(ij) (size: $MN_\rho N^3$), c^(ij) (size: N^3)
 l (vector-field size: N^3), v (size: N)

```

1: for x = 0 to N - 1 do
2:   vx = x - (x ≥ N/2) × N
3: end for
  // See octave function: [lx,ly,lz]=ndgrid(v)
4: l ← ndgrid(v)
  // Subscript x,y,z on symbols denote array-index
5: for x = 1 to Nρ do
6:   for y = 1 to M do
7:     for z = 1 to N3 do
8:       axyz ← π/L × ρx × (lz · σy)
        // ( · ) denotes vector dot-product
9:     end for
10:    for ŷ = 1 to M(pre) do
11:      Bij ← (1 + σy · σŷ(pre))ηij
12:      for z = 1 to N3 do
13:        bxyz(ij) ← bxyz(ij) + Bij × wσ(pre) × ρxγij+2 × exp(-1i × mj/(mi + mj) × π/L × ρx × (lz · σŷ(pre)))
14:        cz(ij) ← cz(ij) + (wρ)x × wσ × Bij × wσ(pre) × ρxγij+2 × exp(-1i × π/L × ρx × (lz · σŷ(pre)))
        // The variables bxyz(ij), cz(ij) needs to be computed for every (i,j) collision pair
15:      end for
16:    end for
17:  end for
18: end for
19: return a, b(ij), c(ij)

```

Next we outline the procedure for computing $\mathcal{Q}^{(ij)}$.

- First, we compute the forward Fourier transform of $\mathcal{F}_{i,l_1}^{(i)}$, and $\mathcal{F}_{i,l_2}^{(j)}$ to obtain $\hat{f}_l^{(i)}$ and $\hat{f}_m^{(j)}$ respectively. This is described in step 1 of Algo. (2).
- Second, we compute $G^{(ij)+}(l, m)$ as per Eq. (2.32). Recall that $(\pi/L \rho l \cdot \sigma)$ has been already precomputed and stored as a_{xyz} . Also recall that $F(l + m, \rho, \sigma)$ has been precomputed and stored as $b_{xyz}^{(ij)}$. These can be reused to compute $G(l, m)$. This is described in step 2–8 of Algo. (2). In our implementation, we explicitly unroll the nested loops so that variables $\mathbf{t1}, \mathbf{t2}$ in steps 4 and 5 are computed in a single kernel call (thereby requiring a space of $MN_\rho N^3$ each), and the FFT transforms in the step 6 are rather MN_ρ batched FFT transforms, each of size N^3 .
- Third, in order to perform convolution for the loss-term $G^{(ij)-}(l, m)$, we prepare the variable \mathbf{QG} in step 7 of Algo. (2).
- Fourth, we perform convolutions to compute $\hat{\mathcal{Q}}_k^{(ij)}$ as in Eq. (2.31). Recall that $G^{(ij)-}(m)$ has now been precomputed and stored as \mathbf{QG} , and can be reused here. An inverse Fourier transform is then performed to obtain final $\mathcal{Q}^{(ij)}$. This is described in step 10 of Algo. (2).

In summary, this chapter meets the following objectives:

- Construct a deterministic, accurate, robust, and efficient method for solving the multi-species Boltzmann equation of some engineering value.
- Construct a deterministic method for multi-species Boltzmann equation that can handle general repulsive interactions: the special cases of these are the aforementioned, which are widely used in DSMC simulations. The formulation should be consistent with kinetic theory and DSMC. This ensures that the results from deterministic method can be verified easily; which in turn helps with easy adaptation of the method.

Algorithm 2: Collision-Algorithm Pseudo-code

Input: Number of points in each-direction of velocity mesh N , Distribution-functions $\mathcal{F}_{i,l_1}^{(i)}$ and $\mathcal{F}_{i,l_2}^{(j)}$ (size: N^3), number of points on half-sphere M , spherical quadrature weight w_σ , Gauss quadrature-weights w_ρ (size: N_ρ), precomputed variable a (size: $MN_\rho \times N^3$), precomputed variable $b^{(ij)}$ (size: $MN_\rho \times N^3$), precomputed variable $c^{(ij)}$ (size: N^3), the kernel prefactor $\beta^{(ij)}$, normalized mass m_i, m_j of species-pair (i, j)

Output: Q

Declare:
 $\{t1, \dots, t3\}$ (each size: N^3); Q, QG (each size: N^3)

- 1: Compute forward FFT:
 $FTf \leftarrow \text{fft}(\mathcal{F}_{i,l_1}^{(i)})$
 $FTg \leftarrow \text{fft}(\mathcal{F}_{i,l_2}^{(j)})$
// Subscript x,y on symbols denote array-index
// Inner-most loop $r \in \{1, \dots, N^3\}$ has been ignored
- 2: **for** $x = 1$ to N_ρ **do**
- 3: **for** $y = 1$ to M **do**
- 4: $t1 \leftarrow \exp(1i \times m_j / (m_i + m_j) \times a_{xy}) \times FTf$
// Note: These are array-operations over N^3 (z index)
// 1i denotes the complex number $\sqrt{-1}$
- 5: $t2 \leftarrow \exp(-1i \times m_i / (m_j + m_i) \times a_{xy}) \times FTg$
// ifft denotes inverse FFT
- 6: $t3 \leftarrow \text{fft}(\text{ifft}(t1) \times \text{ifft}(t2))$
- 7: $QG \leftarrow QG + (w_\rho)_x \times w_\sigma \times b_{xy}^{(ij)} \times t3$
- 8: **end for**
- 9: **end for**
// real returns real part of complex number
- 10: $Q = \beta^{(ij)} \times \text{real}(\text{ifft}(QG) - \mathcal{F}_{i,l_1}^{(i)} \times \text{ifft}(c^{(ij)} \times FTg))$
- 11: **return** Q

3. THE IMPLICIT-EXPLICIT SCHEMES FOR BOLTZMANN EQUATION AND RELATED KINETIC MODELS

3.1 Background and motivation

As we noted in the introduction, the explicit deterministic methods suffer from time-stepping restrictions. In conventional deterministic schemes, the timestep should be smaller than mean collision timescale, which naturally decreases with decrease in mean free path. Simply speaking, the time-step is dependent on the Knudsen number, Kn . Even if the timestep can be, magically, kept fixed as the Knudsen number is decreased, the total number of timesteps required for the low Knudsen number flow to relax to equilibrium is generally high. Noting that time-stepping is inherently linear in traditional stochastic schemes such as DSMC, the time integration errors gradually accumulate.

To circumvent the aforementioned issues, the so called asymptotic-preserving (AP) schemes for stiff kinetic equations have been recently proposed. These AP schemes preserve the asymptotic transition from the microscopic kinetic regime to the macroscopic fluid regime, thereby removing the dependence of timestep on the Knudsen number. These schemes, generally, decompose the kinetic equation into a stiff and non-stiff part, wherein the stiff part is treated implicitly, and the non-stiff part is treated explicitly. For general non-linear collision operators, this is achieved by penalizing the collision operator, $\mathcal{Q}(f, f)$, by a penalty function $\mathcal{P}(f)$ i.e.,

$$\underbrace{\mathcal{L}(f)}_{\text{non stiff part}} + \underbrace{\frac{\mathcal{Q}(f, f)}{\text{Kn}}}_{\text{stiff part}} = \underbrace{\mathcal{L}(f) + \frac{\mathcal{Q}(f, f) - \mathcal{P}(f)}{\text{Kn}}}_{\text{non-stiff part}} + \underbrace{\frac{\mathcal{P}(f)}{\text{Kn}}}_{\text{stiff part}}. \quad (3.1)$$

From a historical perspective of asymptotic schemes, Pareschi introduced a hybrid Monte Carlo method in [54] wherein the solution was represented as a convex combination of a non-equilibrium distribution function and a Maxwellian, obtained using implicit time-differencing of solution via a generalized Wild expansion. A time-relaxed Monte Carlo was introduced in [55] by setting $\mathcal{P}(f) = \beta f$, where $\beta \geq 0$, and applied to engineering problems in [56].

A Bhatnagar-Gross-Krook (BGK) penalization based asymptotic scheme was introduced by Filbet in [57] by setting $P(f) = \beta(\mathcal{M} - f)$, where \mathcal{M} refers to the Maxwellian. Based on the so-called successive penalty, the idea was later extended in [58] to devise a scheme with *stronger*¹ AP property in addition to a positivity-preserving (PP) property. It was later implemented in [59] within a direct simulation Monte Carlo framework.

Recently, the so-called asymptotic-preserving Implicit-Explicit (IMEX) Runge-Kutta schemes [60] have been (re)introduced for the stiff kinetic equations in [61]. Dimarco [62] introduced it within the explicit Runge-Kutta (ExpRK) framework for BGK and non-linear Boltzmann equation. The scheme was subsequently coupled with the high-order Weighted Essentially Non Oscillatory (WENO) spatial discretization scheme in [63], and applied to several non-homogeneous cases of engineering interest. The idea was further explored in [64] for quantum Boltzmann equation. More recently, Hu [65] proposed a second order asymptotic-preserving and *positivity-preserving* ExpRK scheme, applicable for BGK, Fokker-Planck, and nonlinear Boltzmann equation. Notably, the scheme was coupled with a high-order spatially-accurate WENO scheme, and tested on 1D BGK and Fokker-Planck equation systems. In general, the asymptotic schemes capture the Euler limit in the limit of vanishing Knudsen number. However, in general for engineering flows, Kn is small but not zero. Consequently a family of IMEX schemes capturing the Navier-Stokes asymptotics has been recently developed in [66] for BGK and ESBGK kinetic systems. We want to emphasize that both Euler and Navier-Stokes can be derived from asymptotics of the collision operator – this is different from the Chapman-Enskog theory [5]². Finally, we mention the nodal-DG scheme, based

¹↑In the work [57], the authors devised a scheme with relaxed AP property i.e., $f - \mathcal{M} \rightarrow O(\text{Kn})$, after some initial transient time $t \geq t_0$, $t_0 > 0$. The later scheme in [58] has a strong AP property in the sense that $f - \mathcal{M} \rightarrow O(\text{Kn})$ for $t \geq 0$.

²↑With regard to the Chapman-Enskog theory, we mention that these are formal procedures for solving the Boltzmann equation in terms of a series expansion in terms of the small parameter Kn, which we know as Hilbert and Chapman-Enskog expansions [1], [2], [5], [67]–[69]. These procedures have never received a satisfactory mathematical justification in general, but have become very popular tools for deriving hydrodynamical equations [70]. It should be pointed out that equations obtained by keeping “many” terms of the Hilbert or Chapman-Enskog series, like the so-called Burnett or super-Burnett equations, seem to be irrelevant (an ad-hoc recipe to fix this problem can be found in [71]). These expansions are not expected to be convergent, but only “asymptotic”. In fact, a solution of the Boltzmann equation which could be represented as the sum of such a series would be a very particular one: it would be entirely determined by the fields of “macroscopic” local density, mean velocity and pressure associated with it – an idea essentially on the lines of Grad’s method of moments [72] and/or Wild expansions [54]. Just because we know moments of a

on micro-macro decomposition, was applied to BGK equation in [73] for 1-D problems. All of these schemes were largely applied within deterministic framework, and were extremely limited in the complexity of the space non-homogeneous cases addressed: A major portion of these works test the schemes for initial value problems.

In what follows, we devise and implement asymptotic-preserving (AP) deterministic scheme along the lines of [66], [74] with the properties noted in objective (3). In particular, we implement a new family of high order IMEX-BDF time integration schemes which require "only one" collision kernel evaluation per time-step, thereby making it computationally optimal. These AP schemes unnesessite the use of so called hybrid Navier-Stokes + Boltzmann coupling techniques for simulating flows which involve large change in rarefaction levels in subportions of the flow, for example, in micronozzles.

Remark 3.1.1. *In (3.1), we noted a penalty function. This penalty function is usually the simplified collision operators such as BGK [57] or ESBGK [66]. However, these operators are valid for single-species. Many simplified multi-species generalizations of these operators have been proposed and this is a very active research direction in the mathematical and engineering communities, see for instance some early works [75]–[77], and more recently [78]–[81], and references therein. These simplified models perform better at low Knudsen numbers; yet, they often fail to capture the physics at high Knudsen numbers and diffusion dominated flows at low Knudsen numbers (see [19], [82]). Consequently, in this work, rather than searching for a multi-species BGK/ESBGK type penalty functions, we propose to establish the ideas for single-species Boltzmann. A future work may focus on multi-species generalization.*

probability distribution, doesn't mean we know the probability distribution (here's an analogy from physics: measurement of, say, particle position doesn't say much about the particle's wave function. Measurements are observables (say position, velocity, etc): the ideas of classical physics. Classical physics alone doesn't answer everything about the physical world that is inherently quantum. What classical description is to quantum, Navier-Stokes (or method of moments) is to Boltzmann. From the theory of logic, Wittgenstein put it as, all facts (moments) about world cannot explain the world (distribution)). Infact, in [70], authors argue that the Hilbert and Chapman-Enskog methods rely on very sloppy grounds. Rather violent attacks on the convenient illusion of these principles can be found in [68]. In spite of this, these methods are still widely used, and numerical schemes are still being "synthesized" for solving rarefied gas flow problems. Rather harmful is the extension and application of these ideas to non-trivial scenarios, which include, development of Kn-perturbed high-order boundary conditions, the so-called "extended" Navier-Stokes models, effective transport models, etc.; and their purported use to solve mission critical problems.

3.2 A class of single-species kinetic equations

First, we present the simplification of (1.1) with $s = 1$.

We will consider the following prototype kinetic equation

$$\frac{\partial f}{\partial t} + v \cdot \nabla_x f = \mathcal{Q}(f), \quad t > 0, \quad x \in \Omega_x \in \mathbb{R}^3, \quad v \in \mathbb{R}^3. \quad (3.2)$$

Here $f = f(t, x, v)$ is the one-particle distribution function of time t , position x , and velocity v . $\int f \, dx \, dv$ gives the number of particles to be found in an infinitesimal volume $dx \, dv$ centered at the point (x, v) of the phase space. Given f , the macroscopic quantities can be obtained via its moments:

$$\begin{aligned} n &= \int_{\mathbb{R}^3} f \, dv, \quad u = \frac{1}{n} \int_{\mathbb{R}^3} f v \, dv, \quad T = \frac{m}{3k_B n} \int_{\mathbb{R}^3} f |v - u|^2 \, dv, \\ \mathbb{P} &= m \int_{\mathbb{R}^3} f (v - u) \otimes (v - u) \, dv, \quad q = \frac{1}{2} m \int_{\mathbb{R}^3} f (v - u) |v - u|^2 \, dv, \end{aligned} \quad (3.3)$$

where n , u , T , \mathbb{P} , and q are, respectively, the number density, bulk velocity, temperature, stress, and heat-flux. m is the molecular mass and k_B is the Boltzmann's constant. $\mathcal{Q}(f)$ is the collision operator describing the interactions between particles. In this paper, we will consider the full Boltzmann collision operator and three linear penalty functions viz. BGK, ESBGK and Shakov models.

- Boltzmann collision operator [2]:

$$\mathcal{Q}^{\text{Boltz}}(f, f) = \int_{\mathbb{R}^3} \int_{\mathbb{S}^2} B(|v - v_*|, \cos \chi) [f(v')f(v'_*) - f(v)f(v_*)] \, d\sigma \, dv_*, \quad (3.4)$$

where (v, v_*) and (v', v'_*) denote the pre- and post- collision velocity pairs, which are related through momentum and energy conservation as

$$v' = \frac{v + v_*}{2} + \frac{|v - v_*|}{2} \sigma, \quad v'_* = \frac{v + v_*}{2} - \frac{|v - v_*|}{2} \sigma, \quad (3.5)$$

with the vector σ varying over the unit sphere \mathbb{S}^2 . B (≥ 0) is the collision kernel depending only on $|v - v_*|$ and the scattering angle χ ($\cos \chi = \sigma \cdot (v - v_*)/|v - v_*|$). In this paper, we consider the Bird's Variable/Soft Sphere model [24] given by

$$B(|v - v_*|, \cos \chi) = b_{\omega, \alpha} |v - v_*|^{2(1-\omega)} (1 + \cos \chi)^{\alpha-1}, \quad (3.6)$$

where

$$b_{\omega, \alpha} = \frac{d_{\text{ref}}^2}{4} \left(\frac{4k_B T_{\text{ref}}}{m} \right)^{\omega-0.5} \frac{1}{\Gamma(2.5 - \omega)} \frac{\alpha}{2^{\alpha-1}}, \quad (3.7)$$

with

$$d_{\text{ref}}^2 = C_0 \frac{\sqrt{mk_B T_{\text{ref}}/\pi}}{\mu_{\text{ref}}}, \quad C_0 = \frac{5(\alpha + 1)(\alpha + 2)}{4\alpha(5 - 2\omega)(7 - 2\omega)}, \quad (3.8)$$

where d_{ref} , μ_{ref} , T_{ref} are the reference diameter, viscosity, temperature, and ω , α are the viscosity coefficient and scattering parameter.

- BGK model [83]:

$$\mathcal{Q}^{\text{BGK}}(f) = \nu(\mathcal{M}[f] - f), \quad (3.9)$$

where $\mathcal{M}[f]$ is the Maxwellian defined by

$$\mathcal{M}[f] = \frac{n}{(2\pi k_B T/m)^{3/2}} \exp\left(-\frac{m|v - u|^2}{2k_B T}\right), \quad (3.10)$$

and ν is the collision frequency given by

$$\nu = \frac{p}{\mu}, \quad \text{with} \quad p = nk_B T, \quad \mu = \mu_{\text{ref}} \left(\frac{T}{T_{\text{ref}}} \right)^{\omega}. \quad (3.11)$$

Here p is the pressure and μ is the dynamic viscosity.

- ESBGK model [84]:

$$\mathcal{Q}^{\text{ESBGK}}(f) = \text{Pr} \nu(\mathcal{G}[f] - f), \quad (3.12)$$

where $\mathcal{G}[f]$ is a generalized Gaussian given by

$$\mathcal{G}[f] = \frac{n}{\sqrt{\det(2\pi k_B \mathbb{T}/m)}} \exp\left(-\frac{m}{2k_B} (v-u)^T \mathbb{T}^{-1} (v-u)\right), \quad (3.13)$$

with

$$\mathbb{T} = \frac{1}{\text{Pr}} T \text{Id} + \left(1 - \frac{1}{\text{Pr}}\right) \frac{\mathbb{P}}{k_B n}. \quad (3.14)$$

Here Pr is the Prandtl number.

- Shakov model [85]:

$$\mathcal{Q}^{\text{Shakov}}(f) = \nu(\mathcal{S}[f] - f), \quad (3.15)$$

where

$$\mathcal{S}[f] = \mathcal{M}[f] \left[1 + \frac{1 - \text{Pr}}{5} \frac{q \cdot (v-u)}{n(k_B T)^2/m} \left(\frac{|v-u|^2}{k_B T/m} - 5 \right) \right]. \quad (3.16)$$

3.3 Non-dimensional form

We follow the non-dimensionalization convention as defined in [32]. We first choose the characteristic length H_0 , characteristic temperature T_0 , and characteristic number density n_0 , and then define the characteristic velocity $u_0 = \sqrt{2k_B T_0/m}$ and characteristic time $t_0 = H_0/u_0$.

We rescale t , x , v , and f as follows

$$\tilde{t} = \frac{t}{t_0}, \quad \tilde{x} = \frac{x}{H_0}, \quad \tilde{v} = \frac{v}{u_0}, \quad \tilde{f} = \frac{f}{n_0/u_0^3}, \quad (3.17)$$

the macroscopic quantities as

$$\tilde{n} = \frac{n}{n_0}, \quad \tilde{u} = \frac{u}{u_0}, \quad \tilde{T} = \frac{T}{T_0}, \quad \tilde{\mathbb{P}} = \frac{\mathbb{P}}{n_0 k_B T_0}, \quad \tilde{q} = \frac{q}{n_0 k_B T_0 u_0}. \quad (3.18)$$

In the Boltzmann equation, we rescale the collision kernel as

$$\tilde{B} = \frac{B}{B_0}, \quad B_0 = \sqrt{2\pi} u_0 d_{\text{ref}}^2 (T_{\text{ref}}/T_0)^{\omega-0.5}. \quad (3.19)$$

In the relaxation-type kinetic models, we rescale the collision frequency as

$$\tilde{\nu} = \frac{\nu}{\nu_0}, \quad \nu_0 = n_0 B_0 = 2C_0 \sqrt{\pi} \frac{n_0 k_B T_0}{\mu_{\text{ref}} (T_0/T_{\text{ref}})^\omega}. \quad (3.20)$$

Hence all equations will have the same Knudsen number defined as

$$\text{Kn} = \frac{u_0}{n_0 B_0 H_0} = \frac{u_0}{\nu_0 H_0} = \frac{1}{\sqrt{2\pi} n_0 d_{\text{ref}}^2 (T_{\text{ref}}/T_0)^{\omega-0.5} H_0}. \quad (3.21)$$

First of all, the definition in (3.3) is changed to (we drop the \sim in the following for simplicity):

$$\begin{aligned} n &= \int_{\mathbb{R}^3} f \, dv, \quad u = \frac{1}{n} \int_{\mathbb{R}^3} f v \, dv, \quad T = \frac{2}{3n} \int_{\mathbb{R}^3} f |v - u|^2 \, dv, \\ \mathbb{P} &= 2 \int_{\mathbb{R}^3} f (v - u) \otimes (v - u) \, dv, \quad q = \int_{\mathbb{R}^3} f (v - u) |v - u|^2 \, dv. \end{aligned} \quad (3.22)$$

The equation (3.2) after non-dimensionalization becomes

$$\frac{\partial f}{\partial t} + v \cdot \nabla_x f = \frac{1}{\varepsilon} \mathcal{Q}(f), \quad \varepsilon := \text{Kn}, \quad (3.23)$$

with the non-dimensionalized collision operator given by

- Boltzmann:

$$\mathcal{Q}^{\text{Boltz}}(f, f) = \int_{\mathbb{R}^3} \int_{\mathbb{S}^2} B(|v - v_*|, \cos \chi) [f(v') f(v'_*) - f(v) f(v_*)] \, d\sigma \, dv_*, \quad (3.24)$$

with

$$B(|v - v_*|, \cos \chi) = \frac{\alpha}{2^{2-\omega+\alpha} \Gamma(2.5 - \omega) \pi} |v - v_*|^{2(1-\omega)} (1 + \cos \chi)^{\alpha-1}. \quad (3.25)$$

- BGK:

$$\mathcal{Q}^{\text{BGK}}(f) = \nu(\mathcal{M}[f] - f), \quad (3.26)$$

with

$$\mathcal{M}[f] = \frac{n}{(\pi T)^{3/2}} \exp\left(-\frac{|v-u|^2}{T}\right), \quad \nu = \frac{1}{2C_0\sqrt{\pi}} n T^{1-\omega}. \quad (3.27)$$

- ESBGK:

$$\mathcal{Q}^{\text{ESBGK}}(f) = \text{Pr} \, \nu(\mathcal{G}[f] - f), \quad (3.28)$$

with

$$\mathcal{G}[f] = \frac{n}{\sqrt{\det(\pi \mathbb{T})}} \exp\left(-(v-u)^T \mathbb{T}^{-1} (v-u)\right), \quad \mathbb{T} = \frac{1}{\text{Pr}} T \text{Id} + \left(1 - \frac{1}{\text{Pr}}\right) \frac{\mathbb{P}}{n}. \quad (3.29)$$

- Shakov:

$$\mathcal{Q}^{\text{Shakov}}(f) = \nu(\mathcal{S}[f] - f), \quad (3.30)$$

with

$$\mathcal{S}[f] = \mathcal{M}[f] \left[1 + \frac{2(1-\text{Pr})}{5} \frac{q \cdot (v-u)}{nT^2} \left(\frac{2|v-u|^2}{T} - 5 \right) \right]. \quad (3.31)$$

For all the collision operators listed above, they satisfy the following common properties:

- Mass/momentum/energy conservation:

$$\int_{\mathbb{R}^3} \mathcal{Q}(f) \, dv = \int_{\mathbb{R}^3} \mathcal{Q}(f) \, v \, dv = \int_{\mathbb{R}^3} \mathcal{Q}(f) \, |v|^2 \, dv = 0. \quad (3.32)$$

- Equilibrium state is the Maxwellian:

$$\mathcal{Q}(f) = 0 \iff f = \mathcal{M}[f]. \quad (3.33)$$

- H-theorem (not for Shakov model):

$$- \int_{\mathbb{R}^3} \mathcal{Q}(f) \ln(f) \, dv \geq 0. \quad (3.34)$$

- Some additional properties for $\mathcal{M}[f]$, $\mathcal{G}[f]$, and $\mathcal{S}[f]$:

$$\begin{aligned} \int_{\mathbb{R}^3} \mathcal{M}[f] (v - u) \otimes (v - u) \, dv &= \frac{1}{2} n T \text{Id}, & \int_{\mathbb{R}^3} \mathcal{G}[f] (v - u) \otimes (v - u) \, dv &= \frac{1}{2} n \mathbb{T}, \\ \int_{\mathbb{R}^3} \mathcal{S}[f] (v - u) |v - u|^2 \, dv &= (1 - \text{Pr}) q. \end{aligned} \quad (3.35)$$

Using (3.32), if we take the moments

$$\int_{\mathbb{R}^3} \cdot (1, v, |v|^2)^T \, dv \quad (3.36)$$

on both sides of (3.23), we obtain

$$\begin{cases} \partial_t n + \nabla_x \cdot (nu) = 0, \\ \partial_t(nu) + \nabla_x \cdot (nu \otimes u + \mathbb{P}/2) = 0, \\ \partial_t E + \nabla_x \cdot (Eu + \mathbb{P}u + q) = 0, \end{cases} \quad (3.37)$$

where $E := \frac{3}{2}nT + nu^2$ is the total energy. This is the local conservation law which is not closed. Using the Chapman-Enskog expansion, one can close the system and derive the following Navier-Stokes equations by dropping $O(\varepsilon^2)$ terms:

$$\begin{cases} \partial_t n + \nabla_x \cdot (nu) = 0, \\ \partial_t(nu) + \nabla_x \cdot (nu \otimes u + nT\text{Id}/2) = \varepsilon \nabla_x \cdot (\mu(T)\sigma(u)), \\ \partial_t E + \nabla_x \cdot ((E + nT)u) = \varepsilon \nabla_x \cdot (2\mu(T)\sigma(u)u + \kappa(T)\nabla_x T), \end{cases} \quad (3.38)$$

where $\mu(T) := C_0\sqrt{\pi}T^\omega$, and $\kappa(T) = \frac{5}{2}\mu(T)$ in the BGK model, and $\kappa(T) = \frac{5}{2\text{Pr}}\mu(T)$ in the ESBGK and Shakov models.

Transforming back to the dimensional form, we get

$$\begin{cases} \partial_t \rho + \nabla_x \cdot (\rho u) = 0, \\ \partial_t(\rho u) + \nabla_x \cdot (\rho u \otimes u + nk_B T\text{Id}) = \nabla_x \cdot (\mu(T)\sigma(u)), \\ \partial_t(\rho u^2/2 + 3nk_B T/2) + \nabla_x \cdot ((\rho u^2/2 + 5nk_B T/2)u) = \nabla_x \cdot (\mu(T)\sigma(u)u + \kappa(T)\nabla_x T), \end{cases} \quad (3.39)$$

where $\rho = mn$, $\sigma(u) = \nabla_x u + (\nabla_x u)^T - \frac{2}{3}\nabla_x \cdot u\text{Id}$, $\mu(T) = \mu_{\text{ref}}(T/T_{\text{ref}})^\omega$, $\kappa(T) = \frac{5}{2}\frac{k_B}{m}\mu(T)$ in the BGK model, and $\kappa(T) = \frac{5}{2\text{Pr}}\frac{k_B}{m}\mu(T)$ in the ESBGK and Shakov models.

3.4 Implicit-explicit schemes for linear models

Before, we begin, we would like to recall the closely related family of IMEX-RK schemes for relaxation-type kinetic models: IMEX RK applied to BGK equation [61], first order IMEX RK applied to the ES-BGK equation [86], high order IMEX RK applied to ESBGK equation [66], and IMEX RK applied to Shakov equation [87]. In what follows, we will assume reader's familiarity with the aforementioned references.

We first briefly describe the general IMEX-BDF schemes applied to the relaxation-type kinetic equations (3.1).

$$\begin{aligned}
f^{(0)} &= f^{l-q+1}, \\
\sum_{i=0}^q a_i f^{(i)} &= \Delta t \sum_{i=0}^{q-1} \tilde{a}_i \mathcal{T}(f^{(i)}) + \frac{\Delta t}{\varepsilon} b \left[\mathcal{Q}(f^{(q)}) \right], \\
f^{l+1} &= f^{(q)}.
\end{aligned} \tag{3.40}$$

where $-\mathcal{T}$ is the convection operator; \mathcal{Q} is the collision operator; \tilde{a}_j are the vector of coefficients for the IMEX-BDF scheme. These coefficients, up to third order, are provided in Table 3.1. Note that IMEX-BDF1 is same as the ARS (1,1,1) scheme [61], [66]. To initiate

Table 3.1. Coefficients of IMEX-BDF schemes up to third order.

| q | a | \tilde{a} | b |
|-----|---|--|----------------|
| 1 | $(-1, 1)$ | 1 | 1 |
| 2 | $\left(\frac{1}{3}, -\frac{4}{3}, 1\right)$ | $\left(-\frac{2}{3}, \frac{4}{3}\right)$ | $\frac{2}{3}$ |
| 3 | $\left(-\frac{2}{11}, \frac{9}{11}, -\frac{18}{11}, 1\right)$ | $\left(\frac{6}{11}, -\frac{18}{11}, \frac{18}{11}\right)$ | $\frac{6}{11}$ |

the scheme (3.40), one needs $2q$ starting values: $f^{(0)}, \dots, f^{(q-1)}$; $\mathcal{T}(f^{(0)}), \dots, \mathcal{T}(f^{(q-1)})$. In practice, they can be obtained using IMEX-RK type schemes. With proper starting values, the scheme, nonetheless, may appear nonlinearly implicit since $\mathcal{Q}(f^{(q)})$ depends on $f^{(q)}$. To circumvent this, we use the moment computation strategy. To this end, we begin by defining the moment operator $\mathbb{M}_\Phi : \mathbb{R}^d \mapsto 1$

$$\mathbb{M}_\Phi [\cdot] = \int_{\mathbb{R}^3} \Phi(v) \cdot dv \tag{3.41}$$

where $\Phi(v)$ are some real valued functions. In general, for our purpose, \mathbb{M} is a bounded operator, admits the properties of inner product in *finite dimensional* Sobolev spaces.

3.4.1 IMEX-BDF-BGK scheme

We start by setting $\mathcal{Q} = \mathcal{M}$ in (3.40). The simplified scheme reads as:

$$\sum_{i=0}^q a_i f^{(i)} = \Delta t \sum_{i=0}^{q-1} \tilde{a}_i \mathcal{T}(f^{(i)}) + \frac{\Delta t}{\varepsilon} b \left[\nu^{(q)} (\mathcal{M}[f^{(q)}] - f^{(q)}) \right]. \quad (3.42)$$

To compute $f^{(q)}$, one needs $\nu^{(q)}$ and $\mathcal{M}[f^{(q)}]$. These quantities can be constructed from the moments of $f^{(q)}$. To this end, let $\Phi_B(v) = \{1, v, |v|^2\}$ in (3.41) and apply the moment operator to both sides of scheme (3.42):

$$\sum_{i=0}^q a_i \mathbb{M}_{\Phi_B} [f^{(i)}] = \Delta t \sum_{i=0}^{q-1} \tilde{a}_i \mathbb{M}_{\Phi_B} [\mathcal{T}(f^{(i)})]. \quad (3.43)$$

where $\mathbb{M}_{\Phi_B} [\mathcal{M}[f^{(q)}] - f^{(q)}] = 0$ owing to (3.32). From (3.43), $\mathbb{M}_{\Phi_B} [f^{(q)}]$ can be evaluated explicitly. One can rewrite (3.43) using (3.22) as

$$\begin{aligned} n^{(q)} &= a_q^{-1} \left[- \sum_{i=0}^{q-1} a_i n^{(i)} + \Delta t \sum_{i=0}^{q-1} \tilde{a}_i \int_{\mathbb{R}^3} \mathcal{T}(f^{(i)}) \, dv \right] \\ n^{(q)} u^{(q)} &= a_q^{-1} \left[- \sum_{i=0}^{q-1} a_i n^{(i)} u^{(i)} + \Delta t \sum_{i=0}^{q-1} \tilde{a}_i \int_{\mathbb{R}^3} \mathcal{T}(f^{(i)}) v \, dv \right] \\ E^{(q)} &= a_q^{-1} \left[- \sum_{i=0}^{q-1} a_i E^{(i)} + \Delta t \sum_{i=1}^{q-1} \tilde{a}_i \int_{\mathbb{R}^3} \mathcal{T}(f^{(i)}) |v|^2 \, dv \right]. \end{aligned} \quad (3.44)$$

Given these bulk properties, one can directly compute $\nu^{(q)}$ and construct $\mathcal{M}[f^{(q)}]$. The final scheme (3.42) then reads:

$$\begin{aligned} f^{(q)} &= \xi^{(q)} \left[- \sum_{i=0}^{q-1} a_i f^{(i)} + \Delta t \sum_{i=0}^{q-1} \tilde{a}_i \mathcal{T}(f^{(i)}) + \frac{\Delta t}{\varepsilon} b \nu^{(q)} \mathcal{M}[f^{(q)}] \right], \\ \text{with } \xi^{(q)} &= \left(a_q + \frac{\Delta t}{\varepsilon} b \nu^{(q)} \right)^{-1}. \end{aligned} \quad (3.45)$$

3.4.2 IMEX-BDF-ESBGK scheme

We start by setting $\mathcal{Q} = \mathcal{G}$ in (3.40). The simplified scheme reads as:

$$\sum_{i=0}^q a_i f^{(i)} = \sum_{i=0}^{q-1} \tilde{a}_i \mathcal{T}(f^{(i)}) + \frac{\Delta t}{\varepsilon} b \left[\text{Pr } \nu^{(q)} (\mathcal{G}[f^{(j)}] - f^{(j)}) \right]. \quad (3.46)$$

To compute $f^{(q)}$, one needs $\text{Pr } \nu^{(q)}$ and $\mathcal{G}[f^{(q)}]$. To this end, let $\Phi_E(v) = \{1, v, |v|^2, v \otimes v\}$ in (3.41). Applying this operator to both sides of scheme (3.46) results in 14 equations. The first five equations are same as (3.44). The last nine equations are

$$\begin{aligned} \Sigma^{(q)} = \zeta^{(q)} \left[- \sum_{i=0}^{q-1} a_i \Sigma^{(i)} + \Delta t \sum_{i=0}^{q-1} \tilde{a}_i \int_{\mathbb{R}^3} \mathcal{T}(f^{(i)}) v \otimes v \, dv + \frac{\Delta t}{\varepsilon} b \nu^{(q)} \left[n^{(q)} \left(\frac{1}{2} T^{(q)} \text{Id} + u^{(q)} \otimes u^{(q)} \right) \right] \right], \\ \text{with} \quad \zeta^{(q)} = \left(a_q + \frac{\Delta t}{\varepsilon} b \nu^{(j)} \right)^{-1}. \end{aligned} \quad (3.47)$$

Given the bulk properties, one can directly compute $\mathcal{G}[f^{(q)}]$ and $\text{Pr } \nu^{(q)}$. The final scheme (3.46) then reads:

$$\begin{aligned} f^{(q)} = \xi^{(q)} \left[- \sum_{i=0}^{q-1} a_i f^{(i)} + \Delta t \sum_{i=0}^{q-1} \tilde{a}_i \mathcal{T}(f^{(i)}) + \frac{\Delta t}{\varepsilon} b \, \text{Pr } \nu^{(q)} \mathcal{G}[f^{(q)}] \right], \\ \text{with} \quad \xi^{(q)} = \left(a_q + \frac{\Delta t}{\varepsilon} b \, \text{Pr } \nu^{(q)} \right)^{-1}. \end{aligned} \quad (3.48)$$

3.4.3 IMEX-BDF-Shakov scheme

We start by setting $\mathcal{Q} = \mathcal{S}$ in (3.40). The simplified scheme reads as:

$$\sum_{i=0}^q a_i f^{(i)} = \Delta t \sum_{i=0}^{q-1} \tilde{a}_i \mathcal{T}(f^{(i)}) + \frac{\Delta t}{\varepsilon} b \left[\nu^{(q)} (\mathcal{S}[f^{(j)}] - f^{(j)}) \right]. \quad (3.49)$$

To compute $f^{(q)}$, one needs $\nu^{(q)}$ and $\mathcal{S}[f^{(q)}]$. To this end, let $\Phi_S(v) = \{1, v, |v|^2, v \otimes v, v|v|^2\}$ in (3.41). Apply this operator to both sides of scheme (3.49) results in 17 equations. The first five equations are same as (3.44). The last twelve equations are

$$\begin{aligned}\Sigma^{(q)} &= \zeta^{(q)} \left[-\sum_{i=0}^{q-1} a_i \Sigma^{(i)} + \Delta t \sum_{i=0}^{q-1} \tilde{a}_i \int_{\mathbb{R}^3} \mathcal{T}(f^{(i)}) v \otimes v \, dv + \frac{\Delta t}{\varepsilon} b \nu^{(q)} \left[n^{(q)} \left(\frac{1}{2} T^{(q)} \text{Id} + u^{(q)} \otimes u^{(q)} \right) \right] \right], \\ \Lambda_p^{(q)} &= \zeta^{(q)} \left[-\sum_{i=0}^{q-1} a_i \Lambda_p^{(i)} + \Delta t \sum_{i=0}^{q-1} \tilde{a}_i \int_{\mathbb{R}^3} \mathcal{T}(f^{(i)}) v_p |v|^2 \, dv \right. \\ &\quad \left. + \frac{\Delta t}{\varepsilon} b \nu^{(q)} \left[(1 - \text{Pr}) \left(-2 \Sigma_{pr}^{(q)} u_r^{(q)} + n u_p^{(q)} |u^{(q)}|^2 - \frac{3}{2} n^{(q)} u_p^{(q)} T^{(q)} \right) + n^{(q)} u_p^{(q)} \left(\frac{5}{2} T^{(q)} + |u^{(q)}|^2 \right) \right] \right] \\ \text{with} \quad \zeta^{(q)} &= \left(a_q + \text{Pr} \frac{\Delta t}{\varepsilon} b \nu^{(q)} \right)^{-1}.\end{aligned}\tag{3.50}$$

Given the bulk properties, one can directly compute $\mathcal{S}[f^{(q)}]$ and $\nu^{(q)}$. The final scheme (3.49) then reads:

$$\begin{aligned}f^{(q)} &= \xi^{(q)} \left[-\sum_{i=0}^{q-1} a_i f^{(i)} + \Delta t \sum_{i=0}^{q-1} \tilde{a}_i \mathcal{T}(f^{(i)}) + \frac{\Delta t}{\varepsilon} b \nu^{(q)} \mathcal{S}[f^{(q)}] \right], \\ \text{with} \quad \xi^{(q)} &= \left(a_q + \frac{\Delta t}{\varepsilon} b \nu^{(q)} \right)^{-1}.\end{aligned}\tag{3.51}$$

Remark 3.4.1. *If we look closely at three schemes, we will find a pattern common to these relaxation-type kinetic models. First, we recall that while devising kinetic models for single species system, the collision term $\mathbb{Q} := (\mathcal{M}, \mathcal{G}, \mathcal{S})$ is expected to have the following four properties [2]:*

- *It guarantees the conservation of mass, momentum, and energy, i.e.,*

$$\int_{\mathbb{R}^3} \mathbb{Q} \, dv = \int_{\mathbb{R}^3} v \mathbb{Q} \, dv = \int_{\mathbb{R}^3} v^2 \mathbb{Q} \, dv = 0.\tag{3.52}$$

- The entropy production is always positive, i.e.,

$$-\int_{\mathbb{R}^3} \ln(f) \mathbb{Q} \, dv \geq 0$$

- Due to specific form of \mathbb{Q} , the phase density in equilibrium is a Maxwellian i.e.,

$$\mathbb{Q} = 0 \Leftrightarrow \int_{\mathbb{R}^3} \ln(f) \mathbb{Q} \, dv = 0 \Leftrightarrow f = \mathcal{M}$$

- The Prandtl number is close to 2/3 for monoatomic gases, i.e.,

$$\text{Pr} = \frac{5}{2} \frac{k_B \mu}{m \kappa},$$

where μ and κ , respectively, refer to dynamic viscosity and thermal conductivity.

Of these four, for devising an IMEX AP “numerical” scheme, the first and third property (3.52) are only relevant: the first one is utilized for implicit evaluation, whereas third ensures asymptotic-preserving property.

Kinetic models of relaxation type ($\mathbb{Q} - f$) are, generally, devised to match the first k moments of \mathbb{Q} and f . For example, ESBGK model matches the first 10 moments ($\sum_{l=0}^2 d^l$, $d = 3$), whereas Shakov matches the 13 moments (3 additional from higher rank tensor i.e., heat flux). Now consider a relaxation type fictitious collision model \mathbb{Q} which we have devised to match the first $k = \sum_{l=0}^r d^l$, for some natural number $r \geq 1$, moments i.e.,

$$\int (\mathbb{Q}[f] - f) \underbrace{v \otimes \cdots \otimes v}_{l \text{ times}} \, dv = \mathbb{F} \left(\int f \, dv, \int f v \, dv, \dots, \int f \underbrace{v \otimes \cdots \otimes v}_{l \text{ times}} \, dv \right), \quad l = \{0, 1, 2, \dots, r\}, \quad (3.53)$$

where \mathbb{F} is some implicit function of moments. Now, an IMEX-BDF scheme for our fictitious kernel \mathbb{Q} with relaxation parameter ν should read

$$\sum_{i=0}^q a_i f^{(i)} = \Delta t \sum_{j=1}^{i-1} \tilde{a}_i \mathcal{T}(f^{(i)}) + \frac{\Delta t}{\varepsilon} \sum_{j=1}^i a_{ij} \nu^{(j)} (\mathbb{Q}[f^{(j)}] - f^{(j)}), \quad i = 1, \dots, s. \quad (3.54)$$

Now we compute the first k moments of (3.54), and use (3.53) to construct a “linear” matrix system of size $k \times k$ with rank at most k . By solving the matrix system, one can obtain the first k moments, and use it to construct the distribution \mathbb{Q} . Once \mathbb{Q} is known, $f^{(i)}$ can be obtained directly from (3.54).

Of course, the caveat is that higher k implies a finer velocity mesh for enforcing discrete conservation. Moreover, moment matching can go only so far. Entropy is a further concern (Shakov model includes higher moments, but does not strictly satisfy the H-theorem [85]).

3.5 Implicit-explicit schemes for Boltzmann equation

In this section, we extend the approach described in the previous section to the case of non-linear stiff full Boltzmann equation.

The general IMEX-BDF schemes applied to the non-linear stiff Boltzmann equation (3.23) reads

$$\begin{aligned} f^{(0)} &= f^{l-q+1}, \\ \sum_{i=0}^q a_i f^{(i)} &= \Delta t \sum_{i=0}^{q-1} \tilde{a}_i \mathcal{T}(f^{(i)}) + \frac{\Delta t}{\varepsilon} b \left[\mathcal{Q}(f^{(q)}) - \mathcal{P}(f^{(q)}) + \mathcal{P}(f^{(q)}) \right], \\ f^{l+1} &= f^{(q)}. \end{aligned} \quad (3.55)$$

where $a_i; \tilde{a}_j; b$ are the usual coefficients for the IMEX-BDF scheme. Now we use the property $\sum_{i=0}^{q-1} \tilde{a}_i = b$ in the last term to perform an implicit-explicit splitting:

$$\begin{aligned} f^{(0)} &= f^{l-q+1}, \\ \sum_{i=0}^q a_i f^{(i)} &= \Delta t \sum_{i=0}^{q-1} \tilde{a}_i \mathcal{T}(f^{(i)}) + \frac{\Delta t}{\varepsilon} \sum_{i=0}^{q-1} \tilde{a}_i \left[\mathcal{Q}(f^{(i)}) - \mathcal{P}(f^{(i)}) \right] + \frac{\Delta t}{\varepsilon} b \left[\mathcal{P}(f^{(q)}) \right], \\ f^{l+1} &= f^{(q)}. \end{aligned} \quad (3.56)$$

In this form, $[\mathcal{Q}(f^{(i)}) - \mathcal{P}(f^{(i)})]$ is evaluated explicitly; and $\mathcal{P}[f^{(q)}]$ is evaluated implicitly. The ideas from the previous section follow in a straightforward manner.

3.5.1 IMEX-BDF Boltzmann-BGK scheme

AP Boltzmann-BGK scheme is constructed by setting $\mathcal{Q} = \mathcal{Q}^{\text{Boltz}}$ and $\mathcal{P} = \mathcal{M}$ in (3.56).

The simplified scheme reads as:

$$\sum_{i=0}^q a_i f^{(i)} = \Delta t \sum_{i=0}^{q-1} \tilde{a}_i \mathcal{T}(f^{(i)}) + \frac{\Delta t}{\varepsilon} \sum_{i=0}^{q-1} \tilde{a}_i \left[\mathcal{Q}^{\text{Boltz}} - \nu^{(i)} (\mathcal{M}[f^{(i)}] - f^{(i)}) \right] + \frac{\Delta t}{\varepsilon} b \nu^{(q)} (\mathcal{M}[f^{(q)}] - f^{(q)}). \quad (3.57)$$

Remark 3.5.1. As per [61], ν is selected so that it is a valid estimate for the largest value of the negative term in the Boltzmann operator i.e.,

$$\nu \geq \int_{\mathbb{R}^3} \int_{\mathbb{S}^2} B(|\mathbf{v} - \mathbf{v}_*|, \cos \chi) f(v_*) d\omega d\mathbf{v}_*.$$

For the Variable Hard sphere scattering model considered, assuming that velocity space is truncated [22], [31] in an interval $[-\eta\sqrt{T}, \eta\sqrt{T}]^3$ so that $|\mathbf{v} - \mathbf{v}_*| \leq |2\mathbf{v}| \leq 2\eta\sqrt{T}$; and utilizing the bounds $\omega \in [0.5, 1]$ and $\alpha \in (1, 2]$; one can show that

$$\nu \propto nT^{1-\omega} \implies \nu = \bar{s} nT^{1-\omega}, \quad (3.58)$$

where \bar{s} is some safety factor. There is no precise rule for selecting ν : (3.58) works well for the numerical problems that we have studied in the present work. However, we do not claim that (3.58) are optimal.

To compute $f^{(i)}$, one needs $\nu^{(i)}$ and $\mathcal{M}[f^{(i)}]$. To this end, apply the moment operator, \mathbb{M}_{ϕ_B} , to both sides of scheme (3.57):

$$\sum_{i=0}^q a_i \mathbb{M}_{\phi_B} [f^{(i)}] = \Delta t \sum_{i=0}^{q-1} \tilde{a}_i \mathbb{M}_{\phi_B} [\mathcal{T}(f^{(i)})] \quad (3.59)$$

where $\mathbb{M}_{\phi_B} [\mathcal{M}[f^{(i)}] - f^{(i)}] = \mathbb{M}_{\phi_B} [\mathcal{Q}^{\text{Boltz}}] = 0$ owing to (3.32). From (3.59), $\mathbb{M}_{\phi_B} [f^{(i)}]$ can be evaluated explicitly, and therefore $\mathcal{M}^{(q)}$ can be constructed.

The final scheme reads:

$$\begin{aligned} f^{(q)} = \zeta^{(q)} \Bigg[& - \sum_{i=0}^{q-1} a_i f^{(i)} + \Delta t \sum_{i=0}^{q-1} \tilde{a}_i \mathcal{T}(f^{(i)}) + \frac{\Delta t}{\varepsilon} \sum_{i=0}^{q-1} \tilde{a}_i \mathcal{Q}_B(f^{(i)}) \\ & - \frac{\Delta t}{\varepsilon} \sum_{i=0}^{q-1} \tilde{a}_i \nu^{(i)} (\mathcal{M}[f^{(i)}] - f^{(i)}) + \frac{\Delta t}{\varepsilon} b \nu^{(q)} \mathcal{M}[f^{(q)}] \Bigg], \\ & \text{with } \zeta^{(q)} = \left(a_q + \frac{\Delta t}{\varepsilon} b \nu_B^{(q)} \right)^{-1}. \end{aligned} \quad (3.60)$$

3.5.2 IMEX-BDF Boltzmann-ESBGK scheme

AP Boltzmann-ESBGK scheme is constructed by setting $\mathcal{Q} = \mathcal{Q}^{\text{Boltz}}$ and $\mathcal{P} = \mathcal{G}$ in (3.56).

The simplified scheme reads as:

$$\sum_{i=0}^q a_i f^{(i)} = \Delta t \sum_{i=0}^{q-1} \tilde{a}_i \mathcal{T}(f^{(i)}) + \frac{\Delta t}{\varepsilon} \sum_{i=0}^{q-1} \tilde{a}_i \left[\mathcal{Q}^{\text{Boltz}} - \text{Pr } \nu^{(i)} (\mathcal{G}[f^{(i)}] - f^{(i)}) \right] + \frac{\Delta t}{\varepsilon} b \text{Pr } \nu^{(q)} (\mathcal{G}[f^{(q)}] - f^{(q)}). \quad (3.61)$$

To compute $f^{(i)}$, one needs $\nu^{(i)}$ and $\mathcal{G}[f^{(i)}]$. To this end, apply the moment operator, \mathbb{M}_{ϕ_E} , to both sides of scheme (3.61):

$$\begin{aligned} \sum_{i=0}^q a_i \mathbb{M}_{\phi_E}[f^{(i)}] &= \Delta t \sum_{i=0}^{q-1} \tilde{a}_i \mathbb{M}_{\phi_E}[\mathcal{T}(f^{(i)})] + \frac{\Delta t}{\varepsilon} b \Pr \nu^{(q)} \mathbb{M}_{\phi_E}[\mathcal{G}[f^{(q)}] - f^{(q)}] \\ &\quad + \frac{\Delta t}{\varepsilon} \sum_{i=0}^{q-1} \tilde{a}_i \mathbb{M}_{\phi_E}[\mathcal{Q}^{\text{Boltz}} - \Pr \nu^{(i)}(\mathcal{G}[f^{(i)}] - f^{(i)})] \end{aligned} \quad (3.62)$$

Using $\mathbb{M}_{\phi_B}[\mathcal{G}[f^{(q)}] - f^{(q)}] = \mathbb{M}_{\phi_B}[\mathcal{Q}^{\text{Boltz}}] = 0$ owing to (3.32), one can rewrite first 5 terms of (3.62) as

$$\sum_{i=0}^q \mathbb{M}_{\phi_B}[f^{(i)}] = \Delta t \sum_{i=0}^{q-1} \tilde{a}_i \mathbb{M}_{\phi_B}[\mathcal{T}(f^{(i)})], \quad (3.63)$$

which is essentially (3.43).

We now need to define last 9 terms of (3.62) to fully construct \mathcal{G} . Let $\Sigma^{(i)} = \mathbb{M}_{v \otimes v}[f^{(i)}]$.

Using (3.29) and (3.35), we get

$$\begin{aligned} \sum_{i=0}^q a_i \Sigma^{(i)} &= \Delta t \sum_{i=0}^{q-1} \tilde{a}_i \int_{\mathbb{R}^3} \mathcal{T}(f^{(i)}) v \otimes v \, dv \\ &\quad + \frac{\Delta t}{\varepsilon} \sum_{i=0}^{q-1} \tilde{a}_i \left\{ \int_{\mathbb{R}^3} \mathcal{Q}^{\text{Boltz}}(f^{(i)}) v \otimes v \, dv - \nu^{(i)} \left[n^{(i)} \left(\frac{1}{2} T^{(i)} \text{Id} + (u^{(i)} \otimes u^{(i)}) \right) - \Sigma^{(i)} \right] \right\} \\ &\quad + \frac{\Delta t}{\varepsilon} b \nu^{(q)} \left[n^{(q)} \left(\frac{1}{2} T^{(q)} \text{Id} + (u^{(q)} \otimes u^{(q)}) \right) - \Sigma^{(q)} \right] \end{aligned}$$

which can be rearranged to evaluate $\Sigma^{(i)}$. Using this, and (3.62), $\mathcal{G}^{(q)}$ can be now constructed.

The final scheme reads:

$$\begin{aligned}
f^{(q)} = \xi^{(q)} \Bigg[& - \sum_{i=0}^{q-1} a_i f^{(i)} + \Delta t \sum_{i=0}^{q-1} \tilde{a}_{ij} \mathcal{T}(f^{(i)}) + \frac{\Delta t}{\varepsilon} \sum_{i=0}^{q-1} \tilde{a}_{ij} \mathcal{Q}^{\text{Boltz}}(f^{(i)}) \\
& - \frac{\Delta t}{\varepsilon} \sum_{i=0}^{q-1} \tilde{a}_i \text{Pr } \nu^{(i)}(\mathcal{G}[f^{(i)}] - f^{(i)}) + \frac{\Delta t}{\varepsilon} b \text{Pr } \nu^{(q)} \mathcal{G}[f^{(q)}] \Bigg], \\
& \text{with } \xi^{(q)} = \left(a_q + \frac{\Delta t}{\varepsilon} b \text{Pr } \nu^{(q)} \right)^{-1}.
\end{aligned} \tag{3.64}$$

3.5.3 IMEX-BDF Boltzmann-Shakov scheme

AP Boltzmann-Shakov scheme is constructed by setting $\mathcal{Q} = \mathcal{Q}^{\text{Boltz}}$ and $\mathcal{P} = \mathcal{S}$ in (3.56).

The simplified scheme reads as:

$$\sum_{i=0}^q f^{(i)} = \Delta t \sum_{i=0}^{q-1} \tilde{a}_i \mathcal{T}(f^{(i)}) + \frac{\Delta t}{\varepsilon} \sum_{i=0}^{q-1} \tilde{a}_i \left[\mathcal{Q}^{\text{Boltz}} - \nu^{(i)}(\mathcal{S}[f^{(i)}] - f^{(i)}) \right] + \frac{\Delta t}{\varepsilon} b \nu^{(q)}(\mathcal{S}[f^{(q)}] - f^{(q)}). \tag{3.65}$$

To compute $f^{(i)}$, one needs $\nu^{(i)}$ and $\mathcal{S}[f^{(i)}]$. Again these quantities can be constructed from the moments of $f^{(i)}$. To this end, first apply the moment operator, \mathbb{M}_{ϕ_B} , to both sides of scheme (3.65):

$$\sum_{i=0}^q a_i \mathbb{M}_{\phi_B} [f^{(i)}] = \Delta t \sum_{i=0}^{q-1} \tilde{a}_i \mathbb{M}_{\phi_B} [\mathcal{T}(f^{(i)})], \tag{3.66}$$

where we used $\mathbb{M}_{\phi_B} [\mathcal{S}[f^{(i)}] - f^{(i)}] = \mathbb{M}_{\phi_B} [\mathcal{Q}^{\text{Boltz}}] = 0$ owing to (3.32).

To define heat flux $q^{(i)}$, so as to fully construct \mathcal{S} , apply the moment operator $\mathbb{M}_{(v-u^{(i)})|v-u^{(i)}|^2}$ to both sides of scheme (3.65):

$$\begin{aligned} \sum_{i=0}^q a_i q^{(i)} = & \Delta t \sum_{i=0}^{q-1} \tilde{a}_i \int_{\mathbb{R}^3} \mathcal{T}(f^{(i)}) (v - u^{(i)}) |v - u^{(i)}|^2 dv \\ & + \frac{\Delta t}{\varepsilon} \sum_{i=0}^{q-1} \tilde{a}_i \left\{ \int_{\mathbb{R}^3} \mathcal{Q}^{\text{Boltz}}(f^{(i)}) (v - u^{(i)}) |v - u^{(i)}|^2 dv - \nu^{(i)} \left[q^{(i)}(1 - \text{Pr}) - q^{(i)} \right] \right\} \\ & + \frac{\Delta t}{\varepsilon} b \nu^{(q)} \left[q^{(q)}(1 - \text{Pr}) - q^{(q)} \right] \end{aligned}$$

which can be rearranged as

$$\begin{aligned} q^{(q)} = \zeta^{(q)} \left[- \sum_{i=0}^{q-1} a_i q^{(i)} + \Delta t \sum_{i=0}^{q-1} \tilde{a}_i \int_{\mathbb{R}^3} \mathcal{T}(f^{(i)}) (v - u^{(i)}) |v - u^{(i)}|^2 dv \right. \\ \left. + \frac{\Delta t}{\varepsilon} \sum_{i=0}^{q-1} \tilde{a}_i \left\{ \int_{\mathbb{R}^3} \mathcal{Q}^{\text{Boltz}}(f^{(i)}) (v - u^{(i)}) |v - u^{(i)}|^2 dv - \nu^{(i)} \left[q^{(i)}(1 - \text{Pr}) - q^{(i)} \right] \right\} \right] \\ \text{with} \quad \zeta^{(q)} = \left(1 + \text{Pr} \frac{\Delta t}{\varepsilon} b \nu^{(q)} \right)^{-1}. \end{aligned} \quad (3.67)$$

From (3.66, 3.67), all the bulk properties can be evaluated explicitly, and $\mathcal{S}[f^{(q)}]$ can be constructed. The final scheme reads:

$$\begin{aligned} f^{(q)} = \xi^{(q)} \left[- \sum_{i=0}^{q-1} a_i f^{(i)} + \Delta t \sum_{i=0}^{q-1} \tilde{a}_i \mathcal{T}(f^{(i)}) \right. \\ \left. - \frac{\Delta t}{\varepsilon} \sum_{i=0}^{q-1} \tilde{a}_i \nu^{(i)} (\mathcal{S}[f^{(i)}] - f^{(i)}) + \frac{\Delta t}{\varepsilon} b \nu^{(q)} \mathcal{S}[f^{(q)}] \right], \\ \text{with} \quad \xi^{(q)} = \left(a_q + \frac{\Delta t}{\varepsilon} b \nu^{(q)} \right)^{-1}. \end{aligned} \quad (3.68)$$

4. VERIFICATION PROBLEMS

Verification tests are required to assess the developed method. A diverse set of verification problems for single/multi-species problems have been developed.

4.1 Multi-species: Spatially homogeneous Krook-Wu exact solution

For constant collision kernel, an exact solution to the spatially homogeneous multi-species Boltzmann equation can be constructed (see [88]). We use this solution to verify the accuracy of the proposed fast spectral method for approximating the collision operator. Considering a binary mixture, the equation simplifies to

$$\partial_t f^{(i)} = \sum_{j=1}^2 \int_{\mathbb{R}^3} \int_{S^2} B_{ij} \left[f^{(i)}(v') f^{(j)}(v'_*) - f^{(i)}(v) f^{(j)}(v_*) \right] d\sigma dv_*, \quad (4.1)$$

where $B_{ij} = B_{ji} := \frac{\lambda_{ji}}{4\pi n^{(j)}}$ and λ_{ij} is some positive constant. The exact solution is given by

$$f^{(i)}(t, v) = n^{(i)} \left(\frac{m_i}{2\pi K} \right)^{3/2} \exp \left(- \frac{m_i v^2}{2K} \right) \left((1 - 3Q_i) + \frac{m_i}{K} Q_i v^2 \right), \quad i = 1, 2, \quad (4.2)$$

where

$$\begin{aligned} \mu &= \frac{4m_1 m_2}{(m_1 + m_2)^2}, \quad p_1 = \lambda_{22} - \lambda_{21} \mu (3 - 2\mu), \quad p_2 = \lambda_{11} - \lambda_{12} \mu (3 - 2\mu), \\ A &= \frac{1}{6} \left(\lambda_{11} + \lambda_{21} \mu \left(3 - 2\mu \frac{p_2}{p_1} \right) \right), \quad B = \frac{1}{3} \left(\lambda_{11} p_1 + \lambda_{21} \mu (3 - 2\mu) p_2 \right), \\ Q(t) &= \frac{A}{A \exp(At) - B}, \quad Q_i(t) = p_i Q(t), \\ K(t) &= \frac{n^{(1)} + n^{(2)}}{(n^{(1)} + n^{(2)}) + 2(n^{(1)} p_1 + n^{(2)} p_2) Q(t)}. \end{aligned} \quad (4.3)$$

Furthermore, the following condition needs to be satisfied

$$(p_1 - p_2) \left(2\mu^2 \left(\frac{\lambda_{21}}{p_1} - \frac{\lambda_{12}}{p_2} \right) - 1 \right) = 0. \quad (4.4)$$

For simplicity, we choose $n^{(1)} = n^{(2)} = 1$, $\lambda_{11} = \lambda_{22} = 1$, $\lambda_{12} = \lambda_{21} = 1/2$ but vary the mass ratio m_1/m_2 in the following tests.

It is also helpful to take the derivative of eqn. (4.2), which yields

$$\begin{aligned}\partial_t f^{(i)} &= f^{(i)} \left(-\frac{3}{2K} K' + \frac{m_i v^2}{2K^2} K' \right) \\ &+ n^{(i)} \left(\frac{m_i}{2\pi K} \right)^{3/2} \exp \left(-\frac{m_i v^2}{2K} \right) \left(-3Q'_i + \frac{m_i}{K} Q'_i v^2 - \frac{m_i}{K^2} K' Q_i v^2 \right) \\ &:= \sum_{j=1}^2 \mathcal{Q}^{(ij)}(f^{(i)}, f^{(j)}),\end{aligned}\tag{4.5}$$

where

$$\begin{aligned}Q'(t) &= -\frac{A^3 \exp(At)}{(A \exp(At) - B)^2}, \quad Q'_i(t) = p_i Q'(t), \\ K'(t) &= -\frac{2(n^{(1)} + n^{(2)})(n^{(1)} p_1 + n^{(2)} p_2)}{[(n^{(1)} + n^{(2)}) + 2(n^{(1)} p_1 + n^{(2)} p_2)Q(t)]^2} Q'(t).\end{aligned}\tag{4.6}$$

This allows us to check the accuracy of the collision solver without introducing time discretization error.

Figure 4.1 depicts the convergence behavior of the proposed fast algorithm with respect to N for different mass ratios. Due to the isotropic nature of the solution, we observe that the errors remain relatively unaffected for different M (number of quadrature points used on the sphere). On the other hand, the method exhibits a spectral convergence as N (number of discretization points in each velocity dimension) increases. It is also clear that the accuracy deteriorates for large mass ratios (to keep the same level of accuracy, larger N is needed). To understand the influence of N_ρ (number of quadrature points in the radial direction), we list in Table 4.1 the errors of the method with respect to different N_ρ . It can be observed that the error is relatively unaffected upon reducing N_ρ from N to $N/2$.

Next we evolve the solution using the SSP-RK2 with time step $\Delta t = 0.01$. Figure 4.2 illustrates the time evolution of the distribution function sliced along the velocity domain

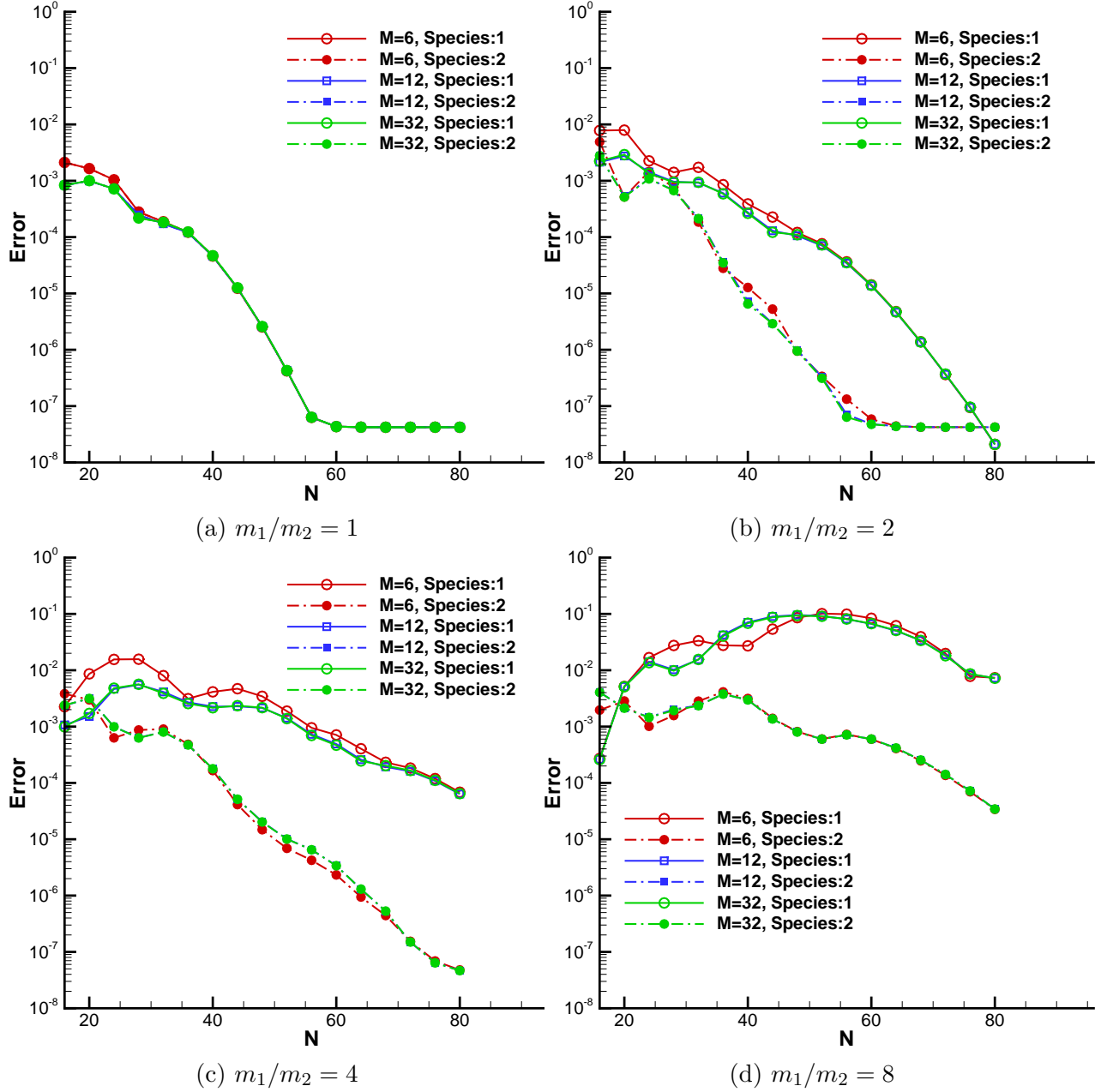


Figure 4.1. Spatially homogeneous Krook-Wu solution. L^∞ error $\mathcal{E}^{(i)} = \|\partial_t f_{exact}^{(i)} - \partial_t f_{numerical}^{(i)}\|_{L^\infty}$, $i = \{1, 2\}$ at $t = 4$ for different mass ratios. N is the number of discretization points in each velocity dimension and M is the number of spherical design quadrature points used on the sphere. Number of Gauss-Legendre quadrature points N_ρ in the radial direction is fixed to N . A fixed velocity domain $[-12, 12]^3$ has been used for all cases.

Table 4.1. Spatially homogeneous Krook-Wu solution. L^∞ error $\mathcal{E}^{(i)} = \|\partial_t f_{exact}^{(i)} - \partial_t f_{numerical}^{(i)}\|_{L^\infty}$, $i = \{1, 2\}$ at $t = 4$ for different mass ratios. N is the number of discretization points in each velocity dimension and N_ρ is the number of Gauss quadrature points used in the radial direction. Number of quadrature points M used on the sphere is fixed to 6. A fixed velocity domain $[-12, 12]^3$ has been used for all cases.

| N | N_ρ | $m_1/m_2 = 1$ | | $m_1/m_2 = 2$ | | $m_1/m_2 = 4$ | | $m_1/m_2 = 6$ | | $m_1/m_2 = 8$ | |
|-----|----------|---------------------|---------------------|---------------------|---------------------|---------------------|---------------------|---------------------|---------------------|---------------------|---------------------|
| | | $\mathcal{E}^{(1)}$ | $\mathcal{E}^{(2)}$ | $\mathcal{E}^{(1)}$ | $\mathcal{E}^{(2)}$ | $\mathcal{E}^{(1)}$ | $\mathcal{E}^{(2)}$ | $\mathcal{E}^{(1)}$ | $\mathcal{E}^{(2)}$ | $\mathcal{E}^{(1)}$ | $\mathcal{E}^{(2)}$ |
| 16 | 4 | 1.528e-03 | 1.528e-03 | 6.675e-03 | 4.444e-03 | 2.048e-03 | 3.633e-03 | 1.414e-03 | 4.941e-04 | 2.709e-04 | 2.481e-03 |
| | 8 | 2.114e-03 | 2.114e-03 | 7.795e-03 | 4.917e-03 | 2.253e-03 | 3.828e-03 | 1.425e-03 | 7.087e-04 | 2.715e-04 | 1.963e-03 |
| | 16 | 2.114e-03 | 2.114e-03 | 7.795e-03 | 4.917e-03 | 2.253e-03 | 3.828e-03 | 1.425e-03 | 7.086e-04 | 2.715e-04 | 1.963e-03 |
| 24 | 6 | 1.052e-03 | 1.052e-03 | 2.752e-03 | 1.390e-03 | 1.786e-02 | 6.280e-04 | 1.595e-02 | 1.434e-03 | 1.719e-02 | 1.037e-03 |
| | 12 | 1.041e-03 | 1.041e-03 | 2.254e-03 | 1.458e-03 | 1.557e-02 | 6.312e-04 | 1.422e-02 | 1.527e-03 | 1.676e-02 | 1.013e-03 |
| | 24 | 1.041e-03 | 1.041e-03 | 2.254e-03 | 1.458e-03 | 1.557e-02 | 6.312e-04 | 1.422e-02 | 1.527e-03 | 1.676e-02 | 1.013e-03 |
| 32 | 8 | 1.526e-04 | 1.526e-04 | 1.671e-03 | 2.237e-04 | 7.249e-03 | 9.770e-04 | 1.692e-02 | 1.701e-03 | 3.029e-02 | 2.928e-03 |
| | 16 | 1.873e-04 | 1.873e-04 | 1.729e-03 | 1.852e-04 | 8.018e-03 | 9.020e-04 | 1.935e-02 | 1.652e-03 | 3.338e-02 | 2.822e-03 |
| | 32 | 1.873e-04 | 1.873e-04 | 1.729e-03 | 1.852e-04 | 8.018e-03 | 9.020e-04 | 1.935e-02 | 1.652e-03 | 3.338e-02 | 2.822e-03 |
| 40 | 10 | 5.239e-05 | 5.239e-05 | 3.794e-04 | 1.146e-05 | 4.243e-03 | 1.404e-04 | 9.435e-03 | 8.260e-04 | 3.272e-02 | 3.285e-03 |
| | 20 | 4.603e-05 | 4.603e-05 | 3.881e-04 | 1.274e-05 | 4.137e-03 | 1.658e-04 | 9.493e-03 | 8.394e-04 | 2.713e-02 | 3.149e-03 |
| | 40 | 4.603e-05 | 4.603e-05 | 3.881e-04 | 1.274e-05 | 4.137e-03 | 1.658e-04 | 9.493e-03 | 8.394e-04 | 2.713e-02 | 3.149e-03 |
| 48 | 12 | 2.456e-06 | 2.456e-06 | 1.248e-04 | 2.395e-06 | 3.315e-03 | 3.119e-05 | 2.541e-02 | 2.271e-04 | 8.516e-02 | 9.661e-04 |
| | 24 | 2.539e-06 | 2.539e-06 | 1.207e-04 | 9.495e-07 | 3.446e-03 | 1.477e-05 | 2.559e-02 | 1.951e-04 | 8.580e-02 | 8.142e-04 |
| | 48 | 2.539e-06 | 2.539e-06 | 1.207e-04 | 9.495e-07 | 3.446e-03 | 1.477e-05 | 2.559e-02 | 1.951e-04 | 8.580e-02 | 8.142e-04 |
| 56 | 14 | 6.378e-08 | 6.378e-08 | 3.666e-05 | 1.944e-07 | 9.013e-04 | 1.173e-05 | 1.725e-02 | 1.068e-04 | 9.893e-02 | 7.127e-04 |
| | 28 | 6.297e-08 | 6.297e-08 | 3.635e-05 | 1.328e-07 | 9.517e-04 | 4.236e-06 | 1.726e-02 | 9.870e-05 | 9.896e-02 | 7.260e-04 |
| | 56 | 6.297e-08 | 6.297e-08 | 3.635e-05 | 1.328e-07 | 9.517e-04 | 4.236e-06 | 1.726e-02 | 9.870e-05 | 9.896e-02 | 7.260e-04 |
| 64 | 16 | 4.227e-08 | 4.227e-08 | 4.704e-06 | 4.749e-08 | 4.201e-04 | 3.460e-06 | 5.263e-03 | 4.056e-05 | 6.231e-02 | 4.053e-04 |
| | 32 | 4.227e-08 | 4.227e-08 | 4.754e-06 | 4.422e-08 | 4.043e-04 | 9.441e-07 | 5.153e-03 | 3.381e-05 | 6.186e-02 | 4.082e-04 |
| | 64 | 4.227e-08 | 4.227e-08 | 4.754e-06 | 4.422e-08 | 4.043e-04 | 9.441e-07 | 5.153e-03 | 3.381e-05 | 6.186e-02 | 4.082e-04 |
| 72 | 18 | 4.211e-08 | 4.211e-08 | 3.612e-07 | 4.238e-08 | 1.819e-04 | 4.868e-07 | 2.382e-03 | 1.160e-05 | 1.941e-02 | 1.363e-04 |
| | 36 | 4.211e-08 | 4.211e-08 | 3.632e-07 | 4.225e-08 | 1.836e-04 | 1.540e-07 | 2.435e-03 | 7.506e-06 | 1.983e-02 | 1.363e-04 |
| | 72 | 4.211e-08 | 4.211e-08 | 3.632e-07 | 4.225e-08 | 1.836e-04 | 1.540e-07 | 2.435e-03 | 7.506e-06 | 1.983e-02 | 1.363e-04 |

centerline, i.e., $f^{(i)}(:, N/2, N/2)$. It is observed that: a) the distribution function of the heavy particles becomes more skewed as the mass ratio increases; b) as time goes by, the distribution function tends toward the Maxwellian.

4.2 Multi-species: Couette flow

The aforementioned fast spectral methodology allows us to compute the collision operator efficiently. To solve the fully spatial in-homogeneous equation (2.19), we also need an accurate and efficient spatial and time discretization. We mention that evaluation of collision operator consumes $> 98\%$ of computation time, and hence, in the present case, we focus on the collision operator behavior.

4.2.1 Verification

For general Boltzmann equation (2.19), analytical solutions do not exist. Therefore, we compare our results with widely accepted direct simulation Monte Carlo (DSMC) [24] method. We want to reemphasize that DSMC is a stochastic method for solution of the N-particle master kinetic equation which converges to the Boltzmann equation in the limit of infinite number of particles [13]. In the current test case, we consider the effect of velocity gradient on the solution. The coordinates are chosen such that the walls are parallel to the y direction and x is the direction perpendicular to the walls. The geometry as well as boundary conditions are shown in Figure 4.3.

4.2.1.1 Bulk properties

Figure 4.4 illustrates the velocity and temperature along the domain length for both species, wherein we observe an excellent agreement between DGFS and DSMC. The small discrepancies, however, are primarily due to: a) statistical fluctuations inherent to the Monte Carlo methods, b) practical limitations on number of particles used in DSMC simulations. From a computational viewpoint, the present DGFS simulations on a single GPU took 138 sec-

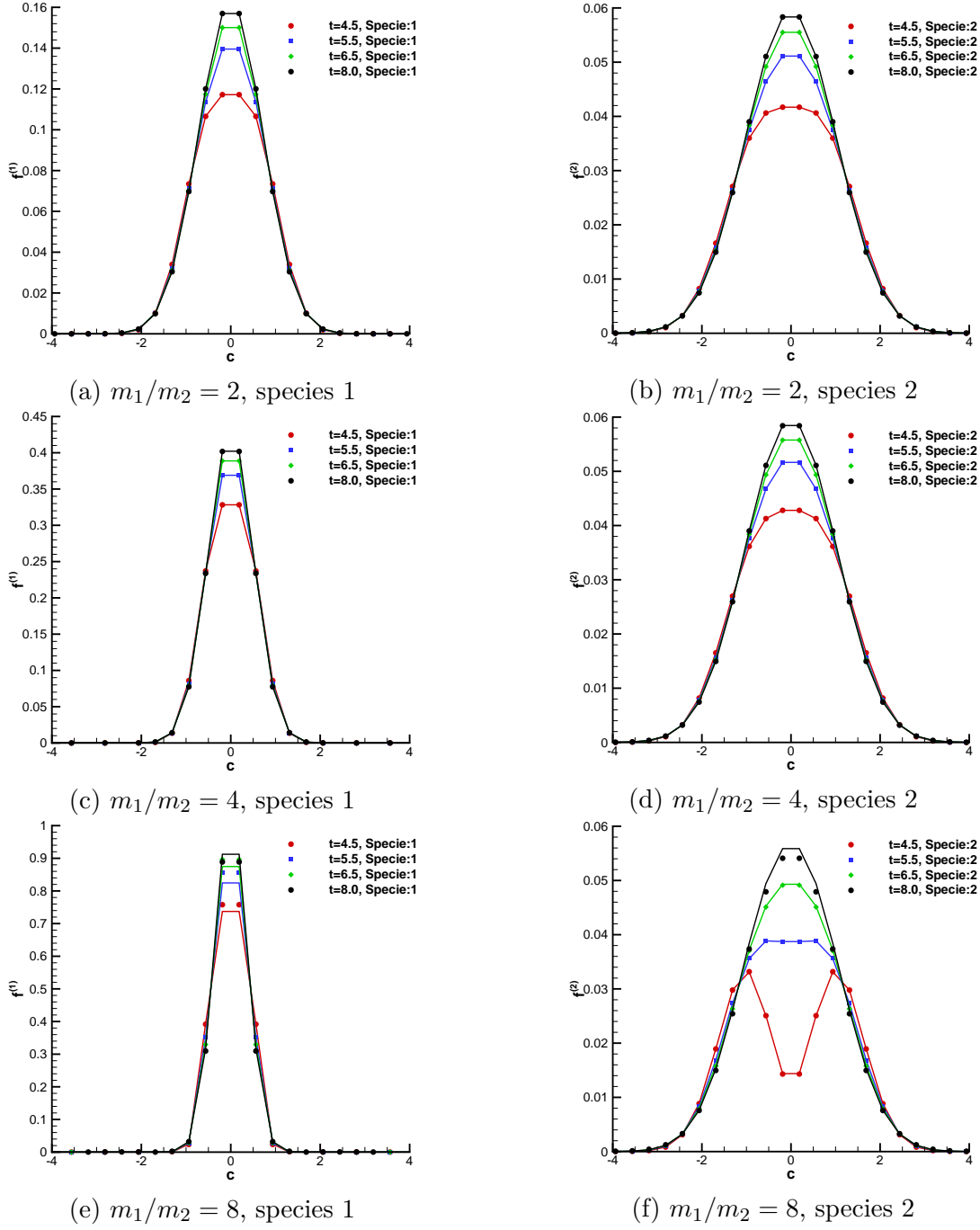


Figure 4.2. Spatially homogeneous Krook-Wu solution. Evolution of $f^{(i)}$, $i = \{1, 2\}$ sliced along the velocity domain centerline, i.e., $f^{(i)}(\cdot, N/2, N/2)$ for different mass ratios. The exact solutions (solid lines) are plotted using $N = 64$. The numerical solutions (symbols) are evaluated using $N = 64$, $M = 6$, $N_\rho = 64$. A fixed velocity domain $[-12, 12]^3$ has been used for all cases. SSP-RK2 with $\Delta t = 0.01$ is used for time stepping. Note that the x-axis has been zoomed to $[-4, 4]$ for better visibility.

onds to acquire the steady state, in contrast to 26086.45 sec on 24 processors for DSMC simulations as reported in [89], for achieving comparable accuracy.

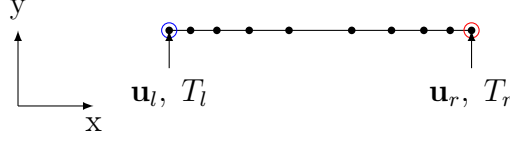


Figure 4.3. Numerical setup for 1D Couette flow.

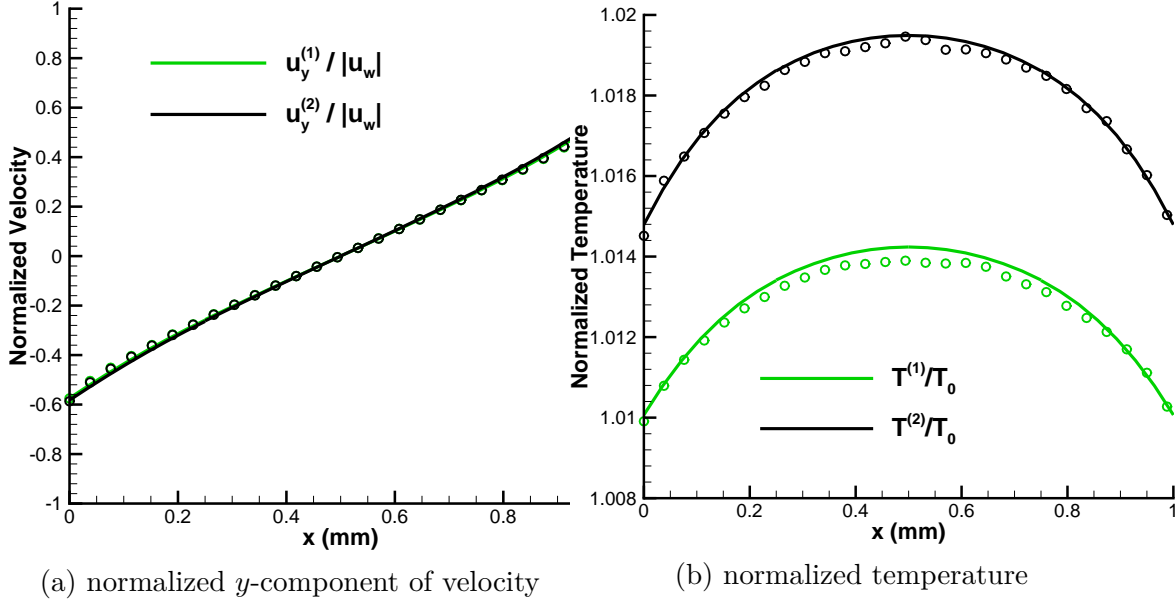


Figure 4.4. Variation of normalized y -velocity, and temperature along the domain for Couette flow (Case C-01) obtained with DSMC and DGFS using VSS collision kernel for Argon-Krypton mixture. Symbols denote DSMC solutions, and lines denote DGFS solutions.

4.2.1.2 Transport property: Viscosity

The viscosity $\mu^{(i)}$ can be recovered from the 1-D Couette flow simulations using the relation between shear-stress and velocity-gradient [90], [91]:

$$\mu^{(i)} = -\frac{\mathbb{P}_{xy}^{(i)}}{\partial u_y^{(i)} / \partial x}. \quad (4.7)$$

Table 4.2. Numerical parameters for Couette flow [89]. Based upon our observations from Table 4.1, we have used $N_\rho = 8$, in contrast to $N_\rho = 32$ used in [89]. This does not affect the recovered bulk properties as illustrated in Fig. 4.3, however, it speeds up the computation by a factor of 4.

| Parameter | Case C-01 |
|--|-------------------------------|
| Molecular mass: $\{m_1, m_2\}$ ($\times 10^{27} \text{ kg}$) | $\{66.3, 139.1\}$ |
| Non-dim physical space | $[0, 1]$ |
| Non-dim velocity space | $[-7, 7]^3$ |
| $\{N^3, N_\rho, M\}$ | $\{32^3, 8, 12\}$ |
| Spatial elements | 4 |
| DG order | 3 |
| Time stepping | Euler |
| Viscosity index: $\omega_{\{11, 12, 21, 22\}}$ | $\{0.81, 0.805, 0.805, 0.8\}$ |
| Scattering parameter: $\alpha_{\{11, 12, 21, 22\}}$ | $\{1.4, 1.36, 1.36, 1.32\}$ |
| Ref. diameter: $d_{\text{ref}, ij}$ ($\times 10^{10} m$) | $\{4.11, 4.405, 4.405, 4.7\}$ |
| Ref. temperature: $T_{\text{ref}, ij}$ (K) | $\{273\}$ |
| Characteristic mass: m_0 ($\times 10^{27} \text{ kg}$) | 66.3 |
| Characteristic length: H_0 (mm) | 1 |
| Characteristic velocity: \mathbf{u}_0 (m/s) | 337.2 |
| Characteristic temperature: T_0 (K) | 273 |
| Characteristic number density: n_0 (m^{-3}) | 1.680×10^{21} |
| Initial conditions | |
| Velocity: \mathbf{u} (m/s) | 0 |
| Temperature: T (K) | 273 |
| Number density: $n^{(1)}$ (m^{-3}) | 1.680×10^{21} |
| Number density: $n^{(2)}$ (m^{-3}) | 8.009×10^{20} |
| Knudsen number: (Kn ₁₁ , Kn ₂₂) | (0.793, 0.606) |
| Knudsen number: (Kn ₁₂ , Kn ₂₁) | (0.803, 0.555) |
| Left wall (purely diffuse) boundary conditions (subscript l) | |
| Velocity: \mathbf{u}_l (m/s) | (0, -50, 0) |
| Temperature: T_l (K) | 273 |
| Right wall (purely diffuse) boundary conditions (subscript r) | |
| Velocity: \mathbf{u}_r (m/s) | (0, +50, 0) |
| Temperature: T_r (K) | 273 |

For consistency, we use eqn. (4.7) for both DSMC and DGFS. For computing the derivative in (4.7), we use centered finite difference for DSMC, and the polynomial derivative for DGFS. Figure 4.5 illustrates the variation of viscosity along the domain for both species. It is observed that: (a) the viscosity is lower for the heavier (Kr) species since the mixture contains $\sim 32\%$ Kr, and $\sim 68\%$ Ar; and (b) both DSMC and DGFS match well within the expected statistical scatter inherent to DSMC simulations. Note that, in the present simulation, we use DG scheme with $K = 3$ which implies that the underlying polynomial is quadratic. Hence all the bulk properties including velocity should be a quadratic polynomial. Since the viscosity (4.7) contains the derivative of the velocity, the overall reconstructed viscosity should be linear, as we observe in Figure 4.5a. Upon increasing K , we recover the smooth high order polynomial for viscosity as illustrated in Figure 4.5b.

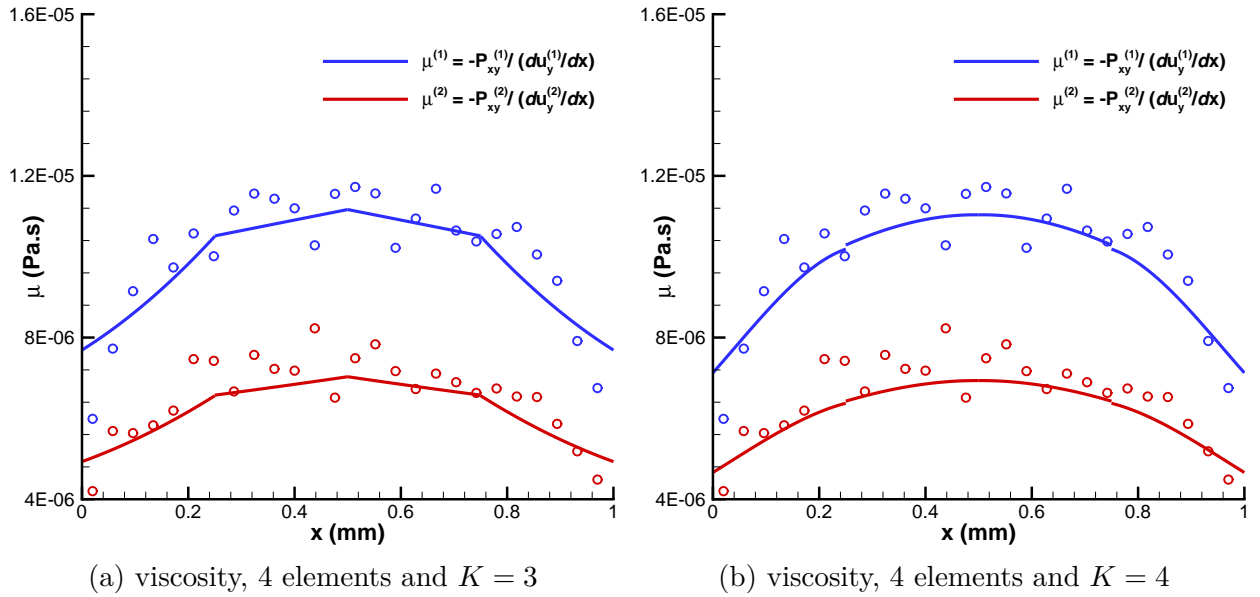


Figure 4.5. Variation of viscosity along the domain for Couette flow (Case C-01) obtained with DSMC and DGFS using VSS collision model for Argon-Krypton mixture. The physical space is discretized using 4 elements: a) $K = 3$, b) $K = 4$. Symbols denote DSMC solutions, and lines denote DGFS solutions.

4.2.2 Scaling Behavior

The simulations are carried out for different test-cases by varying element-count (N_e), polynomial approximation order ($N_p = K - 1$), and velocity-space sizes (N). The spatial elements

Table 4.3. Performance of the solver for Couette flow test cases. The phase-space is defined using a convenient triplet notation $\mathbf{N}_e/\mathbf{K}/\mathbf{N}^3$, which corresponds to \mathbf{N}_e elements in physical space, \mathbf{K} order DG (equivalently $N_p = K - 1$ order polynomial for 1-D domain), and \mathbf{N}^3 points in velocity space. $n\mathbf{G}$ ($n > 1$) denotes GPU/CUDA/MPI/parallel execution on n GPUs shared equally across $(n/3)$ nodes. Work units represent the total simulation time for first 52 timesteps. Efficiency is defined as ratio $(1\mathbf{G}/n\mathbf{G})/n$, where $1\mathbf{G}$ and $n\mathbf{G}$ are execution-times on one GPU and n GPU respectively. $M = 12$ and $N_\rho = 8$ is used for all cases.

| Phase space | Work Units (s) | | | | | | Efficiency | | | | | | |
|-----------------------|----------------|---------|---------|---------|---------|--------|------------|-------|-------|-------|--------|--------|--------|
| | 1G | 3G | 6G | 9G | 12G | 24G | 36G | 1G/3G | 1G/6G | 1G/9G | 1G/12G | 1G/24G | 1G/36G |
| 72/3/20 ³ | 47.580 | 16.155 | 8.339 | 5.698 | 4.392 | 2.423 | 1.774 | 0.98 | 0.95 | 0.93 | 0.90 | 0.82 | 0.84 |
| 72/3/32 ³ | 126.601 | 42.616 | 21.551 | 14.563 | 11.038 | 5.784 | 4.030 | 0.99 | 0.98 | 0.97 | 0.96 | 0.91 | 0.98 |
| 72/3/48 ³ | 391.943 | 131.081 | 65.913 | 44.218 | 33.513 | 17.224 | 11.621 | 1.00 | 0.99 | 0.98 | 0.97 | 0.95 | 1.05 |
| 72/6/20 ³ | 94.682 | 31.957 | 16.197 | 10.944 | 8.331 | 4.392 | 3.079 | 0.99 | 0.97 | 0.96 | 0.95 | 0.90 | 0.96 |
| 72/6/32 ³ | 253.016 | 84.834 | 42.741 | 28.697 | 21.703 | 11.158 | 7.693 | 0.99 | 0.99 | 0.98 | 0.97 | 0.94 | 1.03 |
| 72/6/48 ³ | 782.343 | 261.601 | 131.217 | 87.755 | 66.009 | 33.520 | 22.509 | 1.00 | 0.99 | 0.99 | 0.99 | 0.97 | 1.09 |
| 216/3/20 ³ | 141.754 | 47.641 | 24.033 | 16.182 | 12.326 | 6.356 | 4.388 | 0.99 | 0.98 | 0.97 | 0.96 | 0.93 | 1.01 |
| 216/3/32 ³ | 378.956 | 126.853 | 63.676 | 42.636 | 32.066 | 16.295 | 11.041 | 1.00 | 0.99 | 0.99 | 0.98 | 0.97 | 1.07 |
| 216/3/48 ³ | 1172.907 | 391.916 | 196.439 | 131.153 | 98.538 | 49.652 | 33.471 | 1.00 | 1.00 | 0.99 | 0.99 | 0.98 | 1.10 |
| 216/6/20 ³ | 283.091 | 94.737 | 47.679 | 31.903 | 24.060 | 12.262 | 8.320 | 1.00 | 0.99 | 0.99 | 0.98 | 0.96 | 1.06 |
| 216/6/32 ³ | 759.149 | 253.498 | 127.004 | 84.932 | 63.780 | 32.212 | 21.672 | 1.00 | 1.00 | 0.99 | 0.99 | 0.98 | 1.09 |
| 216/6/48 ³ | 2347.099 | 783.642 | 392.470 | 261.817 | 196.552 | 98.680 | 66.018 | 1.00 | 1.00 | 1.00 | 1.00 | 0.99 | 1.11 |

are distributed to p processors using the well-known linear domain-decomposition strategy requiring sharing of $O(pN^3)$ floating-point during MPI communication phase. Speed up obtained with multi-GPU solver is presented in Table (4.3). As evident from the table, the acceleration due to GPU parallelization increases with increase in the size of computational grid. More specifically, the increase in N_e and K have small-effect on overall speedup which suggests that DG-operators (for instance derivative, time-evolution) are rather computationally inexpensive operations. On the other hand, increase in velocity-grid improves the observed speedup. The weak/strong scaling behavior is also evident from the table.

4.2.3 Flat profile

Recall that the fast Fourier spectral collision operator algorithm 2 is split into multiple parts. It is therefore interesting to see what performance level is attained by each part of the operator. Fig (4.6) presents the percentage of time spent in various parts of Algo. 2 vs. order of DG scheme (K). First, we note that the DG operators denoted in yellow, requires 1% of the total simulation time. The collision operator, however, consumes nearly $> 98\%$ of the total time for both $N^3 = 20^3$ and $N^3 = 32^3$.

4.3 Multi-species: Fourier heat transfer

In the current test case, we consider the effect of temperature gradient on the solution. The coordinates are chosen such that the walls are parallel to the y direction and x is the direction perpendicular to the walls. The geometry as well as boundary conditions are shown in Figure 4.3. We consider six cases for a range of temperature gradients and rarefaction levels. The numerical parameters for these six cases are given in Table 4.4.

Figure 4.7 shows the variation of normalized temperature along the domain length for different initial mixture densities: a–b) $\Delta T = 20$ (Case F-01, F-02, F-03), and c–d) $\Delta T = 100$ (Case F-05, F-06, F-07). The results are compared against DSMC. We note minor ($1 - 2\%$) discrepancy between DGFS and DSMC for Krypton in the bulk-region away from the walls.

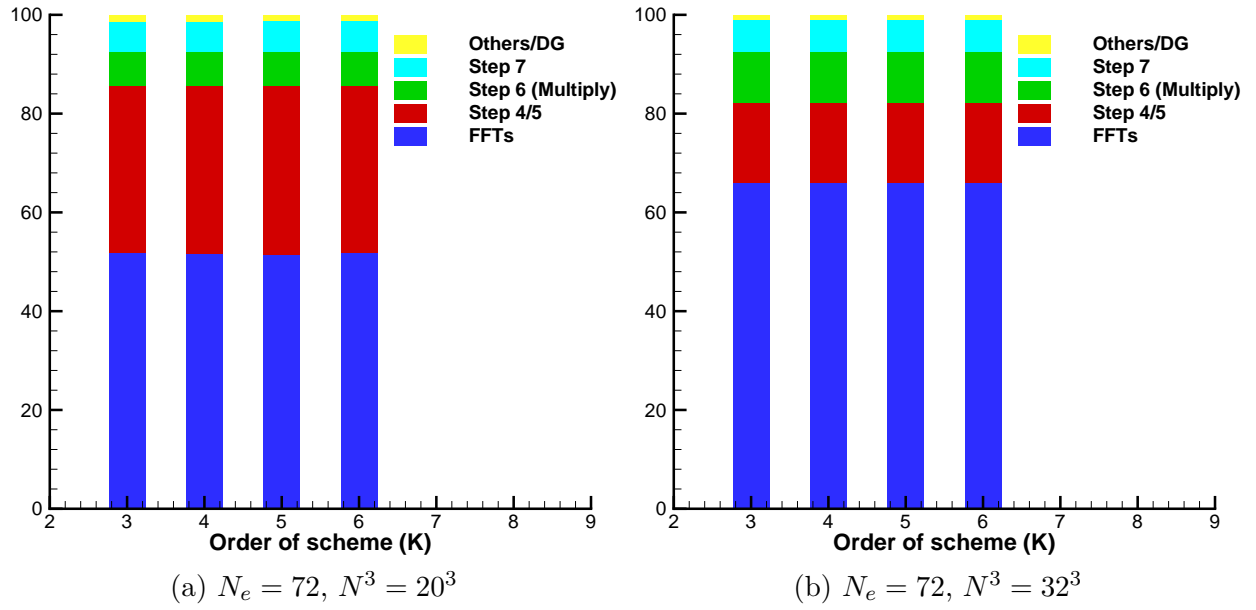


Figure 4.6. Percentage of time spent in various parts of Algo. 2 vs. order of DG scheme (K). For both $N^3 = 20^3$ and $N^3 = 32^3$, the collision operator consumes $> 98\%$ of the simulation time.

Table 4.4. Numerical parameters for Fourier heat transfer. The molecular collision parameters for Ar-Kr system are provided in Table 4.7.

| Parameter | Case F-01 | Case F-02 | Case F-03 | Case F-04 | Case F-05 | Case F-06 |
|--|------------------------|------------------------|------------------------|------------------------|------------------------|------------------------|
| Mixture | Ar-Kr | Ar-Kr | Ar-Kr | Ar-Kr | Ar-Kr | Ar-Kr |
| Collision kernel | VHS | VHS | VHS | VHS | VHS | VHS |
| Non-dim physical space | [0, 1] | [0, 1] | [0, 1] | [0, 1] | [0, 1] | [0, 1] |
| Non-dim velocity space | $[-5, 5]^3$ | $[-5, 5]^3$ | $[-5, 5]^3$ | $[-9, 9]^3$ | $[-9, 9]^3$ | $[-9, 9]^3$ |
| N^3 | 32^3 | 32^3 | 32^3 | 64^3 | 64^3 | 64^3 |
| N_ρ | 32 | 32 | 32 | 64 | 64 | 64 |
| M | 12 | 12 | 12 | 12 | 12 | 12 |
| Spatial elements | 4 | 4 | 4 | 4 | 4 | 4 |
| DG order | 3 | 3 | 3 | 3 | 3 | 3 |
| Time step (s) | 2×10^{-8} | 2×10^{-8} | 2×10^{-8} | 2×10^{-8} | 2×10^{-8} | 2×10^{-8} |
| Mass: m_0 | $m_{\text{Ar}} = m_1$ | $m_{\text{Ar}} = m_1$ | $m_{\text{Ar}} = m_1$ | $m_{\text{Ar}} = m_1$ | $m_{\text{Ar}} = m_1$ | $m_{\text{Ar}} = m_1$ |
| Length: H_0 (mm) | 1 | 1 | 1 | 1 | 1 | 1 |
| Velocity: u_0 (m/s) | 337.2 | 337.2 | 337.2 | 337.2 | 337.2 | 337.2 |
| Temperature: T_0 (K) | 273 | 273 | 273 | 273 | 273 | 273 |
| Number density: n_0 (m^{-3}) | 1.680×10^{21} | 8.401×10^{20} | 1.680×10^{20} | 1.680×10^{21} | 8.401×10^{20} | 1.680×10^{20} |
| Left wall (purely diffuse) boundary conditions (subscript l) | | | | | | |
| Velocity: u_l (m/s) | 0 | 0 | 0 | 0 | 0 | 0 |
| Temperature: T_l (K) | 263 | 263 | 263 | 223 | 223 | 223 |
| Right wall (purely diffuse) boundary conditions (subscript r) | | | | | | |
| Velocity: u_r (m/s) | 0 | 0 | 0 | 0 | 0 | 0 |
| Temperature: T_r (K) | 283 | 283 | 283 | 323 | 323 | 323 |
| Initial conditions | | | | | | |
| Velocity: u (m/s) | 0 | 0 | 0 | 0 | 0 | 0 |
| Temperature: T (K) | 273 | 273 | 273 | 273 | 273 | 273 |
| Number density: $n^{(1)}$ (m^{-3}) | 1.680×10^{21} | 8.401×10^{20} | 1.680×10^{20} | 1.680×10^{21} | 8.401×10^{20} | 1.680×10^{20} |
| Number density: $n^{(2)}$ (m^{-3}) | 8.009×10^{20} | 4.004×10^{20} | 8.009×10^{19} | 8.009×10^{20} | 4.004×10^{20} | 8.009×10^{19} |
| Knudsen: (Kn ₁₁ , Kn ₂₂) | (0.770, 0.591) | (1.541, 1.182) | (7.703, 5.912) | (0.770, 0.591) | (1.541, 1.182) | (7.703, 5.912) |
| Knudsen: (Kn ₁₂ , Kn ₂₁) | (0.782, 0.540) | (1.564, 1.080) | (7.820, 5.399) | (0.782, 0.540) | (1.564, 1.080) | (7.820, 5.399) |

Note however that the amount of predicted temperature jump is consistent between DSMC and DGFS for both species.

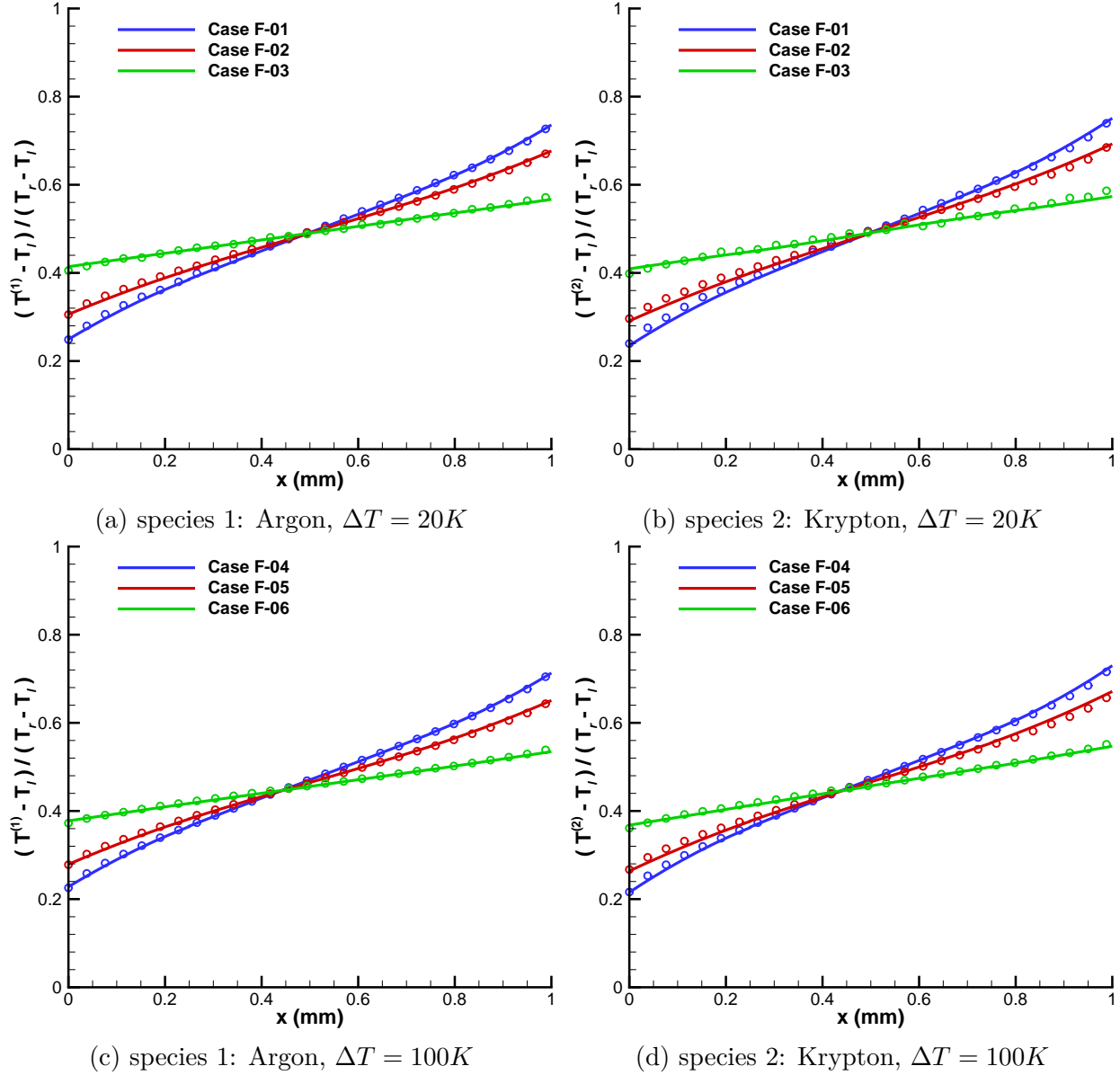


Figure 4.7. Variation of normalized temperature $(T^{(i)} - T_l)/(T_r - T_l)$, $i = \{1, 2\}$ along the domain length for Fourier heat transfer obtained with DSMC and DGFS using VHS collision kernel for Argon-Krypton mixture. Symbols denote DSMC solutions, and lines denote DGFS solutions. Numerical parameters are provided in Table 4.4.

4.4 Multi-species: Oscillatory Couette flow

In the current test case, we consider the effect of *transient* momentum transport for verifying the temporal accuracy of the DGFS. The schematic remains the same as in the previous test case. The left wall is at rest, and the right wall moves with a velocity of $u = (0, v_a \sin(\zeta t), 0)$ m/s, where v_a is the amplitude of oscillation. The simulation parameters are given in Table 4.5. The present case is run for two different wall velocities: a) $v_a = 50$ m/s, and b) $v_a = 500$ m/s. Argon-Krypton mixture with VHS collision model is taken as the working gas. Specifically for DSMC simulations, the domain is discretized into 50 cells with 100000 particles per cell (PPC). For $v_a = 50$ m/s case, a time step of 2×10^{-10} sec is employed. For $v_a = 500$ m/s case, a time step of 2×10^{-11} sec is employed. The results are averaged for every 1000 (Navg) time steps. These DSMC simulation parameters have been taken from [32]. Note that such low DSMC time steps are particularly needed for obtaining time accurate results since the time stepping is inherently linear in traditional DSMC method [24].

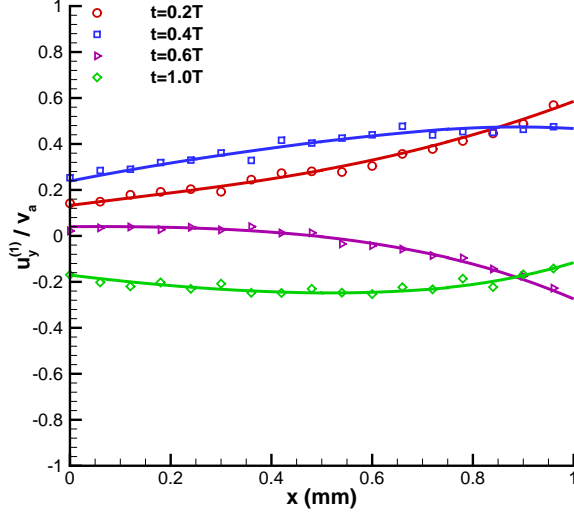
Figure 4.8 illustrates the results for the oscillatory Couette flow along the domain length for different v_a . Ignoring the statistical noise, we observe a good agreement between DGFS and DSMC. Note in particular that for both species, the amount of slip at the left wall are different – which is in accordance with the conservation principles. Moreover, the amount of slip is consistent between DSMC and DGFS.

4.5 Multi-species: Normal shock

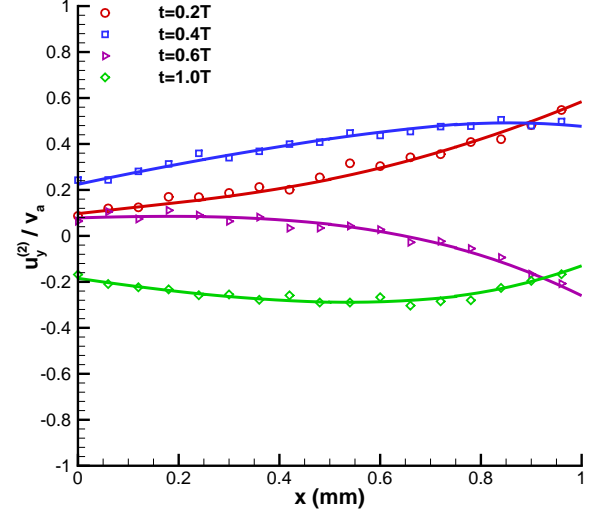
We consider the normal shock wave and compare our results with the finite difference solutions reported in [92]. Four cases are considered here whose numerical parameters are described in Table 4.6. The boundary conditions at upstream and downstream are the in-flow equilibrium boundary. We solve the Boltzmann equation until the solution reaches a steady state. A convergence criterion of $(\|f^{n+1} - f^n\|_{L^2} / \|f^n\|_{L^2}) / (\|f^2 - f^1\|_{L^2} / \|f^1\|_{L^2}) < 2 \times 10^{-5}$ has been used, where f^n denotes the distribution function at n^{th} time step.

Table 4.5. Numerical parameters for oscillatory Couette flow. The molecular collision parameters for Ar-Kr system are provided in Table 4.7.

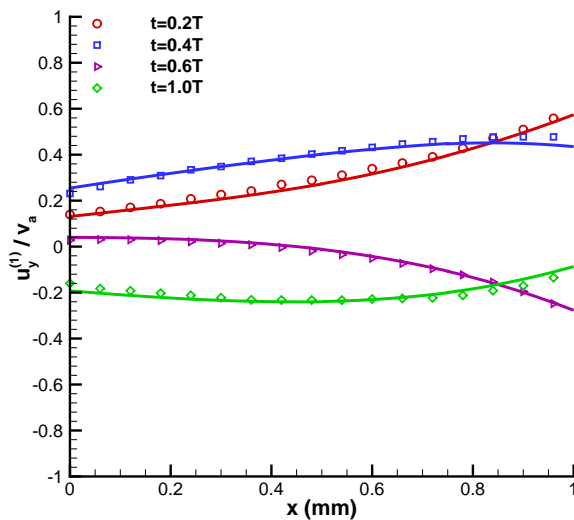
| Parameter | Case OC-01 | Case OC-02 |
|--|----------------------------|-----------------------------|
| Mixture | Ar-Kr | Ar-Kr |
| Collision kernel | VHS | VHS |
| Non-dim physical space | $[0, 1]$ | $[0, 1]$ |
| Non-dim velocity space | $[-5, 5]^3$ | $[-9, 9]^3$ |
| N^3 | 24^3 | 48^3 |
| N_ρ | 24 | 48 |
| M | 6 | 6 |
| Spatial elements | 4 | 4 |
| DG order | 3 | 3 |
| Time step (s) | 2×10^{-8} | 2×10^{-8} |
| Characteristic mass: m_0 | $m_{\text{Ar}} = m_1$ | $m_{\text{Ar}} = m_1$ |
| Characteristic length: H_0 (mm) | 1 | 1 |
| Characteristic velocity: u_0 (m/s) | 337.2 | 337.2 |
| Characteristic temperature: T_0 (K) | 273 | 273 |
| Characteristic number density: n_0 (m^{-3}) | 8.401×10^{20} | 8.401×10^{20} |
| Initial conditions | | |
| Velocity: u (m/s) | 0 | 0 |
| Temperature: T (K) | 273 | 273 |
| Number density: $n^{(1)}$ (m^{-3}) | 8.401×10^{20} | 8.401×10^{20} |
| Number density: $n^{(2)}$ (m^{-3}) | 4.004×10^{20} | 4.004×10^{20} |
| Knudsen number: (Kn ₁₁ , Kn ₂₂) | (1.541, 1.182) | (1.541, 1.182) |
| Knudsen number: (Kn ₁₂ , Kn ₂₁) | (1.564, 1.080) | (1.564, 1.080) |
| Left wall (purely diffuse) boundary conditions (subscript l) | | |
| Velocity: u_l (m/s) | (0, 0, 0) | (0, 0, 0) |
| Temperature: T_l (K) | 273 | 273 |
| Right wall (purely diffuse) boundary conditions (subscript r) | | |
| Velocity: u_r (m/s) | (0, $50\sin(\zeta t)$, 0) | (0, $500\sin(\zeta t)$, 0) |
| Temperature: T_r (K) | 273 | 273 |
| Period of oscillation: ζ (s^{-1}) | $2\pi/(5 \times 10^{-5})$ | $2\pi/(5 \times 10^{-5})$ |
| Velocity amplitude: v_a (m/s) | 50 | 500 |



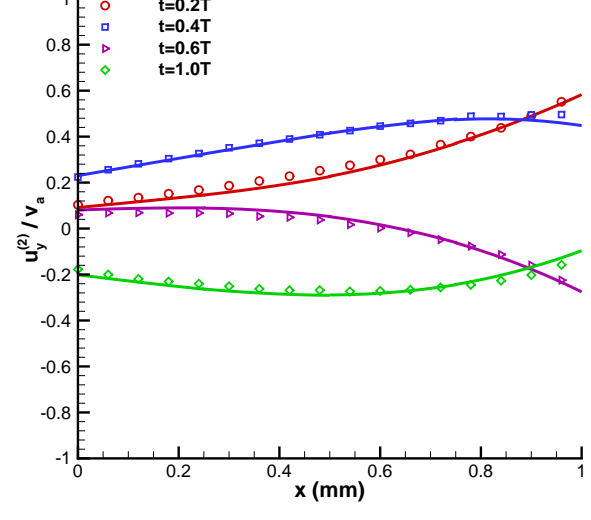
(a) Case OC-01, $v_a = 50 \text{ m/s}$, species 1: Argon



(b) Case OC-01, $v_a = 50 \text{ m/s}$, species 2: Krypton



(c) Case OC-02, $v_a = 500 \text{ m/s}$, species 1: Argon



(d) Case OC-02, $v_a = 500 \text{ m/s}$, species 2: Krypton

Figure 4.8. Variation of normalized velocity $u_y^{(i)}/v_a$, $i = \{1, 2\}$ along the domain length for oscillatory Couette flow obtained with DSMC and DGFS using VHS collision model for Argon-Krypton mixture. Symbols denote DSMC solutions, and lines denote DGFS solutions.

Table 4.6. Numerical parameters for normal shock wave [92].

| Parameter | Case NS-01 | Case NS-02 | Case NS-03 | Case NS-04 |
|--|---|------------------------|------------------------|------------------------|
| Molecular mass: m_1 ($\times 10^{27} kg$) | 6.63 | 6.63 | 6.63 | 6.63 |
| Molecular mass: m_2 ($\times 10^{27} kg$) | 3.315 | 1.6575 | 3.315 | 3.315 |
| Mass Ratio: m_2/m_1 | 0.5 | 0.25 | 0.5 | 0.5 |
| Mach number | 1.5 | 1.5 | 1.5 | 3.0 |
| Concentration: $n_-^{(2)}/n_- = n_+^{(2)}/n_+$ | 0.5 | 0.5 | 0.1 | 0.1 |
| Non-dim physical space | $[-0.5, 0.5]$ | $[-0.5, 0.5]$ | $[-0.5, 0.5]$ | $[-0.5, 0.5]$ |
| Non-dim velocity space | $[-9, 9]^3$ | $[-15, 15]^3$ | $[-9, 9]^3$ | $[-15, 15]^3$ |
| N^3 | 32^3 | 64^3 | 32^3 | 48^3 |
| N_ρ | 32 | 16 | 32 | 48 |
| M | 12 | 12 | 12 | 12 |
| Spatial elements | 8, 16 | 16 | 16 | 16 |
| DG order | 3 | 3 | 3 | 3 |
| Time step ($s \times 10^8$) | 5.57, 2.77 | 1.64 | 2.77 | 1.64 |
| Viscosity index: ω_{ij} | 0.5 | 0.5 | 0.5 | 0.5 |
| Scattering parameter: α_{ij} | 1 | 1 | 1 | 1 |
| Ref. diameter: $d_{\text{ref},ij}$ ($\times 10^{10} m$) | 2.17 | 2.17 | 2.17 | 2.17 |
| Ref. temperature: $T_{\text{ref},ij}$ (K) | 273 | 273 | 273 | 273 |
| Characteristic mass: m_0 ($\times 10^{27} kg$) | 6.63 | 6.63 | 6.63 | 6.63 |
| Characteristic length: H_0 (mm) | 30 | 30 | 30 | 30 |
| Characteristic velocity: u_0 (m/s) | 963.7 | 963.7 | 963.7 | 963.7 |
| Characteristic temperature: T_0 (K) | 223 | 223 | 223 | 223 |
| Characteristic number density: n_0 (m^{-3}) | 2.889×10^{21} | 2.889×10^{21} | 2.889×10^{21} | 2.889×10^{21} |
| Upstream conditions (subscript -) | | | | |
| Velocity: u_- (m/s) | 1523.737 | 1669.171 | 1353.876 | 2707.753 |
| Temperature: T_- (K) | 223 | 223 | 223 | 223 |
| Mean free path: $\lambda_- = (\sqrt{2}\pi(n_-^{(1)} + n_-^{(2)})d_{\text{ref},ij}^2)^{-1}$ (m) | 0.000827 | 0.000827 | 0.00148 | 0.00148 |
| Number density: $n_-^{(1)}$ (m^{-3}) | 2.889×10^{21} | 2.889×10^{21} | 2.889×10^{21} | 2.889×10^{21} |
| Number density: $n_-^{(2)}$ (m^{-3}) | 2.889×10^{21} | 2.889×10^{21} | 3.209×10^{20} | 3.209×10^{20} |
| Downstream conditions (subscript +) | | | | |
| Velocity: u_+ (m/s) | 888.847 | 973.683 | 789.761 | 902.584 |
| Temperature: T_+ (K) | 333.338 | 333.338 | 333.338 | 817.667 |
| Number density: $n_+^{(1)}$ (m^{-3}) | 4.953×10^{21} | 4.953×10^{21} | 4.953×10^{21} | 8.669×10^{21} |
| Number density: $n_+^{(2)}$ (m^{-3}) | 4.953×10^{21} | 4.953×10^{21} | 5.502×10^{20} | 9.633×10^{20} |
| Initial conditions | | | | |
| Velocity: u (m/s) | $u_- + (u_+ - u_-) x/H_0$ | | | |
| Temperature: T (K) | $T_- + (T_+ - T_-) x/H_0$ | | | |
| Number density: $n^{(1)}$ (m^{-3}) | $n_-^{(1)} + (n_+^{(1)} - n_-^{(1)}) x/H_0$ | | | |
| Number density: $n^{(2)}$ (m^{-3}) | $n_-^{(2)} + (n_+^{(2)} - n_-^{(2)}) x/H_0$ | | | |

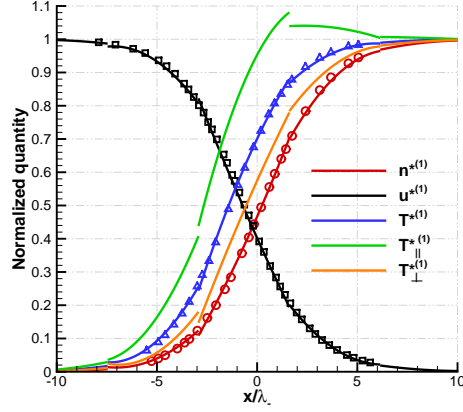
Figure 4.9 shows the bulk properties (number density, temperature, velocity, parallel/perpendicular temperature components) for Mach 1.5 normal shock with mass ratios $m_2/m_1 = 0.5$ and $m_2/m_1 = 0.25$. The normalized quantities are defined using: $n^{*(i)} = (n^{(i)} - n_-^{(i)}) / (n_+^{(i)} - n_-^{(i)})$, $T^{*(i)} = (T^{(i)} - T_-) / (T_+ - T_-)$, $u^{*(i)} = (u^{(i)} - u_+) / (u_- - u_+)$, $T_{\parallel}^{*(i)} = (T_{\parallel}^{(i)} - T_-) / (T_+ - T_-)$, and $T_{\perp}^{*(i)} = (T_{\perp}^{(i)} - T_-) / (T_+ - T_-)$. Based on these results, one can infer that DGFS recovers the normal shock reasonably well. In particular, from Figures 4.9a, 4.9b, we observe that a Mach 1.5 shock can be captured with just 8 elements within *engineering* $\pm 5\%$ accuracy. Note that the discontinuity in the flow profile is the characteristic of the DG method. The discontinuity expectedly vanishes upon refining the grid as in Figures 4.9c, 4.9d.

Figure 4.10 shows the bulk properties (number density, temperature, and velocity, parallel/perpendicular temperature components) for Mach 1.5 and Mach 3 normal shock for mass ratio $m_2/m_1 = 0.5$ at low concentration $n_-^{(2)}/n_- = 0.1$. Again, we observe a fair agreement with the reference solutions.

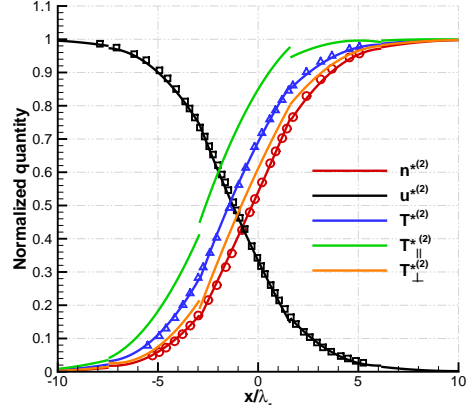
4.6 Multi-species: Self diffusion of Argon-Argon mixture

In the current test case, we consider the effect of diffusive transport. The schematic remains the same as in the previous test case. Argon-Argon mixture with VSS collision kernel is taken as the working gas. To differentiate between two types of Argon, we tag the molecules as Ar_1 and Ar_2 . At the left boundary, Ar_1 enters and exits at the right boundary. At the right boundary, Ar_2 enters and exits at the left boundary. The molecules enter the domain with zero mean velocity. The simulation parameters are provided in Table 4.8.

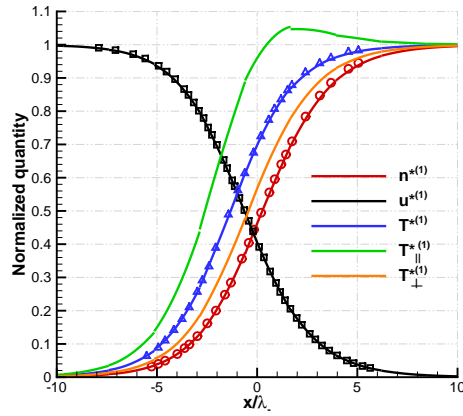
Figure 4.11a shows the variation of concentration $n^{(i)}/n$ along the domain. Since the species-1 enters from the left boundary and exits at right, we observe a drop in species-1 concentration as we move towards the right boundary. Conversely for species-2, since the species-2 enters from the right boundary and exits at left, we observe a drop in species-2 concentration as we move towards the left boundary. The non-linearity of the concentration profile and the associated slip at the boundaries can be explained through the low mixture density, and the fact that the flow is in slip regime. It is also worth noting that throughout the domain at



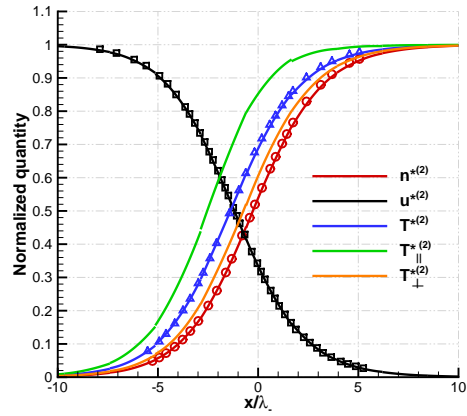
(a) Case NS-01, 8 elements, species 1



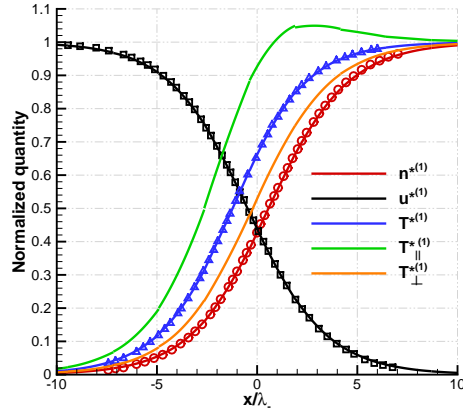
(b) Case NS-01, 8 elements, species 2



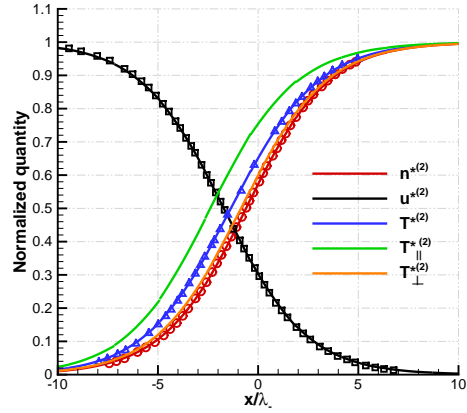
(c) Case NS-01, 16 elements, species 1



(d) Case NS-01, 16 elements, species 2



(e) Case NS-02, 16 elements, species 1



(f) Case NS-02, 16 elements, species 2

Figure 4.9. Variation of normalized flow properties along the domain for Mach 1.5 normal shock with $n_-^{(2)}/n_- = 0.5$: (a–b) $m_2/m_1 = 0.5$ (Case NS-01) with 8 elements, (c–d) $m_2/m_1 = 0.5$ (Case NS-01) with 16 elements, and (e–f) $m_2/m_1 = 0.25$ (Case NS-02) with 16 elements. Symbols denote results from [92], and lines denote DGFS solutions. Note that the position of the shock wave has been adjusted to the location with the average number density $(n_- + n_+)/2$ as per [92].

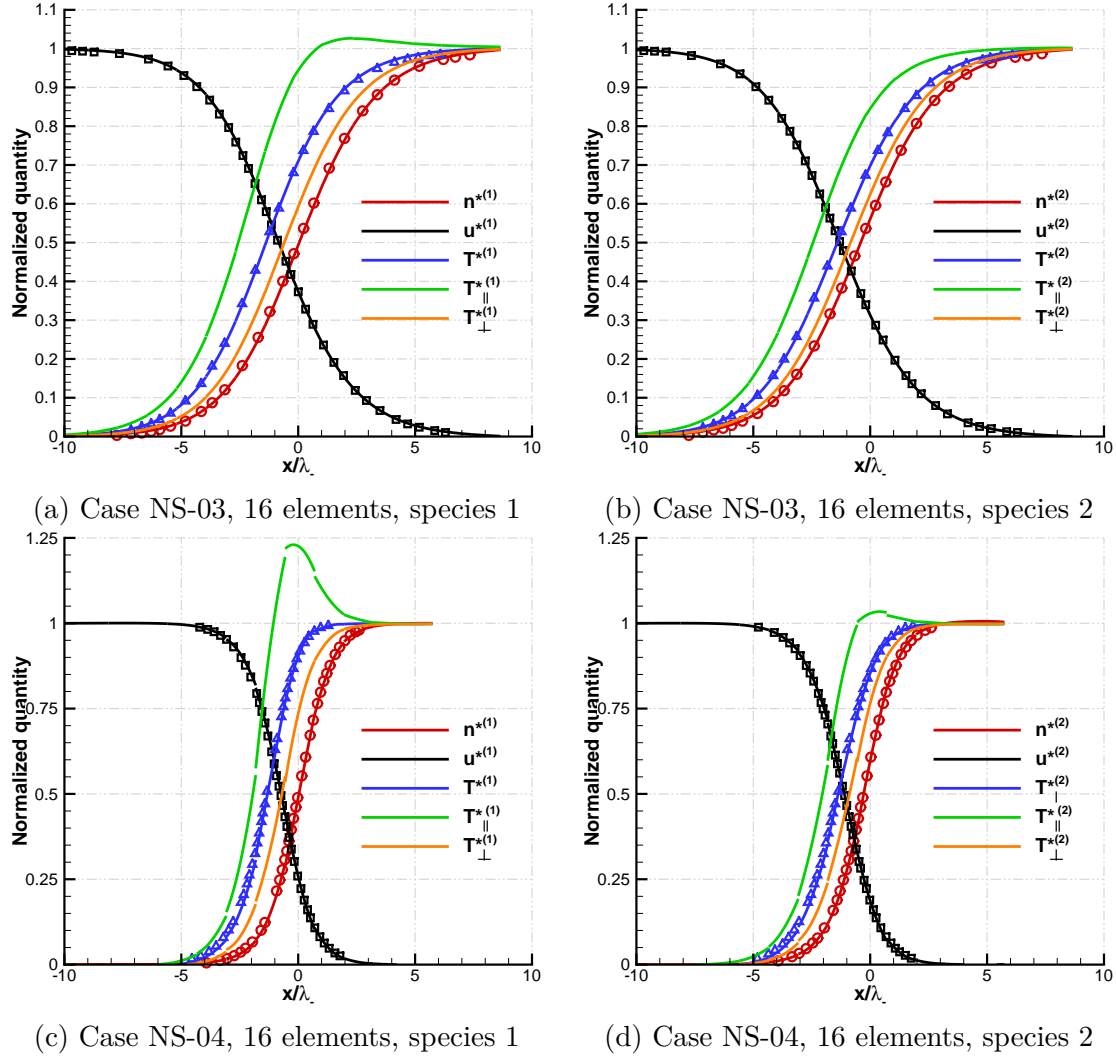


Figure 4.10. Variation of normalized flow properties along the domain for normal shock with $m_2/m_1 = 0.5$, $n_-^{(2)}/n_- = 0.1$: (a–b) Mach 1.5 (Case NS-03), and (c–d) Mach 3 (Case NS-04). Symbols denote results from [92], and lines denote DGFS solutions. Note that the position of the shock wave has been adjusted to the location with the average number density $(n_- + n_+)/2$ as per [92].

Table 4.7. VHS and VSS model parameters for different mixture systems [24].

| Mixture | Ar-Kr | Ar-Kr |
|--|----------------|----------------|
| Collision kernel | VHS | VSS |
| Molecular mass: m_1 ($\times 10^{27} kg$) | 66.3 | 66.3 |
| Molecular mass: m_2 ($\times 10^{27} kg$) | 139.1 | 139.1 |
| Reference viscosity: $\mu_{\text{ref},1}$ ($\times 10^5 \text{ Pa} \cdot s$) | 2.117 | 2.117 |
| Reference viscosity: $\mu_{\text{ref},2}$ ($\times 10^5 \text{ Pa} \cdot s$) | 2.328 | 2.328 |
| Viscosity index: $(\omega_{11}, \omega_{22})$ | (0.81, 0.8) | (0.81, 0.8) |
| Viscosity index: $(\omega_{12}, \omega_{21})$ | (0.805, 0.805) | (0.805, 0.805) |
| Scattering parameter: $(\alpha_{11}, \alpha_{22})$ | (1, 1) | (1.4, 1.32) |
| Scattering parameter: $(\alpha_{12}, \alpha_{21})$ | (1, 1) | (1.36, 1.36) |
| Ref. diameter: $(d_{\text{ref},11}, d_{\text{ref},22})$ ($\times 10^{10} m$) | (4.17, 4.76) | (4.11, 4.7) |
| Ref. diameter: $(d_{\text{ref},11}, d_{\text{ref},22})$ ($\times 10^{10} m$) | (4.465, 4.465) | (4.405, 4.405) |
| Ref. temperature: $(T_{\text{ref},11}, T_{\text{ref},22})$ (K) | (273, 273) | (273, 273) |
| Ref. temperature: $(T_{\text{ref},12}, T_{\text{ref},21})$ (K) | (273, 273) | (273, 273) |

Table 4.8. Numerical parameters for Ar-Ar self diffusion. The molecular collision parameters for Ar are provided in Table 4.7.

| Parameter | Case SD-01 | Case SD-02 |
|--|------------------------|------------------------|
| Mixture | Ar-Ar | Ar-Ar |
| Collision kernel | VSS | VSS |
| Non-dim physical space | [0, 1] | [0, 1] |
| Non-dim velocity space | $[-5.09, 5.09]^3$ | $[-5.09, 5.09]^3$ |
| N^3 | 32^3 | 32^3 |
| N_ρ | 32 | 32 |
| M | 12 | 12 |
| Spatial elements | 4 | 4 |
| DG order | 3 | 3 |
| Time step (s) | 2×10^{-8} | 2×10^{-8} |
| Viscosity index: (ω_{ij}) | 0.81 | 0.81 |
| Scattering index: (α_{ij}) | 1.4 | 1.4 |
| Characteristic mass: m_0 | $m_{\text{Ar}} = m_1$ | $m_{\text{Ar}} = m_1$ |
| Characteristic length: H_0 (mm) | 1 | 1 |
| Characteristic velocity: u_0 (m/s) | 337.2 | 337.2 |
| Characteristic temperature: T_0 (K) | 273 | 273 |
| Characteristic number density: n_0 (m^{-3}) | 1.680×10^{21} | 8.401×10^{21} |
| Initial conditions | | |
| Velocity: u (m/s) | 0 | 0 |
| Temperature: T (K) | 273 | 273 |
| Number density: $n^{(1)}$ (m^{-3}) | 1.680×10^{21} | 8.401×10^{21} |
| Number density: $n^{(2)}$ (m^{-3}) | 1.680×10^{21} | 8.401×10^{21} |
| Knudsen number: $(\text{Kn}_{11}, \text{Kn}_{22})$ | (0.793, 0.793) | (0.159, 0.159) |
| Knudsen number: $(\text{Kn}_{12}, \text{Kn}_{21})$ | (0.793, 0.793) | (0.159, 0.159) |
| Left boundary conditions (subscript l) | | |
| Ar ₁ enters: inlet boundary condition for Ar ₁ | | |
| Velocity: u_l (m/s) | (0, 0, 0) | (0, 0, 0) |
| Temperature: T_l (K) | 273 | 273 |
| Number density: $n^{(1)}$ (m^{-3}) | 1.680×10^{21} | 8.401×10^{21} |
| Ar ₂ freely exits | | |
| Right boundary conditions (subscript r) | | |
| Ar ₂ enters: inlet boundary condition for Ar ₂ | | |
| Velocity: u_r (m/s) | (0, 0, 0) | (0, 0, 0) |
| Temperature: T_r (K) | 273 | 273 |
| Number density: $n^{(2)}$ (m^{-3}) | 1.680×10^{21} | 8.401×10^{21} |
| Ar ₁ freely exits | | |

any given x location, the sum of the concentrations of two species is unity which asserts that the numerical formulation is conservative.

Figure 4.11b shows the variation of diffusion velocity along the domain. Since the species-1 enters from the left boundary and exits at right, we observe a low net diffusion speed (magnitude of the diffusion velocity) for the first species and a high diffusion speed for the second species. Conversely at the right boundary, since the species-2 enters from the right boundary and exits at left, we observe a low diffusion speed for the second species and high diffusion speed for the first species.

Figure 4.12 illustrates the temperature profile along the domain, where we observe a drop in temperatures of the two species. Based upon these results, it can be inferred that DGFS can resolve the strong gradients in temperature and diffusion velocity with just 4 elements and $K = 3$ within *engineering* accuracy.

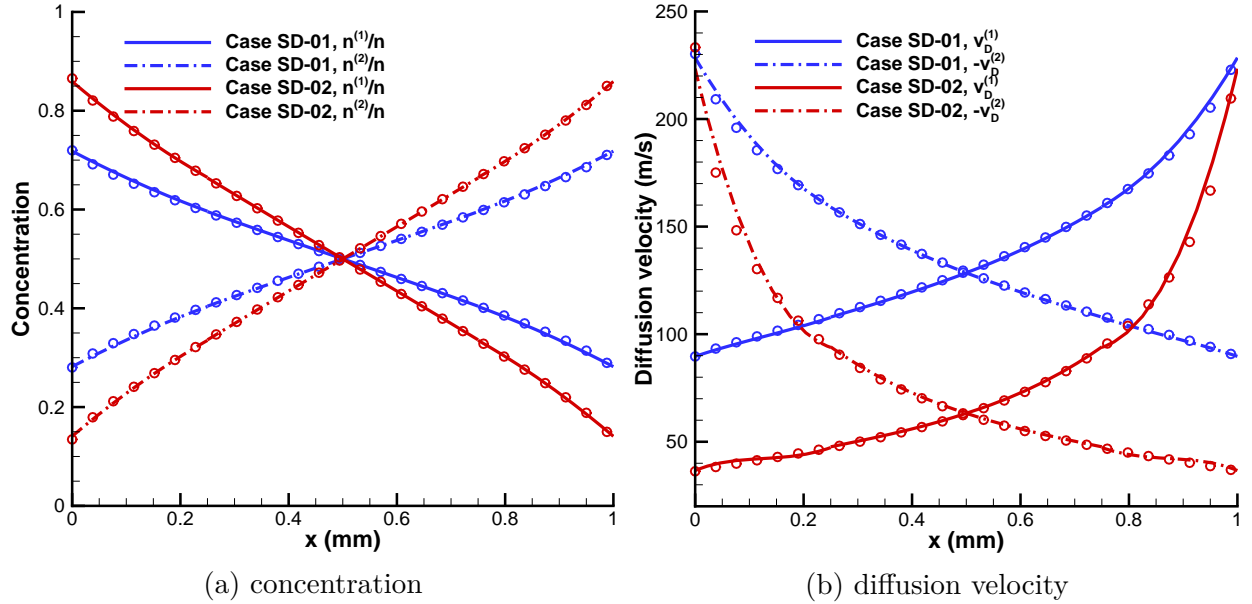
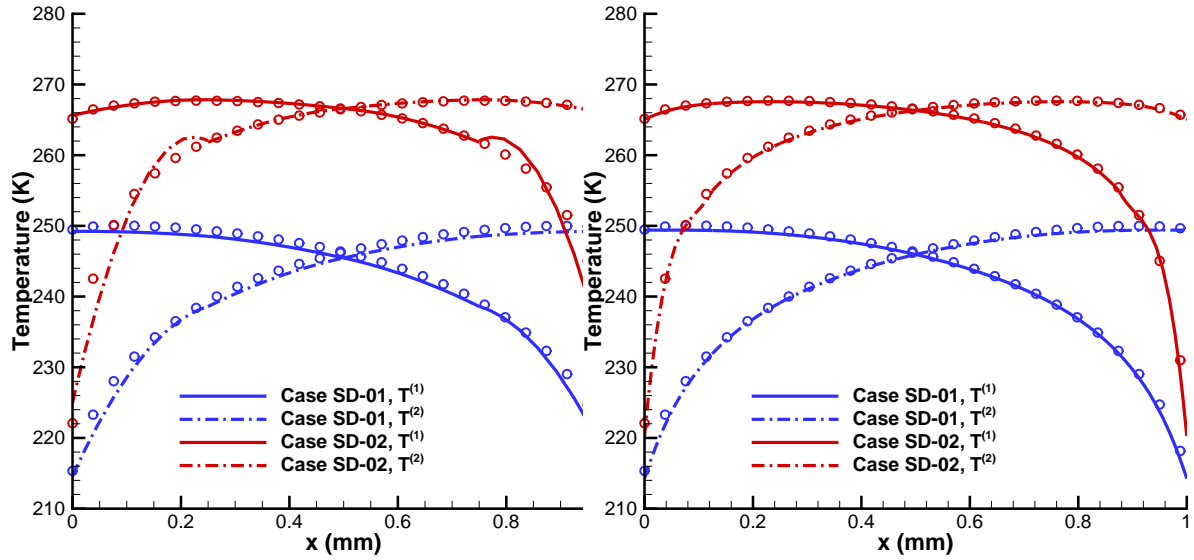


Figure 4.11. Variation of number density and diffusion velocity along the domain for self-diffusion cases obtained with DSMC and DGFS using VSS collision kernel for Argon-Argon mixture. Symbols denote DSMC results, and lines denote DGFS results.



(a) temperature, 4 elements and $K = 3$

(b) temperature, 8 elements and $K = 4$

Figure 4.12. Variation of temperature along the domain for self-diffusion cases obtained with DSMC and DGFS using VSS collision kernel for Argon-Argon mixture ($\alpha_{ij} = 1.4$). The physical space is discretized using: a) 4 elements and $K = 3$, b) 8 elements and $K = 4$. Symbols denote DSMC results, and lines denote DGFS results.

For this test case, the self-diffusion coefficient is given as (cf. eqn. (12.18) in [24])

$$D^{(11)} = D^{(12)} = -(u_x^{(1)} - u_x^{(2)}) \frac{n^{(1)} n^{(2)}}{n^2} \frac{\Delta x}{\Delta(n^{(1)}/n)}. \quad (4.8)$$

While writing this equation, it is also assumed that the coefficient of thermal diffusion is low [93], and therefore the effect of temperature gradient is negligible (see eqn. (8.4.7) in [5]). Note that this equation is an approximation to the diffusion equation, derived from leading order Chapman expansion (see section 8.4 in [5]), and therefore, strictly speaking, the values computed from this equation might not be fully accurate especially for the rarefied flows, since the higher order terms have not been accounted for. For consistency, we use (4.8) for both DSMC and DGFS. For computing the derivatives in (4.8), we use centered finite difference for DSMC, and the polynomial derivative for DGFS. In particular, for DSMC simulations, we used 500 cells, 2000 particles per cell, a time step of 1×10^{-8} sec, and averaged the results for 1 million time steps to minimize the statistical scatter in diffusion coefficients.

Figure 4.13 illustrates the variation of self-diffusion coefficient along the domain as a function of scattering parameter α_{ij} . It is observed that: (a) the diffusion coefficient increases with increase in α_{ij} in accordance with the VSS model (cf. eqn. (3.75) in [24]), (b) both DSMC and DGFS match well within the expected statistical scatter inherent to DSMC simulations, and (c) with increase in number density from Case 01 to Case 02, the diffusion coefficient decreases in accordance with (4.8). Note that, in the present simulation, we use DG scheme with $K = 3$ which implies that the underlying polynomial is quadratic. Hence all the bulk properties including number density should be a quadratic polynomial. Recall that the diffusion (4.8) contains the derivative of the number density, and hence the overall reconstructed diffusion coefficient should be linear, which is what we observe in Figures 4.13a, 4.13b. Upon increasing K , we recover the smooth high-order polynomial for diffusion coefficient.

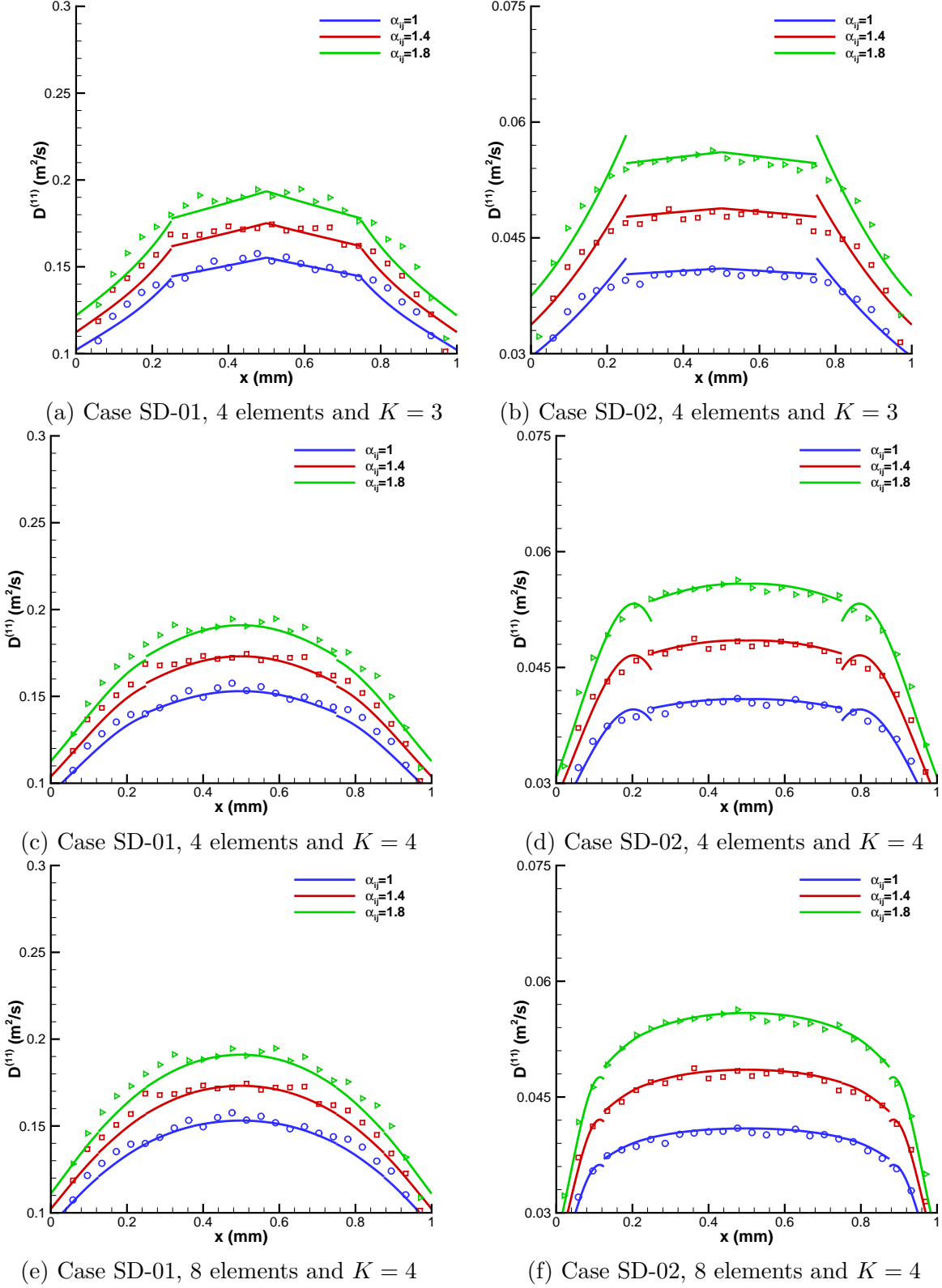


Figure 4.13. Variation of diffusion coefficient along the domain for self-diffusion cases obtained with DSMC and DGFS using VSS collision model for Argon-Argon mixture. Note that only α_{ij} is varied by keeping all other parameters fixed as in Table 4.8. Symbols denote DSMC results, and lines denote DGFS results.

4.7 Multi-species: Mass diffusion of Argon-Krypton mixture

In the current test case, we consider the effect of mass diffusion. The conditions remain the same as in previous case, except that Argon-Krypton mixture with VSS collision model is taken as the working gas. More specifically, Argon enters the left boundary and exits at the right boundary; and Krypton enters through the right and exits at left. The molecules enter the domain with zero mean velocity. We consider two cases with different initial number density. The numerical parameters for both the cases are given in Table 4.9.

Figure 4.14a shows the variation of concentration profile for the two species. We observe that the concentration of Argon remains greater than Krypton throughout the domain, except for a small portion near the right boundary. This can be directly inferred from the mass/momentum conservation principle i.e., the heavier species diffuses slower and the lighter species diffuses faster. Therefore, after a sufficiently long time, the concentration of lighter species will be greater than that of heavier species in the major part of the domain. As in the self-diffusion case, the sum of the concentrations of both species is unity throughout the domain at any given x location. The effect of the momentum conservation is more apparent in Figure 4.14b wherein we observe a higher diffusion speed for the lighter species and a lower diffusion speed for the heavier species.

4.8 Single species: Spatial and temporal accuracy for a range of Knudsen numbers

In this section, we test the spatial and temporal accuracy of the schemes of various orders. We consider an initially consistent distribution for testing IMEX BDF-2 and ARS-222 schemes with BGK model (only),

$$f(0, x, v) = \mathcal{M}(\rho, u, T) \tag{4.9}$$

Table 4.9. Numerical parameters for Ar-Kr mass diffusion. The molecular collision parameters for Ar-Kr system are provided in Table 4.7.

| Parameter | Case MD-01 | Case MD-02 |
|--|------------------------|------------------------|
| Mixture | Ar-Kr | Ar-Kr |
| Collision kernel | VSS | VSS |
| Non-dim physical space | [0, 1] | [0, 1] |
| Non-dim velocity space | $[-5.09, 5.09]^3$ | $[-5.09, 5.09]^3$ |
| N^3 | 32^3 | 32^3 |
| N_ρ | 32 | 32 |
| M | 12 | 12 |
| Spatial elements | 4 | 4 |
| DG order | 3 | 3 |
| Time step (s) | 2×10^{-8} | 2×10^{-8} |
| Characteristic mass: m_0 | $m_{\text{Ar}} = m_1$ | $m_{\text{Ar}} = m_1$ |
| Characteristic length: H_0 (mm) | 1 | 1 |
| Characteristic velocity: u_0 (m/s) | 337.2 | 337.2 |
| Characteristic temperature: T_0 (K) | 273 | 273 |
| Characteristic number density: n_0 (m^{-3}) | 1.680×10^{21} | 8.401×10^{21} |
| Initial conditions | | |
| Velocity: u (m/s) | 0 | 0 |
| Temperature: T (K) | 273 | 273 |
| Number density: $n^{(1)}$ (m^{-3}) | 1.680×10^{21} | 8.401×10^{21} |
| Number density: $n^{(2)}$ (m^{-3}) | 8.009×10^{20} | 4.004×10^{21} |
| Knudsen number: (Kn ₁₁ , Kn ₂₂) | (0.793, 0.606) | (0.159, 0.121) |
| Knudsen number: (Kn ₁₂ , Kn ₂₁) | (0.803, 0.555) | (0.161, 0.111) |
| Left boundary conditions (subscript l) | | |
| Ar enters: inlet boundary condition for Ar | | |
| Velocity: u_l (m/s) | (0, 0, 0) | (0, 0, 0) |
| Temperature: T_l (K) | 273 | 273 |
| Number density: $n^{(1)}$ (m^{-3}) | 1.680×10^{21} | 8.401×10^{21} |
| Kr freely exits | | |
| Right wall (purely diffuse) boundary conditions (subscript r) | | |
| Kr enters: inlet boundary condition for Kr | | |
| Velocity: u_r (m/s) | (0, 0, 0) | (0, 0, 0) |
| Temperature: T_r (K) | 273 | 273 |
| Number density: $n^{(2)}$ (m^{-3}) | 8.009×10^{20} | 4.004×10^{21} |
| Ar freely exits | | |

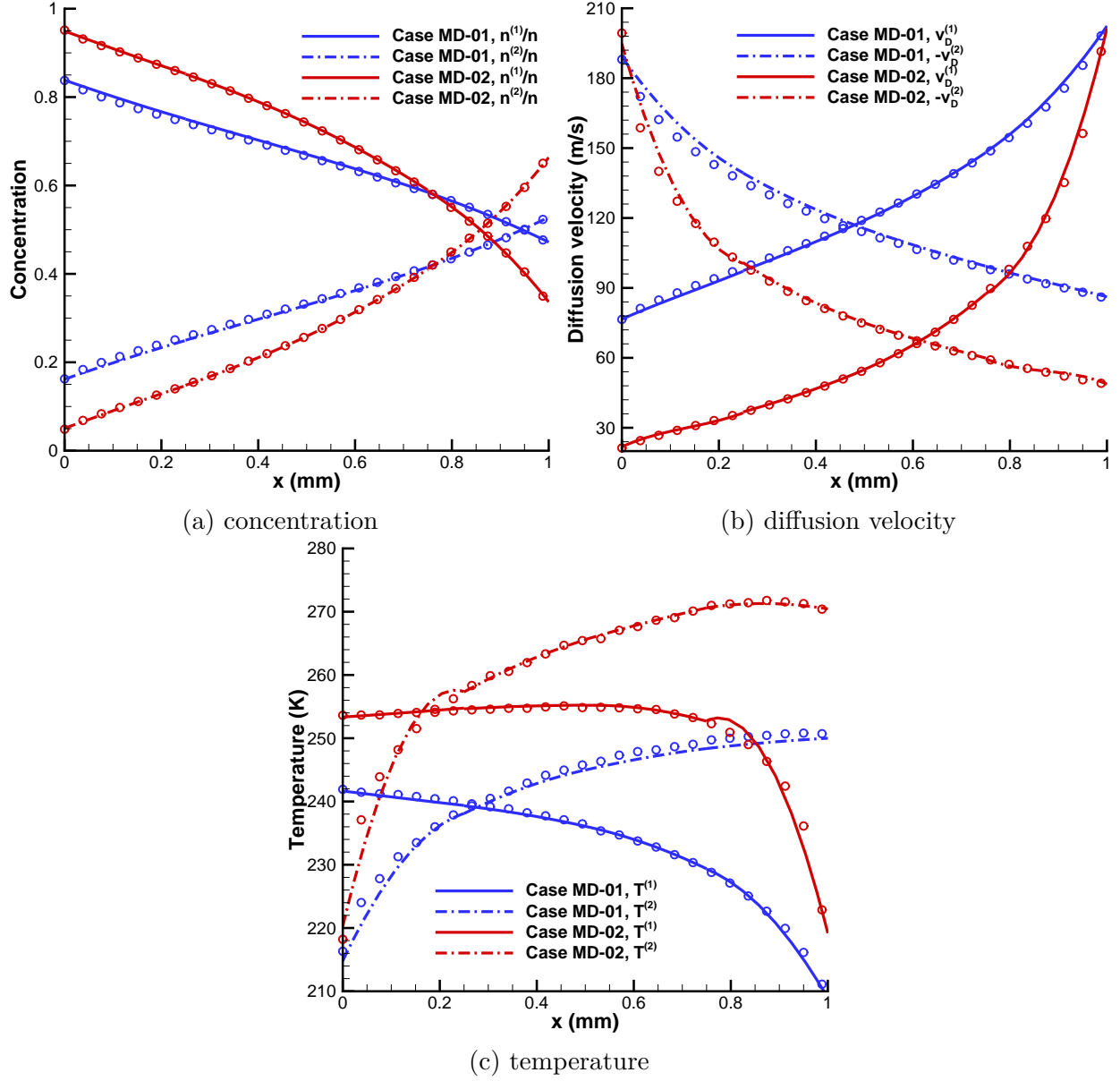


Figure 4.14. Variation of number density, diffusion velocity, and temperature along the domain for mass-diffusion cases obtained with DSMC and DGFS using VSS collision model for Argon-Krypton mixture. Symbols denote DSMC results, and lines denote DGFS results.

and an initially prepared distribution for testing IMEX BDF-3 (as per the uniform accuracy requirements put forward in [74]),

$$f(0, x, v) = \mathcal{M}(\rho, u, T) - \frac{\varepsilon}{\nu}(I - \Pi_{\mathcal{M}})(v \cdot \nabla_x \mathcal{M}) \quad (4.10)$$

where $\nu = \{\nu, \text{Pr } \nu, \nu\}$ for IMEX-BGK, IMEX-ESBGK, and IMEX-Shakov models respectively, with

$$\rho = 1 + 0.2 \sin(\pi x), \quad u = (1, 0, 0), \quad T = \frac{1}{1 + 0.2 \sin(\pi x)}.$$

We use (4.10) for testing ESBGK and Shakov models using IMEX BDF-2, and IMEX BDF-3 schemes.

The spatial domain is taken as $x \in [0, 2]$ with periodic boundary condition along with a third order DG scheme. The velocity domain is truncated into $[-|v|_{\max}, |v|_{\max}]^3$ with $|v|_{\max} = 10$ and discretized by a finite difference scheme using $N^3 = 48^3$ grid points. We choose $\Delta x = 2/N_e$ and set $\Delta t = 0.1 \Delta x/|v|_{\max}$. Δt is kept fixed for all time-integration schemes and all kinetic models; it changes if and only if we increase/decrease the number of elements in the spatial domain. The solution is computed for a range of ε . To compute the “starting” values for IMEX BDF- k scheme, we use the k^{th} order ARS scheme with very small time-step $(\Delta t)^{(0)} = \Delta t/100$.

Since the exact solution is not available, the numerical solution on a finer mesh $\Delta x/2$ is used as a reference solution to compute the error for the solution on the mesh size Δx i.e.,

$$\mathcal{E}_{\Delta t, \Delta x} := \|f_{\Delta t, \Delta x} - f_{\Delta t/2, \Delta x/2}\|_{L_{x,v}^1} = \frac{1}{(2|v|_{\max})^3} \int \frac{1}{2} \int |f_{\Delta t, \Delta x} - f_{\Delta t/2, \Delta x/2}| \, dx \, dv. \quad (4.11)$$

Since, this is an initial value problem with periodic boundaries, we ask ourselves a simple question: starting with a 3rd order DG scheme, wherein the initial solution is approximated by a second order orthonormal polynomial [94], can IMEX BDF-3 schemes maintain the third order solution accuracy over a sufficiently long time evolution? Such a test should

give us an insight into both the spatial and temporal accuracy of the scheme, as well as the conservation properties of the “discrete” schemes.

In Tabs. (4.10, 4.11, 4.12), we present the error, (4.11), at $t = 5$ (this results in 256,000 time-steps for $N_e = 1024$ element mesh). Observe that a third order DG scheme with IMEX BDF-3 scheme maintains a 3rd order accuracy. If we use IMEX BDF-2 scheme instead, keeping everything else fixed, the accuracy, expectantly, degenerates to a second order overall.

The key point to note here is that IMEX BDF schemes require one kernel evaluation per time-step, and therefore is more efficient. This fact is reiterated in Tab. (4.13), wherein we present the “computational times per time-step per degree of freedom (CPTPD)” for all the schemes at different ε and N_e . These cases are run for 100 time-steps, each. For the third order DG scheme that we use, total degree of freedoms are $3N_e N^3$ with $N = 48$. Three observations are to be made: a) CPTPD is independent of ε ; b) for a given time-integration scheme, CPTPD for all the three kinetic models are approximately same, hence there is no reason to prefer BGK model over ESBGK model; c) CPTPD of IMEX BDF- k schemes are approximately the same.

We mention that the magnitude of the error norms at $\varepsilon = \mathcal{O}(1)$ and $\varepsilon = \mathcal{O}(10^{-2})$ are different since flows closer to equilibrium relax much slower than the flows closer to free molecular regime: an observation that we iterated in the introduction. So, after a sufficiently long time, at a fixed time $t = 5$, while the flow with $\varepsilon = \mathcal{O}(1)$ has relaxed to equilibrium, the flow at $\varepsilon = \mathcal{O}(10^{-2})$ hasn’t. In the former case, the flow physics is dominated by convection, and in the latter by collisions.

From these results, the schemes meet the following objectives:

- 1) the timestep is independent of the Knudsen number
- 2) the collision kernel is evaluated explicitly without use of any iteration

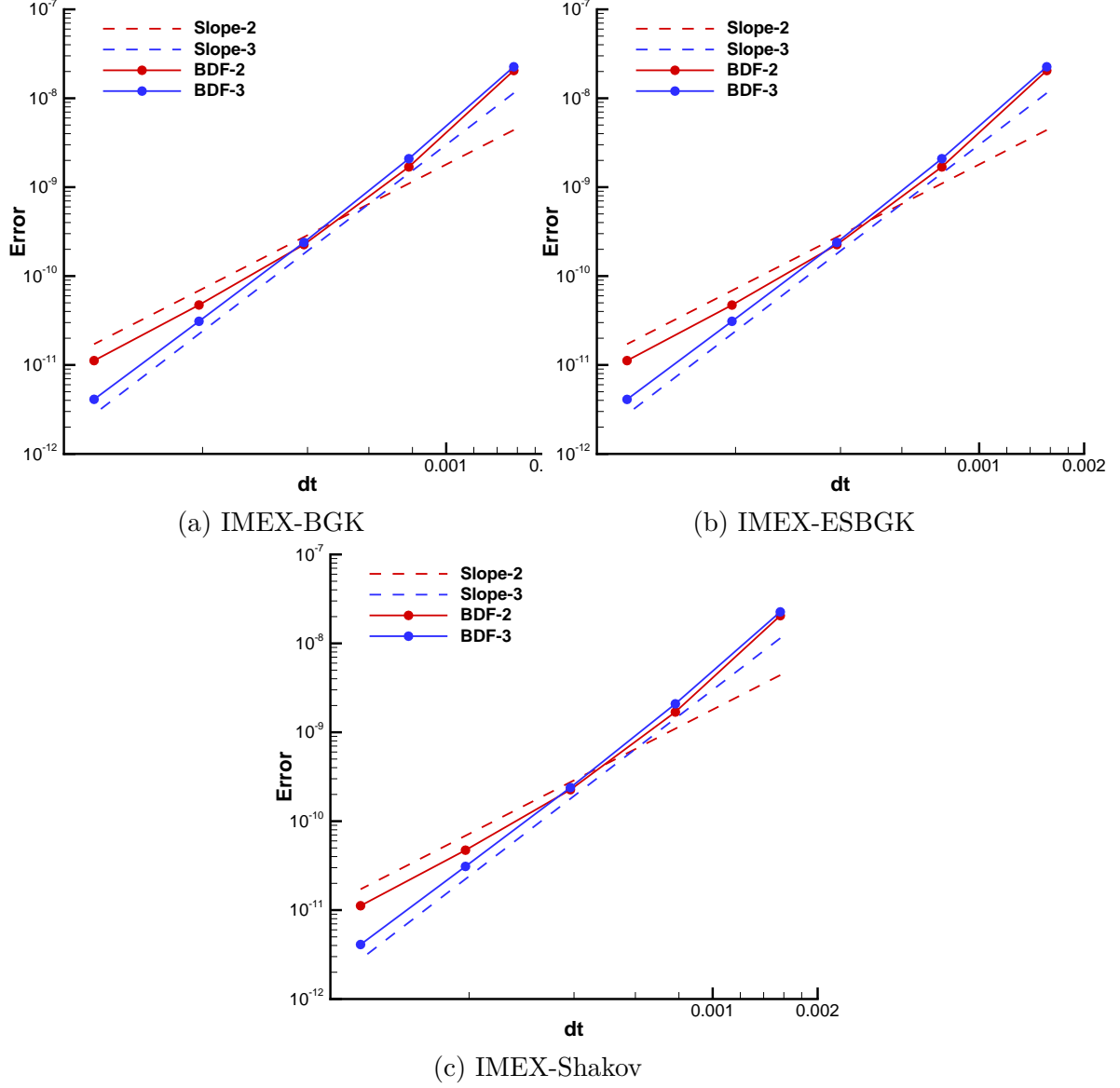


Figure 4.15. Error decay for linear kinetic schemes. Figure is obtained by taking the maximal \mathcal{E} error, from Tab. (4.10), among all values of ε for a fixed Δt .

Table 4.10. Accuracy test for 1D-3V IMEX-BGK equation with $\alpha = 0.49$.

| $\varepsilon \rightarrow$ $\downarrow N_e$ | $\alpha \times 1$ | | $\alpha \times 10^{-2}$ | | $\alpha \times 10^{-4}$ | | $\alpha \times 10^{-6}$ | |
|---|------------------------------------|---------------|------------------------------------|---------------|------------------------------------|---------------|------------------------------------|---------------|
| | $\mathcal{E}_{\Delta t, \Delta x}$ | \mathcal{O} | $\mathcal{E}_{\Delta t, \Delta x}$ | \mathcal{O} | $\mathcal{E}_{\Delta t, \Delta x}$ | \mathcal{O} | $\mathcal{E}_{\Delta t, \Delta x}$ | \mathcal{O} |
| IMEX BDF-2, t=5 | | | | | | | | |
| 16 | 5.57×10^{-11} | - | 1.85×10^{-8} | - | 2.04×10^{-8} | - | 2.05×10^{-8} | - |
| 32 | 4.68×10^{-12} | 3.57 | 1.48×10^{-9} | 3.64 | 1.67×10^{-9} | 3.61 | 1.69×10^{-9} | 3.60 |
| 64 | 8.44×10^{-13} | 2.47 | 1.71×10^{-10} | 3.11 | 2.12×10^{-10} | 2.98 | 2.26×10^{-10} | 2.90 |
| 128 | 2.05×10^{-13} | 2.04 | 3.65×10^{-11} | 2.23 | 4.18×10^{-11} | 2.34 | 4.73×10^{-11} | 2.26 |
| 256 | 5.13×10^{-14} | 2.00 | 9.18×10^{-12} | 1.99 | 1.03×10^{-11} | 2.02 | 1.12×10^{-11} | 2.08 |
| 512 | 1.29×10^{-14} | 1.99 | 2.32×10^{-12} | 1.98 | 2.60×10^{-12} | 1.99 | 2.69×10^{-12} | 2.06 |
| IMEX BDF-3, t=5 | | | | | | | | |
| 16 | 7.69×10^{-11} | - | 1.99×10^{-8} | - | 2.25×10^{-8} | - | 2.26×10^{-8} | - |
| 32 | 6.07×10^{-12} | 3.66 | 1.78×10^{-9} | 3.48 | 2.07×10^{-9} | 3.44 | 2.09×10^{-9} | 3.43 |
| 64 | 5.18×10^{-13} | 3.55 | 1.77×10^{-10} | 3.33 | 2.27×10^{-10} | 3.19 | 2.39×10^{-10} | 3.13 |
| 128 | 5.02×10^{-14} | 3.37 | 1.91×10^{-11} | 3.21 | 2.57×10^{-11} | 3.14 | 3.10×10^{-11} | 2.95 |
| 256 | 5.61×10^{-15} | 3.16 | 2.20×10^{-12} | 3.12 | 3.03×10^{-12} | 3.08 | 4.11×10^{-12} | 2.92 |
| 512 | 1.80×10^{-15} | 1.64 | 2.67×10^{-13} | 3.04 | 3.67×10^{-13} | 3.05 | 5.33×10^{-13} | 2.95 |

Table 4.11. Accuracy test for 1D-3V IMEX-ESBGK equation with $\alpha = 0.49 \times 1.5$.

| $\varepsilon \rightarrow$ $\downarrow N_e$ | $\alpha \times 1$ | | $\alpha \times 10^{-2}$ | | $\alpha \times 10^{-4}$ | | $\alpha \times 10^{-6}$ | |
|---|------------------------------------|---------------|------------------------------------|---------------|------------------------------------|---------------|------------------------------------|---------------|
| | $\mathcal{E}_{\Delta t, \Delta x}$ | \mathcal{O} | $\mathcal{E}_{\Delta t, \Delta x}$ | \mathcal{O} | $\mathcal{E}_{\Delta t, \Delta x}$ | \mathcal{O} | $\mathcal{E}_{\Delta t, \Delta x}$ | \mathcal{O} |
| IMEX BDF-2, t=5 | | | | | | | | |
| 16 | 8.59×10^{-10} | - | 1.80×10^{-8} | - | 2.04×10^{-8} | - | 2.05×10^{-8} | - |
| 32 | 5.50×10^{-11} | 3.97 | 1.42×10^{-9} | 3.66 | 1.67×10^{-9} | 3.61 | 1.69×10^{-9} | 3.60 |
| 64 | 6.88×10^{-12} | 3.00 | 1.60×10^{-10} | 3.15 | 2.10×10^{-10} | 2.99 | 2.26×10^{-10} | 2.90 |
| 128 | 1.85×10^{-12} | 1.89 | 3.42×10^{-11} | 2.23 | 4.14×10^{-11} | 2.34 | 4.72×10^{-11} | 2.26 |
| 256 | 4.76×10^{-13} | 1.96 | 8.66×10^{-12} | 1.98 | 1.03×10^{-11} | 2.01 | 1.12×10^{-11} | 2.08 |
| 512 | 1.20×10^{-13} | 1.99 | 2.19×10^{-12} | 1.98 | 2.60×10^{-12} | 1.99 | 2.69×10^{-12} | 2.06 |
| IMEX BDF-3, t=5 | | | | | | | | |
| 16 | 9.33×10^{-10} | - | 1.93×10^{-8} | - | 2.24×10^{-8} | - | 2.26×10^{-8} | - |
| 32 | 6.90×10^{-11} | 3.76 | 1.70×10^{-9} | 3.50 | 2.07×10^{-9} | 3.44 | 2.09×10^{-9} | 3.43 |
| 64 | 5.19×10^{-12} | 3.73 | 1.66×10^{-10} | 3.36 | 2.25×10^{-10} | 3.20 | 2.39×10^{-10} | 3.13 |
| 128 | 4.42×10^{-13} | 3.55 | 1.77×10^{-11} | 3.23 | 2.54×10^{-11} | 3.15 | 3.10×10^{-11} | 2.95 |
| 256 | 4.30×10^{-14} | 3.36 | 2.04×10^{-12} | 3.12 | 3.00×10^{-12} | 3.08 | 4.10×10^{-12} | 2.92 |
| 512 | 5.26×10^{-15} | 3.03 | 2.50×10^{-13} | 3.03 | 3.65×10^{-13} | 3.04 | 5.27×10^{-13} | 2.96 |

Table 4.12. Accuracy test for 1D-3V IMEX-Shakov equation with $\alpha = 0.49$.

| $\varepsilon \rightarrow$ $\downarrow N_e$ | $\alpha \times 1$ | | $\alpha \times 10^{-2}$ | | $\alpha \times 10^{-4}$ | | $\alpha \times 10^{-6}$ | |
|---|------------------------------------|---------------|------------------------------------|---------------|------------------------------------|---------------|------------------------------------|---------------|
| | $\mathcal{E}_{\Delta t, \Delta x}$ | \mathcal{O} | $\mathcal{E}_{\Delta t, \Delta x}$ | \mathcal{O} | $\mathcal{E}_{\Delta t, \Delta x}$ | \mathcal{O} | $\mathcal{E}_{\Delta t, \Delta x}$ | \mathcal{O} |
| IMEX BDF-2, t=5 | | | | | | | | |
| 16 | 7.07×10^{-11} | - | 1.80×10^{-8} | - | 2.04×10^{-8} | - | 2.05×10^{-8} | - |
| 32 | 4.81×10^{-12} | 3.88 | 1.44×10^{-9} | 3.64 | 1.67×10^{-9} | 3.61 | 1.69×10^{-9} | 3.60 |
| 64 | 7.25×10^{-13} | 2.73 | 1.63×10^{-10} | 3.14 | 2.10×10^{-10} | 2.99 | 2.26×10^{-10} | 2.90 |
| 128 | 1.89×10^{-13} | 1.94 | 3.45×10^{-11} | 2.24 | 4.14×10^{-11} | 2.34 | 4.72×10^{-11} | 2.26 |
| 256 | 4.83×10^{-14} | 1.97 | 8.69×10^{-12} | 1.99 | 1.03×10^{-11} | 2.01 | 1.12×10^{-11} | 2.08 |
| 512 | 1.23×10^{-14} | 1.97 | 2.20×10^{-12} | 1.98 | 2.60×10^{-12} | 1.99 | 2.69×10^{-12} | 2.06 |
| IMEX BDF-3, t=5 | | | | | | | | |
| 16 | 7.64×10^{-11} | - | 1.94×10^{-8} | - | 2.24×10^{-8} | - | 2.26×10^{-8} | - |
| 32 | 5.70×10^{-12} | 3.74 | 1.72×10^{-9} | 3.50 | 2.07×10^{-9} | 3.44 | 2.09×10^{-9} | 3.43 |
| 64 | 4.54×10^{-13} | 3.65 | 1.69×10^{-10} | 3.35 | 2.25×10^{-10} | 3.20 | 2.39×10^{-10} | 3.13 |
| 128 | 4.14×10^{-14} | 3.45 | 1.81×10^{-11} | 3.22 | 2.54×10^{-11} | 3.15 | 3.10×10^{-11} | 2.95 |
| 256 | 4.42×10^{-15} | 3.23 | 2.07×10^{-12} | 3.13 | 3.01×10^{-12} | 3.08 | 4.10×10^{-12} | 2.92 |
| 512 | 1.72×10^{-15} | 1.36 | 2.51×10^{-13} | 3.04 | 3.67×10^{-13} | 3.04 | 5.28×10^{-13} | 2.96 |

Table 4.13. Computational cost per time-step per degree of freedom (CPTPD) for 1D-3V IMEX-BGK ($\alpha = 0.49$), IMEX-ESBGK ($\alpha = 0.49 \times 1.5$), and IMEX-Shakov ($\alpha = 0.49$). These cases are run for 100 time-steps, each. For the third order DG scheme that we use, degree of freedom is $3N_e N^3$ with $N = 48$.

| $\varepsilon \rightarrow$ $\downarrow N_e$ | $\alpha \times 1$ | $\alpha \times 10^{-2}$ | $\alpha \times 10^{-4}$ | $\alpha \times 10^{-6}$ | $\alpha \times 10^{-8}$ | $\alpha \times 10^{-10}$ |
|---|------------------------|-------------------------|-------------------------|-------------------------|-------------------------|--------------------------|
| | CPTPD | CPTPD | CPTPD | CPTPD | CPTPD | CPTPD |
| BGK | | | | | | |
| IMEX BDF-2 | | | | | | |
| 128 | 5.10×10^{-10} | 5.11×10^{-10} | 5.12×10^{-10} | 5.13×10^{-10} | 5.11×10^{-10} | 5.12×10^{-10} |
| 256 | 4.87×10^{-10} | 4.90×10^{-10} | 4.88×10^{-10} | 4.87×10^{-10} | 4.86×10^{-10} | 4.87×10^{-10} |
| IMEX BDF-3 | | | | | | |
| 128 | 6.03×10^{-10} | 6.01×10^{-10} | 6.02×10^{-10} | 6.04×10^{-10} | 6.02×10^{-10} | 6.02×10^{-10} |
| 256 | 5.79×10^{-10} | 5.81×10^{-10} | 5.80×10^{-10} | 5.79×10^{-10} | 5.77×10^{-10} | 5.79×10^{-10} |
| ESBGK | | | | | | |
| IMEX BDF-2 | | | | | | |
| 128 | 4.89×10^{-10} | 4.88×10^{-10} | 4.87×10^{-10} | 4.88×10^{-10} | 4.88×10^{-10} | 4.90×10^{-10} |
| 256 | 4.65×10^{-10} | 4.67×10^{-10} | 4.66×10^{-10} | 4.66×10^{-10} | 4.66×10^{-10} | 4.66×10^{-10} |
| IMEX BDF-3 | | | | | | |
| 128 | 5.79×10^{-10} | 5.78×10^{-10} | 5.79×10^{-10} | 5.80×10^{-10} | 5.81×10^{-10} | 5.80×10^{-10} |
| 256 | 5.57×10^{-10} | 5.55×10^{-10} | 5.57×10^{-10} | 5.55×10^{-10} | 5.56×10^{-10} | 5.55×10^{-10} |
| Shakov | | | | | | |
| IMEX BDF-2 | | | | | | |
| 128 | 5.19×10^{-10} | 5.15×10^{-10} | 5.18×10^{-10} | 5.16×10^{-10} | 5.15×10^{-10} | 5.19×10^{-10} |
| 256 | 4.93×10^{-10} | 4.92×10^{-10} | 4.92×10^{-10} | 4.92×10^{-10} | 4.92×10^{-10} | 4.92×10^{-10} |
| IMEX BDF-3 | | | | | | |
| 128 | 6.07×10^{-10} | 6.10×10^{-10} | 6.07×10^{-10} | 6.08×10^{-10} | 6.09×10^{-10} | 6.08×10^{-10} |
| 256 | 5.85×10^{-10} | 5.83×10^{-10} | 5.84×10^{-10} | 5.86×10^{-10} | 5.83×10^{-10} | 5.83×10^{-10} |

- 3) the scheme utilizes high order time-stepping so that the time integration over sufficiently long number of timesteps, needed for modelling near-continuum flows, can be carried out more accurately
- 4) the scheme is high order accurate in physical space for minimum dispersion
- 5) the scheme is applicable for modelling both rarefied and near-continuum compressible flows.

4.9 Single-species: Couette flow for a range of Knudsen numbers

In the current test case, we consider the effect of velocity gradient on the solution. The coordinates are chosen such that the walls are parallel to the y direction and x is the direction perpendicular to the walls. The geometry as well as boundary conditions are shown in Figure 4.3. Specific case details have been provided in Tabs. 4.14 and 4.15.

Figures (4.16, 4.18) illustrate the velocity and temperature along the domain length, wherein we note an excellent agreement between DGFS and DSMC. The velocity profiles from BGK/ESBGK/Shakov are in good agreement with DGFS and DSMC, whereas the temperature profiles from ESBGK/Shakov are in good agreement with DGFS and DSMC. The deviation in BGK temperature profiles is due to its Prandtl number defect. Notably, all the schemes resolve the continuum cases at a fixed time-step Δt which is solely decided by CFL condition and not the Knudsen number.

In Table 4.16, we explicitly illustrate the performance of the explicit-DG [32] and the proposed IMEX-BDF scheme for the BGK and ESBGK models. Here, expectantly, we note that the computational cost of explicit schemes increases with decrease in Knudsen number.

From this test case, the schemes meet the following primary objectives:

- 1) the timestep is independent of the Knudsen number
- 2) the collision kernel is evaluated explicitly without use of any iteration

Table 4.14. Common numerical parameters for Couette flow cases.

| Common Parameters | |
|--|------------------------|
| Molecular mass: m (kg) | 66.3×10^{-27} |
| Non-dim physical space | $[0, 1]$ |
| Non-dim velocity space ¹ | $[-5, 5]^3$ |
| $\{N^3\}$ | $\{24^3\}$ |
| Spatial elements | 2 |
| DG order | 3 |
| Time step: Δt (s) | 3×10^{-8} |
| Viscosity index: ω | 0.81 |
| Scattering parameter: α | 1.0 |
| Ref. diameter: d_{ref} (m) | 4.17×10^{-10} |
| Ref. temperature: T_{ref} (K) | 273 |
| Ref. viscosity: μ_{ref} ($\text{Pa} \cdot s$) | 2.117×10^{-5} |
| Characteristic length: H_0 (mm) | 1 |
| Characteristic velocity: u_0 (m/s) | 337.2 |
| Characteristic temperature: T_0 (K) | 273 |
| Characteristic no. density: n_0 (m^{-3}) | 3.469×10^{22} |
| Initial conditions | |
| Velocity: u (m/s) | 0 |
| Temperature: T (K) | 273 |
| Left wall conditions | |
| Velocity: u (m/s) | $(0, -250, 0)$ |
| Right wall conditions | |
| Velocity: u (m/s) | $(0, 250, 0)$ |

Table 4.15. Numerical parameters for Couette flow cases.

| Parameter | Case C-01 | Case C-02 | Case C-03 |
|------------------------------------|------------------------|------------------------|------------------------|
| Initial conditions | | | |
| Number density: n (m^{-3}) | 3.469×10^{22} | 3.469×10^{24} | 3.469×10^{26} |
| Knudsen number ¹ : (Kn) | 0.037 | 0.00037 | 0.0000037 |

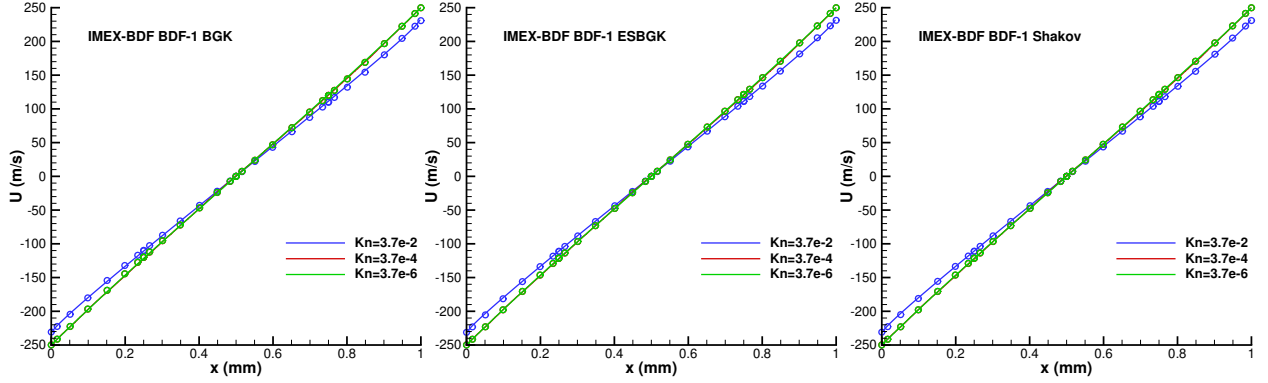


Figure 4.16. Variation of y -velocity along the domain for Couette flow cases at different Knudsen numbers using IMEX-BDF scheme for linear kinetic models. Lines denote the results from DSMC and symbols denote the results from IMEX-BDF scheme.

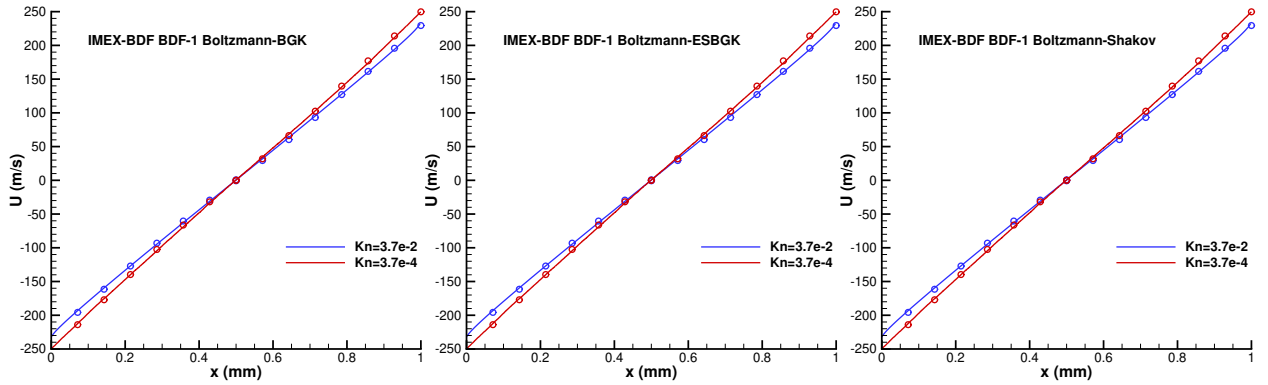


Figure 4.17. Variation of y -velocity along the domain for Couette flow cases at different Knudsen numbers using IMEX-BDF scheme for Boltzmann equation. Lines denote the results from DSMC and symbols denote the results from IMEX-BDF scheme. Boltzmann-BGK refers to Boltzmann equation penalized with BGK operator; Boltzmann-ESBGK refers to Boltzmann equation penalized with ESGBK operator; Boltzmann-Shakov refers to Boltzmann equation penalized with Shakov operator.

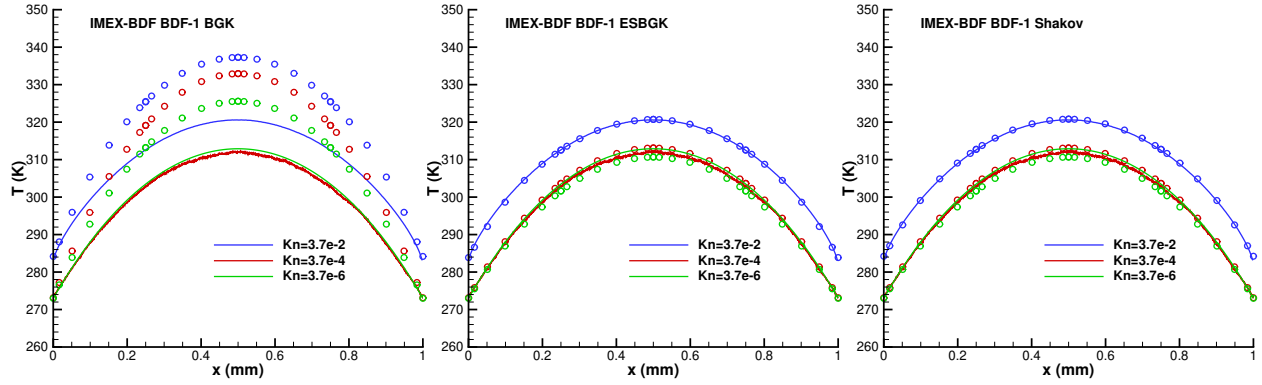


Figure 4.18. Variation of temperature along the domain for Couette flow cases at different Knudsen numbers using IMEX-BDF scheme for linear kinetic models. Lines denote the results from DSMC and symbols denote the results from IMEX-BDF scheme.

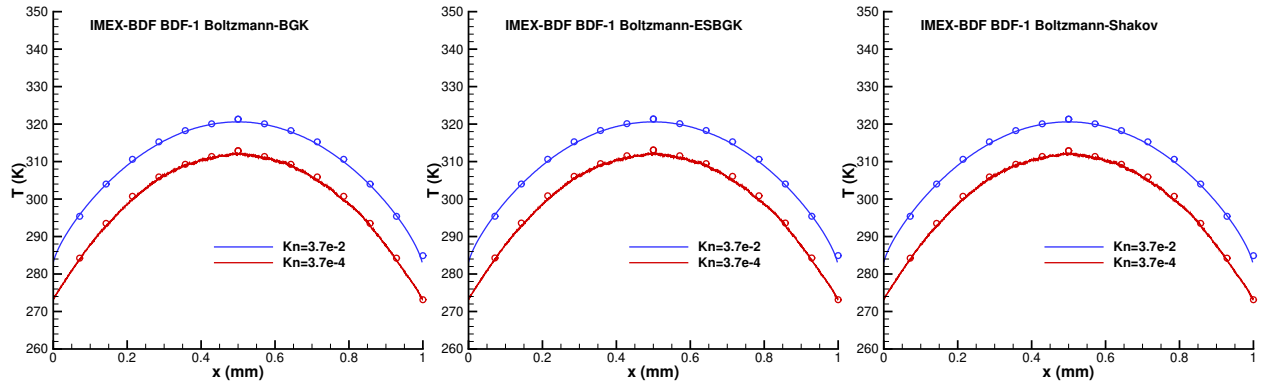


Figure 4.19. Variation of temperature along the domain for Couette flow cases at different Knudsen numbers using IMEX-BDF scheme for Boltzmann equation. Lines denote the results from DSMC and symbols denote the results from IMEX-BDF scheme. Boltzmann-BGK refers to Boltzmann equation penalized with BGK operator; Boltzmann-ESBGK refers to Boltzmann equation penalized with ESBGK operator; Boltzmann-Shakov refers to Boltzmann equation penalized with Shakov operator.

Table 4.16. Performance of the asymptotic and explicit schemes for Couette flow case. Each test-case is conveniently defined by 4 numbers: $(N_e, K, N^3); [-L, L]^3$, which corresponds to N_e elements in physical space, K order DG, N^3 points in velocity space, and L denotes the extent of the isotropic velocity-mesh. The residual is defined as $(\|f^{l+1} - f^n\|_{L^2} / \|f^n\|_{L^2}) / (\|f^2 - f^1\|_{L^2} / \|f^1\|_{L^2})$, where f^n denotes the distribution function at n^{th} timestep.

| Model | Case | Temporal scheme | Kn | timestep $\Delta t (s)$ | Time steps (Total) | Residual | Computational time (s) |
|-------|--|----------------------------|---------|-------------------------|--------------------|-----------------------|------------------------|
| BGK | C-01 (2/3/24 ³) [-5, 5] ³ | Explicit Forward-Euler | 0.037 | 3×10^{-8} | 3,000 | 8.49×10^{-7} | 7.65 |
| | | IMEX BDF-1 | 0.037 | 3×10^{-8} | 3,000 | 8.93×10^{-7} | 2.73 |
| | C-02 (2/3/24 ³) [-5, 5] ³ | Explicit* Forward-Euler | 0.00037 | 3×10^{-10} | 15,000,000 | 6.02×10^{-7} | 29318.16 |
| | | IMEX BDF-1 | 0.00037 | 3×10^{-8} | 150,000 | 6.12×10^{-7} | 103.68 |
| ESBGK | C-01 (2/3/24 ³) [-5, 5] ³ | Explicit Forward-Euler | 0.037 | 3×10^{-8} | 3,000 | 3.97×10^{-8} | 9.87 |
| | | IMEX BDF-1 | 0.037 | 3×10^{-8} | 3,000 | 4.14×10^{-8} | 2.81 |
| | C-02 (2/3/24 ³) [-5, 5] ³ | Explicit* Forward-Euler | 0.00037 | 3×10^{-10} | 15,000,000 | 1.17×10^{-7} | 39006.82 |
| | | IMEX BDF-1 | 0.00037 | 3×10^{-8} | 150,000 | 4.94×10^{-8} | 109.06 |

* Unstable at $\Delta t = \{3 \times 10^{-8}, 3 \times 10^{-9}\}$

- 3) the scheme utilizes high order time-stepping so that the time integration over sufficiently long number of timesteps, needed for modelling near-continuum flows, can be carried out more accurately.

4.10 Single-species: Sod shock tube problem

In the current test case, we consider the classical Sod shock tube problem [95]. The full set of simulation parameters have been reiterated in Tab. (4.17). In summary, we utilize three different (upstream, downstream) densities $[kg/m^3]$: a) $(1 \times 10^{-5}, 0.125 \times 10^{-5})$; b) $(1 \times 10^{-4}, 0.125 \times 10^{-4})$; c) $(1 \times 10^{-3}, 0.125 \times 10^{-3})$. These upstream densities correspond to Knudsen number [32] of a) 4.96×10^{-2} ; b) 4.96×10^{-3} ; c) 4.96×10^{-4} . We use a 256 element 3rd order DG scheme with a time step of $\approx 4 \times 10^{-6} s$ for all cases. The velocity domain $[-6.14, 6.14]^3$ is discretized using 32^3 points.

The results from asymptotic ESBGK model and asymptotic Boltzmann-BGK model have been shown in Figs. (4.20) and (4.21) respectively, wherein we show the variation of conserved flow properties, viz. density, mass-flux, and energy for the Sod shock tube problem using asymptotic (A) ESBGK model. The reference compressible Navier-Stokes (C-NS) and Euler (C-Euler) solutions were obtained using a 10000 cell, 2nd order finite volume central scheme based density solver, rhoCentralFoam, available with OpenFOAM-2.3.1. The primary intent, here, is to show conservation properties of the scheme, as well as its capability to capture the Navier-Stokes limit.

From this test case, the schemes meet the following primary objectives:

- 1) the timestep is independent of the Knudsen number
- 5) the scheme is applicable for modelling both rarefied and near-continuum compressible flows.

Table 4.17. Numerical parameters for the Sod shock tube problem. The molecular parameters for “Air” are as indicated in Appendix-A of [24].

| Parameter | SOD-01 | SOD-02 | SOD-03 |
|---------------------------------------|-------------------------|------------------------|------------------------|
| Working Gas | Air | | |
| Physical space (m) | $[-5, 5]$ | | |
| Characteristic length: H_0 (m) | 1 | | |
| Char. velocity: u_0 (m/s) | 400.05 | | |
| Char. temperature: T_0 (K) | 278.746 | | |
| Char. no. density: n_0 (m^{-3}) | 2.599×10^{19} | 2.599×10^{20} | 2.599×10^{21} |
| Velocity space | $[-6.14u_0, 6.14u_0]^3$ | | |
| Points in velocity mesh: N_v | 32^3 | | |
| Number of elements: N_e | 256 | | |
| Polynomial degree: p | 2 | | |
| Time step: Δt (s): | 4×10^{-6} | | |
| Upstream region: $[-5, 0]$: | | | |
| Kn: | 4.96×10^{-2} | 4.96×10^{-3} | 4.96×10^{-4} |
| Density: n/n_0 | 8 | | |
| Velocity: u/u_0 | 0 | | |
| Temperature: T/T_0 | 1.25 | | |
| Downstream region: $(0, 5]$: | | | |
| Density: n/n_0 | 1 | | |
| Velocity: u/u_0 | 0 | | |
| Temperature: T/T_0 | 1 | | |

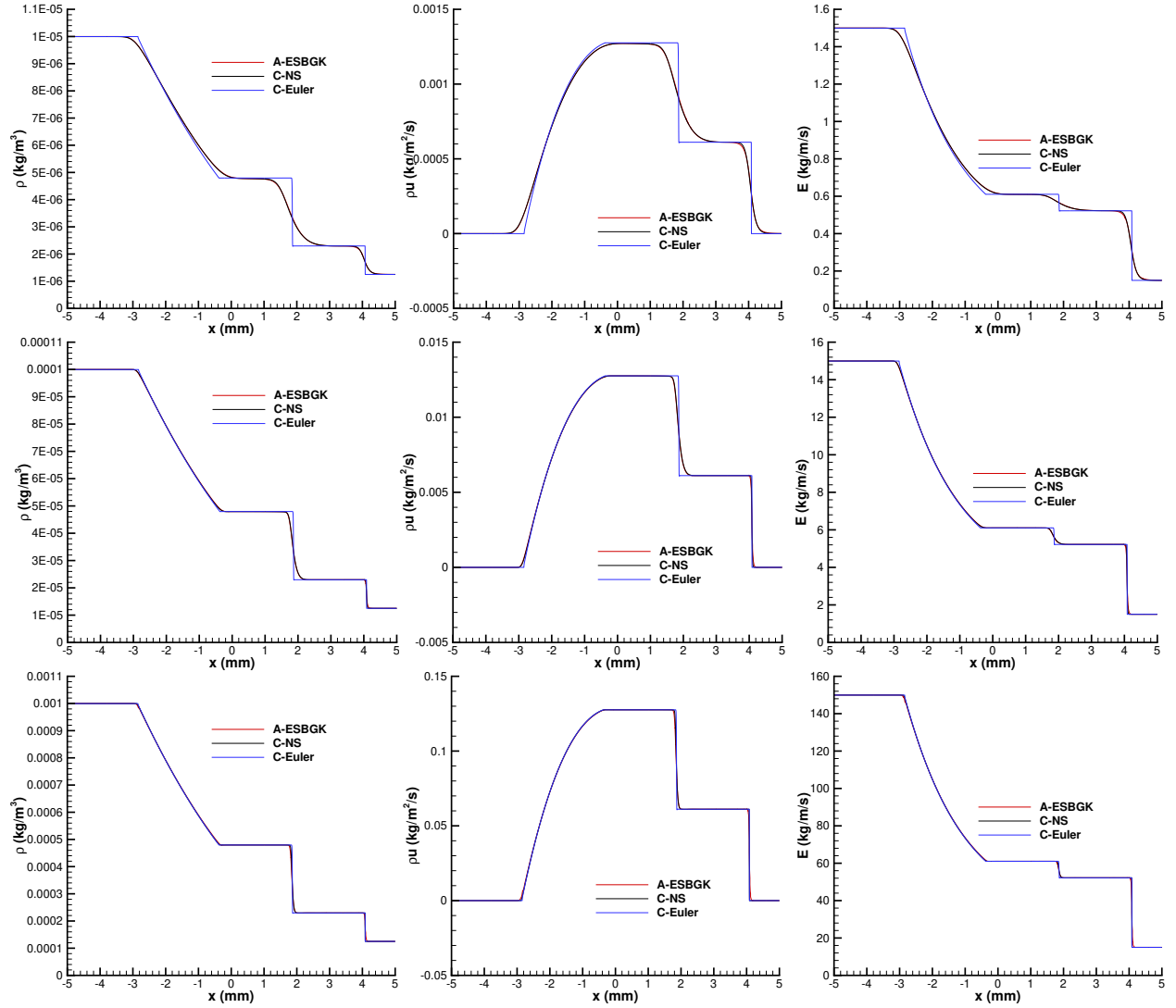


Figure 4.20. Variation of conserved flow properties, viz. density, mass-flux, and energy for the Sod shock tube problem using asymptotic (A) ESBGK model. The reference compressible Navier-Stokes (C-NS) and Euler (C-Euler) solutions were obtained using a 10000 cell, 2nd order finite volume central scheme based density solver, rhoCentralFoam, available with OpenFOAM-2.3.1. The primary intent, here, is to show conservation properties of the scheme, as well as its capability to capture the Navier-Stokes limit.

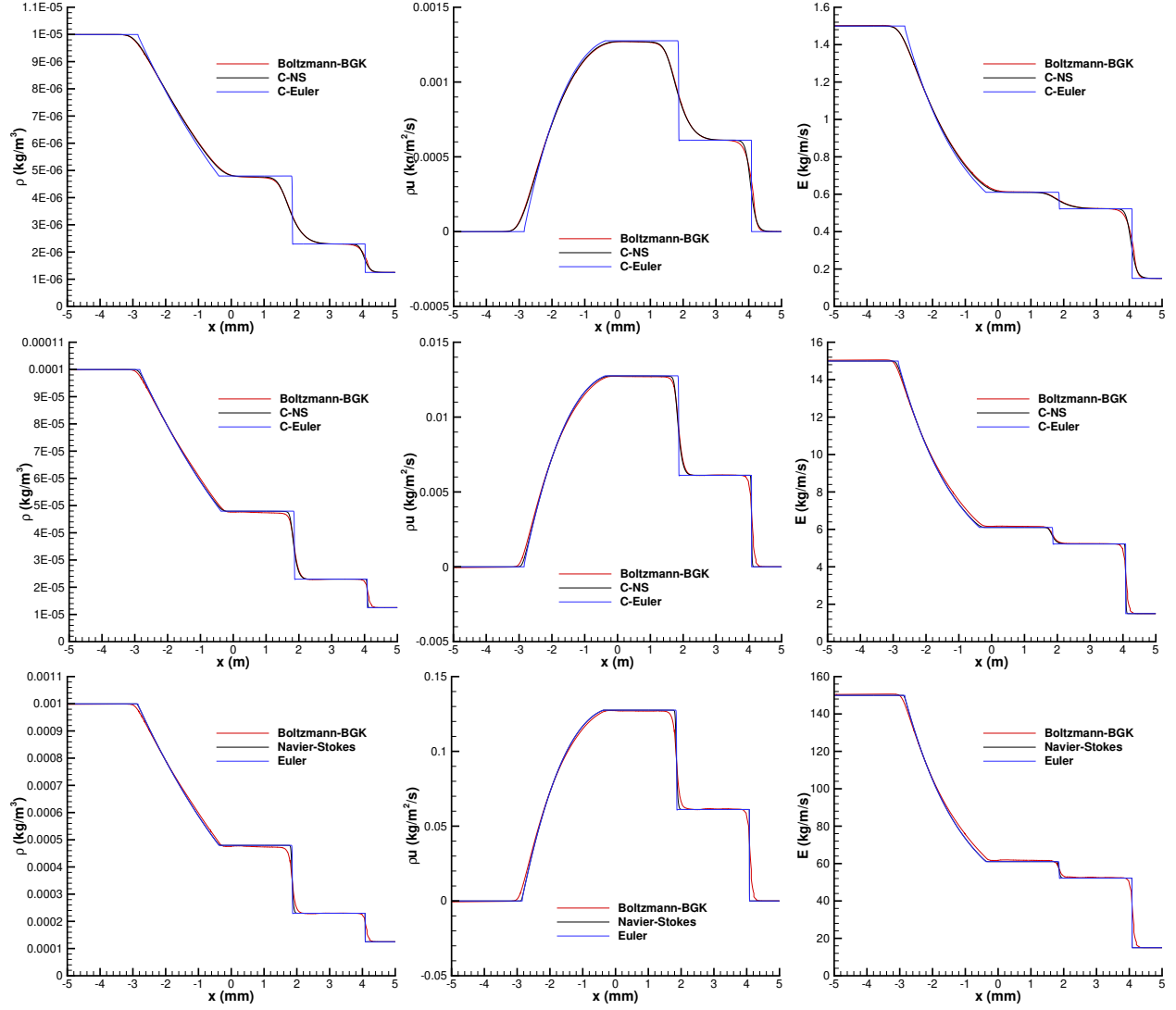
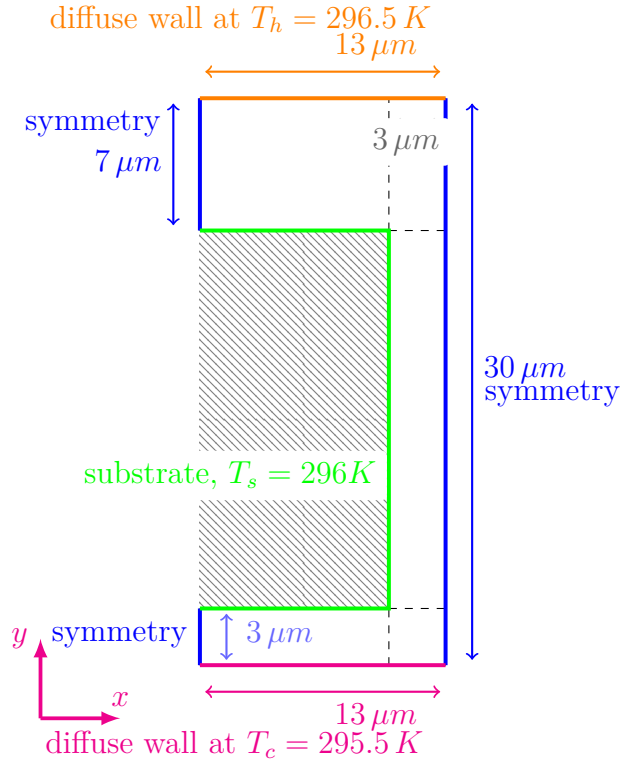


Figure 4.21. Variation of conserved flow properties, viz. density, mass-flux, and energy for the Sod shock tube problem using asymptotic Boltzmann-BGK model. Boltzmann-BGK refers to Boltzmann equation penalized with BGK operator.

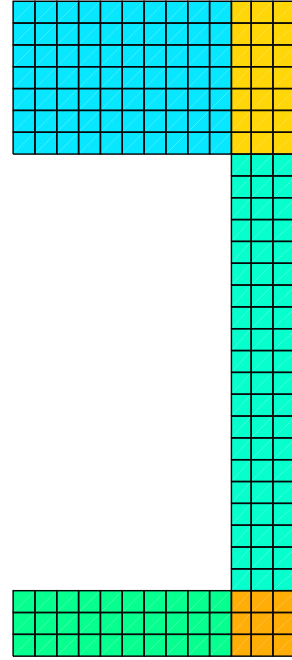
- 6) When Kn is small, $O(10^{-3})$, Navier-Stokes can be recovered from the asymptotics of the Boltzmann equation. Hence, the results from the implicit-explicit Boltzmann equation should be consistent with that recovered from Navier-Stokes.

4.11 Single-species: Flow around a micro-electronic chip

In the current test case, we consider the effect of temperature gradients on a solid substrate placed in a rarefied environment. The problem schematic, geometry, as well as boundary conditions are shown in Figure 4.22. Case details have been provided in Tab. 4.19. We mention that, to the best of our knowledge, an analysis of such a low-temperature flow hasn't been carried out previously within a deterministic full Boltzmann framework.



(a) Schematic



(b) Mesh for DGFS simulations. For DSMC simulations, we subdivide each cell of the mesh above into 5×5 sub-cells.

Figure 4.22. Numerical setup for the flow around a micro-electronic chip.

4.11.1 Numerical details

We employ DSMC and DGFS to carry out simulation of flow around a micro-electronic chip. The simulation specific numerical parameters as well as differences between stochastic (DSMC) and deterministic (DGFS) modelling is described next.

- **DSMC:** SPARTA[19] has been employed for carrying out DSMC simulations in the present work. It implements the DSMC method as proposed by Bird [24]. The solver takes into account the translational/rotational/vibrational kinetic energies associated with the molecular motion. The solver has been benchmarked [19] and widely used for studying hypersonic, subsonic and thermal [29], [32], [89], [96]–[100] gas flow problems. In this work, cell size less than $\lambda/3$ has been ensured in all the test cases. The no-time collision (NTC) algorithm is used in conjunction with Bird’s VHS scattering model. The simulations are first run for 200,000 unsteady steps wherein the particles move, collide, and allowed to equilibrate. No sampling is performed at this stage. Next, the simulation is run for another 4,000,000 steady steps wherein the samples of flow properties namely number density, flow velocity, temperature, stress, and heat-flux, are taken for sufficiently long time so as to produce a meaningful bulk properties as well as minimize the statistical noise therein. In the present case, the DSMC domain is discretized with a uniform cell size of $0.2\ \mu m$, with 300 particles per cell on average during initialization. A time step of 10^{-9} sec is used during *move* step of DSMC algorithm throughout the course of simulation. N_2 is used as the working gas in simulations. The properties of the working gas is given in Tab. 4.18. We want to emphasize that for DSMC simulations, we take rotational/vibrational degrees of freedom into account i.e., N_2 is treated as a diaatomic species. DSMC simulations on 30 cores of Intel(R) Xeon(R) CPU E5-2670 v2 2.50GHz, took ~ 73 hours.
- **DGFS:** We use the DGFS implementation described in Ref. [32]. The spatial domain consists of 281 uniform square cells of $1\ \mu m$ each. Since we are seeking a steady state solution, the time-step is selected based on the CFL constraints of the forward Euler scheme. Other case specific DGFS parameters have been provided in Tab. 4.19. Note

that, we employ N_2 as the working gas in simulations, since MIKRA experiments[43] were performed in N_2 medium. N_2 is diatomic, however, DGFS, as of now, is applicable for monoatomic gases only. Since the working temperature range is low, we anticipate the effects of vibrational degrees of freedom to be negligible. DGFS simulations on 2 Nvidia-P100 GPUs took ~ 9 hours.

Table 4.18. N_2 gas VHS parameters used in 2-D single-species DSMC and DGFS simulations. Note that DGFS, being in very early stage of research, treats N_2 as a monoatomic species.

| | |
|--|---------------------------------|
| Mass: m (kg) | 46.5×10^{-27} |
| Viscosity index: ω ($-$) | 0.74 |
| Scattering index: α ($-$) | 1.0 |
| Ref. diameter: d_{ref} (m) | 4.17×10^{-10} |
| Ref. temperature: T_{ref} (K) | 273 |
| Ref. viscosity: μ_{ref} ($\text{Pa} \cdot s$) | 1.656×10^{-5} |
| DSMC specific parameters | |
| Rotational degrees of freedom: ζ_R ($-$) | 2 |
| Rotational relaxation: Z_R ($-$) | 1/2 |
| Vibrational degrees of freedom: ζ_V ($-$) | 2 |
| Vibrational relaxation Z_V ($-$) | $(1.90114 \times 10^{-5})^{-1}$ |
| Vibrational temperature T_V (K) | 3371 |

4.11.2 Results and discussion

Figures 4.23 illustrate the contours of various flow properties for the flow around the solid chip/substrate. Ignoring the statistical noise, we observe excellent agreement between DSMC and DGFS. In particular, DGFS reproduces noise-free smooth results.

Next we compute the force acting on the substrate as a result of the temperature gradients initially present in the flow. In general, the pressure force on a surface is given by

$$F = - \int_{dA} p n dA \quad (4.12)$$

where n is the unit surface normal, p is the pressure on the surface, and A is the area of the surface.

Table 4.19. Numerical parameters for flow around micro-electronic chip.

| Parameters | MEC-01 |
|--|------------------------|
| Spatial elements | 190 quadrilaterals |
| DG order | 3 |
| Time stepping | Euler |
| Points in velocity mesh: N^3 | 24^3 |
| Points in radial direction ² : N_ρ | 6 |
| Points on <i>half</i> sphere ² : M | 6 |
| Size of velocity mesh ³ | $[-5, 5]^3$ |
| Characteristic length: H_0 (μm) | 3 |
| Characteristic velocity: u_0 (m/s) | 402.54 |
| Characteristic temperature: T_0 (K) | 273 |
| Characteristic no. density: n_0 (m^{-3}) | 4.894×10^{23} |
| Initial conditions | |
| Velocity: u (m/s) | 0 |
| Temperature: T (K) | 273 |
| Number density: n (m^{-3}) | 4.894×10^{23} |
| Knudsen number ¹ : (Kn) | 0.88158 |

Table 4.20. x -component of force on the substrate for MEC-01 case, obtained using DSMC and DGFS simulations.

| Pressure (Pa) | Kn | Force ($\mu N/\mu m$) | |
|---------------|---------|-------------------------|--------------|
| | | DSMC | DGFS |
| 2000 | 0.88158 | -0.040008843 | -0.040010413 |

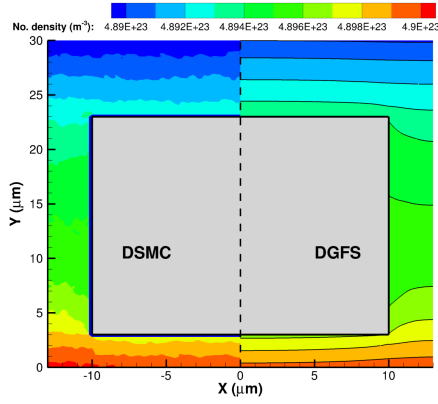
Table 4.20 presents the x -component of force on the substrate for the micro-electronic chip verification case. Again, we note reasonable agreement between the values recovered from DSMC and DGFS simulations.

4.12 Single-species: Flow in short microchannels

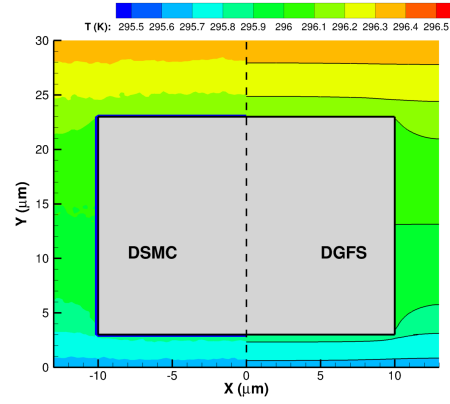
The present test case closely follows case-I(a) from Ref. [101]. In the current test case, two reservoirs filled with N_2 gas, at different temperatures, are connected by a two-dimensional capillary tube, both with a finite length L and height $H/2$, are considered. The problem schematic, geometry, as well as boundary conditions are shown in Figure 4.24. Case details have been provided in Tab. 4.21. Note in particular, we introduce a linearly decreasing temperature profile at the top wall. Previous studies for flow in short microchannels have been restricted to model kinetic equations [101]–[103] or moment methods [104]. To the best of our knowledge, an analysis of such a low-temperature flow hasn’t been carried out previously within a deterministic full Boltzmann framework.

4.12.1 Numerical details

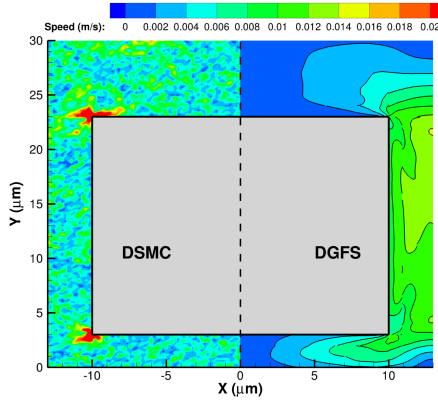
- **DSMC:** The no-time collision (NTC) algorithm is used in conjunction with Bird’s VHS scattering model. The simulations are first run for 500,000 unsteady steps wherein the particles move, collide, and allowed to equilibrate. Next, the simulation is run for another 100,000 steady steps wherein the samples of flow properties are taken. In the present case, the DSMC domain is discretized with a uniform cell size of $0.01\ \mu m$, with 30 particles per cell on average during initialization (Note that SPARTA uses hierarchical Cartesian grid over the simulation domain: used to track particles and to co-locate particles in the same grid cell for performing collision and chemistry operations. At the junction, where the walls join the inlet and outlet regions, one can identify two boundary cells. We further refine, specifically, these two boundary cells into 10×10 sub-cells. These two cells are unique i.e., for each of these cells, the top face is marked as inlet, and the left face is marked as solid wall. The cell-size has been made smaller



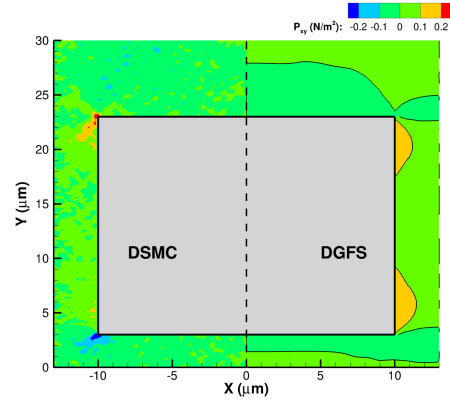
(a) Number density (m^{-3})



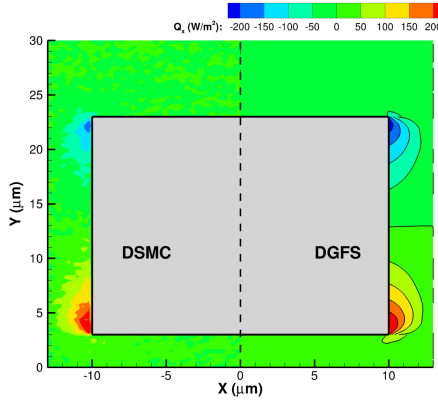
(b) Temperature (K)



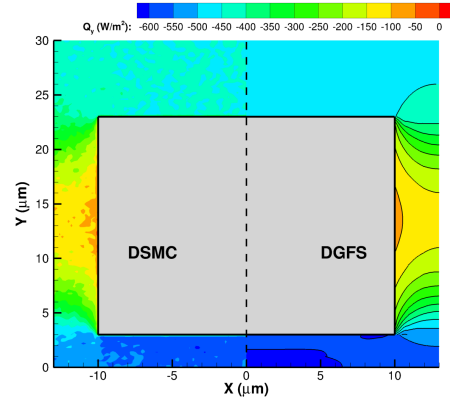
(c) Speed (m/s)



(d) xy -component of stress (N/m^2)

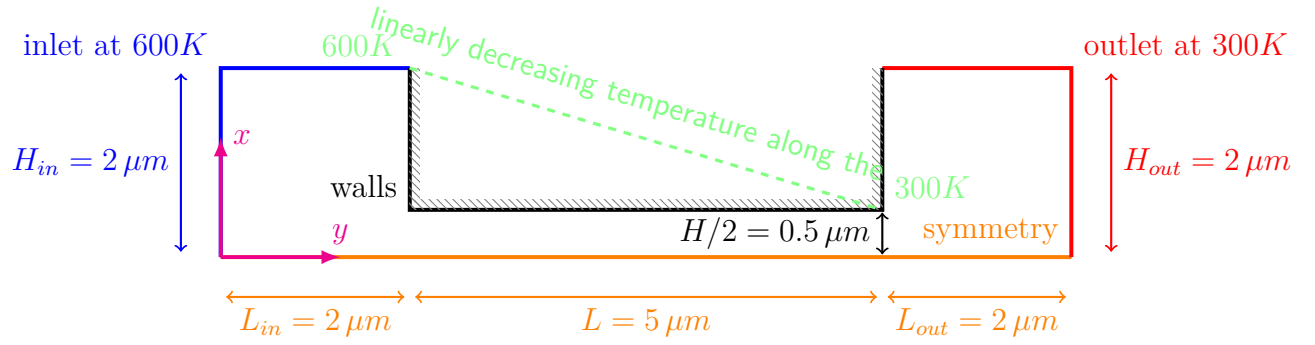


(e) x -component of heat-flux (W/m^2)

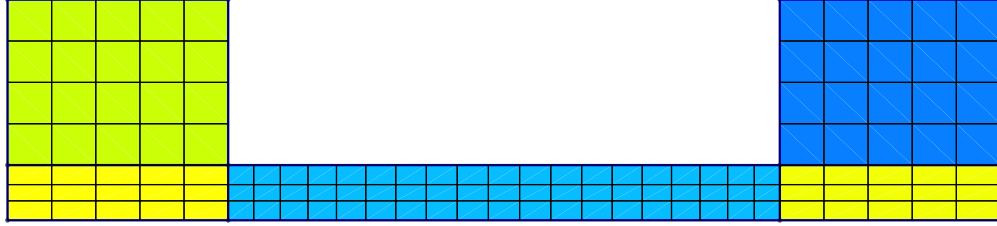


(f) y -component of heat-flux (W/m^2)

Figure 4.23. Flow properties at steady state for micro-electronic chip obtained from DSMC and DGFS using VHS collision model. For each of these figures, DSMC results (mirrored along y -axis) have been shown in the second quadrant ($-17 \mu m \leq x < 0 \mu m$), whereas DGFS results have been illustrated in the first quadrant ($0 \mu m \leq x < 17 \mu m$). Observe the legend for number-density.



(a) Schematic



(b) Mesh for DGFS simulations.

Figure 4.24. Numerical setup for the flow in short microchannels. On the horizontal channel walls, we impose a linearly decreasing temperature profile similar to case I(a) in Ref. [101].

to avoid any potential leakage). A time step of 10^{-10} sec is used. N_2 is (Tab. 4.18) used as the working gas in simulations. DSMC simulations on 32 cores of Intel(R) Xeon(R) CPU E5-2670 v2 2.50GHz, took ~ 74.67 hours..

- **DGFS:** The spatial domain consists of 127 non-uniform quadrilateral elements as shown in Fig. (4.24b). Case specific DGFS parameters have been provided in Tab. 4.21. DGFS simulations on 2 Nvidia-P100 GPUs took ~ 8 hour 31 minutes.

Table 4.21. Numerical parameters for flow in short microchannels.

| Parameters | SM-01 |
|--|-----------------------|
| Spatial elements | 127 quadrilaterals |
| DG order | 3 |
| Time stepping | Euler |
| Points in velocity mesh: N^3 | 32^3 |
| Points in radial direction ² : N_ρ | 8 |
| Points on <i>half</i> sphere ² : M | 6 |
| Size of velocity mesh ³ | $[-5.72, 5.72]^3$ |
| Characteristic length: H_0 (μm) | 1 |
| Characteristic velocity: u_0 (m/s) | 421.98 |
| Characteristic temperature: T_0 (K) | 300 |
| Characteristic no. density: n_0 (m^{-3}) | 6.62×10^{24} |
| Initial conditions | |
| Velocity: u (m/s) | 0 |
| Temperature: T (K) | 300 |
| Number density: n (m^{-3}) | 6.62×10^{24} |
| Knudsen number ¹ : (Kn) | 0.2 |
| Inlet condition | |
| Velocity: u_{in} (m/s) | 0 |
| Temperature: T_{in} (K) | 600 |
| Number density: n_{in} (m^{-3}) | 3.31×10^{24} |
| Pressure: p_{in} (N/m) | 27420 |
| Outlet condition | |
| Velocity: u_{out} (m/s) | 0 |
| Temperature: T_{out} (K) | 300 |
| Number density: n_{out} (m^{-3}) | 6.62×10^{24} |
| Pressure: p_{out} (N/m) | 27420 |

4.12.2 Results and discussion

Figures 4.26 illustrate the contours of various flow properties for the flow around the solid chip/substrate. Ignoring the statistical noise, we gain note excellent agreement between DSMC and DGFS. In particular, minor differences in x -component of heat-flux i.e., Q_x can be attributed to the fact that DSMC simulations consider rotational degrees-of-freedom of N_2 into account, whereas DGFS doesn't.

Figures 4.25 shows the variation of flow properties over the vertical centerline, wherein we again observe an excellent agreement.

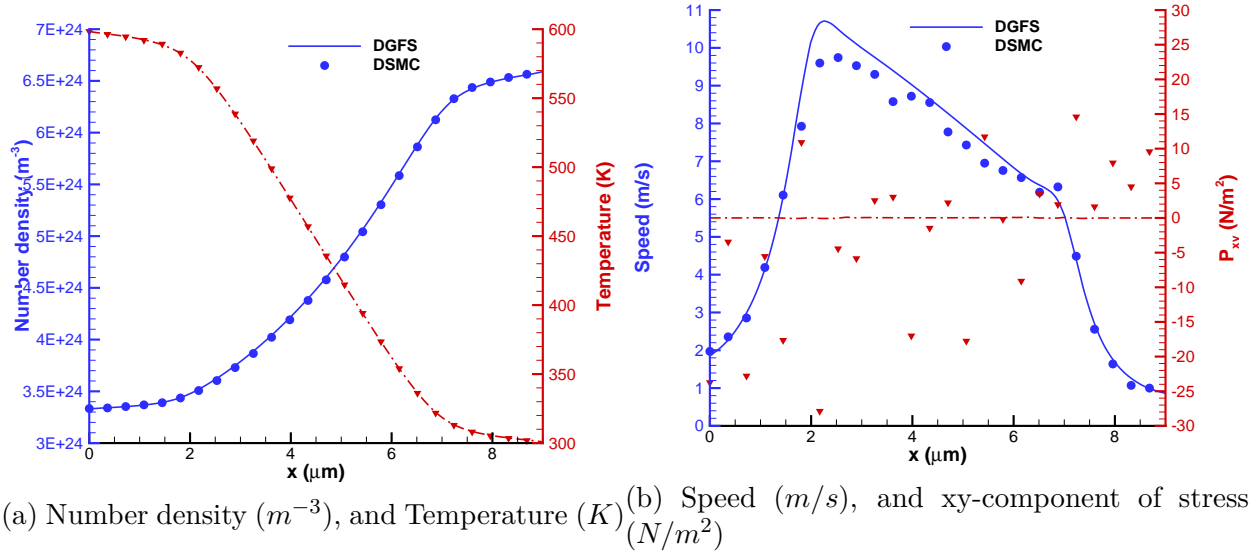


Figure 4.25. Flow properties on the horizontal centerline ($y = 0 \mu m$) for short microchannel test-case obtained from DSMC and DGFS using VHS collision model.

4.13 Single-species: Lid-driven cavity flow

As a 3D example, we consider the standard lid driven cavity flow. Consider a cube of length $H = 1 \times 10^{-3}$ meters. All the walls are kept at temperature of $T = 273K$. At the top wall xy -plane, a velocity of $u = (50, 0, 0) m/s$ is introduced. The Knudsen number is fixed at $Kn = 0.1$ and $Kn = 1$. Forward euler scheme is used for time evolution. The velocity space $[-6, 6]^3$ is discretized using $N^3 = 32^3$ points, $N_r = 6$ points in the radial

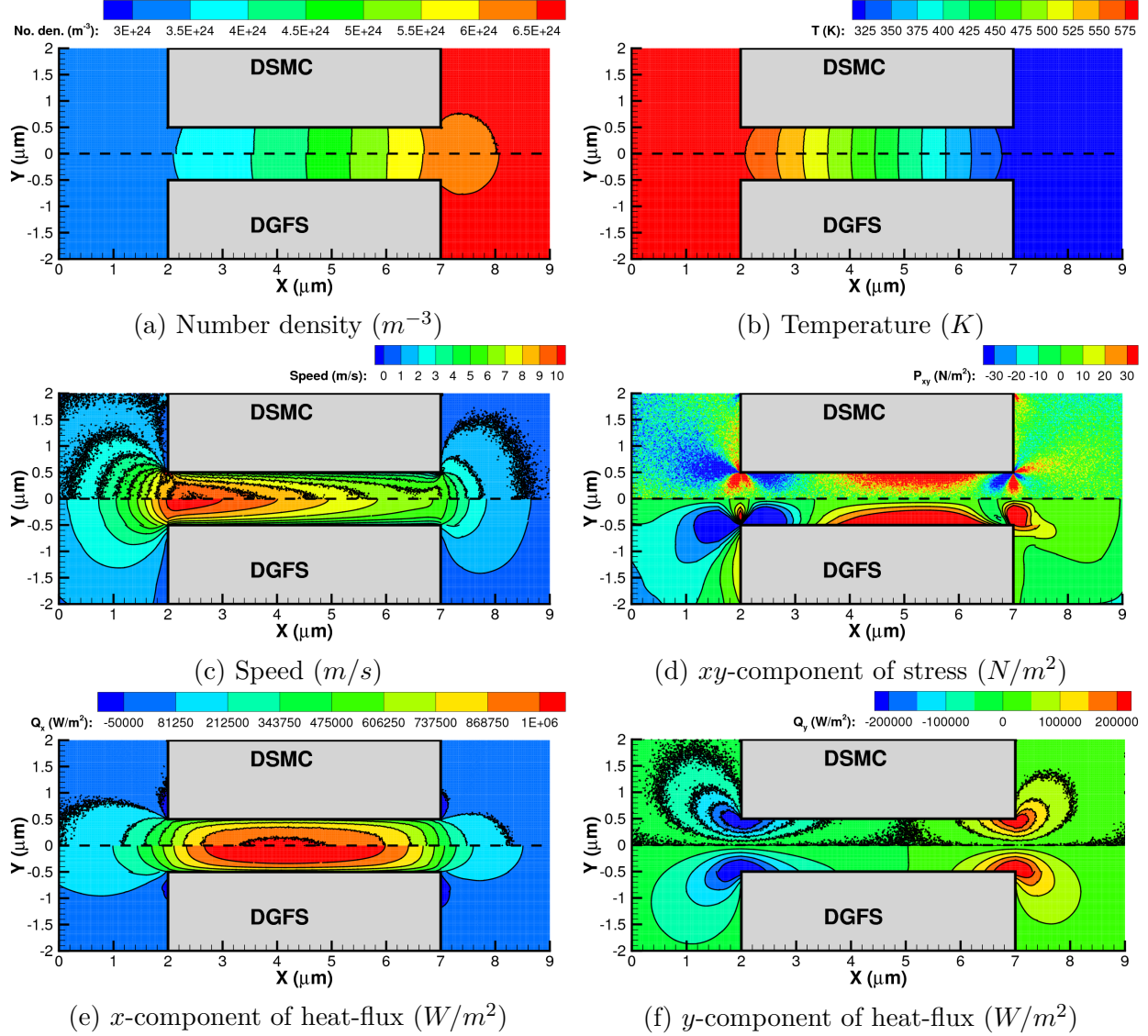


Figure 4.26. Flow properties for short microchannel test-case obtained from DSMC and DGFS using VHS collision model. For each of these figures, DSMC results have been shown in the first quadrant ($0 \mu m \leq y < 2 \mu m$), whereas DGFS results (mirrored along x -axis) have been illustrated in the fourth quadrant ($-2 \mu m \leq y < 0 \mu m$). Differences in Q_x can be attributed to the fact that DSMC simulations consider rotational degrees-of-freedom of N_2 into account, whereas DGFS doesn't.

direction and $M = 6$ points on half sphere. A convergence criterion of $(\|f^{n+1} - f^n\|/\|f^n\|_{L_2}) / (\|f^2 - f^1\|/\|f^1\|_{L_2}) < 1 \times 10^{-5}$ has been used.

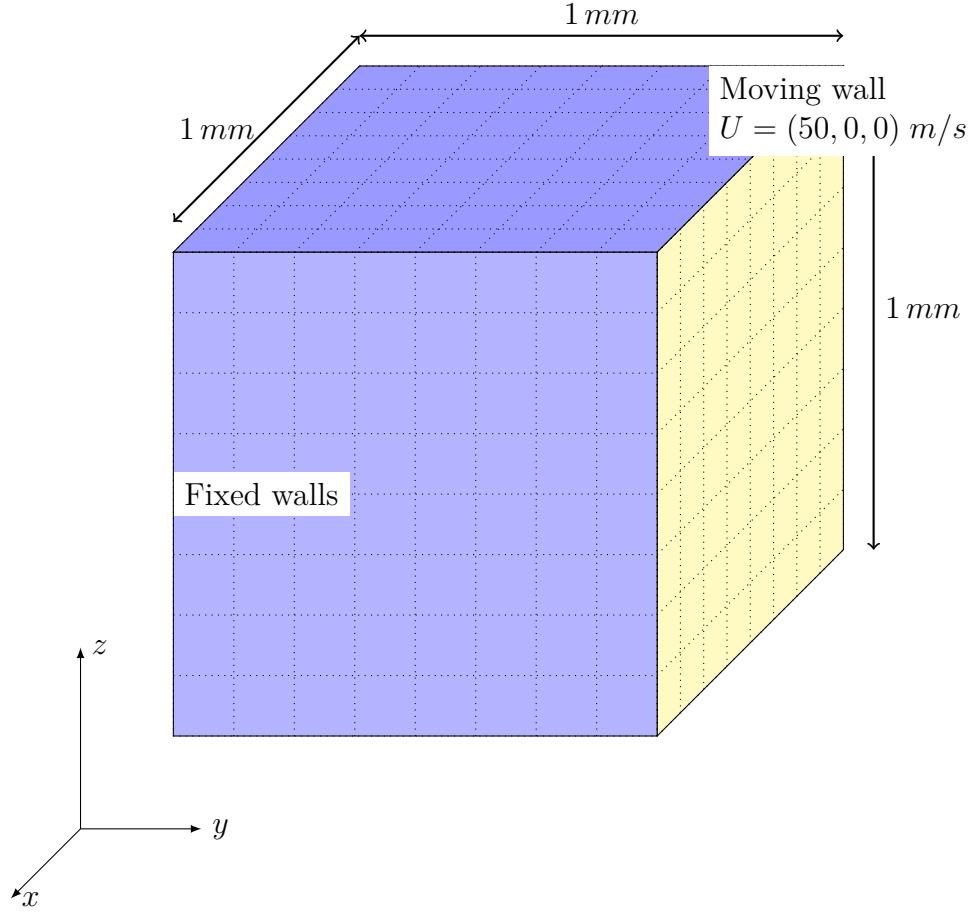


Figure 4.27. Numerical setup for 3-D lid driven cavity flow.

Figures 4.28 shows the comparison of residual for different mesh sizes in physical and velocity spaces at $\text{Kn} = 0.1$ and $\text{Kn} = 1$. This shows that all the cases have converged.

Figures 4.29 illustrate the comparison of flow properties between DSMC and DGFS on body diagonal of the cube for different mesh sizes at $\text{Kn} = 0.1$. Figures 4.31 show the analogous result for $\text{Kn} = 1$. From these results, the combination $4^3, 32^3$ appears suitable.

Fig (4.30) depicts the flow properties on the 3-D volume. DGFS results are recovered using 8^3 elements in physical space and 32^3 points in the velocity space. Figures 4.32 show the

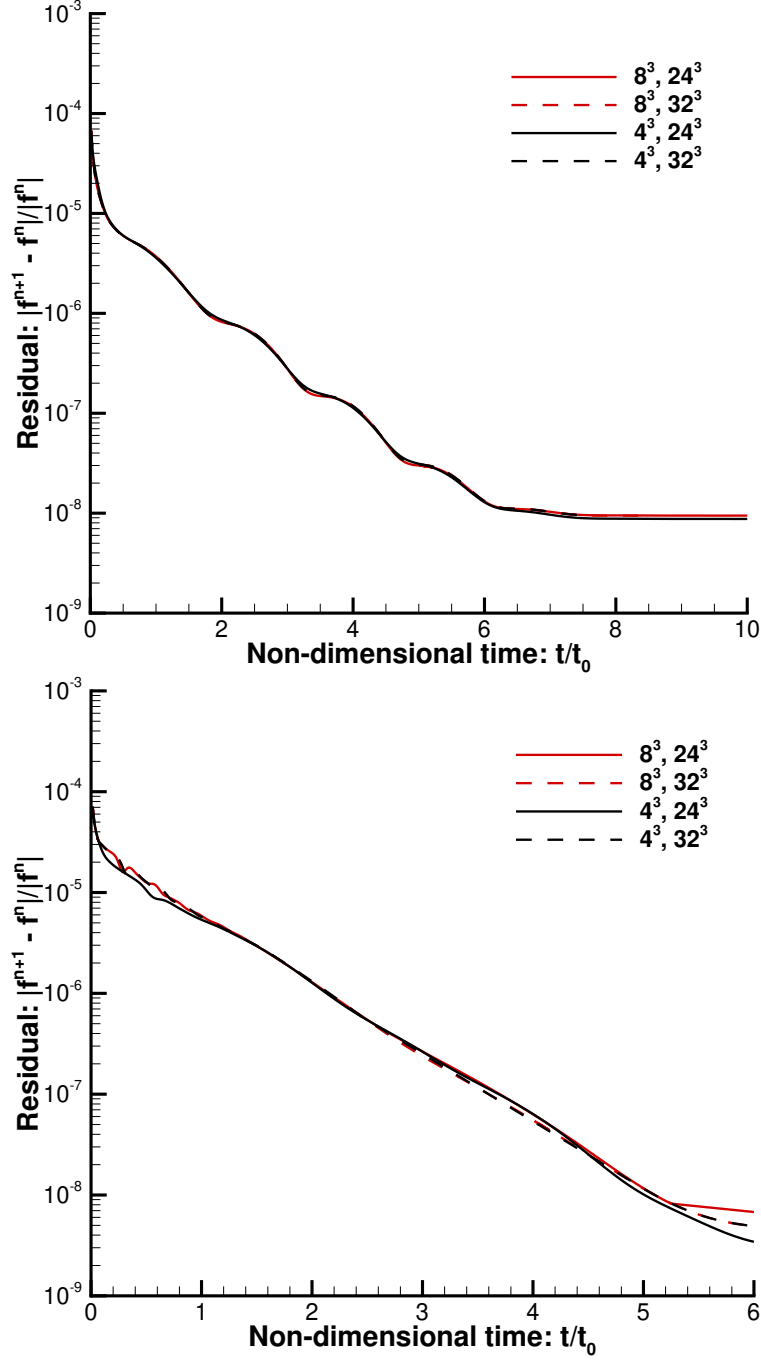


Figure 4.28. Residual history: $\|f^{n+1} - f^n\| / \|f^n\|_{L_2}$ for different mesh sizes in physical and velocity spaces: (top) $\text{Kn} = 0.1$, (bottom) $\text{Kn} = 1$. The plot legend is defined using notation N_e^3, N^3 , where N_e refers to number of elements in each direction of physical space, and N refers to number of points in each direction of velocity space.

analogous result for $\text{Kn} = 1$. From these results, ignoring the statistical fluctuations, one can infer that DGFS results match well with DSMC.

At $\text{Kn} = 0.1$, DSMC simulations on 32 cores of Intel Xeon Silver 4114 CPU 2.20GHz, for 550000 steps took 24 hours. DGFS simulations were run on 2 Nvidia-P100 GPUs. For 133,000 steps, the simulation with 4^3 spatial grid and 24^3 velocity grid took 15 hours; 4^3 spatial grid and 32^3 velocity grid took 191 hours; 8^3 spatial grid and 24^3 velocity grid took 91 hours; 8^3 spatial grid and 32^3 velocity grid took 206 hours.

At $\text{Kn} = 1$, DSMC simulations on 32 cores of Intel Xeon Silver 4114 CPU 2.20GHz, took 24 hours. DGFS simulations were run on 2 Nvidia-P100 GPUs. For 40,000 steps, the simulation with 4^3 spatial grid and 24^3 velocity grid took 5.8 hours; 4^3 spatial grid and 32^3 velocity grid took 27.4 hours; 8^3 spatial grid and 24^3 velocity grid took 57.2 hours; 8^3 spatial grid and 32^3 velocity grid took 85.6 hours.

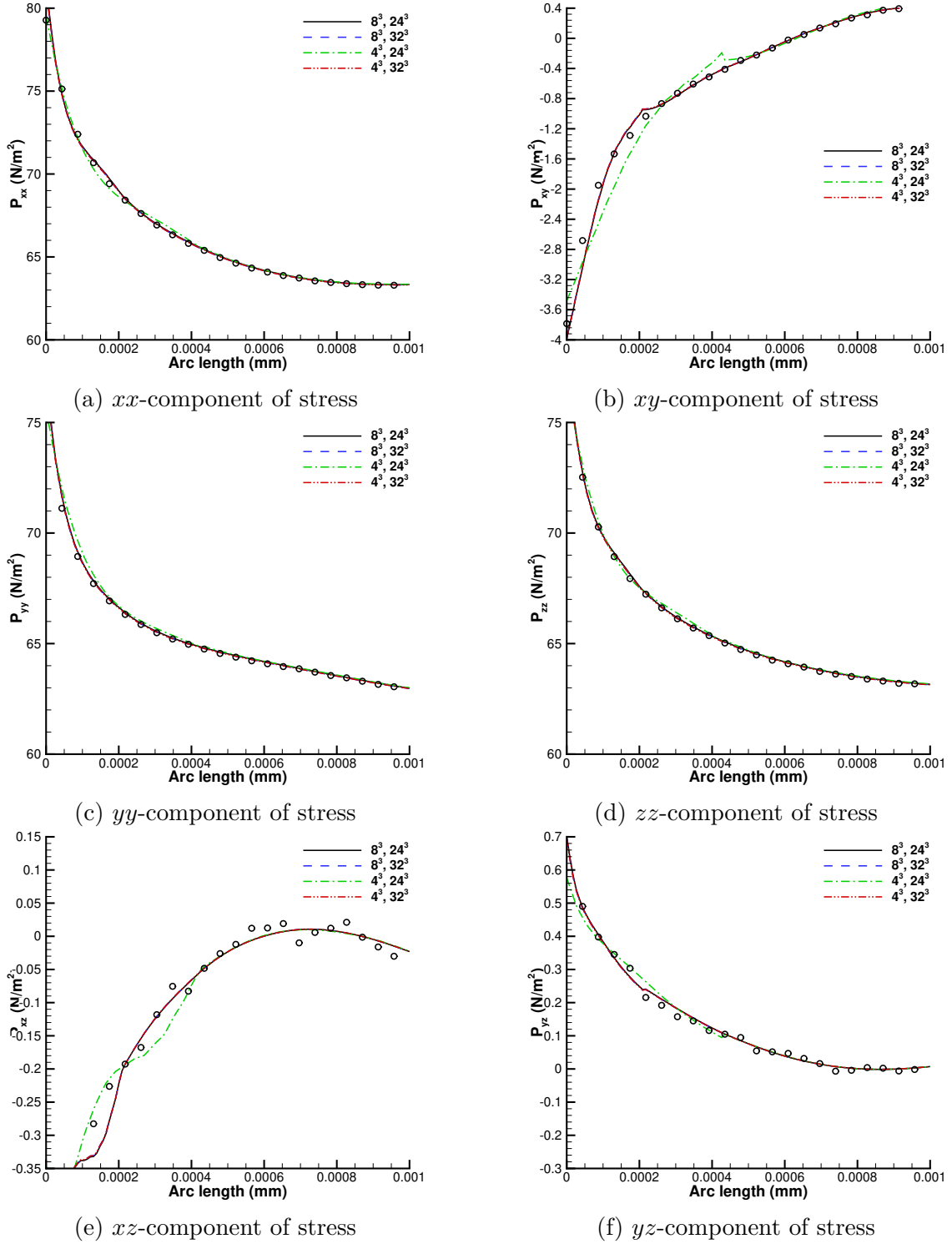
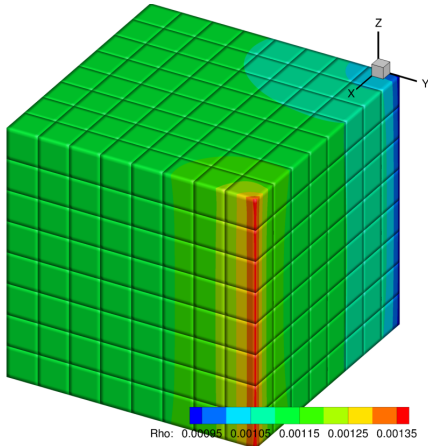
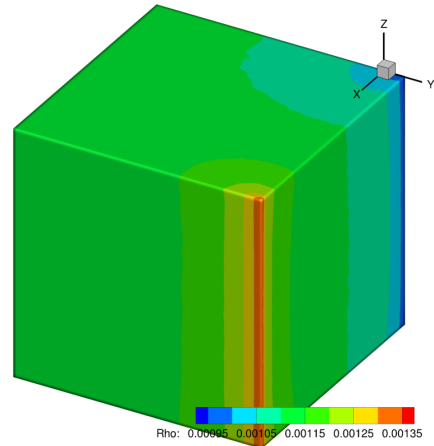


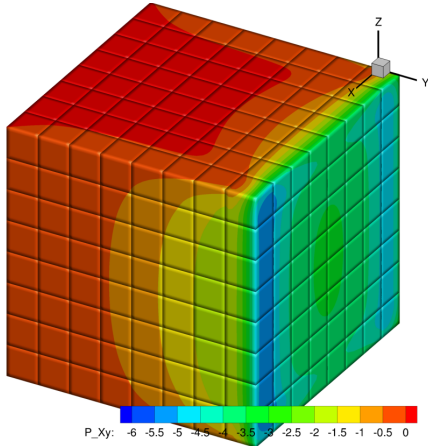
Figure 4.29. Variation of shear-stresses on body-diagonals for lid-driven cavity flow at $\text{Kn} = 0.1$. Symbols denote DSMC results, dashed lines denote DGFS solutions on diagonal $(10^{-3}, 10^{-3}, 0) - (0, 0, 10^{-3})$.



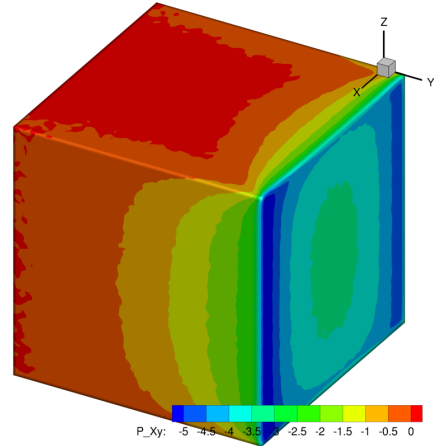
(a) DGFS: Density (kg/m^3)



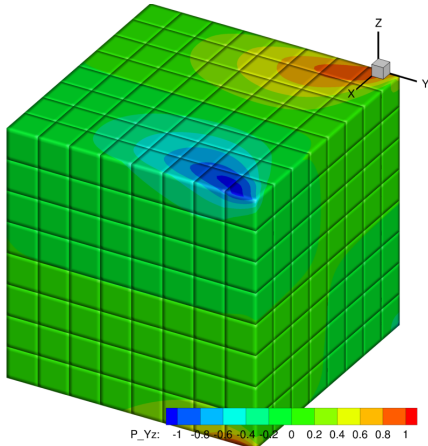
(b) DSMC: Density (kg/m^3)



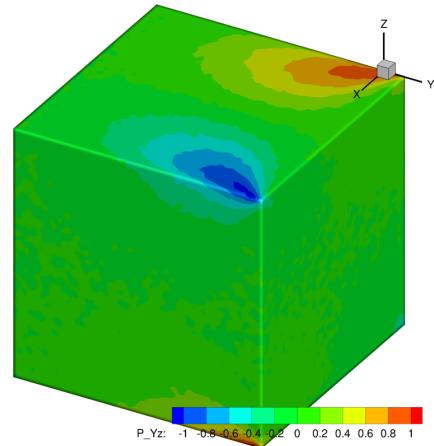
(c) DGFS: xy -component of stress (N/m^2)



(d) DSMC: xy -component of stress (N/m^2)

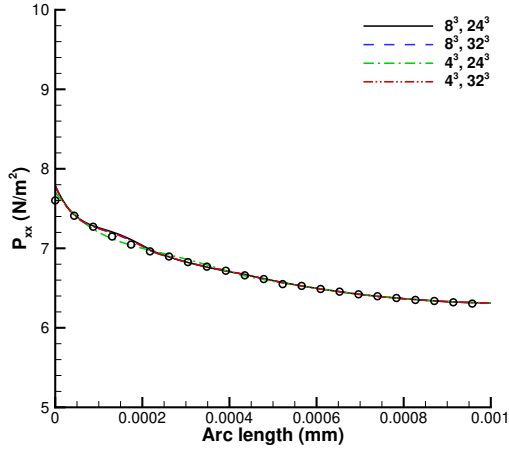


(e) DGFS: yz -component of stress (N/m^2)

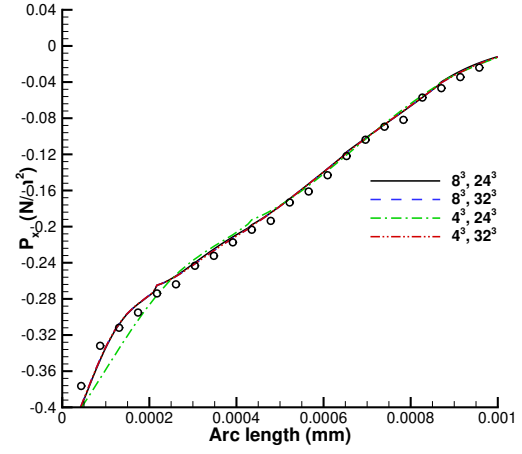


(f) DSMC: yz -component of stress (N/m^2)

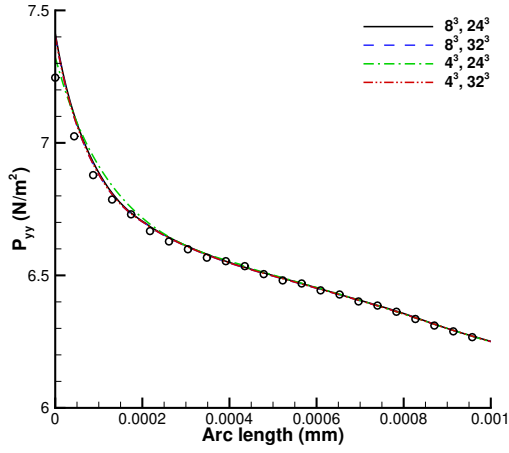
Figure 4.30. Variation of flow properties for lid-driven cavity flow at $Kn = 0.1$ from DGFS.



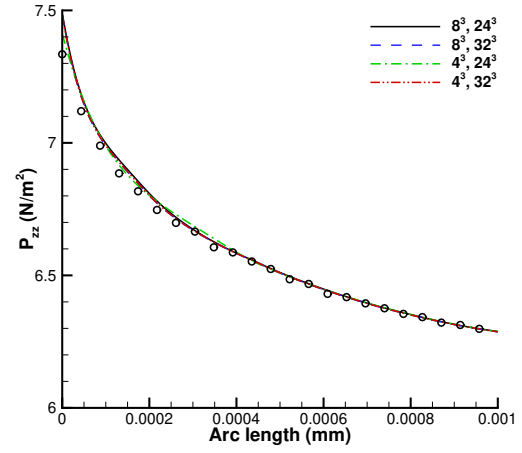
(a) xx -component of stress



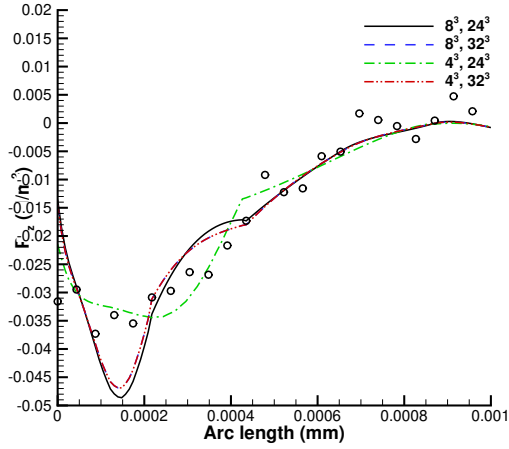
(b) xy -component of stress



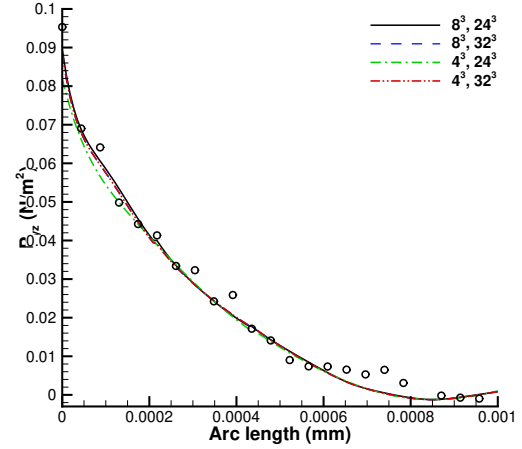
(c) yy -component of stress



(d) zz -component of stress

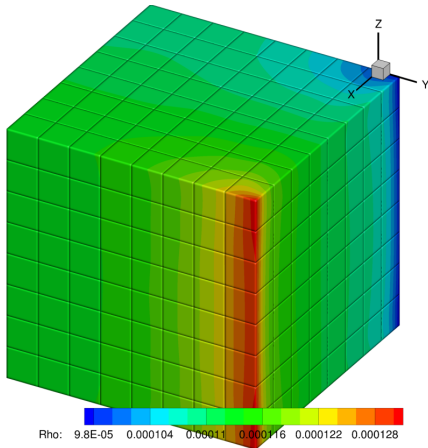


(e) xz -component of stress

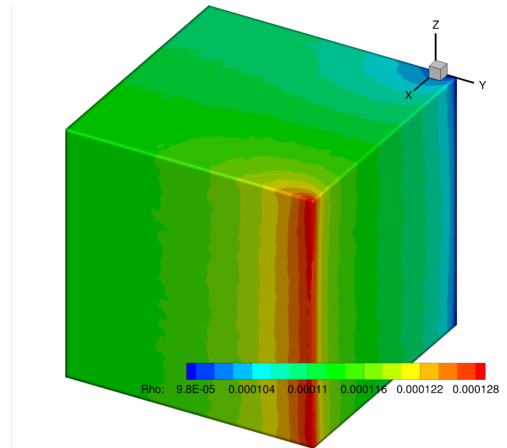


(f) yz -component of stress

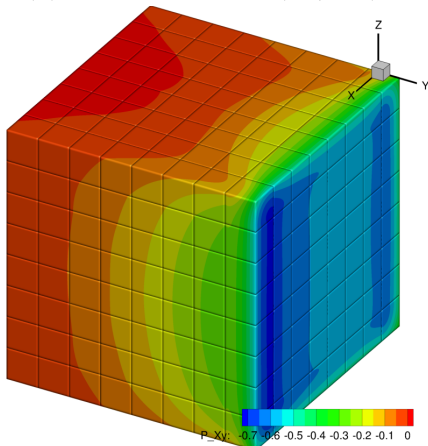
Figure 4.31. Variation of shear-stresses on body-diagonals for lid-driven cavity flow at $\text{Kn} = 1$. Symbols denote DSMC results, dashed lines denote DGFS solutions on diagonal $(10^{-3}, 10^{-3}, 0) - (0, 0, 10^{-3})$.



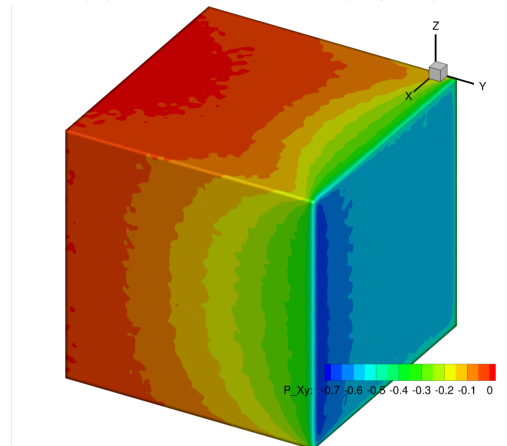
(a) DGFS: Density (kg/m^3)



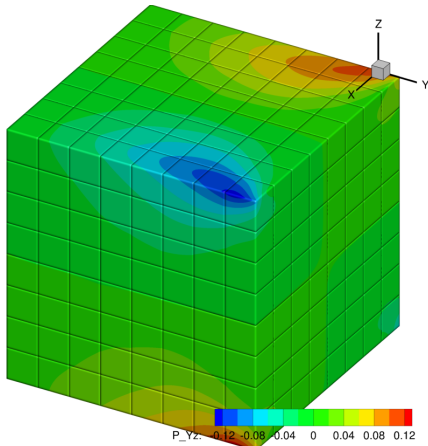
(b) DSMC: Density (kg/m^3)



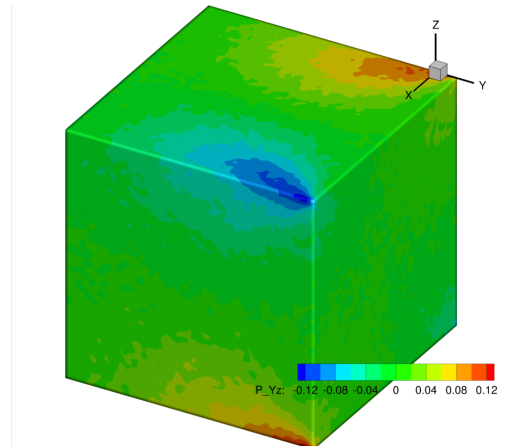
(c) DGFS: xy -component of stress (N/m^2)



(d) DSMC: xy -component of stress (N/m^2)



(e) DGFS: yz -component of stress (N/m^2)



(f) DSMC: yz -component of stress (N/m^2)

Figure 4.32. Variation of flow properties for lid-driven cavity flow at $Kn = 1$ from DGFS.

5. APPLICATION: QUANTIFICATION OF THERMALLY DRIVEN FLOWS IN MICROSYSTEMS

Feynman [105], on 29th December 1960 at the Annual meeting of the American Physical Society, in his talk titled *There's plenty of room at the bottom*, envisioned a future of micro-devices wherein the miniaturization would be potentially achieved via evaporation and itching process. Almost 60 years later, the idea forms an essential element for manufacturing of MEMS devices. How do study the flows in microsystems, wherein the flow is too slow for DSMC to be effective, and the Navier-Stokes too inaccurate to predict the rich structure within?

5.1 Background and motivation

In microscale flows, the length scale dictates the type of forces governing the physical phenomena. The surface to the volume ratio is high and hence the surface forces dominate. The Reynolds number is low and the viscous shear stresses are significantly increased [106]. Under sufficiently rarefied flow conditions, an application of temperature gradient, say, between two parallel plates separated by few mean free paths, induces a low velocity gas flow commonly identified as thermo-stress convection effects [39]. A necessary condition to induce a sufficiently *useful* gaseous velocity requires the characteristic length scale of the thermal gradients $T/|\nabla_x T|$ to be comparable to the molecular mean free path λ . At macroscale, such magnitudes are prohibitive, necessitating thermal gradients on the order of $10^6 K/m$. However, at microscale, such conditions are readily achieved allowing the thermo-stress effects to overcome the classically dominant viscous forces [43].

From a historical and experimental viewpoint, Knudsen, in 1910, explored the possibility of gas actuation under the influence of temperature gradients using evacuated glass bulbs separated by a long narrow tube, wherein heating one of the bulbs resulted in a pumping action creating a high pressure at the hot end and low pressure at the cold end [107], [108]. In 1950's [109], Knudsen carried out various experiments using Crooke's radiometer [40],

wherein a device consisting of a long thin and narrow platinum band with dark (hot) and bright (cold) sides, in a rarefied environment, exhibits a net force due to momentum imbalance of particles reflecting from the dark and bright sides. Without being exhaustive, we refer to (Ref. [110]) for a comprehensive review of the radiometric phenomenon. From a theoretical viewpoint, Maxwell hypothesized that one of the possible causes of radiometric effects are temperature stresses. However, based on linearized kinetic theory and corresponding reduced macroscopic equations of motion (see section 15 in Ref. [111]), the author concluded that no motion can be produced by temperature stresses [39], [111], which, in general, is incorrect. Later, Kogan, in 1976, introduced the theory of thermo-stress convection, wherein the bulk velocity is attributed to presence of higher order terms of temperature stresses (see eq. 2.6 in Ref. [39]), arrived in part by the second order Chapman-Enskog expansion commonly identified as the Burnett approximations. In the multi-species context, however, the phenomenon and the effect of thermo-stress convection on the flow concentration (and the subsequent induced velocity) is more apparent.

Chapman [5], as early as 1953, developed the theory of diffusion processes (see eq. (8.4, 7) in Ref. [5] again derived using Chapman-Enskog expansion) wherein the difference in concentrations of two species is proportional to the thermal gradient term $k_T \nabla \ln T$, where k_T is thermal diffusion factor. At normal conditions, this coefficient is very low, and is therefore not accounted in practice. For instance, as a classical example, Bird [24] devised a self-diffusion test case (see section 12.6) where the diffusion coefficient was measured by ignoring the thermal gradient term $k_T \nabla \ln T$ of eq. (8.4, 7) in Ref. [5]. Note however that there is considerable thermal gradient in self-diffusion cases, see for instance Ref. [89], where we presented the results for temperature variation for self diffusion cases. Although the temperature gradient is unaccounted for, the diffusion coefficient, which is measured by a self diffusion simulation, matches well with the experimentally [5] observed diffusion coefficient. This suggests that k_T is potentially low — which is indeed the case, for instance, see Ref [93], wherein the authors noted thermal diffusion coefficient on order of 10^{-3} . In microscale flows where the per unit temperature drop can easily reach $10^6 K/m$, as noted earlier, $k_T \nabla \ln T$ can have appreciable contributions. This type of process has been interpreted in terms of

thermo-stress convection due to concentration inhomogeneities by Kogan [39]. The overall thermo-stress convection phenomenon/effect is highly coupled and exhibits highly rich flow structures (as will be shown in the following section), and an in-depth understanding can prove to be very useful for development of next generation of microsystems.

To summarize, Sone [112] identified three broad groups of the temperature driven flow based on its application in microsystems: a) thermal creep flow [113]–[115] which is an induced flow around a body with non uniform temperature; b) thermal stress slip flow, which is induced by nonuniform temperature gradient over the boundary [39], [116]–[121]; c) and nonlinear thermal stress flow [39], which is important only when the temperature gradient in the gas is high, and nonlinear terms of temperature variations in stress tensor should be taken into account. The present study is delegated to the third i.e., nonlinear thermal stress flow.

From a practical engineering viewpoint, thermo-stress convection has been applied for micro-structure actuation. Passian [122], [123], in 2003, demonstrated a micro-cantilever suspended over a substrate, which when heated via a pulsed laser generated deflections at the cantilever tip as a consequence of the Knudsen forces in the gap between the substrate and micro-cantilever. Foroutan [124], in 2014, demonstrated untethered levitation in concave micro-flying robots relying on Knudsen force. The phenomenon has been further explored in small satellite and spacecraft attitude control devices [125] and high-altitude propulsion systems [126].

In the present work, we assess the thermo-stress convection process using the fundamental microscopic full Boltzmann equation. Due to the stochastic nature of the DSMC that introduces high statistical noise in low-speed flows. Therefore, we study the thermo-stress convection process using the proposed deterministic discontinuous Galerkin fast spectral (DGFS) method [32], [89] as well as DSMC: the primary tool for rarefied flow simulations. DGFS allows arbitrary unstructured geometries; high order accuracy in physical space time, and velocity space; arbitrary collision kernels, including, the well known VSS model [89]; and provides excellent nearly-linear scaling characteristics on massively parallel architec-

tures [100], [127]. DGFS produces noise-free solutions and can simulate low-speed flows encountered in thermo-stress convection dominated devices.

From a flow modelling viewpoint, Loyalka [128], using a linearized Boltzmann equation, calculated the longitudinal and transversal Knudsen forces on the cylindrical surfaces of a hanging wire of a vacuum micro-balance. The authors noted Knudsen force maximum in the transitional regime for Helium—an observation attributed to the bimodal nature of radiometric forces [129]. Fierro [130] studied the problem using a Bhatnagar-Gross-Krook (BGK) model for range of Knudsen numbers and different molecular species noting an inverted parabolic profile for variation of Knudsen force with pressure (which can be reinterpreted in terms of Knudsen number since a fixed size geometry was used for all cases). The authors observed a peak Knudsen force in $10 - 100 \text{ N/m}^2$ pressure range for Helium, Krypton, Hydrogen, Oxygen, and Carbon dioxide. Alexeenko [131] carried out numerical simulations around heated micro-beams using the conventional Navier-Stokes incorporating first order Maxwell slip and Smoluchowski temperature jump boundary conditions, DSMC, and primarily using a deterministic kinetic ellipsoidal statistical Bhatnagar-Gross-Krook (ESBGK) model employing a finite-difference-discrete-velocity scheme. The gas-damping coefficients on a moving micro-beam for quasi-static isothermal conditions were estimated by the three numerical methods for Knudsen numbers from 0.1 to 1.0. It was concluded that the Navier-stokes simulations overestimate the gas-damping force for Knudsen numbers larger than 0.1, while the ESBGK and DSMC methods are in good agreement for the slip and transitional flow regimes. Moreover, the Knudsen force peaks in the transitional regime at $\text{Kn} \approx 2$, and the numerically predicted variation of the force is consistent with experimental observations of the displacement of a heated micro-beam. Zhu [132] analyzed the problem specifically using DSMC in the slip, transition, and free molecular regimes noting *qualitative* agreements between DSMC and experimental results of Passian [122], [123]. Nabeth [133] analyzed the problem using the ESBGK model within a finite volume framework. Notably, the authors devised a semi-empirical relation between the force and the Knudsen number based on dynamic similarity. Anikin [134] studied the radiometric forces via a direct solution of Boltzmann equation on 2-D velocity grids via a discrete ordinate projection method [135].

More recently, Lotfian [136] analyzed the various arrangements for radiometric pumps featuring vane and ratchet structures, including, zigzag triangular fins, using DSMC and finite volume based BGK-Shakhov model.

In more complex scenarios, one can stack an array of micro-heaters to significantly enhance the Knudsen force output [41]–[43]. Strongrich [42] demonstrated the possibility of amplifying the Knudsen forces as well as reversing its direction by combining thermal gradients between several solid bodies. The idea was further explored, resulting in development of a Microscale In-Plane Knudsen Radiometric Actuator (MIKRA) sensor for flow actuation and measurement [43]–[45]. MIKRA consists of array of hot and cold micro-beams termed as heater and shuttle arm. When the heater arm is heated under the application of electric current, the Knudsen force is generated in the gap between the shuttle and heater arm. The displacement of shuttle arm is then measured using a capacitor (specific details to follow in next section). MIKRA presents an interesting problem for analyzing thermostress convection due to temperature gradients as well as concentration inhomogeneties, see Ref. [137] where authors observed species separation in MIKRA which *might* be, in part, due to be the effect of $k_T \nabla \ln T$ term. We believe it’s too early to make a definite conclusion on the topic.

A key question, and a subject of ongoing research is the following: How well can the kinetic equations/models, for instance, McCormack model [77], Lattice Boltzmann method (LBM) [138], Bhatnagar-Gross-Krook (BGK) [76], [78], [83], [139], [140], Ellipsoidal statistical Bhatnagar-Gross-Krook (ESBGK) [84], [141], BGK-Shakhov (S-model) [85], Unified Gas Kinetic Scheme (UGKS) [142], [143], Discontinuous Galerkin Fast Spectral (DGFS) [32], and direct simulation Monte Carlo (DSMC) [24], describe the thermo-stress convection process, including, their applicability regimes at wide range of rarefaction levels and temperature gradients, and required computational cost for reproducing the correct induced low speed velocity profile on a *common standard* benchmark problems such as MIKRA where the experimental results are readily available. As noted by Kogan [39], the overall thermo-stress convection process is *complicated* function of concentration, of mass-ratio, molecule-collision cross section, etc. An in-depth understanding of the overall thermo-stress convection process at the microscale may potentially prove useful for development of a series of new MEMS

devices without any moving parts (see, for instance, Refs. [44], [144]). This part of the thesis, in part, focuses on quantifying the fidelity of results recovered from BGK, ESBGK, S-model, DGFS and DSMC for the Knudsen radiometric actuator MIKRA. To the best of our knowledge, analysis of single/multi-species complex flows such as MIKRA hasn't been carried out using deterministic full Boltzmann.

Finally, we mention that there is another class of low-speed gas flow problems which appears within the context of gas damping [145], [146]: an effect generally observed in radio frequency (RF) switches [147] which are used in radar systems, wireless communication systems, and other instrumentation fields. Gas damping sharply influences the dynamic behavior of MEMS devices, including, mechanical quality factors of microfabricated resonators, switching time, impact velocity, and bounceback of contacting MEMS [148]. A commonly identified trade-off in gas damping is as follows: the gas damping must be minimized to achieve high sensitivity of MEMS, such as resonators; and it must be maximized to mitigate the shock response and transient performance of MEMS. This is yet another class of problems where the fidelity of different modelling approaches, in particular, the deterministic ones, can be tested.

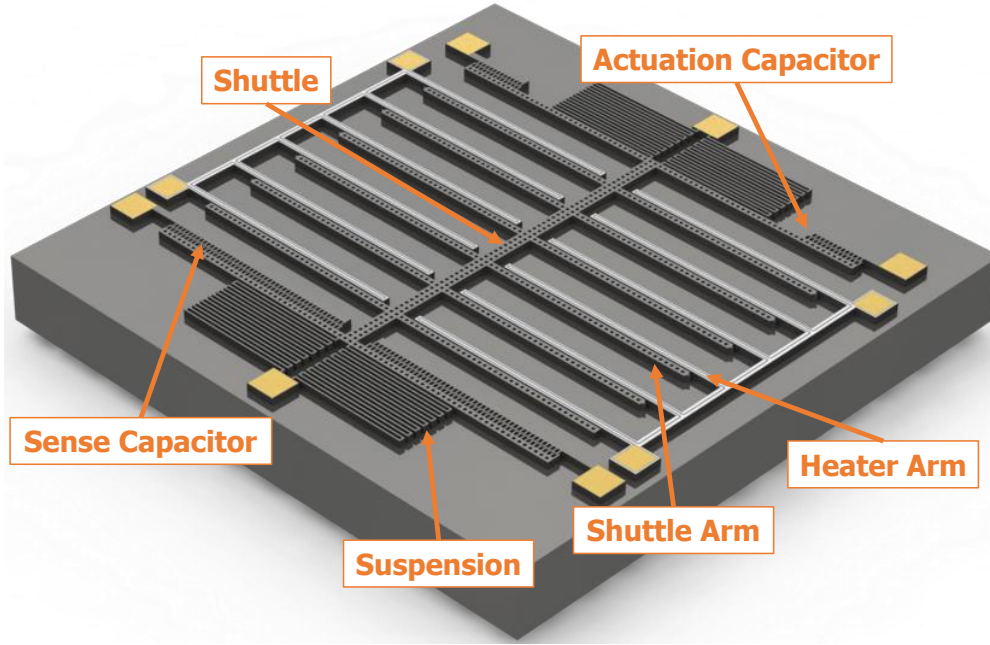


Figure 5.1. The CAD model for Gen1 Micro In-Plane Knudsen Radiometric Actuator (MIKRA) [43].

5.2 MIKRA: Micro In-Plane Knudsen Radiometric Actuator

MIKRA, acronym for Micro In-Plane Knudsen Radiometric Actuator, is a microscale compact low-power pressure sensor. A CAD representation of the device has been illustrated in Fig. 5.1. Simply speaking, the device consists of an array of (twelve) microbeams labelled as *Shuttle Arm* and *Heater Arm* in Fig. 5.1. The heater arm is heated, and a thermal motion is induced in the gap between the heater and the shuttle. Subsequently, the shuttle arm experiences forces on order of few micro-newtons. This force is commonly identified as Knudsen force. Depending on the temperature of the heater, the shuttle gets displaced, and this displacement is measured capacitively. The magnitude of displacement is then used to estimate the ambient pressure. Specific details on MIKRA can be found in Refs. [43], [44], [137].

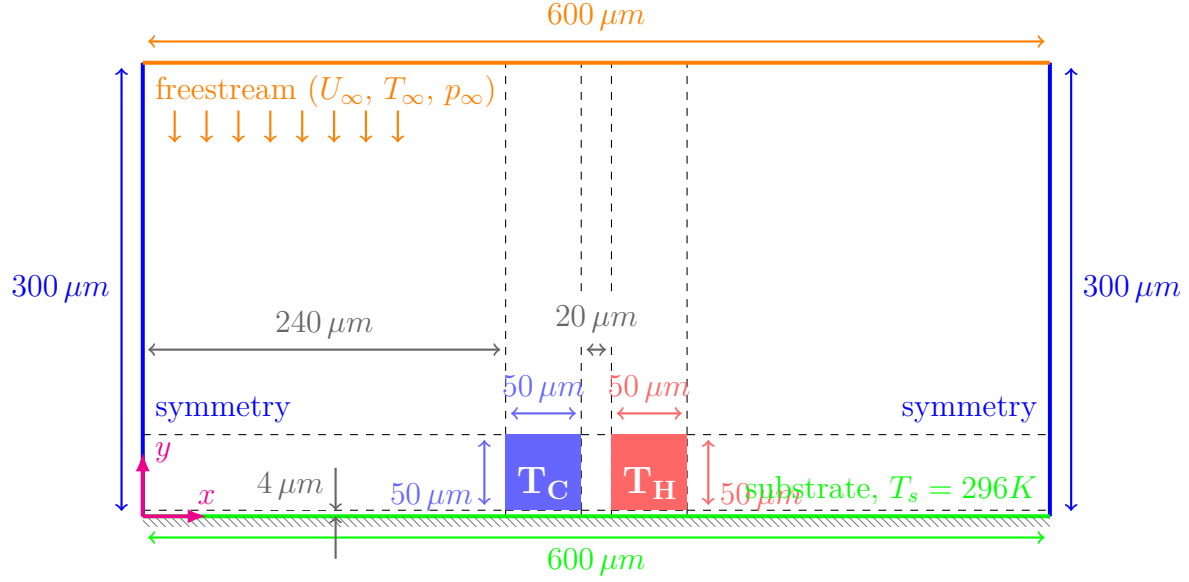


Figure 5.2. Schematic for numerical simulation of thermo-stress convection in MIKRA Gen1[43]. The interior dashed thin black lines indicate the blocks used for structured mesh generation. Specifically for deterministic DGFS simulations, a linear gradient is applied within blocks such that the cells are finer in the near-vane region.

5.2.1 Problem Statement

The flow configuration is shown in Fig. 5.2. Consider the 2D uniform flow of N_2 with freestream velocity U_∞ , freestream temperature T_∞ , and freestream pressure p_∞ over two two-dimensional square vanes, each with side lengths of $50\ \mu m$, separated by a gap of $20\ \mu m$ (also used as the nondimensionalizing length scale). The vanes are modeled as purely diffuse solid walls. The left vane, indicated in blue, is kept at a lower/cold temperature which we denote by T_C . The right vane, indicated in red, is kept at a higher/hot temperature which we denote by T_H . The substrate, indicated in green, forms the lower boundary of the domain, and is modelled as a purely diffuse solid wall. The end goal is to simulate the motion of gas flows in the gap between the two vanes, subject to different initial pressures p_∞ , hot (T_H) and cold (T_C) vane temperatures as listed in Tab. 5.1, in order to identify the correct circulation, induced low velocity, temperature gradient, and Knudsen forces from the vanes. The results are to be obtained from both stochastic (DSMC) and deterministic (DGFS) simulations.

Table 5.1. Numerical parameters for thermo-stress convection in MIKRA Gen1 simulations for DSMC and DGFS using VHS collision model for N_2 molecules.

| Parameter | Cases | | |
|--|-------------|-------------|-------------|
| | M-01 | M-02 | M-03 |
| Pressure: p (Torr) | 1.163 | 2.903 | 7.246 |
| Number density: n ($\times 10^{21} m^{-3}$) | 37.8609 | 94.5058 | 235.8901 |
| Knudsen number ¹ : Kn | 1.85 | 0.74 | 0.30 |
| Cold vane temperature: T_C (K) | 306 | 306 | 304 |
| Hot vane temperature: T_H (K) | 363 | 356 | 331 |
| DGFS parameters | | | |
| Points in velocity mesh: N^3 | 24^3 | 24^3 | 24^3 |
| Points in radial direction ² : N_ρ | 6 | 6 | 6 |
| Points on <i>half</i> sphere ² : M | 6 | 6 | 6 |
| Size of velocity mesh ³ | $[-5, 5]^3$ | $[-5, 5]^3$ | $[-5, 5]^3$ |
| BGK/ESBGK/S-model parameters | | | |
| Points in velocity mesh: N^3 | 48^3 | 24^3 | 24^3 |
| Size of velocity mesh ³ | $[-7, 7]^3$ | $[-5, 5]^3$ | $[-5, 5]^3$ |

5.2.2 Numerical details

The simulation is carried out at wide range of Knudsen number for flows in early slip to early free molecular regime. The simulation specific numerical parameters as well as differences between stochastic (DSMC) and deterministic (DGFS) modelling is described next.

- **DSMC:** SPARTA[19] has been employed for carrying out DSMC simulations in the present work. The simulations are first run for 200,000 unsteady steps wherein the particles move, collide, and allowed to equilibrate. No sampling is performed at this stage. Next, the simulation is run for another 5,000,000 steady steps wherein the samples of flow properties namely number density, flow velocity, temperature, stress, and heat-flux, are taken for sufficiently long time so as to produce a meaningful bulk properties as well as minimize the statistical noise therein. In the present case, the DSMC domain is discretized into 300×150 cells, resulting in a uniform cell size of $2 \mu m$, with 50 particles per cell on average during initialization. A time step of 10^{-9} sec is used during *move* step of DSMC algorithm throughout the course of simula-

tion. Note that these DSMC parameters have been taken from Ref. [43] wherein the authors performed multiple verification cases with different time-steps, grid-size, domain length, particles per cell, etc. N_2 is used as the working gas in simulations, since MIKRA experiments[43] were performed in N_2 medium. The properties of the working gas is given in Tab. 4.18. DSMC simulations treat N_2 as diatomic species, and takes rotational degrees of freedom into account.

- **DGFS:** We use the DGFS implementation described in Ref. [32]. The spatial domain consists of 849 elements (39×23 (total) - $2 \times 6 \times 4$ (remove the vane regions)). We use a linearly refined structured grid as illustrated in Fig. 5.3. While structured grids might seem inflexible compared to unstructured grids, they are known to produce more stable scheme with superior convergence rates[149], [150], are amenable to highly efficient adaptive h/p mesh refinement via recursive element splitting [151] (Nevertheless, DGFS is more general, and test cases on general grids will be reported in future works). Since we are seeking a steady state solution, the time-step is selected based on the CFL constraints of the forward Euler scheme. Other case specific DGFS parameters have been provided in Tab. 5.1.

It is worth noting that both the methods have different cell size requirements. In DSMC method, the contribution of particle collision to the transport properties is affected by strict spatial cell size requirements. In DGFS, however, the transport properties are strongly affected by local 3-D velocity space resolution rather than spatial resolution. As we show later, one can resolve the flow properties with fewer cells using DGFS.

5.2.3 Results and Discussion

Figures 5.4 and 5.5 illustrate the contour plot of various flow properties for the highest pressure case $Kn = 0.3$ (left column) and $Kn = 1.85$ (right column). For each of these plots, the DSMC and DGFS contours have been overlaid, wherein DSMC results have been indicated by thin black lines, and DGFS results have been indicated with thick red lines. Since the flow is strictly driven by temperature gradients, we expect very small deviation

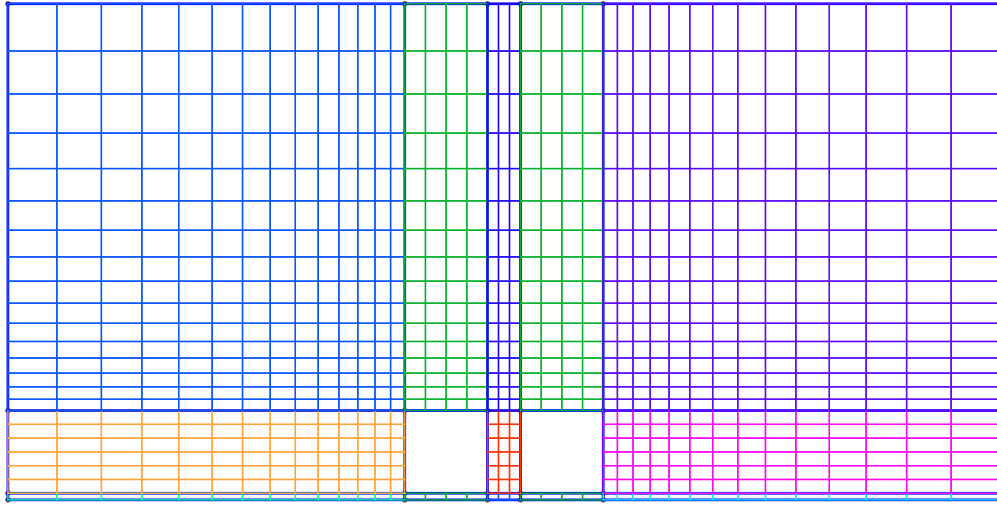


Figure 5.3. Spatial mesh used for carrying out DGFS simulations for MIKRA Gen1 device. A linear gradient is applied within blocks such that the cells are finer in the near-vane region. A 3rd order nodal/sem DG scheme has been used.

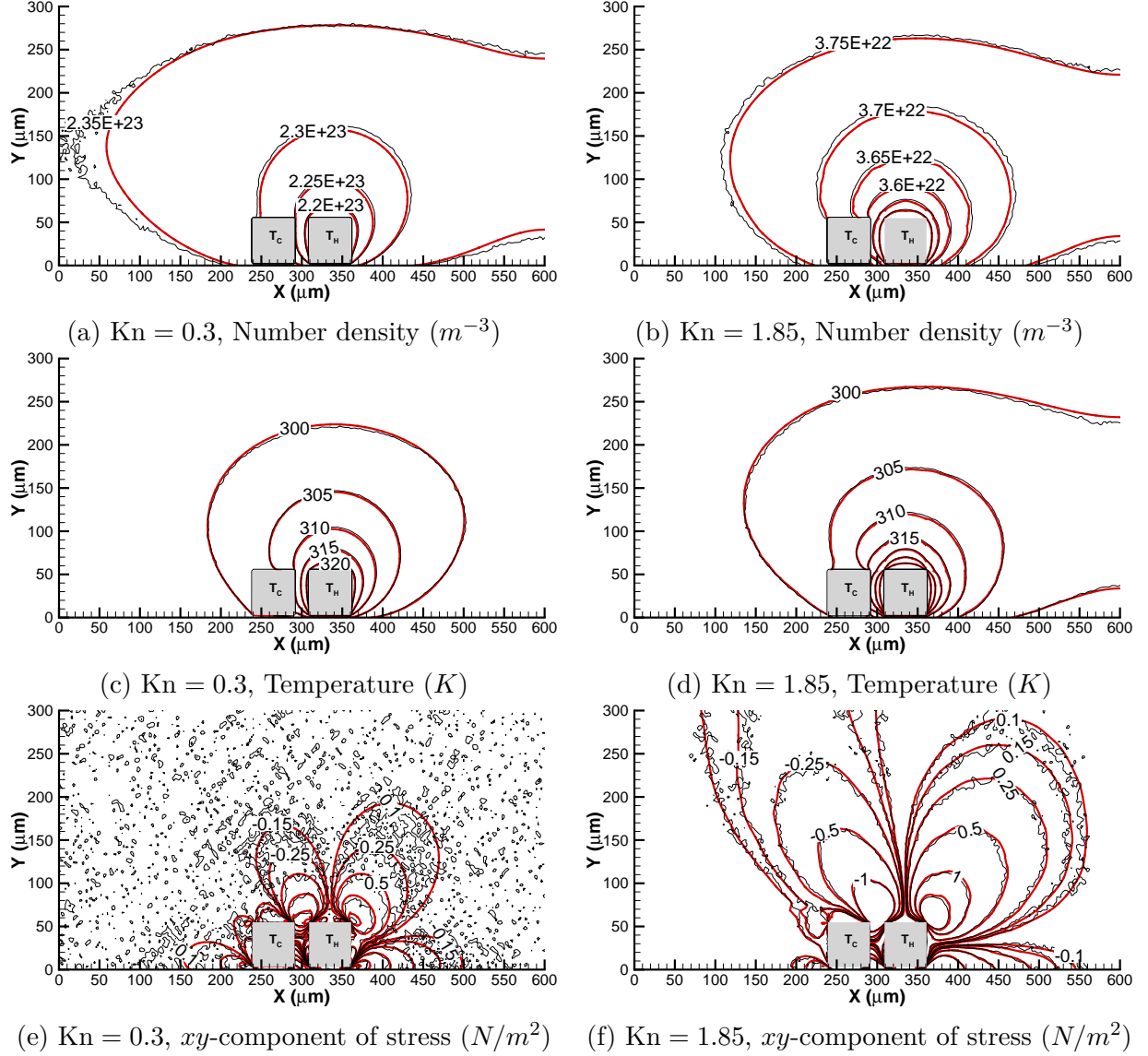


Figure 5.4. Variation of flow properties along the domain for MIKRA Gen1 cases (M-01: $Kn = 1.85$, and M-03: $Kn = 0.3$) obtained from DSMC (thin black lines), and DGFS (thick red lines).

in the number density from the equilibrium value of $235.8901 \times 10^{21} m^{-3}$, as is also evident from Fig. 5.4a. In terms of temperature, in Fig. 5.4c, we observe a rather familiar flow expansion, in the sense that, the hot vane dissipates heat to the surrounding acting as a source, thereby giving rise to a spiral with spiral's origin at the hot vane. Observe the interaction of contour lines (isotherms at $305K$ and $310K$) with the cold vane in the region ($250\mu m \leq X \leq 300\mu m$, $25\mu m \leq Y \leq 60\mu m$). We notice sharply curved isotherms near

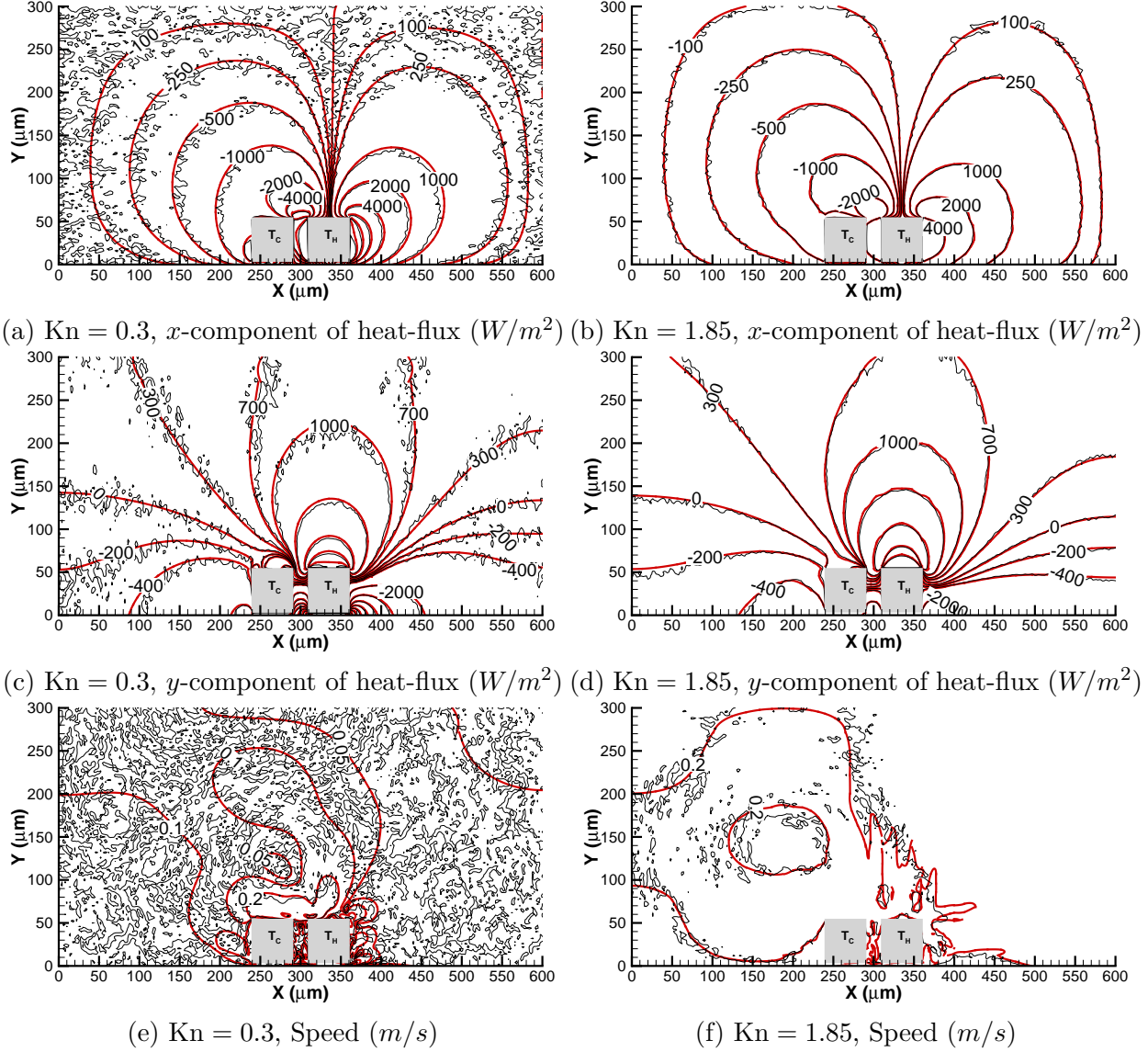


Figure 5.5. Continuation of Fig. 5.4.

the top and right sides of the cold vane (see Fig. 5.6). Taking into account the Knudsen number of 0.3 and the characteristic length scale of system of $20\mu\text{m}$, the Knudsen layer should extend few mean free paths from the solid surfaces i.e., $O(\lambda) \approx O(6\mu\text{m})$. Therefore, one should expect some temperature jump, and therefore non-linearity in the temperature in the near-wall region. More interestingly, we note an inflection in the isotherms at the top surface of the cold vane. This is essentially because the cold vane surface temperature is 304K , while the free-stream is at 296K . Hence, near to the heating source, say top-right

end of the cold vane, the surface temperature is lower than the temperature of a layer of molecules just above the surface; and far away from the heating source, say top-left end of the cold vane, the surface temperature is higher than the temperature of a layer of molecules just above the surface. Therefore, an inflection in isotherms is expected somewhere between the top-left and top-right corner of the cold vane.

The origin of Knudsen force can be appreciated as follows. Consider a differential area dS over the cold vane as shown Fig. 5.6. The molecules impinging on the area dS can be thought as made up of two types of molecules: molecules coming from colder point A and molecules coming from hotter point B , both separated by few mean free paths. Near to the top right end of the cold vane, nearer to the hot vane, one should expect larger concentration of molecules of type B , and smaller concentration of molecules of type A . Conversely, near to the top left end of the cold vane, which is (relatively) far away from the hot vane, one should expect a smaller concentration of molecules of type B , and larger concentration of molecules of type A . Specifically, at the top left end of the cold vane, due to this imbalance of particles hitting the surface area, the momentum transferred to the surface element dS is in the opposite direction to the temperature gradient; however the gas flow is induced in the direction of the temperature gradient [112], [121]. This overall momentum imbalance contributes to the Knudsen force.

Figure 5.4e illustrates the variation of off-diagonal (xy) component of stress tensor at $\text{Kn} = 0.3$. First, we note the development of four ovals/ellipses originating at the four corners/edges of the hot vane. The effect is more pronounced at the right end (top-right and bottom-right corners) of the hot vane i.e., the length of the semi-major axis is larger for the ellipses on the right. At the top-left corner of the hot vane, in particular, we observe interaction of ovals with the top-right edge of the cold vane (note the distorted shape of the oval/ellipse at the top-left boundaries of the hot vane). Since the Knudsen number is in the *slip/early-transition*

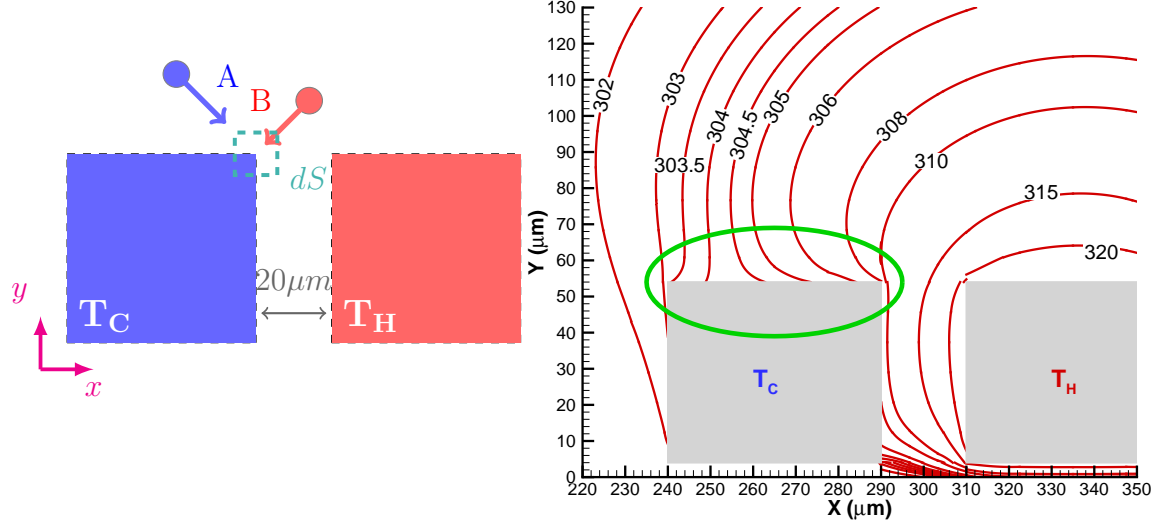


Figure 5.6. Sharp curvature in isotherms near the surface of cold vane at $\text{Kn} = 0.3$. This can be interpreted in terms of imbalance of molecules of type A (cold) and type B (hot) at the top-left/top-right ends of the cold vane.

regime ($\text{Kn} = 0.3$), consider the expression for the stress-tensor, arrived in part by second order Chapman-Enskog expansion[39]:

$$\begin{aligned}
 P_{ij} &= p\delta_{ij} + \tau_{ij}^{(1)} + \tau_{ij}^{(2)} + \dots \\
 \tau_{ij}^{(1)} &= -2\mu \left[\frac{\partial u_i}{\partial x_j} \right] \\
 \tau_{ij}^{(2)} &= \underbrace{K_2 \frac{\mu^2}{\rho T} \left[\frac{\partial^2 T}{\partial x_i \partial x_j} \right] + K_3 \frac{\mu^2}{\rho T^2} \left[\frac{\partial T}{\partial x_i} \frac{\partial T}{\partial x_j} \right]}_{\tau_{ij}^T : \text{Thermal stress tensor}} \\
 &\quad + K_1 \frac{\mu^2}{\rho} \frac{\partial u_k}{\partial x_k} \left[\frac{\partial u_i}{\partial x_j} \right], \quad i, j, k \in \{1, 2\}
 \end{aligned} \tag{5.1}$$

where P_{ij} , p , u , μ , ρ are stress tensor, pressure, velocity, dynamic viscosity, and density respectively. δ_{ij} is the Kronecker delta function, τ_{ij} is the off-diagonal term of the stress

tensor, and $K_i \approx 1$, $i = \{1, 2, 3\}$ are species/molecular-interaction specific constants[39]. This yields

$$\begin{aligned}
 P_{12} &= \tau_{12}^{(1)} + \tau_{12}^{(2)} + \dots = P_{xy} \\
 \tau_{12}^T &= K_2 \frac{\mu^2}{\rho T} \left[\frac{\partial^2 T}{\partial x_1 \partial x_2} \right] + K_3 \frac{\mu^2}{\rho T^2} \left[\frac{\partial T}{\partial x_1} \frac{\partial T}{\partial x_2} \right] \\
 &= K_2 \frac{\mu^2}{\rho T} \left[\frac{\partial^2 T}{\partial x \partial y} \right] + K_3 \frac{\mu^2}{\rho T^2} \left[\frac{\partial T}{\partial x} \frac{\partial T}{\partial y} \right]
 \end{aligned} \tag{5.2}$$

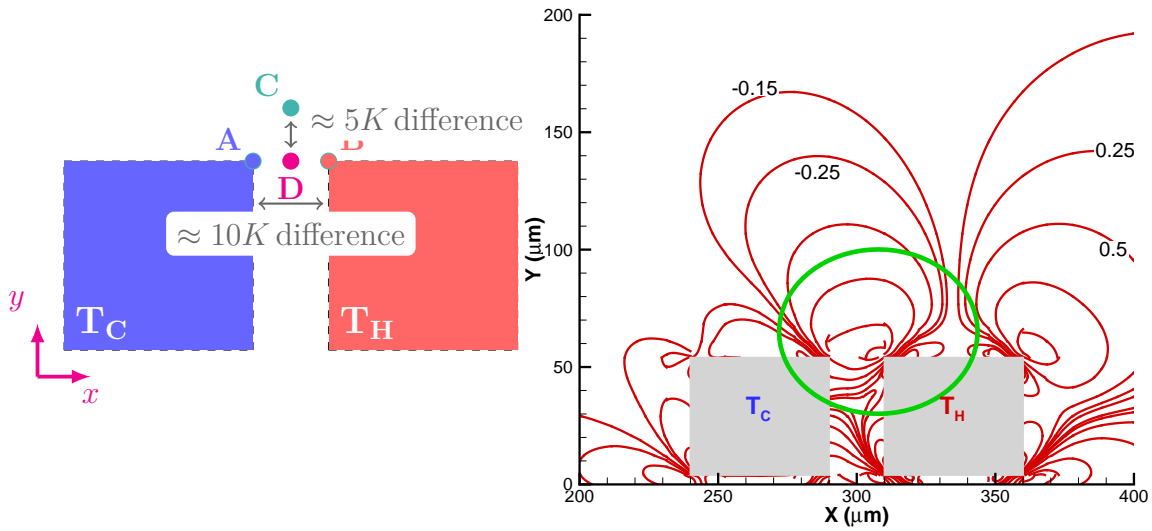


Figure 5.7. xy component of stress tensor at $\text{Kn} = 0.3$: origin of oval/ellipses at the edges of the vanes. Note the distorted shape of the ellipse between the top-right corner of cold vane and top-left corner of hot vane. Since the temperature gradient is stronger between point A and B, compared to point C and D, we expect the semi-major axis of the ellipse to be larger than the semi-minor axis, and hence the distorted ellipse/oval – an observation consistent with Eqs. (5.1, 5.2) since $\partial T/\partial x \gg \partial T/\partial y$.

Let us consider four points in the flow: A (top-right corner of cold vane), B (top-left corner of hot vane), C (third vertex of equilateral triangle $\triangle ABC$ s.t. $\vec{BC} \times \vec{CA} / \|\vec{BC} \times \vec{CA}\| = \hat{k}$), and D (mid point of A and B) as shown in Fig. 5.7. Based on isotherms in Fig. 5.6, it can be inferred that the temperature difference between points A and B is $\approx 10K$, whereas the temperature difference between points C and D is $\approx 5K$. Consistent with the Eq. 5.2, theoretically, we expect the thermal stresses (and therefore P_{xy}) to be larger between points

A and B since $\partial T/\partial x|_{AB} \gg \partial T/\partial y|_{CD}$ (more formally: $\|\nabla T\|_{AB} \gg \|\nabla T\|_{CD}$, $\|\nabla^2 T\|_{AB} \gg \|\nabla^2 T\|_{CD}$). Hence, the distorted ellipse. A more subtle observation is as follows: Why, *precisely*, should an isocontour line of xy component of stress, start from top-left corner of the hot-vane (i.e., point B) and end at the top-right corner of cold-vane (i.e., point A). What happens to the entire flow field if we introduce roughness on the walls, or smooth the vane corners—few questions that we delegate to a future study.

Next, Figs. 5.5a, and 5.5c depict the variation of x and y components of heat flux. We want to reemphasize that DSMC simulations consider the rotational degrees of freedom of N_2 into account, whereas DGFS, being in very early stages of research, doesn't. Nevertheless, we observe a fair agreement between DSMC and DGFS. In Fig. 5.5a, in the region ($250\mu m \leq X \leq 320\mu m$, $50\mu m \leq Y \leq 90\mu m$), we again note presence of iso-contour lines between the top-left and top-right corners of the cold and hot vanes. A more subtle observation is as follows: Multiple iso-contours, for instance $-2000 W/m^2$, $-4000 W/m^2$, $-6000 W/m^2$ (the unlabeled contour just below $-4000 W/m^2$ iso-contour), differing by large magnitudes, start at *approximately* the top-left corner of the hot vane, and end at the top-right corner of the cold vane, resulting in sharply curved isocontours. A partial explanation of such effects appears in Ref. [118], wherein the author attributed the observation to simply *edge effects*, basing the argument on the imbalance of particles of type A (cold) and type B (hot) near to the edges, as was mentioned earlier in the discussion.

Figure 5.5e illustrates the flow speed in the domain. We notice significant statistical fluctuations in DSMC (thin black lines), to an extent that removing DGFS contour lines in red, would make it difficult, if not impossible, to decipher the overall flow structure. A more complete picture of the flow is presented through transient DGFS streamlines in Figs. 5.8. First, we note the streamlines pointing in the upward direction. This is essentially due to the heating of the molecules (and therefore the thermal energy imparted to them) in the lower portions of the domain. In the process, four characteristic vortexes appear at the four corners of the heated vane, relatively early during the course of the simulation, for instance, see Fig. 5.8a at $1.25 ms$. Over the time, secondary vortexes appear in the flow, most notably,

a larger vortex at the top of the cold vane, and a smaller vortex near the top-right corner of hot vane.

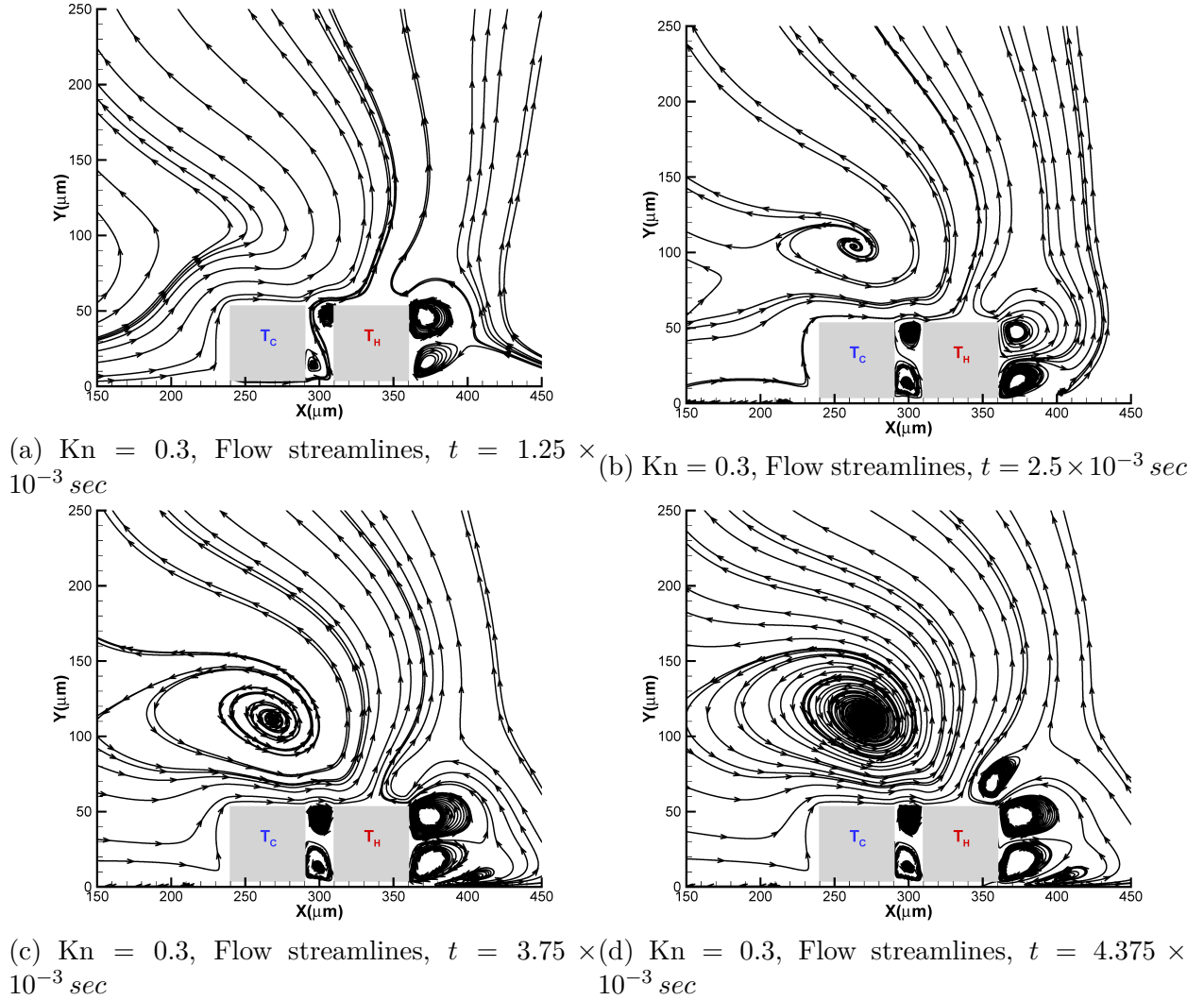
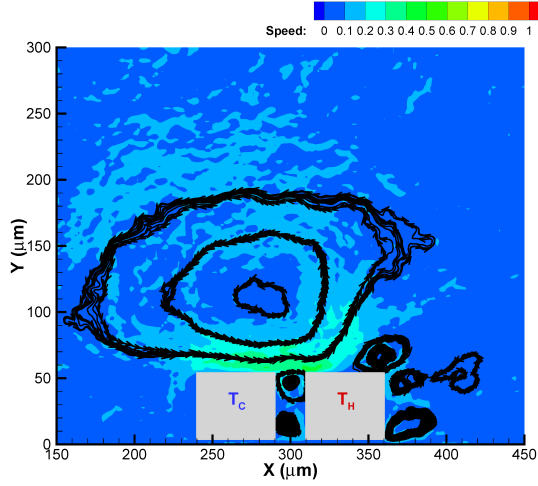


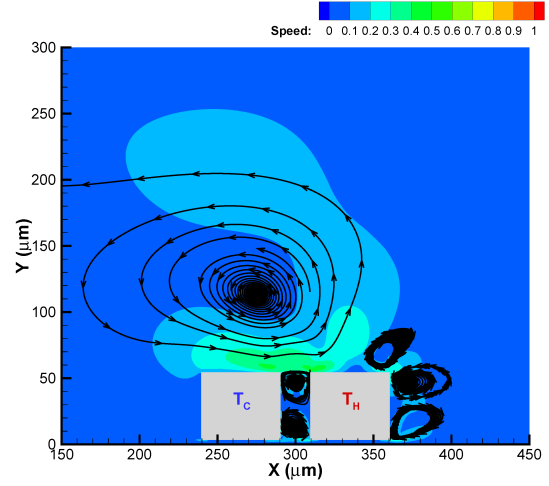
Figure 5.8. Instantaneous streamlines near the vanes of MIKRA Gen1 device at $\text{Kn} = 0.30$ obtained from DGFS using VHS collision model. Observe the vortex formation above the cold vane, and top right corner of hot vane.

Figure 5.9 shows the *steady state* speed contours at different Knudsen numbers with the corresponding flow streamlines overlaid. With increase in Knudsen number from $\text{Kn} = 0.3$ to $\text{Kn} = 0.74$, we note sharp increase in flow velocity, approximately by a factor of two. Consequently, the vortexes grow in size. The change in flow speed, however, from $\text{Kn} = 0.74$ to $\text{Kn} = 1.85$, although appreciable, is relatively mild.

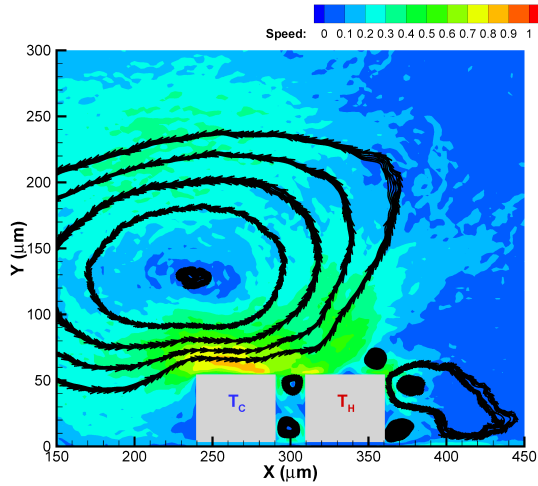
Finally, we compare the variation of flow properties along the vertical centerline ($x = 300\mu m$, $0 \leq y \leq 300\mu m$) in Figs. 5.10 for various models. We observe a fair agreement between DSMC and DGFS results ignoring the statistical noise (see Figs. 5.4, 5.5). In particular, in Fig. 5.10b, we observe peak temperatures near the *edges* of hot and cold vanes i.e., in the region $x = 300\mu m$, $30 \leq y \leq 60\mu m$. Through Figs. 5.10c and 5.10d, we infer that the thermal gradients are stronger in the x -direction. More notably, we observe the highest thermal-stress in the *edge* region (note the valley in the region $x = 300\mu m$, $40 \leq y \leq 60\mu m$). We conjecture the trough of the valley to be shallower if the vane edges ought to be made smoother. A slightly peculiar observation is as follows: the trough of the valley is deeper at $Kn = 0.74$ compared to $Kn = 0.30$, and shallower at $Kn = 1.85$ compared to $Kn = 0.74$. This could be explained as follows: at $Kn = 0.30$ the temperature difference, $T_H - T_C$, is lower than the one corresponding to the $Kn = 0.74$ case and therefore the thermal stress increases in the latter case. For the $Kn = 1.85$ and $Kn = 0.74$ cases, wherein the temperature difference is approximately same, the peak thermal-stress decreases owing to the bimodal nature of the Knudsen forces.



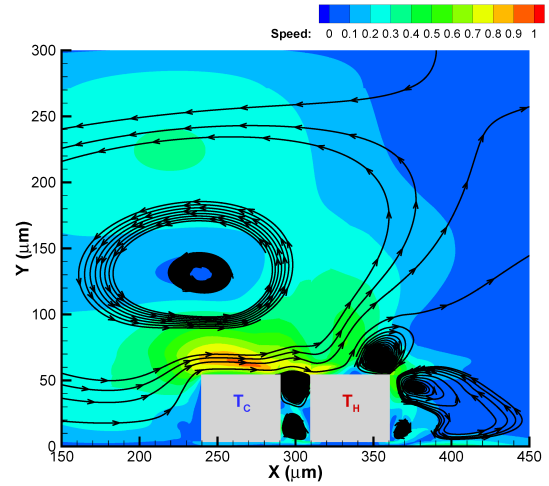
(a) Speed (m/s), $Kn = 0.30$, DSMC



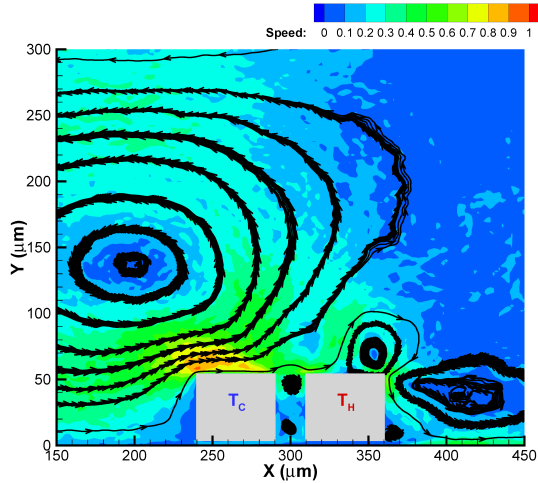
(b) Speed (m/s), $Kn = 0.30$, DGFS



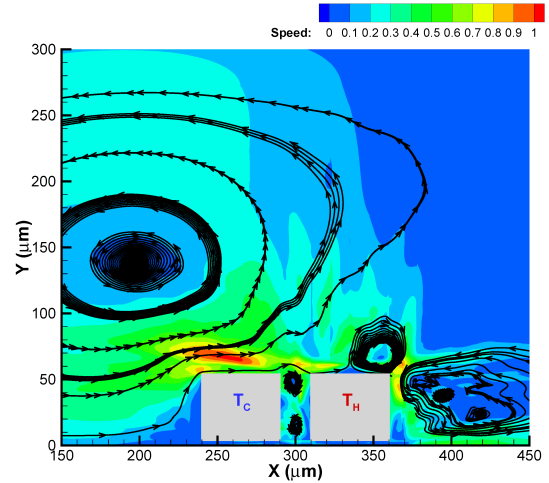
(c) Speed (m/s), $Kn = 0.74$, DSMC



(d) Speed (m/s), $Kn = 0.74$, DGFS



(e) Speed (m/s), $Kn = 1.85$, DSMC



(f) Speed (m/s), $Kn = 1.85$, DGFS

Figure 5.9. Variation of flow speed at steady state for MIKRA Gen1 cases obtained from DSMC and DGFS using VHS collision model.

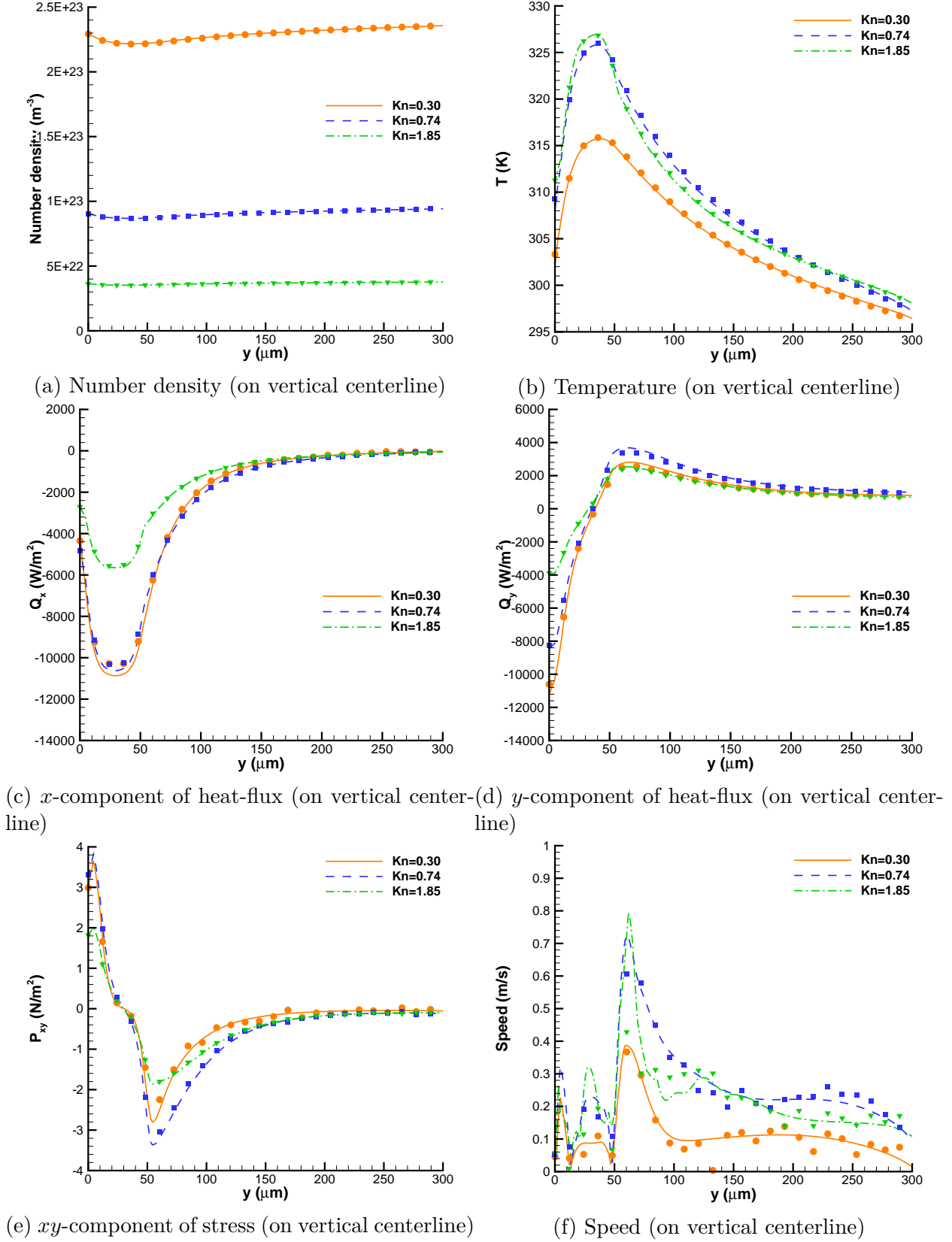


Figure 5.10. Variation of flow properties along the domain vertical centerline ($X = 300\mu\text{m}$) for MIKRA Gen1 cases obtained from DSMC (symbols) and DGFS (lines) using VHS collision model.

5.3 Multi-species MIKRA

In the present section, we carry out the MIKRA simulations for binary mixture consisting of N_2 and H_2O using the variable soft sphere model.

5.3.1 Problem Statement

The flow configuration remains the same as shown in Fig. 5.2. We consider the 2D uniform flow of binary mixture of N_2 and H_2O . The end goal is to simulate the motion of gas flows in the gap between the two vanes, subject to initial pressure p_∞ , hot (T_H) and cold (T_C) vane temperature as listed in Tab. 5.2, in order to identify the correct circulation, induced low velocity, temperature gradient, Knudsen forces, and heat transfer rate from the vanes. The results are to be obtained from both stochastic (DSMC) and deterministic (DGFS) simulations.

Table 5.2. Numerical parameters for thermo-stress convection in MIKRA Gen1 simulations for DSMC and DGFS using VSS collision model for N_2/H_2O binary mixture.

| Parameter | Cases MSM-01 |
|---|-----------------|
| Pressure: p (Torr) | 1.163 |
| Total number density: n ($\times 10^{21} m^{-3}$) | 37.86091 |
| Concentration: $(n^{(N_2)}/n, n^{(H_2O)}/n)$ | (0.05, 0.95) |
| Knudsen number ¹ : Kn | 1.85 |
| Cold vane temperature: T_C (K) | 306 |
| Hot vane temperature: T_H (K) | 363 |
| DGFS parameters | |
| Points in velocity mesh: N^3 | 32^3 |
| Points in radial direction ² : N_ρ | 8 |
| Points on <i>full</i> sphere ² : M | 12 |
| Size of velocity mesh ³ | $[-6, 6]^3$ |

Table 5.3. N_2 and H_2O gas VSS parameters used in MIKRA Gen1 DSMC and DGFS simulations.

| | N_2 | H_2O |
|---|------------------------|------------------------|
| Mass: m (kg) | 46.5×10^{-27} | 29.9×10^{-27} |
| Viscosity index ¹ : ω_i , (–) | 0.74 | 1.00 |
| Scattering index: α_i , (–) | 1.36 | 1.00 |
| Ref. diameter: $d_{\text{ref},i}$ (m) | 4.07×10^{-10} | 5.78×10^{-10} |
| Ref. temperature: $T_{\text{ref},i}$ (K) | 273 | 273 |

5.3.2 Numerical details

The multi-species simulations are carried out for flows in transition regime. The specific differences between stochastic (DSMC) and deterministic (DGFS) modelling is described next.

- **DSMC:** SPARTA[19] has been employed for carrying out DSMC simulations in the present work. The geometric parameters remain the same as described in section 5.2.2. A minimum of 300 DSMC simulator particles per cell is used in conjunction with the no-time collision (NTC) algorithm and VSS scattering model. The simulations are first run for 200,000 unsteady steps, and subsequently another 5,000,000 steady steps wherein the flow sampling is performed. Similar to the previous single-species MIKRA case, the DSMC domain is discretized into 300×150 cells, resulting in a uniform cell size of $2 \mu\text{m}$, with 285 particles of H_2O and 15 particles of N_2 , per cell on average during initialization. A time step of 10^{-9} sec is used during *move* step of DSMC algorithm throughout the course of simulation. N_2 and H_2O are used as the working gases in simulations. The properties of the working gas is given in Tab. 5.3. Note that for N_2 , we consider $\zeta_R = 2$ rotational degrees of freedom, rotational relaxation $Z_R = 0.2$, $\zeta_V = 2$ vibrational degrees of freedom, vibrational relaxation $Z_V = 1.90114 \times 10^{-5}$, and vibrational temperature $T_v = 3371 \text{ K}$; and for H_2O , we consider $\zeta_R = 3$ rotational degrees of freedom, rotational relaxation $Z_R = 0.2$, $\zeta_V = 3$ vibrational degrees of freedom, vibrational relaxation $Z_V = 1.90114 \times 10^{-5}$, and vibrational temperature $T_v = 5261 \text{ K}$.

- **DGFS:** We use the DGFS implementation described in Ref. [89]. The geometrical parameters remain the same as described in section 5.2.2. Multi-species case specific DGFS parameters have been provided in Tab. 5.2. Note that, we employ N_2 and H_2O as the working gas in simulations. N_2 is diatomic, and H_2O is triatomic, however, DGFS, as of now, is applicable for monoatomic gases only. Since the working temperature range is low, we anticipate the effects of vibrational degrees of freedom to be negligible.

5.3.3 Results and Discussion

Figure 5.11 illustrates the contour plot of various flow properties for the MSM-01 case in transition regime, wherein the N_2 and H_2O are in 0.05 : 0.95 concentration ratio. Similar to the single species case, for each of these plots, the DSMC and DGFS contours have been overlaid, wherein DSMC results have been indicated by thin black lines, and DGFS results have been indicated with thick red lines. Since the flow is strictly driven by temperature gradients, we expect very small deviation in the number density from the equilibrium values of $35.9678645 \times 10^{21} m^{-3}$ for H_2O and $1.8930455 \times 10^{21} m^{-3}$ for N_2 , as is also evident from Figs. 5.11a and 5.11b. In terms of temperature, in Figs. 5.11c and 5.11d, we again observe a rather familiar flow expansion, in the sense that, the hot vane dissipates heat to the surrounding acting as a source, thereby giving rise to a spiral with spiral's origin at the hot vane. From the fundamental mass/momentum conservation principles, one can infer that, in the presence of temperature gradients, the heavier species, here N_2 , moves slower and the lighter species, here H_2O , moves faster giving rise to the well-known thermal diffusion. This explain why the isotherms for H_2O spread farther apart compared to the those of N_2 .

Figures 5.11g and 5.11h illustrate the variation of off-diagonal (xy) component of stress tensor. Again, we observe the development of four ovals/ellipses originating at the four corners/edges of the hot vane, wherein the effects are more pronounced at the right end (top-right and bottom-right corners) of the hot vane. The stress is higher for H_2O compared to N_2 . Figures 5.11e and 5.11f illustrate the flow speed in the domain. We notice significant

statistical fluctuations in DSMC (thin black lines) contour lines for N_2 due to lower number of DSMC simulator particles. In particular, we observe that DGFS results/contours are insusceptible to the concentration of the individual species, thereby opening the possibility of its application for simulating flows involving species in trace concentrations.

From these results, the scheme meets the following objective: “Apply the developed deterministic method for the study of the low-speed thermally-driven flows in micro-electro mechanical systems”.

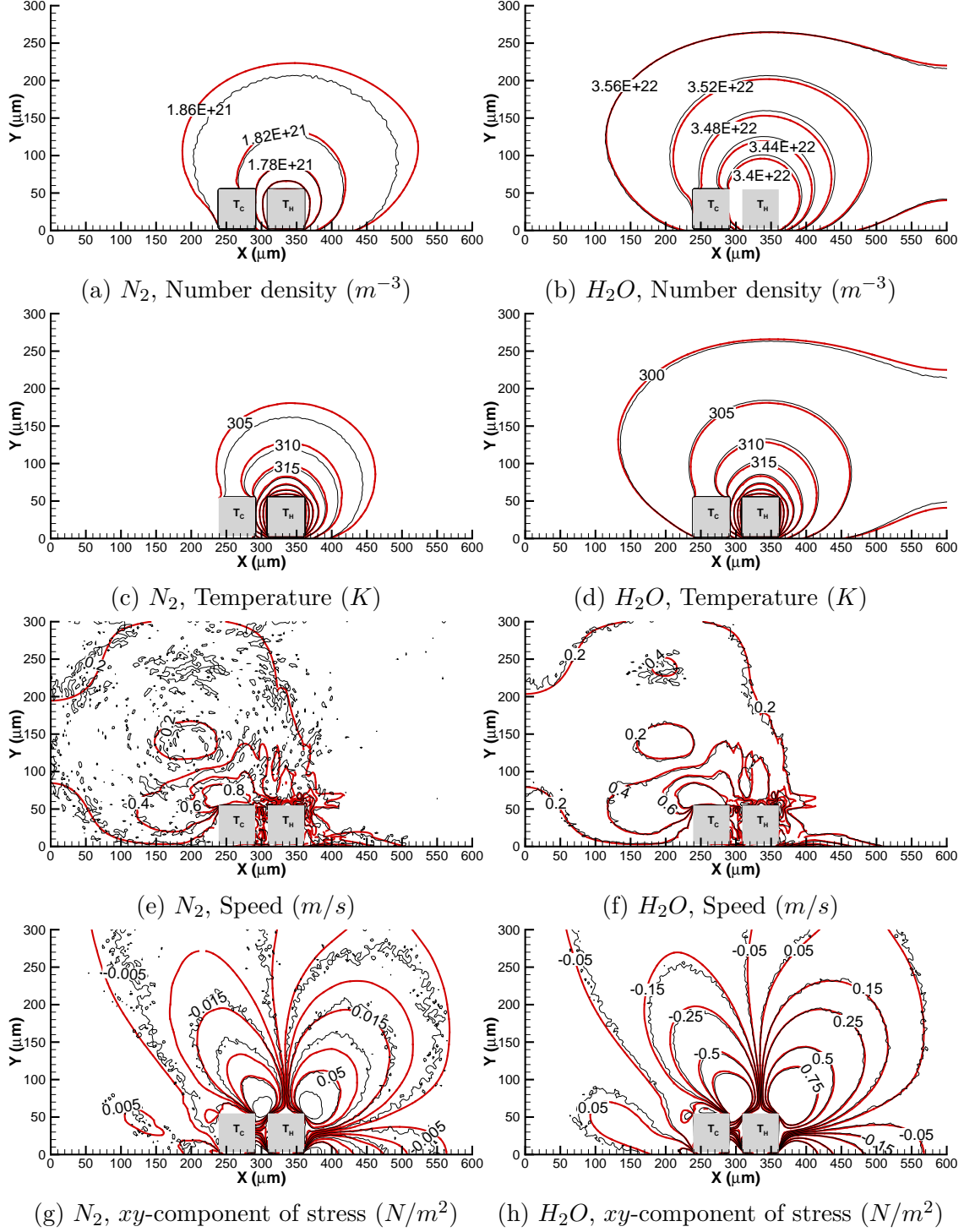


Figure 5.11. Variation of flow properties along the domain for multi-species MIKRA Gen1 case (MSM-01: $Kn = 1.85$) obtained with DSMC (thin black lines) and DGFS (thick red lines) using VSS collision model. We want to reemphasize that DSMC simulations consider the rotational degrees of freedom of N_2 and H_2O into account, whereas DGFS, being in very early stages of research, doesn't; and therefore we expect some differences between DSMC and DGFS results.

6. SUMMARY

This thesis is concerned with construction of highly accurate method for the solution of the full Boltzmann equation and related kinetic models.

In the chapter two of the thesis, a deterministic numerical method for the multi-species full Boltzmann equation has been presented. To achieve this, first, a fast spectral algorithm for solving the multi-species homogeneous collision operator is constructed. The procedure has been shown to exhibit spectral convergence in velocity space. Second, a high order spatial discretization is introduced in the physical space to discretize the full inhomogeneous multi-species Boltzmann system. The resulting method combines the discontinuous Galerkin discretization in the physical space and the fast Fourier spectral method in the velocity space to yield highly accurate numerical solutions. The DG-type formulation employed in the present work has advantage of having arbitrary order accuracy at the element-level, and its element-local compact nature (and that of our collision algorithm) enables effective parallelization on massively parallel architectures. The fast spectral method for evaluating the Boltzmann collision operator does not rely on any ad hoc adjustment or parameter fitting of the collision kernel in contrast to the previously proposed methods in literature. Third, the developed procedure is implemented on multi-GPU/multi-CPU massively parallel systems. The resulting implementation achieved a parallel efficiency of 99% on 36 GPUs.

When the Knudsen number, Kn , of flow is decreased, the traditional deterministic numerical schemes for kinetic equations encounter two difficulties: a) since the mean collision time decreases, the timestep has to be made smaller, b) the flow acquires steady state slowly, and therefore one needs to carry out time integration for large number of time steps. To circumvent these issues, in the chapter three of the thesis, a class of high order spatially and temporally accurate deterministic numerical method for the stiff kinetic equations has been presented. These methods have the following key properties: a) they preserve the asymptotic transition to the Euler equation; b) the timestep is independent of the Knudsen number; c) the collision kernel is evaluated implicitly utilizing their conservative properties without use of any iteration; d) with use of high order multi-stage time-splitting, the time integration

over sufficiently long number of timesteps, needed for modelling near-continuum flows, can be carried out more accurately; e) robust high order accurate scheme in physical space with nearly-linear parallel efficiency; f) applicability for both, general, rarefied and near-continuum compressible flows. In particular, the new family of high order Implicit-Explicit (IMEX) Backward difference (BDF) time integration schemes require “only one” evaluation of implicit and explicit parts per time-step, thereby making them computationally optimal. The Navier-Stokes asymptotic limit is recovered directly from “standard” linear models without need of building Navier-Stokes fluxes or any such adhoc modifications whatsoever.

The chapter three of the thesis is concerned with verification of the proposed schemes. A series of numerical tests is performed to illustrate the efficiency and accuracy of the proposed method. Various benchmarks highlighting different collision kernels, different mass ratios, momentum transfer, heat transfer, and in particular the diffusive transport have been studied. The results are directly compared with the direct simulation Monte Carlo (DSMC) method. The results obtained with the developed deterministic solver and DSMC are inextricable ignoring the statistical noise and the errors therein. Notably, some of the accuracy tests involved ~ 0.4 billion unknowns, resulting in $O(0.9)$ quadrillion calculations. The deterministic solution of the Boltzmann equation by the DGFS method, in particular, is suitable for studying low-speed and unsteady flows.

In chapter four of the thesis, the proposed methodology has been utilized for studying low-speed and unsteady flows in Microscale In-Plane Knudsen Radiometric Actuator (MIKRA) sensor. A good agreement between experiments and DSMC simulations is observed.

7. RECOMMENDATIONS

The proposed fast spectral algorithm for solving the multi-species collision operator requires very large velocity-domain for large mass ratios $m_j/m_i \gg 1$. This is a common issue appearing in multi-species problems. Possible remedies include adaptive mesh in velocity space (cf. [47]), using an asymptotic model valid for large mass ratios (cf. [48]), or introducing independent velocity grid for each species wherein different collision types for every (i, j) pair are treated independently (cf. [49], [50]). In this work, moderate mass ratios have been considered. Future work may address construction of algorithms for high mass ratios.

The proposed implicit-explicit method for the Boltzmann equation and related kinetic models is currently limited to single-species systems. For multi-species systems, a common issue is the selection of an appropriate penalization function. This is important to ensure that, in the limit of vanishing Knudsen number, the system may preserve the asymptotic transition to multi-species Euler system.

In the current era of petaflop-computing and near-future quantum computing, with little-bar on computation power, I believe that this work is a first step towards migration from conventional continuum, near-continuum, and stochastic solvers to deterministic Boltzmann. Future directions of work include the following, but not limited to:

- a) application to general three-dimensional rarefied hypersonic flow problems.
- b) implementation of different interaction models such as Lennard-Jones
- c) implementation of reaction models

REFERENCES

- [1] C. Cercignani, *Rarefied gas dynamics: from basic concepts to actual calculations*. Cambridge University Press, 2000, vol. 21.
- [2] C. Cercignani, *The Boltzmann Equation and Its Applications*. Springer-Verlag, New York, 1988.
- [3] H. Spohn, “The phonon boltzmann equation, properties and link to weakly anharmonic lattice dynamics,” *Journal of statistical physics*, vol. 124, no. 2-4, pp. 1041–1104, 2006.
- [4] W. T. Taitano, L. Chacon, and A. N. Simakov, “An adaptive, implicit, conservative, 1d-2v multi-species vlasov–fokker–planck multi-scale solver in planar geometry,” *Journal of Computational Physics*, vol. 365, pp. 173–205, 2018.
- [5] S. Chapman and T. Cowling, “The mathematical theory of non-uniform gases: An account of the kinetic theory of viscosity, thermal conduction and diffusion in gases. cambridge mathematical library,” *Cambridge University Press*, vol. 1, pp. 27–52, 1970.
- [6] A. Jüngel, *Transport equations for semiconductors*. Springer, 2009, vol. 773.
- [7] C. Cercignani and G. M. Kremer, “Relativistic boltzmann equation,” in *The Relativistic Boltzmann Equation: Theory and Applications*, Springer, 2002, pp. 31–63.
- [8] N. Bellomo, *Modeling complex living systems: a kinetic theory and stochastic game approach*. Springer Science & Business Media, 2008.
- [9] S. Harris, *An Introduction to the Theory of the Boltzmann Equation*. Dover Publications, 2004.
- [10] H. Grad, “On the kinetic theory of rarefied gases,” *Communications on pure and applied mathematics*, vol. 2, no. 4, pp. 331–407, 1949.
- [11] G. Bird, “Approach to translational equilibrium in a rigid sphere gas,” *The Physics of Fluids*, vol. 6, no. 10, pp. 1518–1519, 1963.
- [12] G. Bird, *The DSMC method*. CreateSpace Independent Publishing Platform, 2013.
- [13] W. Wagner, “A convergence proof for bird’s direct simulation monte carlo method for the boltzmann equation,” *Journal of Statistical Physics*, vol. 66, no. 3, pp. 1011–1044, 1992.

- [14] M. A. Gallis, J. Torczynski, D. Rader, and G. A. Bird, “Convergence behavior of a new dsmc algorithm,” *Journal of Computational Physics*, vol. 228, no. 12, pp. 4532–4548, 2009.
- [15] Q. Sun, I. D. Boyd, G. V. Candler, A. D. Ketsdever, and E. Muntz, “A hybrid continuum/particle approach for micro-scale gas flows,” in *AIP Conference Proceedings*, AIP, vol. 663, 2003, pp. 752–759.
- [16] G. Dimarco and L. Pareschi, “Hybrid multiscale methods ii. kinetic equations,” *Multiscale Modeling & Simulation*, vol. 6, no. 4, pp. 1169–1197, 2008.
- [17] L. L. Baker and N. G. Hadjiconstantinou, “Variance reduction for monte carlo solutions of the boltzmann equation,” *Physics of Fluids*, vol. 17, no. 5, p. 051 703, 2005.
- [18] S. K. Stefanov, “On dsmc calculations of rarefied gas flows with small number of particles in cells,” *SIAM Journal on Scientific Computing*, vol. 33, no. 2, pp. 677–702, 2011.
- [19] M. A. Gallis, J. R. Torczynski, S. J. Plimpton, D. J. Rader, T. Koehler, and J. Fan, “Direct simulation monte carlo: The quest for speed,” in *AIP Conference Proceedings*, AIP, vol. 1628, 2014, pp. 27–36.
- [20] L. Mieussens, “A survey of deterministic solvers for rarefied flows,” in *Proceedings of the 29th International Symposium on Rarefied Gas Dynamics, AIP Conf. Proc.*, vol. 1628, 2014, pp. 943–951.
- [21] G. Dimarco and L. Pareschi, “Numerical methods for kinetic equations,” *Acta Numer.*, vol. 23, pp. 369–520, 2014.
- [22] C. Mouhot and L. Pareschi, “Fast algorithms for computing the boltzmann collision operator,” *Mathematics of computation*, vol. 75, no. 256, pp. 1833–1852, 2006.
- [23] G. C. Maitland and E. B. Smith, “Critical reassessment of viscosities of 11 common gases,” *Journal of Chemical and Engineering Data*, vol. 17, no. 2, pp. 150–156, 1972.
- [24] G. A. Bird, *Molecular Gas Dynamics and the Direct Simulation of Gas Flows*. Clarendon Press, Oxford, 1994.
- [25] K. Koura, H. Matsumoto, and T. Shimada, “A test of equivalence of the variable-hard-sphere and inverse-power-law models in the direct-simulation monte carlo method,” *Physics of Fluids A: Fluid Dynamics*, vol. 3, no. 7, pp. 1835–1837, 1991.

- [26] K. Koura and H. Matsumoto, “Variable soft sphere molecular model for inverse-power-law or Lennard-Jones potential,” *Physics of Fluids A: Fluid Dynamics*, vol. 3, no. 10, pp. 2459–2465, 1991.
- [27] A. Kersch, W. Morokoff, and C. Werner, “Selfconsistent simulation of sputter deposition with the monte carlo method,” *Journal of applied physics*, vol. 75, no. 4, pp. 2278–2285, 1994.
- [28] J. Fan, “A generalized soft-sphere model for monte carlo simulation,” *Physics of Fluids*, vol. 14, no. 12, pp. 4399–4405, 2002.
- [29] S. Jaiswal, I. B. Sebastião, and A. A. Alexeenko, “Dsmc-sparta implementation of M-1 scattering model,” in *AIP Conference Proceedings*, AIP Publishing LLC, vol. 2132, 2019, p. 070 023.
- [30] A. B. Weaver, “Assessment of high-fidelity collision models in the direct simulation Monte Carlo method,” PhD thesis, Purdue University, West Lafayette, 2015.
- [31] I. Gamba, J. Haack, C. Hauck, and J. Hu, “A fast spectral method for the Boltzmann collision operator with general collision kernels,” *SIAM J. Sci. Comput.*, vol. 39, B658–B674, 2017.
- [32] S. Jaiswal, A. Alexeenko, and J. Hu, “A discontinuous Galerkin fast spectral method for the full Boltzmann equation with general collision kernels,” *J. Comput. Phys.*, vol. 378, pp. 178–208, 2019.
- [33] C. Villani, “Cercignani’s conjecture is sometimes true and always almost true,” *Communications in mathematical physics*, vol. 234, no. 3, pp. 455–490, 2003.
- [34] M. Shoeybi, M. Svård, F. E. Ham, and P. Moin, “An adaptive implicit–explicit scheme for the dns and les of compressible flows on unstructured grids,” *Journal of Computational Physics*, vol. 229, no. 17, pp. 5944–5965, 2010.
- [35] P.-O. Persson, “High-order les simulations using implicit-explicit runge-kutta schemes,” in *49th AIAA Aerospace Sciences Meeting Including the New Horizons Forum and Aerospace Exposition*, 2011, p. 684.
- [36] E. Muntz, “Rarefied gas dynamics,” *Annual Review of Fluid Mechanics*, vol. 21, pp. 387–417, 1989.
- [37] F. Sharipov and D. Kalempa, “Velocity slip and temperature jump coefficients for gaseous mixtures. i. viscous slip coefficient,” *Physics of Fluids*, vol. 15, no. 6, pp. 1800–1806, 2003.

- [38] F. Sharipov and D. Kalempa, “Velocity slip and temperature jump coefficients for gaseous mixtures. ii. thermal slip coefficient,” *Physics of Fluids*, vol. 16, no. 3, pp. 759–764, 2004.
- [39] M. Kogan, V. Galkin, and O. Fridlender, “Stresses produced in gases by temperature and concentration inhomogeneities. new types of free convection,” *Usp. Fiz. Nauk*, vol. 119, pp. 111–125, 1976.
- [40] W. Crookes *et al.*, “On attraction and repulsion resulting from radiation,” *Philosophical transactions of the Royal society of London*, vol. 164, pp. 501–527, 1874.
- [41] N. Gimelshein, S. Gimelshein, A. Ketsdever, and N. Selden, “Impact of vane size and separation on radiometric forces for microactuation,” *Journal of Applied Physics*, vol. 109, no. 7, p. 074 506, 2011.
- [42] A. D. Strongrich, W. J. O’Neill, A. G. Cofer, and A. A. Alexeenko, “Experimental measurements and numerical simulations of the knudsen force on a non-uniformly heated beam,” *Vacuum*, vol. 109, pp. 405–416, 2014.
- [43] A. Strongrich, A. Pikus, I. B. Sebastião, and A. Alexeenko, “Microscale in-plane knudsen radiometric actuator: Design, characterization, and performance modeling,” *Journal of Microelectromechanical Systems*, vol. 26, no. 3, pp. 528–538, 2017.
- [44] A. Alexeenko and A. Strongrich, *Microelectromechanical gas sensor based on knudsen thermal force*, US Patent App. 15/183,259, Dec. 2016.
- [45] A. Strongrich and A. Alexeenko, “Microstructure actuation and gas sensing by the knudsen thermal force,” *Applied Physics Letters*, vol. 107, no. 19, p. 193 508, 2015.
- [46] L. Pareschi and G. Russo, “Numerical solution of the Boltzmann equation I: Spectrally accurate approximation of the collision operator,” *SIAM J. Numer. Anal.*, vol. 37, pp. 1217–1245, 2000.
- [47] W. T. Taitano, L. Chacon, and A. N. Simakov, “An adaptive, conservative 0D-2V multispecies Rosenbluth-Fokker-Planck solver for arbitrarily disparate mass and temperature regimes,” *J. Comput. Phys.*, vol. 318, pp. 391–420, 2016.
- [48] P. Degond and B. Lucquin-Desreux, “The asymptotics of collision operators for two species of particles of disparate masses,” *Math. Models Methods Appl. Sci.*, vol. 6, pp. 405–436, 1996.
- [49] P. Clarke, P. Varghese, and D. Goldstein, “Discrete velocity computations with stochastic variance reduction of the boltzmann equation for gas mixtures,” in *AIP Conference Proceedings*, AIP, vol. 1628, 2014, pp. 1032–1039.

- [50] L. Wu, J. Zhang, J. M. Reese, and Y. Zhang, “A fast spectral method for the boltzmann equation for monatomic gas mixtures,” *J. Comput. Phys.*, vol. 298, pp. 602–621, 2015.
- [51] R. Womersley, “Symmetric Spherical Designs on the sphere S^2 with good geometric properties, The University of New South Wales,” [Online]. Available: <http://web.maths.unsw.edu.au/~rsw/Sphere/EffSphDes/ss.html>.
- [52] R. S. Womersley, “Efficient spherical designs with good geometric properties,” in *Contemporary Computational Mathematics-A Celebration of the 80th Birthday of Ian Sloan*, Springer, 2018, pp. 1243–1285.
- [53] B. Cockburn and C.-W. Shu, “Runge-Kutta discontinuous Galerkin methods for convection-dominated problems,” *J. Sci. Comput.*, vol. 16, pp. 173–261, 2001.
- [54] L. Pareschi and R. E. Caflisch, “An implicit monte carlo method for rarefied gas dynamics: I. the space homogeneous case,” *Journal of Computational Physics*, vol. 154, no. 1, pp. 90–116, 1999.
- [55] L. Pareschi and G. Russo, “Time relaxed monte carlo methods for the boltzmann equation,” *SIAM Journal on Scientific Computing*, vol. 23, no. 4, pp. 1253–1273, 2001.
- [56] L. Pareschi and S. Trazzi, “Numerical solution of the boltzmann equation by time relaxed monte carlo (trmc) methods,” *International journal for numerical methods in fluids*, vol. 48, no. 9, pp. 947–983, 2005.
- [57] F. Filbet and S. Jin, “A class of asymptotic-preserving schemes for kinetic equations and related problems with stiff sources,” *Journal of Computational Physics*, vol. 229, no. 20, pp. 7625–7648, 2010.
- [58] B. Yan and S. Jin, “A successive penalty-based asymptotic-preserving scheme for kinetic equations,” *SIAM Journal on Scientific Computing*, vol. 35, no. 1, pp. A150–A172, 2013.
- [59] W. Ren, H. Liu, and S. Jin, “An asymptotic-preserving monte carlo method for the boltzmann equation,” *Journal of Computational Physics*, vol. 276, pp. 380–404, 2014.
- [60] U. M. Ascher, S. J. Ruuth, and R. J. Spiteri, “Implicit-explicit runge-kutta methods for time-dependent partial differential equations,” *Applied Numerical Mathematics*, vol. 25, no. 2-3, pp. 151–167, 1997.

- [61] G. Dimarco and L. Pareschi, “Asymptotic preserving implicit-explicit runge–kutta methods for nonlinear kinetic equations,” *SIAM Journal on Numerical Analysis*, vol. 51, no. 2, pp. 1064–1087, 2013.
- [62] G. Dimarco and L. Pareschi, “Exponential runge–kutta methods for stiff kinetic equations,” *SIAM Journal on Numerical Analysis*, vol. 49, no. 5, pp. 2057–2077, 2011.
- [63] Q. Li and L. Pareschi, “Exponential runge–kutta for the inhomogeneous boltzmann equations with high order of accuracy,” *Journal of Computational Physics*, vol. 259, pp. 402–420, 2014.
- [64] J. Hu, Q. Li, and L. Pareschi, “Asymptotic-preserving exponential methods for the quantum boltzmann equation with high-order accuracy,” *Journal of Scientific Computing*, vol. 62, no. 2, pp. 555–574, 2015.
- [65] J. Hu and R. Shu, “A second-order asymptotic-preserving and positivity-preserving exponential runge-kutta method for a class of stiff kinetic equations,” *arXiv preprint arXiv:1807.03728*, 2018.
- [66] J. Hu and X. Zhang, “On a class of implicit–explicit runge–kutta schemes for stiff kinetic equations preserving the navier–stokes limit,” *Journal of Scientific Computing*, vol. 73, no. 2-3, pp. 797–818, 2017.
- [67] C. Cercignani and M. Lampis, “On the h-theorem for polyatomic gases,” *Journal of Statistical Physics*, vol. 26, no. 4, pp. 795–801, 1981.
- [68] C. Truesdell and R. G. Muncaster, *Fundamentals of Maxwell’s Kinetic Theory of a Simple Monatomic Gas: Treated as a Branch of Rational Mechanics*. Academic Press, 1980, vol. 83.
- [69] H. Grad, “Principles of the kinetic theory of gases,” in *Thermodynamik der Gase/Thermodynamics of Gases*, Springer, 1958, pp. 205–294.
- [70] C. Villani, “A review of mathematical topics in collisional kinetic theory,” *Handbook of mathematical fluid dynamics*, vol. 1, no. 71-305, pp. 3–8, 2002.
- [71] S. Jin and M. Slemrod, “Regularization of the burnett equations via relaxation,” *Journal of Statistical Physics*, vol. 103, no. 5-6, pp. 1009–1033, 2001.
- [72] H. Grad, “On the kinetic theory of rarefied gases,” *Communications on pure and applied mathematics*, vol. 2, no. 4, pp. 331–407, 1949.

- [73] T. Xiong, J. Jang, F. Li, and J.-M. Qiu, “High order asymptotic preserving nodal discontinuous galerkin imex schemes for the bgk equation,” *Journal of Computational Physics*, vol. 284, pp. 70–94, 2015.
- [74] J. Hu and R. Shu, “On the uniform accuracy of implicit-explicit backward differentiation formulas (imex-bdf) for stiff hyperbolic relaxation systems and kinetic equations,” *arXiv preprint arXiv:1912.00559*, 2019.
- [75] E. Gross and M. Krook, “Model for collision processes in gases: Small-amplitude oscillations of charged two-component systems,” *Phys. Rev.*, vol. 102, pp. 593–604, 1956.
- [76] L. Sirovich, “Kinetic modeling of gas mixtures,” *Phys. Fluids*, vol. 5, pp. 908–918, 1962.
- [77] F. J. McCormack, “Construction of linearized kinetic models for gaseous mixtures and molecular gases,” *Phys. Fluids*, vol. 16, pp. 2095–2105, 1973.
- [78] P. Andries, K. Aoki, and B. Perthame, “A consistent BGK-type model for gas mixtures,” *J. Stat. Phys.*, vol. 106, pp. 993–1018, 2002.
- [79] S. Brull, “An ellipsoidal statistical model for gas mixtures,” *Commun. Math. Sci.*, vol. 13, pp. 1–13, 2015.
- [80] J. Haack, C. Hauck, and M. Murillo, “A conservative, entropic multispecies BGK model,” *J. Stat. Phys.*, vol. 168, pp. 826–856, 2017.
- [81] A. Bobylev, M. Bisi, M. Groppi, G. Spiga, and I. Potapenko, “A general consistent BGK model for gas mixtures,” *Kinet. Relat. Models*, vol. 11, pp. 1377–1393, 2018.
- [82] M. Gallis, J. Torczynski, D. Rader, M. Tij, and A. Santos, “Normal solutions of the boltzmann equation for highly nonequilibrium fourier flow and couette flow,” *Physics of Fluids*, vol. 18, no. 1, p. 017 104, 2006.
- [83] P. L. Bhatnagar, E. P. Gross, and M. Krook, “A model for collision processes in gases. i. small amplitude processes in charged and neutral one-component systems,” *Physical review*, vol. 94, no. 3, p. 511, 1954.
- [84] L. H. Holway Jr, “New statistical models for kinetic theory: Methods of construction,” *The physics of fluids*, vol. 9, no. 9, pp. 1658–1673, 1966.
- [85] E. Shakhov, “Generalization of the krook kinetic relaxation equation,” *Fluid Dynamics*, vol. 3, no. 5, pp. 95–96, 1968.

- [86] J. Hu, S. Jin, and Q. Li, “Asymptotic-preserving schemes for multiscale hyperbolic and kinetic equations,” in *Handbook of Numerical Analysis*, vol. 18, Elsevier, 2017, pp. 103–129.
- [87] C. Liu, K. Xu, Q. Sun, and Q. Cai, “A unified gas-kinetic scheme for continuum and rarefied flows iv: Full boltzmann and model equations,” *Journal of Computational Physics*, vol. 314, pp. 305–340, 2016.
- [88] M. Krook and T. T. Wu, “Exact solution of Boltzmann equations for multicomponent systems,” *Physical Review Letters*, vol. 38, no. 18, p. 991, 1977.
- [89] S. Jaiswal, A. A. Alexeenko, and J. Hu, “A discontinuous Galerkin fast spectral method for the multi-species full boltzmann equation,” *Comput. Methods Appl. Mech. Engrg.*, vol. 352, pp. 56–84, 2019. [Online]. Available: <https://doi.org/10.1016/j.cma.2019.04.015>.
- [90] A. B. Weaver, A. Venkattraman, and A. A. Alexeenko, “Effect of intermolecular potential on compressible couette flow in slip and transitional regimes,” *Physics of Fluids*, vol. 26, no. 10, p. 107 102, 2014.
- [91] **S. Jaiswal**, I. B. Sebastião, and A. A. Alexeenko, “DSMC-SPARTA implementation of M-1 scattering model,” *AIP Conference Proceedings*, vol. 2132, no. 1, p. 070 023, 2019. DOI: [10.1063/1.5119577](https://doi.org/10.1063/1.5119577). [Online]. Available: <https://doi.org/10.1063/1.5119577>.
- [92] S. Kosuge, K. Aoki, and S. Takata, “Shock-wave structure for a binary gas mixture: Finite-difference analysis of the Boltzmann equation for hard-sphere molecules,” *Eur. J. Mech. B - Fluids*, vol. 20, pp. 87–126, 2001.
- [93] A. V. Pavlov, “Diffusion and thermodiffusion of atmospheric neutral gases: A review,” *Surveys in Geophysics*, vol. 40, no. 2, pp. 247–276, 2019, ISSN: 1573-0956. DOI: [10.1007/s10712-019-09522-2](https://doi.org/10.1007/s10712-019-09522-2). [Online]. Available: <https://doi.org/10.1007/s10712-019-09522-2>.
- [94] C. Canuto and A. Quarteroni, “Approximation results for orthogonal polynomials in sobolev spaces,” *Mathematics of Computation*, vol. 38, no. 157, pp. 67–86, 1982.
- [95] G. A. Sod, “A survey of several finite difference methods for systems of nonlinear hyperbolic conservation laws,” *Journal of computational physics*, vol. 27, no. 1, pp. 1–31, 1978.
- [96] M. A. Gallis, N. P. Bitter, T. P. Koehler, J. R. Torczynski, S. J. Plimpton, and G. Papadakis, “Molecular-level simulations of turbulence and its decay,” *Physical Review Letters*, vol. 118, no. 6, p. 064 501, 2017.

- [97] M. A. Gallis, T. P. Koehler, J. R. Torczynski, and S. J. Plimpton, “Direct simulation monte carlo investigation of the rayleigh-taylor instability,” *Physical Review Fluids*, vol. 1, no. 4, p. 043 403, 2016.
- [98] I. B. Sebastiao, L. Qiao, and A. A. Alexeenko, “Direct Simulation Monte Carlo Modeling of H₂-O₂ deflagration waves,” *Combustion and Flame*, vol. 198, pp. 40–53, C 2018.
- [99] S. Jaiswal, I. B. Sebastião, A. Strongrich, and A. A. Alexeenko, “Femta micropropulsion system characterization by dsmc,” in *AIP Conference Proceedings*, AIP Publishing LLC, vol. 2132, 2019, p. 070 006.
- [100] S. Jaiswal, A. A. Alexeenko, and J. Hu, “Fast Deterministic solution of the full Boltzmann equation on Graphics Processing Units,” in *Proceedings of 31st Rarefied Gas Dynamics Symposium*, (University of Strathclyde), To appear: <http://goo.gl/x4A7sy>, AIP, Glasgow, U.K, 2018.
- [101] A. A. Alexeenko, S. F. Gimelshein, E. P. Muntz, and A. D. Ketsdever, “Kinetic modeling of temperature driven flows in short microchannels,” *International Journal of Thermal Sciences*, vol. 45, no. 11, pp. 1045–1051, 2006.
- [102] H. Yamaguchi, P. Perrier, M. T. Ho, J. G. Méolans, T. Niimi, and I. Graur, “Mass flow rate measurement of thermal creep flow from transitional to slip flow regime,” *Journal of Fluid Mechanics*, vol. 795, pp. 690–707, 2016.
- [103] H. Akhlaghi and E. Roohi, “Mass flow rate prediction of pressure–temperature-driven gas flows through micro/nanoscale channels,” *Continuum Mechanics and Thermodynamics*, vol. 26, no. 1, pp. 67–78, 2014.
- [104] Q. Sheng, G.-H. Tang, X.-J. Gu, D. R. Emerson, and Y.-H. Zhang, “Simulation of thermal transpiration flow using a high-order moment method,” *International Journal of Modern Physics C*, vol. 25, no. 11, p. 1 450 061, 2014.
- [105] R. P. Feynman, “There’s plenty of room at the bottom: An invitation to enter a new field of physics,” in *Handbook of Nanoscience, Engineering, and Technology, Third Edition*, CRC Press, 2012, pp. 26–35.
- [106] C.-M. Ho and Y.-C. Tai, “Micro-electro-mechanical-systems (MEMS) and fluid flows,” *Annual review of fluid mechanics*, vol. 30, no. 1, pp. 579–612, 1998.
- [107] M. Knudsen, “Thermischer molekulardruck der gase in röhren,” *Annalen der Physik*, vol. 338, no. 16, pp. 1435–1448, 1910.

- [108] G. Karniadakis, A. Beskok, and N. Aluru, *Microflows and nanoflows: fundamentals and simulation*. Springer Science & Business Media, 2006, vol. 29.
- [109] M. Knudsen, *The kinetic theory of gases: some modern aspects*. Methuen, 1950.
- [110] A. Ketsdever, N. Gimelshein, S. Gimelshein, and N. Selden, “Radiometric phenomena: From the 19th to the 21st century,” *Vacuum*, vol. 86, no. 11, pp. 1644–1662, 2012.
- [111] J. C. Maxwell, “On stresses in rarified gases arising from inequalities of temperature,” *Philosophical Transactions of the royal society of London*, vol. 170, pp. 231–256, 1879.
- [112] Y. Sone, *Kinetic theory and fluid dynamics*. Springer Science & Business Media, 2012.
- [113] E. H. Kennard *et al.*, *Kinetic theory of gases, with an introduction to statistical mechanics*. McGraw-Hill, 1938., 1938.
- [114] Y. Sone, “Thermal creep in rarefied gas,” *Journal of the Physical Society of Japan*, vol. 21, no. 9, pp. 1836–1837, 1966.
- [115] F. Sharipov and V. Seleznev, “Data on internal rarefied gas flows,” *Journal of Physical and Chemical Reference Data*, vol. 27, no. 3, pp. 657–706, 1998.
- [116] K. Aoki, Y. Sone, and Y. Waniguchi, “A rarefied gas flow induced by a temperature field: Numerical analysis of the flow between two coaxial elliptic cylinders with different uniform temperatures,” *Computers & Mathematics with Applications*, vol. 35, no. 1-2, pp. 15–28, 1998.
- [117] Y. Sone, “Flow induced by thermal stress in rarefied gas,” *The Physics of Fluids*, vol. 15, no. 8, pp. 1418–1423, 1972.
- [118] Y. Sone and M. Yoshimoto, “Demonstration of a rarefied gas flow induced near the edge of a uniformly heated plate,” *Physics of Fluids*, vol. 9, no. 11, pp. 3530–3534, 1997.
- [119] N. Selden, C. Ngalande, S. Gimelshein, E. Muntz, A. Alexeenko, and A. Ketsdever, “Area and edge effects in radiometric forces,” *Physical Review E*, vol. 79, no. 4, p. 041 201, 2009.
- [120] K. Fowee, A. Ibrayeva, A. Strongrich, and A. Alexeenko, “Experimental measurements and numerical modeling of a thermostress convection-based actuator,” in *AIP Conference Proceedings*, AIP Publishing, vol. 1786, 2016, p. 200 004.
- [121] A. Ibrayeva, “Numerical modeling of thermal edge flow,” Master’s thesis, Purdue University, 2017.

- [122] A. Passian, A. Wig, F. Meriaudeau, T. Ferrell, and T. Thundat, “Knudsen forces on microcantilevers,” *Journal of applied physics*, vol. 92, no. 10, pp. 6326–6333, 2002.
- [123] A. Passian, R. Warmack, T. Ferrell, and T. Thundat, “Thermal transpiration at the microscale: A crookes cantilever,” *Physical review letters*, vol. 90, no. 12, p. 124 503, 2003.
- [124] V. Foroutan, R. Majumdar, O. Mahdavi pour, S. Ward, and I. Paprotny, “Levitation of untethered stress engineered microflyers using thermophoretic (knudsen) force,” in *Technical Digest of the Hilton Head Workshop*, 2014, pp. 105–106.
- [125] R. T. Nallapu, A. Tallapragada, and J. Thangavelautham, “Radiometric actuators for spacecraft attitude control,” *arXiv preprint arXiv:1701.07545*, 2017.
- [126] B. M. Cornella, A. D. Ketsdever, N. E. Gimelshein, and S. F. Gimelshein, “Analysis of multivane radiometer arrays in high-altitude propulsion,” *Journal of Propulsion and Power*, vol. 28, no. 4, pp. 831–839, 2012.
- [127] S. Jaiswal, J. Hu, J. K. Brillon, and A. A. Alexeenko, “A discontinuous galerkin fast spectral method for multi-species full boltzmann on streaming multi-processors,” in *Proceedings of the Platform for Advanced Scientific Computing Conference*, ser. PASC ’19, Zurich, Switzerland: ACM, 2019, 4:1–4:9, ISBN: 978-1-4503-6770-7. DOI: [10.1145/3324989.3325714](https://doi.org/10.1145/3324989.3325714). [Online]. Available: <http://doi.acm.org/10.1145/3324989.3325714>.
- [128] S. Loyalka, “Knudsen forces in vacuum microbalance,” *The Journal of Chemical Physics*, vol. 66, no. 11, pp. 4935–4940, 1977.
- [129] N. Selden, C. Ngalande, N. Gimelshein, S. Gimelshein, and A. Ketsdever, “Origins of radiometric forces on a circular vane with a temperature gradient,” *Journal of Fluid Mechanics*, vol. 634, pp. 419–431, 2009.
- [130] J. G. Fierro and A. A. Garcia, “Gas dynamics at low pressures in a vacuum microbalance,” *Vacuum*, vol. 31, no. 2, pp. 79–84, 1981.
- [131] A. Alexeenko, E. P. Muntz, M. Gallis, and J. Torczynski, “Comparison of kinetic models for gas damping of moving microbeams,” in *36th AIAA Fluid Dynamics Conference and Exhibit*, 2006, p. 3715.
- [132] T. Zhu and W. Ye, “Origin of knudsen forces on heated microbeams,” *Physical Review E*, vol. 82, no. 3, p. 036 308, 2010.
- [133] J. Nabeth, S. Chigullapalli, and A. A. Alexeenko, “Quantifying the knudsen force on heated microbeams: A compact model and direct comparison with measurements,” *Physical Review E*, vol. 83, no. 6, p. 066 306, 2011.

- [134] Y. A. Anikin, “Numerical study of radiometric forces via the direct solution of the boltzmann kinetic equation,” *Computational Mathematics and Mathematical Physics*, vol. 51, no. 7, pp. 1251–1266, 2011.
- [135] F. Tcheremissine, “Conservative evaluation of boltzmann collision integral in discrete ordinates approximation,” *Computers & Mathematics with Applications*, vol. 35, no. 1-2, pp. 215–221, 1998.
- [136] A. Lotfian and E. Roohi, “Radiometric flow in periodically patterned channels: Fluid physics and improved configurations,” *Journal of Fluid Mechanics*, vol. 860, pp. 544–576, 2019.
- [137] A. Pikus, I. B. Sebastião, A. Strongrich, and A. Alexeenko, “Characterization of a knudsen force based vacuum sensor for N₂H₂O gas mixtures,” *Vacuum*, vol. 161, pp. 130–137, 2019.
- [138] L.-S. Luo and S. S. Girimaji, “Theory of the lattice boltzmann method: Two-fluid model for binary mixtures,” *Physical Review E*, vol. 67, no. 3, p. 036 302, 2003.
- [139] J. R. Haack, C. D. Hauck, and M. S. Murillo, “A conservative, entropic multispecies bgk model,” *Journal of Statistical Physics*, vol. 168, no. 4, pp. 826–856, 2017.
- [140] A. V. Bobylev, M. Bisi, M. Groppi, G. Spiga, and I. F. Potapenko, “A general consistent bgk model for gas mixtures,” *Kinetic & Related Models*, vol. 11, no. 6, 2018.
- [141] S. Brull, “An ellipsoidal statistical model for gas mixtures,” *Communications in Mathematical Sciences*, vol. 8, pp. 1–13, 2015.
- [142] K. Xu and J.-C. Huang, “A unified gas-kinetic scheme for continuum and rarefied flows,” *Journal of Computational Physics*, vol. 229, no. 20, pp. 7747–7764, 2010.
- [143] Z. Guo, K. Xu, and R. Wang, “Discrete unified gas kinetic scheme for all knudsen number flows: Low-speed isothermal case,” *Physical Review E*, vol. 88, no. 3, p. 033 305, 2013.
- [144] A. Alexeenko, A. G. Cofer, and S. D. Heister, *Microelectronic thermal valve*, US Patent App. 15/370,633, Jun. 2017.
- [145] J. W. Lee, R. Tung, A. Raman, H. Sumali, and J. P. Sullivan, “Squeeze-film damping of flexible microcantilevers at low ambient pressures: Theory and experiment,” *Journal of Micromechanics and Microengineering*, vol. 19, no. 10, p. 105 029, 2009.

- [146] R. A. Bidkar, R. C. Tung, A. A. Alexeenko, H. Sumali, and A. Raman, “Unified theory of gas damping of flexible microcantilevers at low ambient pressures,” *Applied Physics Letters*, vol. 94, no. 16, p. 163 117, 2009.
- [147] M. A. Gallis and J. R. Torczynski, “An improved reynolds-equation model for gas damping of microbeam motion,” *Journal of Microelectromechanical systems*, vol. 13, no. 4, pp. 653–659, 2004.
- [148] A. Granaldi and P. Decuzzi, “The dynamic response of resistive microswitches: Switching time and bouncing,” *Journal of Micromechanics and Microengineering*, vol. 16, no. 7, p. 1108, 2006.
- [149] R. Biswas, K. D. Devine, and J. E. Flaherty, “Parallel, adaptive finite element methods for conservation laws,” *Applied Numerical Mathematics*, vol. 14, no. 1-3, pp. 255–283, 1994.
- [150] B. Cockburn, G. E. Karniadakis, and C.-W. Shu, “The development of discontinuous galerkin methods,” in *Discontinuous Galerkin Methods*, Springer, 2000, pp. 3–50.
- [151] A. Bakhtiari, D. Malhotra, A. Raoofy, M. Mehl, H.-J. Bungartz, and G. Biros, “A parallel arbitrary-order accurate amr algorithm for the scalar advection-diffusion equation,” in *Proceedings of the International Conference for High Performance Computing, Networking, Storage and Analysis*, ser. SC ’16, Salt Lake City, Utah: IEEE Press, 2016, 44:1–44:12, ISBN: 978-1-4673-8815-3. [Online]. Available: <http://dl.acm.org/citation.cfm?id=3014904.3014963>.
- [152] S. Jaiswal, A. Pikus, A. Strongrich, I. B. Sebastião, J. Hu, and A. A. Alexeenko, “Quantification of thermally-driven flows in microsystems using boltzmann equation in deterministic and stochastic contexts,” *Physics of Fluids*, vol. 31, no. 8, p. 082 002, 2019.
- [153] **S. Jaiswal**, J. Hu, and A. A. Alexeenko, “Fast deterministic solution of the full boltzmann equation on graphics processing units,” *AIP Conference Proceedings*, vol. 2132, no. 1, p. 060 001, 2019. DOI: [10.1063/1.5119541](https://doi.org/10.1063/1.5119541). [Online]. Available: <https://doi.org/10.1063/1.5119541>.
- [154] **S. Jaiswal**, I. B. Sebastião, A. Strongrich, and A. A. Alexeenko, “FEMTA micro-propulsion system characterization by DSMC,” *AIP Conference Proceedings*, vol. 2132, no. 1, p. 070 006, 2019. DOI: [10.1063/1.5119560](https://doi.org/10.1063/1.5119560). [Online]. Available: <https://doi.org/10.1063/1.5119560>.

- [155] A. Pikus, I. B. Sebastião, **S. Jaiswal**, M. Gallis, and A. A. Alexeenko, “DSMC-SPARTA implementation of majorant collision frequency scheme,” *AIP Conference Proceedings*, vol. 2132, no. 1, p. 070026, 2019. DOI: [10.1063/1.5119580](https://doi.org/10.1063/1.5119580). [Online]. Available: <https://doi.org/10.1063/1.5119580>.
- [156] **S. Jaiswal**, R. Reddy, R. Banerjee, S. Sato, D. Komagata, M. Ando, and J. Okada, “An efficient GPU parallelization for arbitrary collocated polyhedral finite volume grids and its application to incompressible fluid flows.,” in *23rd IEEE High Performance Computing Workshop*, IEEE, Dec. 2016. [Online]. Available: <https://doi.org/10.1109/HiPCW.2016.020>.
- [157] S. Holay, R. Reddy, **S. Jaiswal**, and R. Banerjee, “High fidelity simulations of binary collisions of liquid drops.,” in *18th Annual Conference on Liquid Atomization and Spray Systems*, ILASS, Nov. 2016. [Online]. Available: <http://goo.gl/bvgzjH>.
- [158] **S. Jaiswal** and N. Dongari, “Implementation of knudsen layer effects in open source cfd solver for effective modeling of microscale gas flows.,” in *Proceedings of 1st International ISHMT-ASTFE and 23rd National Heat and Mass Transfer conference*, Kerala, India: ISHMT-ASTFE, Dec. 2015. [Online]. Available: <http://goo.gl/sLO2Jg>.
- [159] F. G. Pikus and **S. Jaiswal**, “Limited basis quantum particle definitions in applications of quantum computing to electronic design automation processes,” US Patent 10,846,448, Nov. 2020.

A. VITA

Shashank Jaiswal

EDUCATION

Purdue University, West Lafayette

PhD in Aeronautics and Astronautics,

Major: Aerodynamics, CGPA : 3.89/4.0 May'18 - Present

MS in Physics and Astronomy,

Major: Quantum Information Science, CGPA: 3.80/4.0 Aug'19 - May'21

MS in Aeronautics and Astronautics,

Major: Aerodynamics, CGPA : 3.88/4.0 Aug'16 - May'18

Indian Institute of Technology (IIT), Hyderabad

B.Tech in Mechanical Engineering (Honors),

Focus: Computational Fluid Dynamics, CGPA : 8.28/10.0 Aug'12 - May'16

WORK EXPERIENCE

Mentor Graphics (Siemens), Wilsonville, OR May'19 - Aug'19

R&D Calibre Design-to-silicon Intern with Dr. Fedor Pikus (Chief engineering scientist)

- Research in development of quantum algorithms for Electronic Design Automation (EDA).

RESEARCH INTERESTS

Computational Fluid Dynamics, High performance computing, Kinetic theory, Quantum computing, Augmented Reality, Direct simulation Monte Carlo, Finite elements, Rarefied Gas Dynamics.

SKILLS

- Excellent quantitative programming skills in Python, C++ (8+ years)
- Experience with development of numerical schemes for solving partial differential equations (PDE)

- Experience with finite element, isogeometric schemes, multi-physics design, simulation, and analysis
- Experience with PDE based machine-learning models (optimal transport viewpoint)
- Experience with development of quantum algorithms and quantum software stacks
- Experience with parallel computing: MPI, GPU, OpenMP, pThreads,
- Experience with writing performance portable codes, profiling
- Proficient working in a Linux/UNIX environment; git/subversion, automated build/test systems, testing and release processes

OPEN SOURCE CODES (AS SOLE DEVELOPER)

dgfs1D: Discontinuous Galerkin fast spectral

(https://github.com/jaisw7/dgfs1D_gpu)

A multi-CPU/multi-GPU code for solving single/multi-species 1D-3V full Boltzmann equation. This code achieved a parallel efficiency of 99% on 36 GPUs.

frfs: Flux-reconstructed fast spectral

(<https://github.com/jaisw7/frfs>)

A multi-CPU/multi-GPU code for solving single/multi-species full 3D-3V Boltzmann equation.

DISTINCTIONS

- Awarded **ACM SIGHPC Travel Grant for PASC'19** (1/4 awardees internationally, 1/2 awardees outside EU), 2019.
- At 22, I co-wrote the first **National Science Foundation (NSF CDS&E #1854829)** proposal for \sim \$0.35 million based on my Masters research work, 2018. Purdue University, West Lafayette.

- Awarded **Undergraduate Research Excellence** (among $\sim 1\%$ of the batch), 2016. Indian Institute of Technology, Hyderabad.
- **All India Rank 1335** among ~ 1.3 million examinees (top $\sim 0.1\%$), in All India Engineering Entrance Examination ([AIEEE](#)), 2012.

PUBLICATIONS

1. S. Jaiswal, J. Hu, J. K. Brillon, *et al.*, “A discontinuous galerkin fast spectral method for multi-species full boltzmann on streaming multi-processors,” in *Proceedings of the Platform for Advanced Scientific Computing Conference*, ser. PASC '19, Zurich, Switzerland: ACM, 2019, 4:1–4:9, ISBN: 978-1-4503-6770-7. DOI: [10.1145/3324989.3325714](#). [Online]. Available: <http://doi.acm.org/10.1145/3324989.3325714>
2. S. Jaiswal, A. Alexeenko, and J. Hu, “A discontinuous Galerkin fast spectral method for the full Boltzmann equation with general collision kernels,” *J. Comput. Phys.*, vol. 378, pp. 178–208, 2019
3. S. Jaiswal, A. A. Alexeenko, and J. Hu, “A discontinuous Galerkin fast spectral method for the multi-species full boltzmann equation,” *Comput. Methods Appl. Mech. Engrg.*, vol. 352, pp. 56–84, 2019. [Online]. Available: <https://doi.org/10.1016/j.cma.2019.04.015>
4. S. Jaiswal, A. Pikus, A. Strongrich, *et al.*, “Quantification of thermally-driven flows in microsystems using boltzmann equation in deterministic and stochastic contexts,” *Physics of Fluids*, vol. 31, no. 8, p. 082002, 2019
5. **S. Jaiswal**, J. Hu, and A. A. Alexeenko, “Fast deterministic solution of the full boltzmann equation on graphics processing units,” *AIP Conference Proceedings*, vol. 2132, no. 1, p. 060001, 2019. DOI: [10.1063/1.5119541](#). [Online]. Available: <https://doi.org/10.1063/1.5119541>

6. **S. Jaiswal**, I. B. Sebastião, A. Strongrich, *et al.*, “FEMTA micropropulsion system characterization by DSMC,” *AIP Conference Proceedings*, vol. 2132, no. 1, p. 070 006, 2019. DOI: [10.1063/1.5119560](https://doi.org/10.1063/1.5119560). [Online]. Available: <https://doi.org/10.1063/1.5119560>
7. **S. Jaiswal**, I. B. Sebastião, and A. A. Alexeenko, “DSMC-SPARTA implementation of M-1 scattering model,” *AIP Conference Proceedings*, vol. 2132, no. 1, p. 070 023, 2019. DOI: [10.1063/1.5119577](https://doi.org/10.1063/1.5119577). [Online]. Available: <https://doi.org/10.1063/1.5119577>
8. A. Pikus, I. B. Sebastião, **S. Jaiswal**, *et al.*, “DSMC-SPARTA implementation of majorant collision frequency scheme,” *AIP Conference Proceedings*, vol. 2132, no. 1, p. 070 026, 2019. DOI: [10.1063/1.5119580](https://doi.org/10.1063/1.5119580). [Online]. Available: <https://doi.org/10.1063/1.5119580>
9. **S. Jaiswal**, R. Reddy, R. Banerjee, *et al.*, “An efficient GPU parallelization for arbitrary collocated polyhedral finite volume grids and its application to incompressible fluid flows,” in *23rd IEEE High Performance Computing Workshop*, IEEE, Dec. 2016. [Online]. Available: <https://doi.org/10.1109/HiPCW.2016.020>
10. S. Holay, R. Reddy, **S. Jaiswal**, *et al.*, “High fidelity simulations of binary collisions of liquid drops,” in *18th Annual Conference on Liquid Atomization and Spray Systems*, ILASS, Nov. 2016. [Online]. Available: <http://goo.gl/bvgzjH>
11. **S. Jaiswal** and N. Dongari, “Implementation of knudsen layer effects in open source cfd solver for effective modeling of microscale gas flows,” in *Proceedings of 1st International ISHMT-ASTFE and 23rd National Heat and Mass Transfer conference*, Kerala, India: ISHMT-ASTFE, Dec. 2015. [Online]. Available: <http://goo.gl/sLO2Jg>

PATENTS

1. F. G. Pikus and **S. Jaiswal**, “Limited basis quantum particle definitions in applications of quantum computing to electronic design automation processes,” US Patent 10,846,448, Nov. 2020